



# University of HUDDERSFIELD

## University of Huddersfield Repository

Hamad, Naima

THE ANALYSIS OF POWER SUPPLY SIGNALS BY INCLUDING PHASE EFFECTS FOR MACHINE FAULT DIAGNOSIS

### Original Citation

Hamad, Naima (2019) THE ANALYSIS OF POWER SUPPLY SIGNALS BY INCLUDING PHASE EFFECTS FOR MACHINE FAULT DIAGNOSIS. Doctoral thesis, University of Huddersfield.

This version is available at <http://eprints.hud.ac.uk/id/eprint/34951/>

The University Repository is a digital collection of the research output of the University, available on Open Access. Copyright and Moral Rights for the items on this site are retained by the individual author and/or other copyright owners. Users may access full items free of charge; copies of full text items generally can be reproduced, displayed or performed and given to third parties in any format or medium for personal research or study, educational or not-for-profit purposes without prior permission or charge, provided:

- The authors, title and full bibliographic details is credited in any copy;
- A hyperlink and/or URL is included for the original metadata page; and
- The content is not changed in any way.

For more information, including our policy and submission procedure, please contact the Repository Team at: [E.mailbox@hud.ac.uk](mailto:E.mailbox@hud.ac.uk).

<http://eprints.hud.ac.uk/>

**THE ANALYSIS OF POWER SUPPLY SIGNALS BY  
INCLUDING PHASE EFFECTS FOR MACHINE FAULT  
DIAGNOSIS**

---

A thesis submitted to the University of Huddersfield in partial fulfilment  
of the requirements for the degree of Doctor of Philosophy

**By**

**NAIMA HAMAD**

School of Computing and Engineering

The University of Huddersfield

**January 2019**

## **Abstract**

Substantial efforts have been devoted to developing Condition Monitoring techniques to provide timely preventative measures for ensuring a safe and cost-effective operation of electromechanical systems. High investment of installation and implementation in using conventional condition monitoring techniques such as vibration based monitoring makes it difficult to be used in most industries such as petrochemical processing, food and drinking processes, paper mills and so on where large number of motor drives are used but operational profits are very limited. To overcome the shortages of vibration based monitoring, this project focuses on developing condition monitoring techniques based on electrical signal analysis which can offer great savings as electric signatures that can monitor a large system are generally available in most motor drives. However, fault signatures in electrical signatures such as instantaneous current and voltage signals are very weak and contaminated by noise. To enhance the signatures, this study has focused on using two more advanced signal processing approaches: 1) Modulation signal bispectrum analysis, which enhances the modulation and suppresses random noise by including phase linkages.

2) Instantaneous phase quantities including conventional instantaneous power factor and a novel instantaneous phase of voltage and current which highlights instantaneous phase changes through a summation of instantaneous phases in current and voltage signals. It has the ability of enhancing the phase components that are of the same phases in both voltage and current signals, and also cancel out any random components to a great extent, producing more diagnostic information. These two approaches emphasis the use of phase information along with that of amplitudes and frequency in a signal that is based on in most previous methods in the condition monitoring fields.

Based on a general electromechanical system comprising of a AC motor, a gearbox and a DC generator, it firstly explored the characteristics of the signatures by modelling and simulation studies, which lead to that faults in a sensorless Variable speed drive system can produce combined amplitude and frequency modulation effects in both current and voltage signals fed to the AC motor. Moreover, the modulating frequencies and levels are closely associated with the rotational frequencies of the gearbox and fault severity respectively, which become more significant at higher load conditions.

Experimental evaluations have found that these two proposed methods allow common faults in the downstream gearbox including gear tooth breakage, oil shortage and excessive bearing clearances

to be detected and diagnosed under high load conditions, showing the effectiveness and accuracy of these two new approaches. Furthermore, the results show that the electrical signature analysis is capable of detecting and diagnosing different faults in sensorless variable speed drive systems. Instantaneous phase of voltage and current has been shown to provide more consistent and accurate separation between the three different faults under different loads. The use of the modulation signal bispectrum analysis succeed to provide an improved, accurate and reliable diagnostic with the power signal providing the best means of detecting and determining fault severity with good separation between fault levels.

## **DEDICATION**

---

Special thanks to my husband **Nuh**, who has stood by my side and patiently supported me through these past years. Your encouragement and assistance on all things has been, and is, greatly appreciated. Without you, none of this would have been possible.

## ACKNOWLEDGEMENTS

---

My sincere gratitude to my supervisors; **Professor Fengshou Gu** whose expertise, encouragement and direction were vital for the completion of my research project and the writing-up of this thesis. I would like also to thank **Professor Andrew Ball** for his understanding, kindness, guidance, constant encouragement and advice throughout this research.

A special thanks to **Dr. Samieh Abu Saad** for his continued support and assistance.

To the souls of my **father** and **mother**. To all my relatives and friends whose affection, love, encouragement and prayers for my success.

I would like also to convey my thanks to the **Libyan Embassy** for sponsoring and supporting me.

My appreciation and thanks to those in the Centre for Efficiency and Performance Engineering (**CEPE**) research group for their support and friendship.

## **DECLARATION OF ORIGINALITY**

---

This is to certify that I am responsible for the work submitted in this thesis, that the original work is my own except as specified in acknowledgments or in references, and that neither the thesis nor the original work contained therein has been submitted to this or any other institution for a degree.

*Naima Hamad*

## LIST OF PUBLICATIONS

---

1. **Naima. Hamad**, Khaldoon F. Brethee, Fengshou Gu and Andrew D. Ball, An Investigation of Electrical Motor Parameters in a Sensorless Variable Speed Drive for Machine Fault Diagnosis. In the Proceeding of the 22nd International Conference on Automation and Computing, ICAC 2016.
2. **Naima Hamad**, Samieh Abu Saad., Fengshou Gu and Andrew Ball, Electrical Signature Analysis using Modulation Signal Bispectrum for Faults Diagnosis of Induction Motor Systems with Sensorless Variable Speed Drives, Proceedings of the 1<sup>st</sup> Libyan International Conference on Electrical Engineering and Technologies (LICEET2018). Tripoly-Libya. p. 312-318.
3. **Naima. Hamad**, Xiuquan Sun, Ruiliang Zhang, Samieh Abusaad, Fengshou Gu and Andrew D. Ball, The Diagnostics of Lubricant Shortages in a Two Stage Gearbox Using the Instantaneous Phases of the AC Motor with Sensorless Drives. In the Proceeding of the 24th International Conference on Automation and Computing, ICAC 2018.
4. Khaldoon F. Brethee, Ruiliang Zhang, **Naima Hamad**, Fengshou Gu and Andrew D. Ball, Influence of Lubricant Starvation on Gearbox Vibration Signatures for Condition Monitoring. 2016. In the 29th International Congress on Condition Monitoring and Diagnostic Engineering Management COMADEM 2016.

# TABLE OF CONTENTS

---

<b>Abstract.....</b>	<b>1</b>
<b>DEDICATION.....</b>	<b>3</b>
<b>ACKNOWLEDGEMENTS .....</b>	<b>4</b>
<b>DECLARATION OF ORIGINALITY .....</b>	<b>5</b>
<b>LIST OF PUBLICATIONS .....</b>	<b>6</b>
<b>TABLE OF CONTENTS .....</b>	<b>7</b>
<b>LIST OF FIGURES .....</b>	<b>11</b>
<b>LIST OF TABLES .....</b>	<b>15</b>
<b>LIST OF NOTATIONS.....</b>	<b>16</b>
<b>LIST OF ABBREVIATIONS .....</b>	<b>20</b>
<b>CHAPTER ONE: INTRODUCTION.....</b>	<b>21</b>
1.1 Background of Condition Monitoring.....	22
1.2 Research Motivations.....	23
1.3 Aims and Objectives of the Research .....	24
1.4 Research Methodology.....	25
1.5 Organization of the Thesis .....	27
<b>CHAPTER TWO: INDUCTION MOTOR DRIVES AND ITS PRINCIPLES.....</b>	<b>28</b>
2.1 Introduction .....	29
2.2 Induction Machines .....	29
2.2.1 Types and Structure of Induction Motors .....	29
2.2.2 Basics Operation of Induction Motors .....	32
2.3 Slip and Speed.....	33
2.4 Equivalent-Circuit Models .....	33
2.5 IM Rotor Current, Speed, Load and Torque .....	34
2.6 Theory of AC Drives and Traditional Drives.....	36
2.7 Construction and Operation Principles of PWM Drives .....	38

2.8	Traditional VSDs.....	40
2.8.1	Voltage Source Inverter (VSI) .....	40
2.8.2	Current Source Inverter (CSI).....	41
2.8.3	Pulse Width Modulation (PWM) .....	41
2.9	Open- and Closed-Loop Control .....	42
2.10	PID Controllers .....	43
2.11	Sensorless Field-Oriented Control (FOC) .....	45
2.12	Common Induction Motor’s Faults .....	51
2.12.1	Electrical Faults .....	52
2.12.2	Mechanical Faults .....	53
2.13	Key Findings .....	56
<b>CHAPTER THREE: FAULT DIGNOSTIC BASED ON ELEECTRICAL SIGNATURE ANALYSIS .....</b>		<b>57</b>
3.1	Introduction .....	58
3.2	The Need for Condition Monitoring .....	58
3.3	Conventional Condition Monitoring Systems of Induction Motor Drives .....	59
3.3.1	Vibration Monitoring .....	60
3.3.2	Acoustic Monitoring .....	60
3.3.3	Thermal Monitoring.....	61
3.3.4	Electrical Signature Analysis (ESA).....	61
3.4	Key Findings .....	70
<b>CHAPTER FOUR: EXPERIMENTAL FACILITIES.....</b>		<b>72</b>
4.1	Introduction .....	73
4.2	Test Rig Description.....	73
4.2.1	Mechanical Systems.....	73
4.2.2	Electrical System .....	77
4.2.3	Data Acquisition Systems (DAQS) .....	82
4.2.4	Measurements Systems.....	83
4.3	Gears - an Overview.....	86
4.4	Types of Gears .....	87

4.5	Gear Teeth Failure Modes.....	89
4.6	Causes of Gear Failures.....	90
4.7	Gearbox Characteristic Frequencies.....	91
4.8	Data Processing.....	92
4.8.1	Spectrum Analysis .....	92
4.8.2	MSB Analysis .....	92
4.9	Key Findings .....	95
<b>CHAPTER FIVE: MODELLING AND SIMULATION FOR FIELD-ORIENTED INDUCTION MOTOR DRIVES FOR DIAGONSTIC .....</b>		<b>96</b>
5.1	Introduction .....	97
5.2	Induction Motor Model .....	97
5.3	Open-Loop Control (V/Hz).....	105
5.4	Modelling the Field-Oriented Control (FOC) .....	106
5.5	Fault Effect on Electrical Parameters.....	106
5.6	Fault Detection Based on Sensorless Drive .....	110
5.7	Simulation Results and Validation.....	113
5.7.1	Healthy Case .....	113
5.7.2	Faulty Case.....	119
5.8	Key Findings .....	125
<b>CHAPTER SIX: DETECTION AND DIAGNOSIS OF GEAR TOOTH BREAKAGE ...</b>		<b>126</b>
6.1	Introduction .....	127
6.2	Effect of Gear Tooth Breakage .....	127
6.3	Fault Simulated and Test Procedure.....	128
6.4	Results and Findings .....	130
6.4.1	Spectrum Analysis .....	130
6.4.2	MSB Analysis .....	138
6.4.3	Comparison between FFT and MSB.....	142
6.5	Key Findings .....	146
<b>CHAPTER SEVEN: DIAGNOSIS OF DIFFERENT OIL LEVELS TEST.....</b>		<b>147</b>
7.1	Introduction .....	148

7.2	Faults Simulated and Test Procedure .....	151
7.3	Results and Discussion.....	153
7.3.1	Spectrum Analysis .....	153
7.3.2	MSB Analysis .....	161
7.3.3	Comparison between FFT and MSB.....	163
7.4	Key Findings .....	163
<b>CHAPTER EIGHT: ELECTRICAL SIGNATURE BASED DIAGNOSIS OF INCREASED BEARING CLEARANCE.....</b>		<b>165</b>
8.1	Introduction .....	166
8.2	Effect of Bearing Clearance .....	166
8.3	Fault Simulation and Test Procedure .....	168
8.4	Results and Discussion.....	172
8.4.1	Spectrum Analysis .....	172
8.4.2	MSB Analysis .....	179
8.4.3	Comparison between Spectrum and MSB .....	184
8.5	Key Findings.....	185
<b>CHAPTER NINE: CONCLUSIONS AND FUTURE WORK.....</b>		<b>186</b>
9.1	Objectives and Achievements .....	187
9.2	Conclusions .....	188
9.3	Research Contributions to Knowledge.....	190
9.4	Suggestions for Further Work .....	191
<b>REFERENCES.....</b>		<b>192</b>

## LIST OF FIGURES

---

Figure 1-1 Framework for the research work .....	26
Figure 2-1: Basic construction of induction motor (Taken by the author). .....	30
Figure 2-2: Stator lamination .....	30
Figure 2-3: Squirrel cage rotor.....	31
Figure 2-4: Induction motor equivalent circuit [19] .....	34
Figure 2-5: Torque-speed and current-speed curves of a typical IM (modified from [14]). .....	35
Figure 2-6: A block diagram of a PWM drive [25] .....	39
Figure 2-7: Voltage and current waveform of a PWM drive [26] .....	39
Figure 2-8: Voltage and frequency created from a PWM drive [26].....	40
Figure 2-9: Block diagram of a typical VVI drives redrawn from [27].....	40
Figure 2-10: A block diagram of a typical CSI, redrawn from [27] .....	41
Figure 2-11: Open-loop block diagram, redrawn from [28] .....	42
Figure 2-12: Closed-loop block diagram, redrawn from [30].....	43
Figure 2-13: The principle of FOC [39] .....	46
Figure 2-14: Vector control transformations [40].....	47
Figure 2-15: Sensorless FOC block diagram redrawn by the author [45] .....	48
Figure 2-16: Block diagram for MRAS control redrawn from [46] .....	49
Figure 2-17: Classification of induction motor faults, redrawn from [54]. .....	51
Figure 2-18: Problems in induction motor, redrawn from [53] .....	52
Figure 2-19: Graphical representation of stator faults amended from [55] .....	53
Figure 2-20: Bearing main components (Taken by the author).....	55
Figure 3-1: Block diagram of conventional CM, (image redrawn by the author) .....	60
Figure 3-2: Instantaneous power factor's block diagram .....	68
Figure 4-1: Photograph of the test rig .....	74
Figure 4-2: Schematic diagram of the test rig.....	74
Figure 4-3: Two-stage helical gearbox schematic layout [author]. .....	77
Figure 4-4: Control panel interior .....	78
Figure 4-5: Three phase electrical signals measurement device.....	84
Figure 5-1: AC motor equivalent circuit in the d-q framework.....	98

Figure 5-2: The transformation of the voltages from the (a-b-c) to the stationary $d_s$ - $q_s$ axes (image redrawn by the author).....	99
Figure 5-3: The transformation from the stationary $d_s$ - $q_s$ axes to the rotating d-q axes .....	99
Figure 5-4: Three-phase representation of the rotor and stator windings [122] .....	100
Figure 5-5: Three phase currents from the model.....	114
Figure 5-6: Three phase voltages from the model .....	114
Figure 5-7: Power signals under different conditions.....	115
Figure 5-8: Power signals comparison.....	115
Figure 5-9: Model response and speed errors under 0% and 100% load.....	116
Figure 5-10: Speed and torque response to variable loads .....	117
Figure 5-11: Current signals comparison under different loads .....	117
Figure 5-12: Voltage signals comparison under different loads.....	118
Figure 5-13: Current spectra comparison under different loads .....	118
Figure 5-14: Voltage spectra comparison under different loads.....	119
Figure 5-15: Power spectra comparison under different loads .....	119
Figure 5-16: Current spectra comparison under different loads .....	121
Figure 5-17: Voltage spectra comparison under different loads.....	122
Figure 5-18: Power spectra comparison under different loads .....	123
Figure 5-19: Features at $fr_2$ and full speed .....	124
Figure 5-20: Fault case comparison .....	124
Figure 6-1: Typical test cycle .....	129
Figure 6-2: A photograph of the broken gears (20% - 40%) .....	129
Figure 6-3: Oil temperature under different loads and full speed.....	131
Figure 6-4: Current spectrum under 30% and 100% full load at full speed .....	132
Figure 6-5: Voltage spectrum under 30% and 100% full load and full speed.....	132
Figure 6-6: Power spectrum under 30% and 100% full load and full speed .....	133
Figure 6-7: The current amplitudes at upper and lower sidebands frequency .....	134
Figure 6-8: Amplitudes of the upper and lower sidebands in voltage signal.....	134
Figure 6-9: The power amplitudes at upper and lower sidebands frequencies.....	135
Figure 6-10: Instantaneous power factor variations with faults severity at full speed (5th-run) in the time-domain. ....	135

Figure 6-11: Features averaged from instantaneous power factor .....	136
Figure 6-12: The instantaneous power factor spectra .....	136
Figure 6-13: Features averaged from power factor spectrum from the 5th test run .....	137
Figure 6-14: Performance comparison between current, voltage, and power factor from the 5th test run.....	138
Figure 6-15: Current MSB at 100% load for the healthy case.....	138
Figure 6-16: Current MSB for 20% tooth breakage .....	139
Figure 6-17. Current MSB for 40% tooth breakage .....	139
Figure 6-18: Voltage MSB at 100% load for baseline case.....	140
Figure 6-19: Voltage MSB at 20% tooth breakage.....	140
Figure 6-20. Voltage MSB at 40% tooth breakage.....	141
Figure 6-21. Power bispectrum for the healthy case.....	141
Figure 6-22: Power bispectrum at 20% tooth breakage.....	142
Figure 6-23: Power spectrum at 40% tooth breakage.....	142
Figure 6-24: Amplitude of current peaks for sidebands $fr_2$ for FFT .....	143
Figure 6-25: Amplitude of voltage peaks for sidebands $fr_2$ for FFT .....	143
Figure 6-26. Amplitude of power peaks for sidebands $f_{r2}$ for FFT .....	144
Figure 6-27. Amplitude of current peaks for sidebands $fr_2$ for MSB .....	145
Figure 6-28. Amplitude of voltage peaks for sidebands $fr_2$ for MSB .....	145
Figure 6-29. Amplitude of power peaks for sidebands $fr_2$ for MSB .....	145
Figure 7-1: Schematic illustration of the test gearbox and oil levels.....	153
Figure 7-2: Gearbox oil temperature and surface vibration under different operations .....	154
Figure 7-3: Shaft speed under different lubricant levels.....	155
Figure 7-4: The spectra for a typical set of current and voltage signals .....	156
Figure 7-5: Upper panel IPF signal, lower panel IPF spectrum, for three oil levels .....	157
Figure 7-7: IPF at characteristic frequencies .....	159
Figure 7-8: IPVC at characteristic frequencies.....	160
Figure 7-9: IPF MSB magnitudes at feature frequencies, ( $fr_1$ , $fr_2$ and $fr_3$ ), for four loads and three lubrication levels.....	<b>Error! Bookmark not defined.</b>
Figure 8-1: Mechanical elements of the test rig.....	168
Figure 8-2: Schematic diagram of deep groove ball bearing.....	169

Figure 8-3: Schematic diagram of gear arrangement used in the test.....	171
Figure 8-4: Schematic diagram of operating condition profiles .....	171
Figure 8-5: Current signal spectra at different loads and 70% of full speed for three bearings .....	<b>Error! Bookmark not defined.</b>
Figure 8-6: Voltage signal spectra at different loads and 70% of full speed for three bearings.	174
Figure 8-7: Power signal spectra at different loads and 70% of full speed for three bearings ...	175
Figure 8-8: Amplitude of current peaks of sidebands at $f_s \pm f_{r3}$ obtained using FFT .....	176
Figure 8-9: Amplitude of current peaks of sidebands at $f_s \pm f_{r4}$ obtained using FFT .....	176
Figure 8-10: Amplitude of voltage peaks of sidebands at $f_s \pm f_{r3}$ obtained using FFT.....	177
Figure 8-11: Amplitude of voltage peaks for sidebands $f_s \pm f_{r4}$ obtained using FFT .....	177
Figure 8-12: Amplitude of power peaks of sidebands at $2f_s \pm f_{r3}$ obtained using FFT .....	178
Figure 8-13: Amplitude of power peaks for sidebands $2f_s \pm f_{r4}$ obtained using FFT .....	178
Figure 8-14: Current MSB at 70% full speed and full load for the baseline condition of C3 bearing.....	179
Figure 8-15: MSB at 70% speed and full load with C5 bearing.....	180
Figure 8-16: Voltage MSB at 70% full speed and full load for C3 bearing. ....	180
Figure 8-17: Voltage MSB at 70% speed under full load with C5 bearing.....	181
Figure 8-18: Power signal MSB at 70% of full speed under full load for C3 bearing. ....	181
Figure 8-19: Power signal MSB magnitudes at 70% of full speed under full load for C5 bearing. .....	182
Figure 8-20: Current signal at $f_{r3}$ and $f_{r4}$ .....	183
Figure 8-21: Voltage MSB peaks at $f_{r3}$ and $f_{r4}$ .....	183
Figure 8-22: Power signal MSB peaks at $f_{r3}$ and $f_{r4}$ .....	184

## LIST OF TABLES

---

Table 4-1: Induction motor specifications .....	74
Table 4-2: Generator specifications .....	75
Table 4-3: Rubber coupling specifications .....	76
Table 4-4: Gearboxes specifications .....	76
Table 4-5: EM231 input module technical specifications .....	78
Table 4-6: EM232 output module technical specifications .....	79
Table 4-7: AC variable speed drive specifications .....	80
Table 4-8: DC variable speed drive specifications .....	81
Table 4-9: YE6232B DAQS specifications .....	82
Table 4-10: Current transducer specifications .....	84
Table 4-11: Voltage transducer specifications.....	85
Table 4-12: Encoder specifications.....	85
Table 7-1: Specifications of test gearbox, GB1 .....	153
Table 8-1: Bearing clearance values .....	168
Table 8-2: Bearing specifications .....	169
Table 8-3: First gearbox specifications.....	170
Table 8-4: Second gearbox specifications .....	170

## LIST OF NOTATIONS

---

$b_d$	Ball diameter
$b_{MS}(f_x, f_c)$	MSB of two frequency components
$C$	Bearing clearance
$C_m$	Non-dimensional torque parameter
$D_{out}$	Derivative controller output
$d_p$	Pitch diameter
$e(t)$	Error signal
$E[X(f)X^*(f)]$	Statistical expectation.
$f_c$	Carrier frequency
$f_F$	Fault frequency
$f_{i,o}$	Inner and outer race frequencies
$f_r$	Shaft rotational frequency
$f_s$	Supply frequency
$f_x$	Signal information frequency
$H$	Inertia constant
$I$	Current amplitude
$i^*$	Conjugate of complex current
$i_{ds}$	d-axis stator phase current
$i_{dr}$	d-axis rotor phase current
$I_m$	Current RMS value
$I_{out}$	Integral controller output
$i_{qr}$	q-axis rotor phase current
$i_{qs}$	q-axis stator phase current
$i_{sa}, i_{sb}, i_{sc}$	Stator winding currents
$I_{ra}, i_{rb}, i_{rc}$	Rotor winding currents
$J$	Moment of inertia
$K_d$	PI controller derivative gain
$K_i$	PI controller integral gain
$K_p$	PI controller proportional gain

$L_{lr}$	Rotor leakage inductance
$L_{ls}$	Stator leakage inductance
$L_m$	Mutual inductance
$L_r$	Rotor inductance
$L_s$	Stator inductance
$n_b$	Number of bearing balls
$n_r$	Rotor speed
$n_s$	Synchronous speed
$p$	Number of poles
$P$	Active power
$P_g$	Power of the air gap
$P_{out}$	Proportional controller output
$Q$	Reactive power
$QPC$	quadratic phase coupling
$R_c$	Core loss component
$R_P$	Gear pitch radius
$R_r$	Rotor resistance
$R_s$	Stator resistance
$S$	Apparent power
$S_b$	Rated power
$S_m$	Submerged surface area
Subscripts $d$	d-reference frame coordinates
Subscripts $q$	q-reference frame coordinates
$T_{ch}$	Gear churning torque
$T_{em}$	Electromagnetic torque
$T_{load}$	Load torque
$T_m$	Motor torque
$T_r$	Rotor time constant
$V$	Voltage amplitude
$V_a, V_b, V_c$	Phase voltages for the $a$ , $b$ , and $c$ phases
$V_{dr}$	d-axis rotor phase voltage

$V_{ds}$	d-axis stator phase voltage
$V_m$	Voltage RMS value
$V_{qr}$	q-axis rotor phase voltage
$V_{qs}$	q-axis stator phase voltage
$V_{sa}, V_{sb}, V_{sc}$	Stator winding voltages
$V_{ra}, V_{rb}, V_{rc}$	Rotor winding voltages
$x_{ls}$	The stator leakage reactance
$x_{lr}$	Rotor leakage reactance
$x_m$	Magnetization reactance
$X(f)$	Discrete Fourier transform
$X^*(f)$	Complex conjugate of $X(f)$
$Z_1$	Drive gear at first stage
$Z_2$	Driven gear at first stage
$Z_3$	Drive gear at second stage
$Z_4$	Driven gear at second stage
$Z_{ij}$	Gear teeth number of speed increaser gearbox
$Z_{rj}$	Gear teeth number of speed reducer gearbox
$\omega_l$	The input shaft speed in rpm
$\omega_f$	Angular fault frequency
$\omega_m$	Rotor angular mechanical frequency
$\omega_r$	Rotor angular speed
$\omega_s$	Synchronous angular speed
$\omega_{sl}$	Slip angular speed
$\Psi_{dm}$	Magnetizing flux linkage in $d$ axis
$\Psi_{dr}$	d- axis flux linkage of rotor
$\Psi_{ds}$	d- axis flux linkage of stator
$\Psi_{qs}$	q-axis flux linkage of stator
$\Psi_{qr}$	q- axis flux linkage of rotor
$\Psi_r$	Rotor flux
$\Psi_{ra} \Psi_{rb} \Psi_{rc}$	Rotor winding flux
$\Psi_s$	Stator flux

$\Psi_{sa} \Psi_{sb} \Psi_{sc}$	Stator winding flux
$\alpha_I$	Phase angle between voltage and current
$\alpha_\psi$	Phase angle between the stator flux and voltage
$\beta$	Contact angle
$\sigma$	Motor leakage coefficient.
$\rho$	Density of lubricating oil
$\phi_{MS}$	Total phase of the MSB
$\theta_i(t)$	Instantaneous current phase
$\theta_v(t)$	Instantaneous voltage phase

## LIST OF ABBREVIATIONS

---

AC	Alternative current
AM	Amplitude modulation
BL	Baseline
CM	Condition monitoring
CSI	Current source inverter
DAQS	Data acquisition system
DC	Direct current
ESA	Electrical signature analysis
FFT	Fast Fourier transform
FM	Frequency modulation
FOC	Field oriented control
GB	Gearbox
HOS	Higher order spectra
VSI	Voltage source inverter
IMs	Induction motors
IPF	Instantaneous power factor
IPFSA	Instantaneous power factor signature analysis
IPVC	Instantaneous phase of voltage-current
MRAS	Model reference adaptive system
MCSA	Motor current signature analysis
MVSA	Motor voltage signature analysis
MPSA	Motor power signature analysis
MSB	Modulation signal bispectrum
PLC	Programmable logic controller
PWM	Pulse width modulator
SNR	Signal to noise ratio
TB	Tooth breakage
VSDs	Variable speed drives

## CHAPTER ONE: INTRODUCTION

---

*This chapter presents an overview of machine condition monitoring and fault diagnosis necessary for efficient operation and continued high performance using of machines with sensorless variable speed drives. It then presents the motivation for this research. Next, it states the aims and objectives of the study and then describes the methodology pursued. Finally, it presents a brief outline of the content and layout of the thesis.*

## 1.1 Background of Condition Monitoring

Induction motor (IM) driven mechanical transmission systems play an important role in a wide range of industrial applications because of their high efficiency and flexible performance. Despite their inherent reliability, electrical machines are susceptible to many unwanted stresses, which lead to both electrical and mechanical faults causing failure and interruption of the operation of the motor. Thus, condition monitoring in real time is an essential part of industrial applications in order to minimize unforeseen machine breakdowns and enable necessary corrective actions before failures occur. This can provide the information required to accurately determine the optimal schedule for planned maintenance activities [1-3].

There are many methods to monitor the conditions of a machine; including acoustic, vibration and/or thermal monitoring etc. Research to improve condition monitoring (CM) reliability and accuracy is ongoing with the recent advances made in monitoring and analyzing the motor's electrical signature analysis (ESA) to provide means by which the presence of IM faults can be detected and diagnosed. For example, analysis of sidebands in the spectrums of current and voltage has recently been shown to be capable of identifying system faults. A great advantage of ESA is that it permits remote inspection and monitoring of the health of the system via, say, the motor's control-panel [4, 5].

Sensorless variable speed drive (VSD) driven systems act to control the electrical supply of the motor with the target of maintaining constant speed. If, say, a mechanical fault occurs, there is likely to be a fluctuation in the torque "felt" by the motor, which will result in corresponding fluctuations in the motor's speed and which, in turn, will vary the position of the rotation speed of the rotor. These variations from normal operation will affect the slip frequency, and so the presence of a fault can feed through to change the torque current or voltage [6].

The simultaneous increased operational complexity of motor drivers and the rapid progress made in the field of technology, have substantially increased the possibilities for CM and fault detection to use more sophisticated signal processing methods to extract more accurate and reliable characteristics [7]. One of the most powerful signal processing methods used in CM to provide a more accurate diagnosis is modulation signal bispectrum analysis, a higher order spectral (HOS) analysis which has unique properties of nonlinear identification, phase information and noise elimination [8].

## 1.2 Research Motivations

Increasingly, industry is using VSDs to improve the efficiency of production processes. Sensorless VSDs are “sensorless” only in the sense that there is no mechanical or external sensor required. The necessary CM sensing is achieved using the voltage and current sensors already present as part of the VSD, which detect any deviation of, e.g., speed from accepted values and attempt to compensate for the deviation. The compensation applied by the regulatory mechanism will be a measure of such factors as unbalanced load due to, e.g, a broken gear tooth. The use of sensorless VSDs for CM would have the advantage of improving accuracy and speed of response for most applications, and removing the need and cost of additional, externally positioned, sensors [6].

The challenge for CM is to choose the most suitable method capable of identifying and classifying faults in an early stage of their development, thus avoiding consequent damage and costs. Many researches have studied the CM of IMs and many detection techniques have been used over the years. However, there has been only limited investigation of detection and diagnosis of motor and downstream machine faults using sensorless VSDs [9, 10] but now many researchers are investigating the use of ESA. The use of ESA is non-intrusive and can be used to define the condition of the motor without interrupting the machine’s operation, ESA has the additional benefits of allowing remote CM monitoring using the VSD control panel. Analysis of the acquired signals has been shown to be able to detect various faults; changes in the system can be found by inspecting the spectrums of the motor current and voltage signals and extracting characteristic frequency peaks which identify the fault [11, 12]

A literature review has revealed that most ESA studies concerned open-loop or direct feed systems. Despite the importance and present wide use of sensorless VSDs, these systems have received less attention as a possible tool for effective and efficient CM. The literature reviewed has also shown that numerous signal processing methods have been used for extracting information about the health of a machine, but limited work was found that describes modulation signal bispectrum (MSB) analysis of all electric signals from a variable speed drive system. Importantly, no previous work has investigated the potential of using the instantaneous power factor (IPF) signatures for detecting and diagnosing machine faults downstream of the driving motor for different loads and speeds under sensorless control operation.

Moreover, most previous studies have utilized the amplitude and frequency information offered by instantaneous ESA. The phase information in ESA, which was largely ignored due to the deficiency and inaccuracy of computational realisation, has not fully explored for the purpose of machine diagnostics.

### **1.3 Aims and Objectives of the Research**

Because there exist clear gaps in using ESA from VSD systems for machine diagnostics, the main aim of this study is set to develop an efficient method capable of high performance in fault detection and diagnosing of motor and downstream machine faults using electrical signatures. The study will use new analytical technique, the MSB, to detect the different mechanical faults using signals obtained from the VSD.

In order to achieve this aim, certain objectives had to be achieved:

**Objective 1:** Provide an overview of the principles of the induction motors and sensorless VSD.

**Objective 2:** Implement an experimental programme for the practical investigation of different faults; gear tooth breakage, lack of lubricant and excessive bearing clearance, for different degrees of fault severity under different operating conditions.

**Objective 3:** Apply a new signal processing technique, MSB, to analysis the data obtained from the test rig in order to examine its capability for fault detection.

**Objective 4:** Investigate and compare different CM signatures; current, voltage and power obtained under sensorless control for the detection of different mechanical faults under different loading conditions, with particular attention paid to the capability of the system to detect small degrees of mechanical faults.

**Objective 5:** To study the mathematical model for three-phase induction motor with the field oriented control (FOC) drive with different mechanicals faults under different operating conditions, by using a ready-to-use software package “MATLAB/Simulink”. To examine the response of the model to the different faults under different loads and speed conditions.

**Objective 6:** Apply different signal processing methods to extract faults features for use in detection.

**Objective 7:** Detect and diagnose different mechanical faults (including tooth breakage, excessive bearing clearance, and oil levels) in a two-stage helical gearbox using both FFT spectrum analysis and MSB bispectrum analysis.

## 1.4 Research Methodology

The method used in this research was; to formulate the hypothesis that ESA using MSB could detect faults seeded into a mechanical system driven by an IM; to construct a test rig consisting of the necessary equipment to test the hypothesis; run the system without and with seeded faults; experimentally verify whether or not MSB could detect resulting changes in the ESA.

To accomplish the aim and objectives of this research, the main following steps were taken:

- Using the MATALB/Simulink IM model supplied in the ready-to-use software package, to simulate the likely effects a varying load due to a mechanical fault will have on the electrical supply parameters of the motor drive.
- Experimentally verify the results predicted by the model for the performance characteristics using the rig setup.
- Collect measured data based on a two stage helical gearbox to which gear faults, lubricity deficiency and bearing problems are induced under a wide range operating conditions adjusted via a widely used sensorless VSD:
  - 1- A tooth breakage on the gear of the first stage of the gearbox (GB1) with two levels of severity (20% and 40% of tooth broken off) under load setting of 30%, 70% and 100% of full load (15 kW) and three speeds; 50%, 75% and 100% of full speed (1460 rpm).
  - 2- Different level of lubrication in GB1; Manufacturer's recommender level (BL), 2.6 litres; and two abnormal cases; 2.0 litres (LV1= 77% of BL), and 1.5 litres (LV2= 57.7% of BL) under load settings of zero load and 30%, 70%, and 100% of full load, and at three speeds; 50%, 75%, and 100% of the full speed.
  - 3- Different values of bearing clearances in the first stage of GB2, under load settings of 25%, 50%, 75% and 100% of the full load, and at two speeds; 50% and 70% of the full speed.
- ESA was analysed using both FFT and MSB and the relative performances compared, in particular the presence of sidebands for fault detection and diagnosis.

For more clarification, a flowchart of Figure 1.1 is adopted to present the general methodological framework of this research:

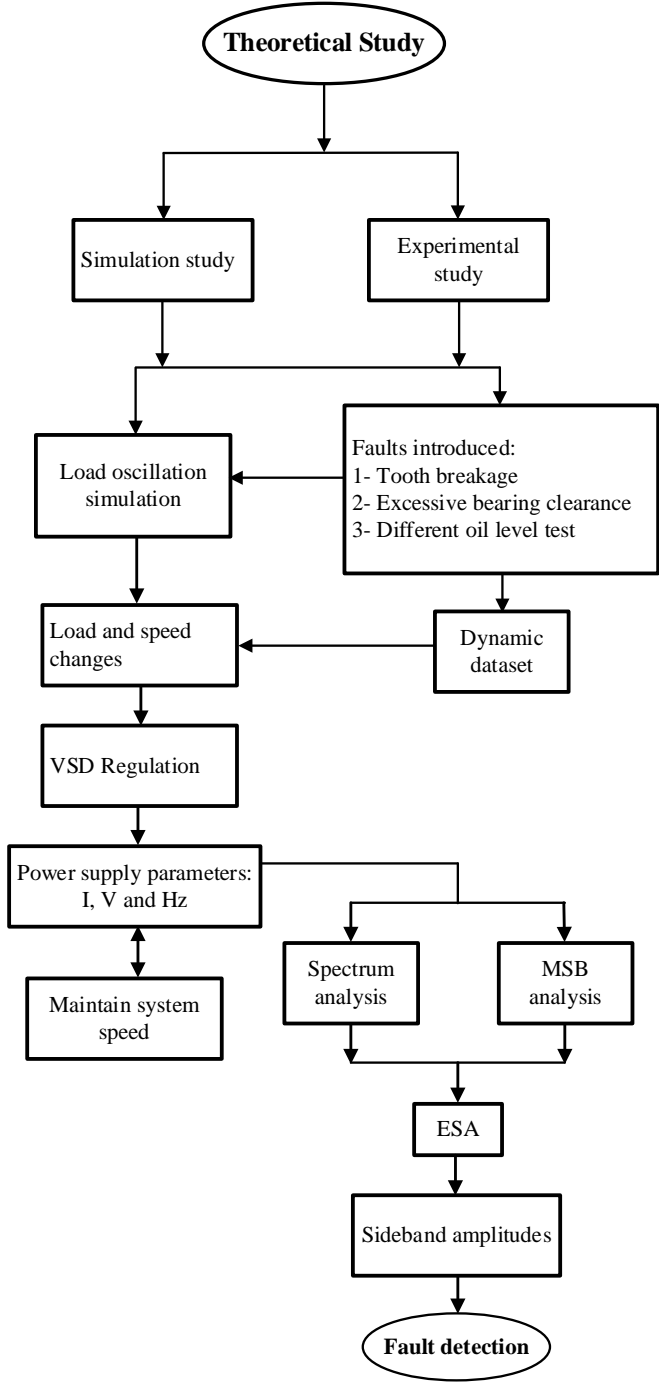


Figure 1-1 Framework for the research work

## 1.5 Organization of the Thesis

This thesis is structured as nine chapters, which describe the work undertaken to achieve the aims and objectives of the investigation.

**Chapter 2:** Introduces an overview of IMs; their operating principles and construction, and the theory of AC VSDs. It details the theoretical background to traditional AC drives, covering open- and closed-loop control, proportional, integral and derivative (PID) controllers, with the focus on field-oriented control and sensorless VSDs. It also presents the Model Reference Adaptive System (MRAS) method for speed estimation. Finally it discusses the most common causes of failure in IMs, including both mechanical and electrical faults.

**Chapter 3:** This chapter begins by demonstrating the importance of CM. It then reviews the conventional CM techniques and presents an in-depth the analysis of the electrical signatures of induction motors.

**Chapter 4:** This chapter presents the experimental facilities and the rig components. Also, the data collection procedure and the data analysis are explained.

**Chapter 5:** This chapter presents the mathematical model of the IM with field-oriented control, explaining the derivation of the mechanical and electrical equations of the IM. It describes the IM model used in this research, then it discusses the model structure of the open-loop and the FOC techniques based on sensorless VSD. Finally, it presents the results of the verification of the simulation by comparing the results gained from the model to the experimental results, obtained as described in Chapter 4.

**Chapter 6:** This chapter reports the results obtained using FFT and MSB with different electrical signatures; current, voltage, power and power factor for gear tooth breakage detection.

**Chapter 7:** This chapter investigates the capability of the instantaneous power factor for fault detection and the response of VSD to lubricant shortage.

**Chapter 8:** This chapter examines the capability of the MSB to evaluate the performance of the ESA in detecting excessive bearing clearance.

**Chapter 9:** Presents conclusions and make suggestions for future work.

## CHAPTER TWO: INDUCTION MOTOR DRIVES AND ITS PRINCIPLES

---

*This chapter, at first, provides a general overview of motor operation, with a focus on the construction and operating principles of induction motors. Moreover, the theory modern and traditional AC drives will be discussed covering open-and closed-loop control, proportional, integral and derivative (PID) controllers, field-oriented control, Model Reference Adaptive System (MRAS) method for speed estimation. Finally, it presents the most common causes of failure in induction motors, including both mechanical and electrical faults.*

## 2.1 Introduction

Induction motors allow the conversion of electrical power into mechanical power, with an efficiency ranging from 85% to 95% [13]. These motors find usage in a wide range of industrial applications, including rotary machinery for manufacturing plants across the world. This is owed to their numerous advantages such as,

- Simplicity and rugged design,
- Low cost,
- Low maintenance,
- High efficiency,
- Good power factor,
- Direct connection to power supply, and
- Equipped with self-starting torque.

## 2.2 Induction Machines

### 2.2.1 Types and Structure of Induction Motors

Induction machine designs usually fall in one of the following categories:

- Squirrel cage, and
- Wound rotor.

This research mainly focuses on CM of power supply squirrel-cage IMs. One of the most commonly used types of IMs in industrial applications is the three-phase induction or asynchronous motor, which is deemed as a reliable electrical machine. This particular motor design has two main parts, namely the “stationary” stator and the “rotating” rotor. These parts are separated from each other by means of a small air gap, ranging from 0.4 mm to 4 mm, depending on the motor power rate. The stator is comprised of a three-phase winding, whereas the rotor is a short-circuited winding. The stator winding is powered by a three-phase supply, inducing an electromagnetic force (EMF) on the rotor winding. The EMF on the rotor winding is a result of the electromagnetic induction principle, which is illustrated in Figure 2.1 for clarity [14, 15].

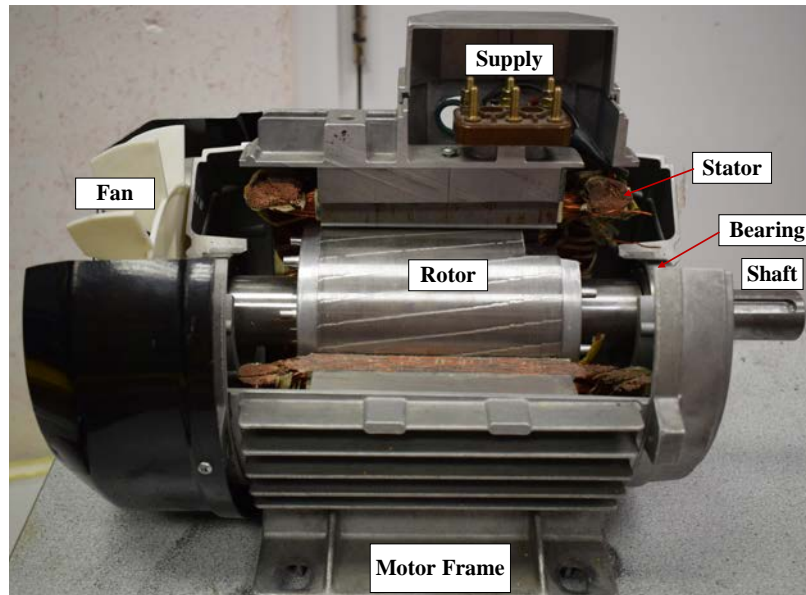


Figure 2-1: Basic construction of induction motor (Taken by the author).

#### 3.3.4.1 Stator Structure

Both squirrel-cage and wound-rotor variants of IMs share the same stator design, which contains numerous thin laminations of aluminum or cast iron, as shown in Figure 2.2 [16]. Each phase of the stator winding is set at an electrical angle of  $120^\circ$ . Once connected to a three-phase power source, the current will magnetise the stator, which in turn will induce a rotary field, causing the rotor to rotate at a synchronous speed ( $N_s$ ) [17].



Figure 2-2: Stator lamination

#### 3.3.4.2 Rotor Structure

In general terms, a motor is comprised of a rotating part, named the rotor, and a stationary part, named the stator. Depending on the motor's design and topology, the magnetic field generated by

its windings on the stator will cause the rotor to move in an angular motion. As shown in Figure 2.3, the rotor is made up of thick conducting (copper or aluminum) bars placed in rotor slots, which are short-circuited by either copper or aluminum rings [18].



Figure 2-3: Squirrel cage rotor

Note that the rotor slots are not perfectly parallel to the shaft, although, they provide a skew for the motor to run quietly, reducing the harmonics induced by the slots. This will minimise the locking tendency of the rotor. The stator and the rotor are physically separated by virtue of an air gap, which acts as a media for the transfer of energy between the static part of the motor (stator) and the rotating part (rotor). The torque generated by through electromagnetic induction is then transferred to the load, which is connected to the rotor [19]

### 3.3.4.3 Magnetomotive Force (MMF)

The magnetomotive force (MMF) is a measurable quantity reflecting on the strength of a magnetic field, which is proportional to the number of current-carrying coils in the stator windings and the amplitude of the current flowing through them. Considering a three-phase IM, the MMF can be described by [20]:

$$F(\theta, t) = \frac{3}{2} F_{\max} \cos(\theta - \omega t) \quad (2.1)$$

where:  $t$  is the time,  $\omega$  is the angular frequency (velocity), and  $\theta$  is the angular displacement of the rotor.  $F_{\max}$  is the peak value of the fundamental component of the MMF that can be calculated by the following equation [19]:

$$F_{\max} = \frac{4}{\pi} K_w \frac{N_{ph}}{P} \sqrt{2} I \quad (2.2)$$

where:  $K_w$  is the winding factor,  $N_{ph}$  is the number of series connected turns per phase,  $p$  is the number of poles,  $I$  is the *rms* value of the phase current.

The instantaneous phase voltages are given by:

$$v_A = \sqrt{2}V_m \cos(\omega t) \quad (2.3)$$

$$v_B = \sqrt{2}V_m \cos(\omega t + \frac{2\pi}{3}) \quad (2.4)$$

$$v_C = \sqrt{2}V_m \cos(\omega t + \frac{4\pi}{3}) \quad (2.5)$$

And these voltages produce varying currents in the stator windings which are given by [21]:

$$i_A = \sqrt{2}I_m \cos(\omega t - \phi) \quad (2.6)$$

$$i_B = \sqrt{2}I_m \cos(\omega t - \phi + \frac{2\pi}{3}) \quad (2.7)$$

$$i_C = \sqrt{2}I_m \cos(\omega t - \phi + \frac{4\pi}{3}) \quad (2.8)$$

where:  $v$  and  $i$  are the input voltage and current (V and A),  $A$ ,  $B$  and  $C$  indicate power supply phases,  $V_m$  and  $I_m$  are the RMS values of input voltage and current,  $\omega$  is the angular frequency of the voltage supply ( $rad\ S^{-1}$ ),  $t$  is the time (s), and  $\Phi$ ,  $\Phi+2\pi/3$ , and  $\Phi+4\pi/3$  are the phase shifts between current and voltage signals ( $rad$ ).

### 2.2.2 Basics Operation of Induction Motors

In induction motors, the speed of the rotation is synchronous to the angular frequency of the AC supply current that induces an alternating magnetic flux within the stator windings. The rotor conductors are short-circuited, which according to Faraday's law of electromagnetic induction will cause a current to flow through the rotor conductors. The induced current in the rotor will also result in an alternating magnetic flux around it and will always lag behind the stator flux. According to Lenz's law, the rotor will rotate in the opposite direction of the causing force that is induced by the stator windings. The rotor current is induced as an effect of the relative velocity between the stator flux and the rotor flux; thus, the rotor's direction of rotation will always be as

that of the stator flux, which will minimise the relative velocity. The speed of the rotating magnetic field is recognized as synchronous  $N_s$  and can be expressed as [22]:

$$N_s = \frac{120f}{p} \quad (2.9)$$

where:  $N_s$  is the synchronous speed (rpm),  $f$  is the supply frequency (Hz), and  $p$  is the number of poles.

### 2.3 Slip and Speed

The “slip”, usually given as a percentage, is said to be one of the most virtues of an IM, which is the difference between the synchronous speed  $N_s$  and the rotor speed  $N_r$ . This parameter is key in optimum operation of induction motors, which is factor of proportionality, relating rotor parameters to those of the stator. In presence of magnetic flux, the rotor accelerates asymptotically towards a speed near the synchronous speed. The related operation slip of a particular motor depends on its size and is usually in the range of 3-10% [18].

$$S = \frac{n_s - n_r}{n_s} \times 100\% \quad (2.10)$$

where:  $S$  is the slip,  $n_s$  is the synchronous speed,  $n_r$  is the rotor speed.

In terms of slip, the rotor speed can be represented in rpm or  $rad\ S^{-1}$  as:

$$n_r = n_s(1 - s) \quad (2.11)$$

$$\omega_r = \omega_s(1 - s) \quad (2.12)$$

### 2.4 Equivalent-Circuit Models

In order to provide analysis and performance predictions in steady-state conditions, simple equivalent-circuit models of the IM in most cases is a necessity. In such models, the IM is always assumed to be a star-connected three-phase system so that the currents are always represented by their line values and the voltages are shown by their line-to-neutral values [17].

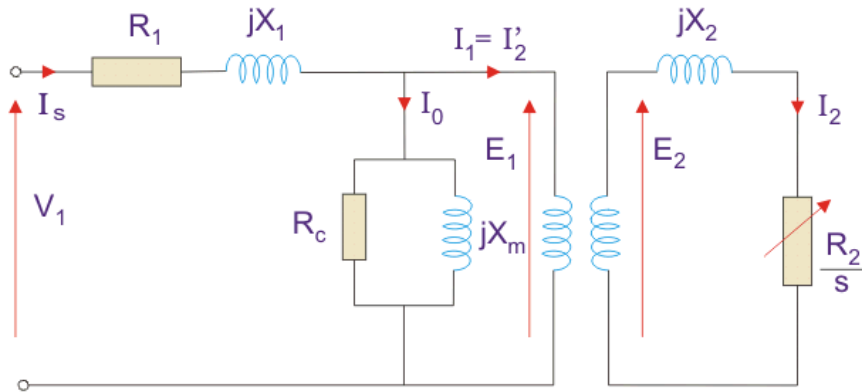


Figure 2-4: Induction motor equivalent circuit [19]

where:  $R_1$  is the stator resistance ( $\Omega$ ),  $R_2$  is the rotor resistance ( $\Omega$ ),  $X_1$  is the stator leakage reactance ( $\Omega$ ),  $X_2$  is the rotor leakage reactance ( $\Omega$ ),  $X_m$  is the magnetizing reactance ( $\Omega$ ),  $R_c$  is the core loss component,  $V_1$  is the stator supply voltage (V),  $I_s$  is the stator current (A) and  $I_2$  is the rotor current (A).

## 2.5 IM Rotor Current, Speed, Load and Torque

The torque is created by the interaction between the current flowing in the rotor bars and the flux in the air gap. During motor operation, the speed of the rotor is always lagging with respect to the synchronous speed, producing a torque, which rotates the rotor at an asynchronous speed. The relative between the rotor speed and synchronous speed is known as the “slip”, which is in proportion to the mechanical load and is key to torque production. However, if the rotor runs at synchronous speed, there would be neither rotor current nor EMF induced in the rotor winding and subsequently, there would be no torque [19].

When the motor starts at full supply voltage, it will draw a very high starting current, which is called the Locked Rotor Current (LRC), and produces the so-called Locked Rotor Torque (LRT). If the supply voltage is kept constant, the starting current will decrease slowly with increasing motor speed and drop significantly at up of 80% of the full speed. If the voltage remains constant, as the motor accelerates, the starting torque decreases slightly to the minimum torque which is denoted by the pull-up torque and then increases to the maximum value of torque, which is known as pull-out or breakdown torque and occurs at almost full speed. Finally, the torque reaches zero at synchronous speed with no load [13].

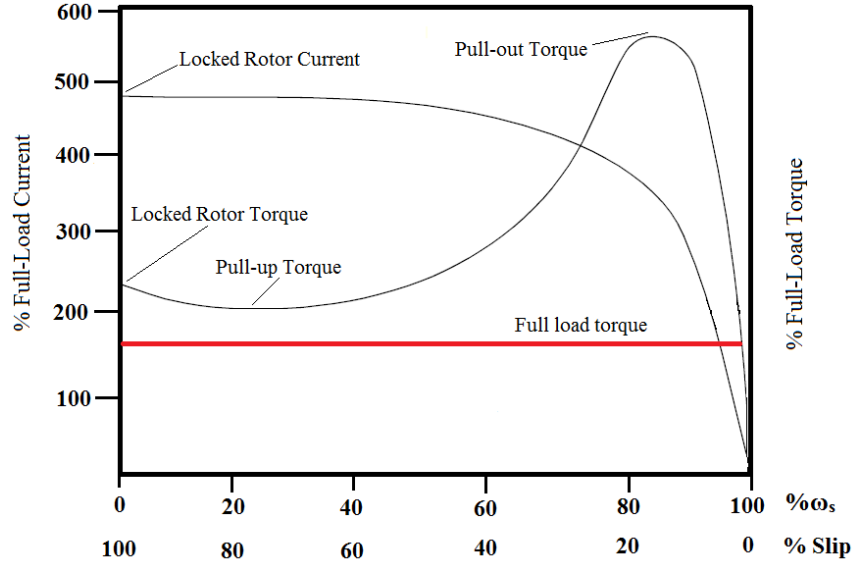


Figure 2-5: Torque-speed and current-speed curves of a typical IM (modified from [14]).

In general, by applying a mechanical load to the motor's shaft, a torque is generated that is related to the motor's output power and its rotor speed. Torque is the rotational equivalent of a linear force in rotating machinery with the units of  $Nm$ . In this case, the mechanical torque corresponding to a mechanical power  $P_m$  can be expressed as:

$$T_m = \frac{P_m}{\omega_r} = \frac{P_g (1 - S)}{\omega_r} \quad (2.13)$$

By substituting Equation (2.12) in Equation (2.13), we will obtain:

$$T_m = \frac{P_g}{\omega_s} \quad (2.14)$$

Where  $T_m$  is the mechanical torque (Nm),  $P_g$  is the air gap power [18].

The equivalent-circuit models of IMs are found useful in determining a wide range of motor characteristics, for example, current, speed, power losses, starting torque, and the maximum torque, given the following impedances are defined as:

$$\begin{aligned} Z_1 &= R_1 + jX_1 \\ Z_2 &= R_c + jX_m \\ Z_3 &= R_2 + jX_2 \end{aligned} \quad (2.15)$$

According to the circuit in Figure 2.4, the total impedance will be:

$$Z_{eq} = \frac{Z_1(Z_2 + Z_3) + Z_2Z_3}{Z_2 + Z_3} \quad (2.16)$$

where  $i_A$  represents the input current which is given by:

$$\bar{I} = \frac{\bar{V}(Z_2 + Z_3)}{Z_1(Z_2 + Z_3) + Z_2Z_3} \quad (2.17)$$

The instantaneous power supplied to each phase is:

$$P_{in} = iv \quad (2.18)$$

With the instantaneous voltage and current signals expressions:

$$v = \sqrt{2}V_m \sin(\omega t) \quad (2.19)$$

$$i = \sqrt{2}I_m \sin(\omega t - \phi) \quad (2.20)$$

where:  $V_m$  and  $I_m$  are the maximum values of the sinusoidal voltage and current.

Thus, the instants power can be obtained as follows:

$$P_A = \sqrt{2}V_m I_m (\cos(\phi) - \cos(2\omega t - \phi)) \quad (2.21)$$

## 2.6 Theory of AC Drives and Traditional Drives

A Variable speed drive, also named Adjustable speed drive (ASD) or Adjustable frequency drive (AFD) is an electrical / electronic device that is responsible for controlling the speed of IM by means of varying/controlling the current/voltage of a fixed frequency electrical supply. This device enables the control of the speed and torque of a motor, allowing for a better dynamic performance. The VSDs can often realise 92-95% efficiency levels, with 5-8% losses that are caused by high-frequency switching and the heat dissipation of the incorporated semiconductor power components [23]. A typical three-phase VSD consists of the following:

- A rectifier that converts the supply's AC current/voltage into a DC from;
- A DC link that filters the DC signal;
- An inverter to convert the DC power into a variable frequency and voltage output; and
- Control circuitry that is responsible for controlling either the inverter and/or the rectifier bridges to yield the desired voltage and frequency levels.

Both rectifier and inverter circuit's use self-controlled and high frequency power switches [24, 25]. The speed of a motor can be conveniently adjusted by varying the frequency and voltage that are applied to the motor [24]. That could be obtained by either the adjustment of the number of poles, but this is a physical change to the motor and needs rewinding by changing the ratio to change motor torque.

As before, synchronous speed can be determined by the following equation:

$$N_s = \frac{120f}{p} \quad (2.22)$$

Also:

$$S = \frac{n_s - n_r}{n_s} \times 100\% \quad (2.23)$$

$$T_m = \frac{P_g}{\omega_s} \quad (2.24)$$

$$T = \frac{3}{\omega_s} = \frac{V_1^2}{(R_1 + \frac{R_2}{S})^2 + X_T^2} * \frac{R_2}{S} \quad (2.25)$$

where:  $N_s$  is the synchronous speed (rpm),  $f$  is the supply frequency (Hz),  $p$  is the number of poles,  $S$  is the slip,  $n_r$  is the rotor speed,  $T_m$  is the motor torque (Nm),  $\omega_s$  is the motor synchronous angular speed (rpm),  $R_1$  is the stator resistance, and  $R_2$  is the rotor resistance.

The equations above imply that the motor's speed depends on the supply frequency, while its torque is governed by the voltage-per-frequency ratio (V/Hz); thus, by changing this ratio, the motor's torque can be adjusted to the load requirements. In order to meet specific speeds under

load conditions, the motor drive is capable of providing variable frequency outputs, consequently, there exists a torque curve at any generated frequency [24].

## **2.7 Construction and Operation Principles of PWM Drives**

In order to control the motor speed, various techniques have been proposed in literature. Pulse-Width Modulation or PWM is a method whereby varying the width of a series of square-shaped pulses in each half cycle, the amplitude of the alternating output voltage can be regulated. In this case, the motor's frequency is determined by the number of changes between the positive and negative pulses in one second [23]. The performance of drives that works with PWM vary according on the control algorithms. In addition, AC drives can be classified into four basic types of control: Volts per Hertz, Sensorless Vector Control, Flux Vector Control, and Field Oriented Control.

- V/Hz control is a fundamental scheme that varies the frequency of the output voltage for applications like fan and pump. It provides a fair precise speed and torque control with a reasonable cost.
- Sensorless Vector control, which can provide a better speed regulation and high starting torque.
- Flux Vector control that produces precise speed, torque control, and dynamic response.
- Field Oriented Control, which has the ability of providing best speed and enhanced torque response.

In general, PWM drives are constructed from three main components, with customised hardware/software for each application.

In Figure 2.6, the first stage of the drive converts the AC voltage to a DC form, using a rectifier with six power diodes arranged in a bridge formation. Then, the DC link section filters the rectified DC voltage using a group of inductors and capacitors, in order to provide a smooth output waveform into the inverter stage, which converts the DC voltage back into an AC form. The inverter stage consists of insulated gate bipolar transistors (IGBTs), which are capable of regulating both voltage and frequency. The switching frequency of the IGBT's in PWM motor drive applications ranges from 2 kHz up to 20 kHz. By increasing the operating frequency of the drive beyond the human audible range of 20 Hz to 20 kHz, it is possible to reduce the whine

associated with VSD systems. Moreover, the inverter will smooth out any ripples in the drive current, as this will manifest itself in the output torque of the motor. Finally, the control board regulates the timing of the positive and negative half cycles, in an effort to reconstruct the three-phase output power required for operating the induction motor, such that, to provide a higher output voltage, the power device should be remained on for long time. [23, 24].

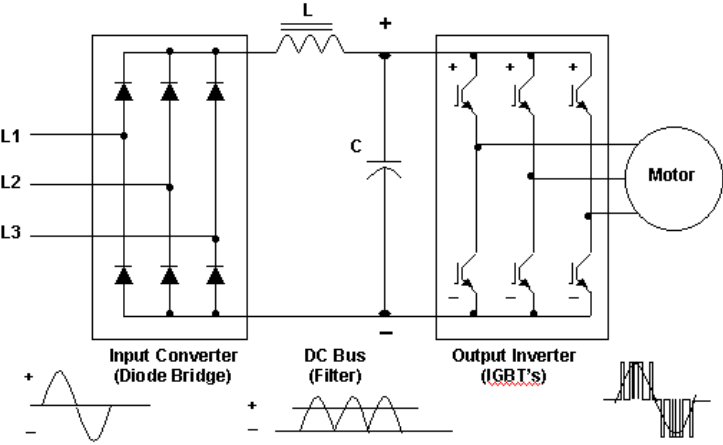


Figure 2-6: A block diagram of a PWM drive [25]

The following figure represents the voltage and current waveforms of a PWM driver:

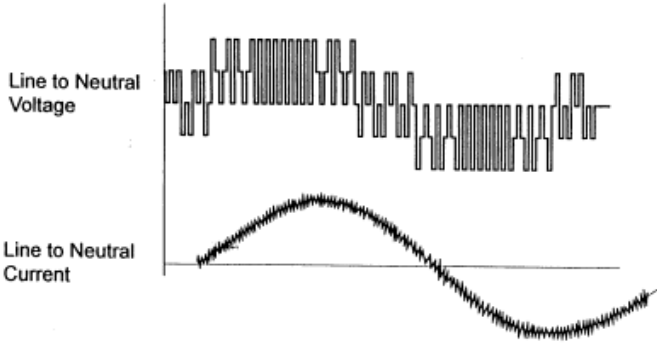


Figure 2-7: Voltage and current waveform of a PWM drive [26]

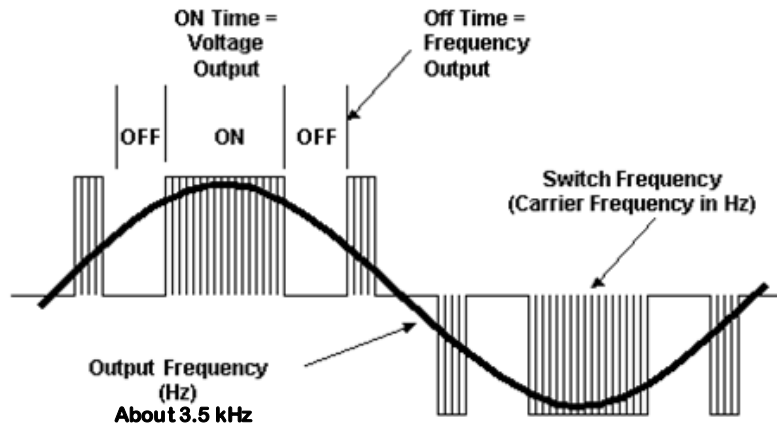


Figure 2-8: Voltage and frequency created from a PWM drive [26]

## 2.8 Traditional VSDs

Traditional VSDs fall into three categories, namely, Voltage Source Inverter (VSI), Current Source Inverter (CSI), and PWM drives.

### 2.8.1 Voltage Source Inverter (VSI)

The VSI uses a diode rectifier that converts the AC input voltage into a DC form. In contrast to CSIs, VSIs are not controlled through electronic firing. As shown in Figure 2.9, the DC link/bus consists of a number of parallel-connected capacitors, which filter out any ripples present on the rectifier's output DC voltage.

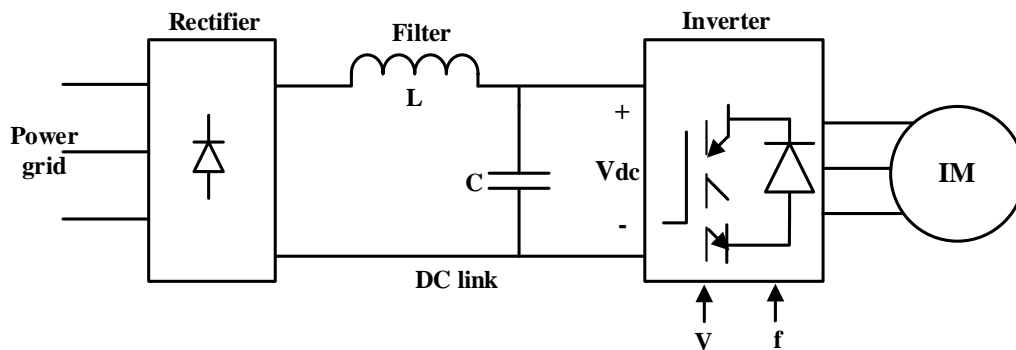


Figure 2-9: Block diagram of a typical VVI drives redrawn from [27]

VSIs benefit from several advantages, including, simplicity, wider speed range and ability to control multiple motors. However, they suffer from a number of disadvantages, some of which are listed below [24]:

- Degraded power factor at lower speeds;
- Generation of line spikes;
- Increased levels of harmonics; and
- Tendency to cause motor cogging (shaft pulsations) at low speeds, sequentially, this could cause problems to the equipment [24].

### 2.8.2 Current Source Inverter (CSI)

The CSIs are similar in design to VSIs [23]. Figure 2.10 presents a block diagram of a typical CSI, where a variable voltage will be provided by the input rectifier to the DC bus, by using silicon-controlled rectifier (SCR) devices. In contrast to VSIs, CSI drives are capable of achieving higher efficiencies and power factors. This can be explained by the internal regulation of the drive current and the reliable short-circuit protection present in these systems, which allows for a continuous operation even with one faulted device. The disadvantages include, lower input power factor at lower speeds, motor cogging, limited operating speed and frequency ranges, line spikes produced by the drive, and performance and stability issues caused by low frequencies and low load conditions. Finally, it is important for the characteristics of the motor to match those of the drive system, thus, in most cases, the drive system is designed as an integral part of the motor [24].

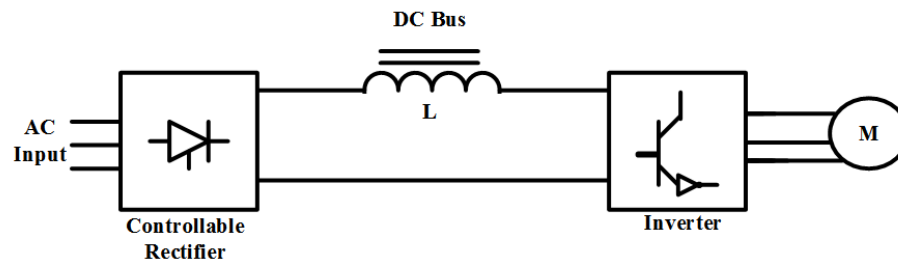


Figure 2-10: A block diagram of a typical CSI, redrawn from [27]

### 2.8.3 Pulse Width Modulation (PWM)

The construction and basic operation of PWM drive systems are explained in Figure 2.6. Such drive systems benefit from the following advantages [23]:

- Excellent power factor due to DC bus voltage;
- Elimination of motor cogging that is inherent to six-step inverters;
- Efficiencies of 92-96%;
- Ability to drive multiple-motors;

- Capable of riding through 3-5 Hz of drop in the frequency;
- Lower initial cost;
- Protection against open circuit faults; and
- Fixed input power factor.

Nevertheless, PWM drives have their own drawbacks, a number of which are listed below:

- Motor overheating and insulation breakdown caused by high switching frequency of incorporated thyristors;
- Non-regenerative operation [23, 27].

## 2.9 Open- and Closed-Loop Control

In an open-loop control system, the action taken by the controller is completely independent of its input, i.e. there is no knowledge of the relationship between the system's input and output [27].

Upon a demand change, the controller tries to adjust the input signal, which in turn affects the process and changes the controlled output, as presented in the following figure.

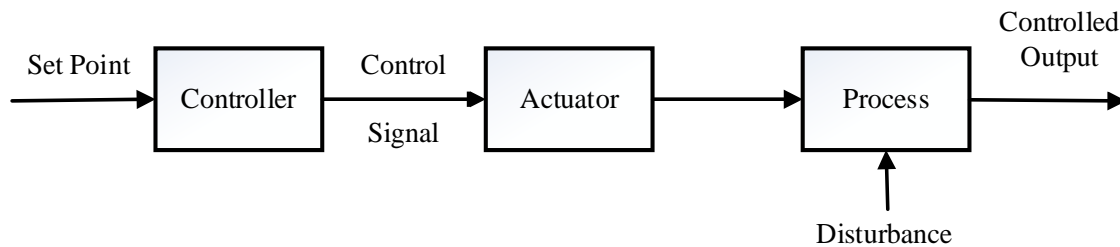


Figure 2-11: Open-loop block diagram, redrawn from [28]

On the other hand, in a closed-loop control type, the controller has a feedback path informing the controller of the difference between the output condition and the reference input. Subsequently, an “error” term is calculated by a comparator, whose output is then transferred to the controller algorithm to produce a new control signal to compensate for the error [27, 29]. The following figure presents the block diagram of the closed-loop control system [26].

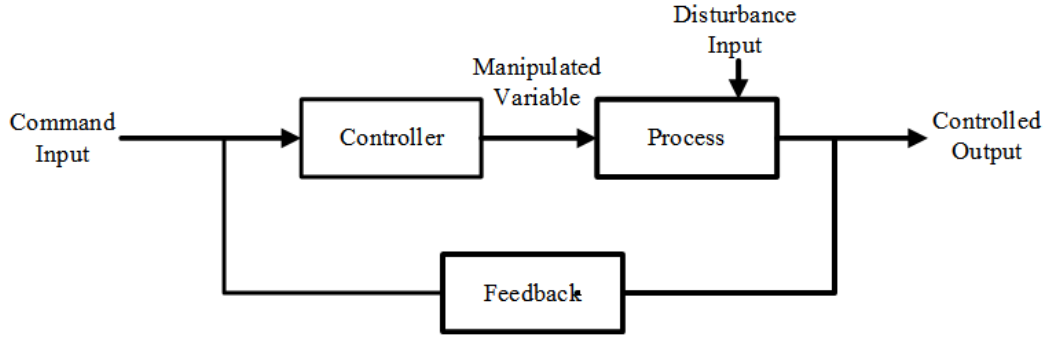


Figure 2-12: Closed-loop block diagram, redrawn from [30]

## 2.10 PID Controllers

In motor drives, a controller serves as a key element, which is responsible for controlling the machine by computing the difference between the commanded or reference signal and that measured at the output, yielding an error term. Depending on the type and mode of the employed controller, this error term is then minimised to achieve the commanded output from the motor.

Proportional-integral-derivative (PID) controllers find usage in wide range of industrial applications. PID controllers can be proportional only (P controller) proportional and integral (PI controller), or proportional, derivative and integral (PID controller). Due to the fact that the PI controller has a simple structure and robust performance, it has been long adopted in numerous industrial applications, including motor drives and control. This type of controller relies on two parameters to reduce the “error” between the controller’s input and output. These parameters are the integral gain ( $k_i$ ) and the proportional gain ( $k_p$ ). In general, the PID controller has three modes of control; 1) the proportional controller changes the output control in proportion to the error signal; 2) the integral control allows for the output to be matched as a proportion of the error integral; and 3) the derivative controller creates an output in proportion to the error derivative. Finally, the PID controller produces an output which is the sum of the three modes described above [28].

$$P_{out} = K_p e(t) \quad (2.26)$$

$$I_{out} = K_p e(t) + K_i \int e(t) dt \quad (2.27)$$

$$D_{out} = K_d \frac{de(t)}{dt} \quad (2.28)$$

The PID controller is the sum of the three modes to produce the output:

$$C_{out} = K_p e(t) + K_i \int e(t) dt + K_d \frac{de(t)}{dt} \quad (2.29)$$

where:  $P_{out}$  is the proportional controller output,  $K_p$  is the proportional gain,  $e(t)$  is the error signal,  $I_{out}$  is the integral controller output,  $K_i$  is the integral time,  $D_{out}$  is the derivative controller output, and  $K_d$  is the derivative time.

In order to create an accurate and stable process,  $K_p$ ,  $K_i$  and  $K_d$  must be well tuned.

Due to the non-linear characteristics of induction motors and the complex mathematical models adopted, the control of these machines necessitate for high-performance control techniques, such as, vector control or FOC. For induction motors, the vector control can provide the following:

- Enhanced angular speed;
- Better dynamic torque response;
- Higher starting torque; and
- More accurate speed control [31, 32].

In vector-controlled induction motors, the torque and the magnetising current vectors are controlled independently, yielding a better and more accurate speed/torque control. This is usually realised by employing equivalent-circuit models of the motor under operation, whereby entering the model data into the drive system, the controller will perform an auto-tune function to produce a software model of the motor for an improved speed/torque control.

Sensorless vector control operates more or less like a frequency control drive, whereby providing slip compensation, the motor's speed is kept close to the commanded speed. The Torque Current Estimator block provides an approximation for the torque current by comparing the proportion of the drive current that is in phase with the voltage, which then calculates the slip; in turn, this will provide a more accurate motor speed response when applied with loading.

Depending on the type of speed control, it is possible to control the VSD via scalar- or vector-based methods. The most widespread kind of VSD control is a scalar-based method called the "volts per hertz" (V/Hz) or volts per frequency (V/f), whereby its concept is to keep the ration of

(V/Hz) constant which will eventuate the air gap flux to be constant and thus, the torque component will be constant.

V/Hz drives only control the magnitude of voltage, current, and flux linkage space vectors, while the volts-angle (V angle in the figure) has a Torque Current Estimator that regulates the current feed into the motor's flux. This will ensure that the low speed and poor torque control of the standard V/Hz drive systems can be improved, which in turn will provide a better speed regulation. This strategy has the advantage of simplicity in implementation, however, it provides inferior achievement compared to other control methods [31-34].

## **2.11 Sensorless Field-Oriented Control (FOC)**

Over the recent years, VSDs have been increasingly appearing in many industrial applications to improve production efficiencies. The FOC or the so-called FVC (Flux Vector Control) strategy is based on assumptions that are only valid under dynamic conditions [31, 32]. In such controllers, both the magnitude and the phase of the supply current are controlled in real time to provide a speed control in IMs. This method operates based on simulating the behavioural response of the underlying DC motor, where there is a decoupling between the motor's torque and flux. This decoupling allows the AC motor to be controlled [35]. The FOC is designed with the following three fundamental goals in mind:

- Mapping motor's current and voltage measurements into space vectors;
- Three-phase to two-stage system transformation based on time and speed observations;  
and
- Creating of a Space Vector Pulse Width Modulator (SVPWM) control strategy.

Sensorless FOC systems benefit from the following advantages:

- Enhanced torque response;
- Improved torque control at low frequencies and speeds;
- Smaller drive machine dimensions;
- No need for sensor cabling;
- Enhanced reliability;
- Less noise;
- Reduced maintenance requirements;

- Improved machine performance and efficiency;
- Highly accurate speed and torque control; and
- Reduces the cost and power consumption [9, 10].

In the FOC-based drive systems, there is a feedback loop to provide an enhanced dynamic response. Although, it is established that due to the closed-loop nature of the such systems, noise can have detrimental impact on the acquired current and voltage signals, hiding important information regarding a particular fault signature around the affected frequency ranges [36, 37].

In case of an IM, the stator windings are fed from a drive with current magnitudes of  $i_a$ ,  $i_b$  and  $i_c$  which are all separated by a phase angle of  $120^\circ$  with respect to one another. The torque and flux components of the induction motor are then individually controlled based on mathematical decomposition of the stator currents [38]. The stator current is mathematically decomposed into torque and flux components, and both of these components can be controlled separately. In order to implement the FOC scheme, the phase voltages and currents must be transformed into a two-phase  $d-q$  reference framework, where  $d$  is the current component which controls the rotor’s flux, and  $q$  is the current component which controls the torque [9, 10].

During the control process, a mathematical model of the motor is embedded on a microprocessor and FOC is implemented through electronic means, indirectly regulating the motor’s output torque [38].

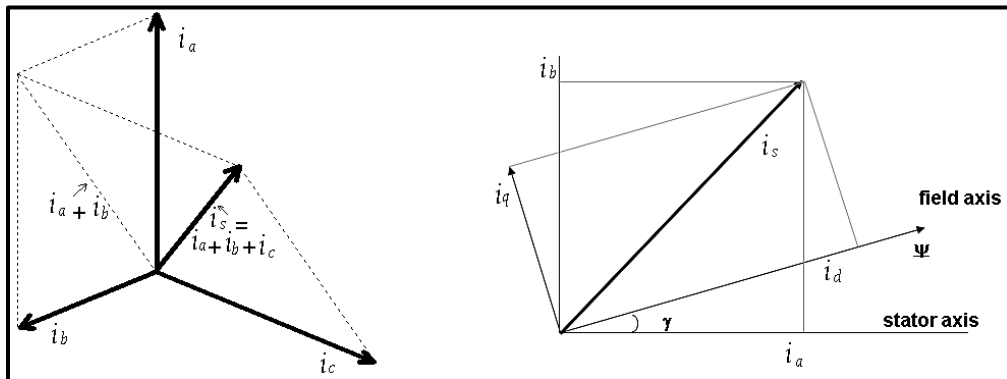


Figure 2-13: The principle of FOC [39]

In induction motor drives, the two-phase current is measured and transformed into a stationary framework ( $i_{sa}$  and  $i_{sb}$ ) using Clarke transformation and then a Park transformation is performed to map the stationary framework into a rotating one (i.e.  $d-q$  framework). Then, the measured and the commanded values are compared using a PI controller and an “error” term is minimised until

the desired set point is reached. Thereafter, the output signal is converted into a stationary framework and subsequently into a PWM duty cycle using the Park transformation [40, 41].

The following figure illustrates the orientation that takes place inside the motor.

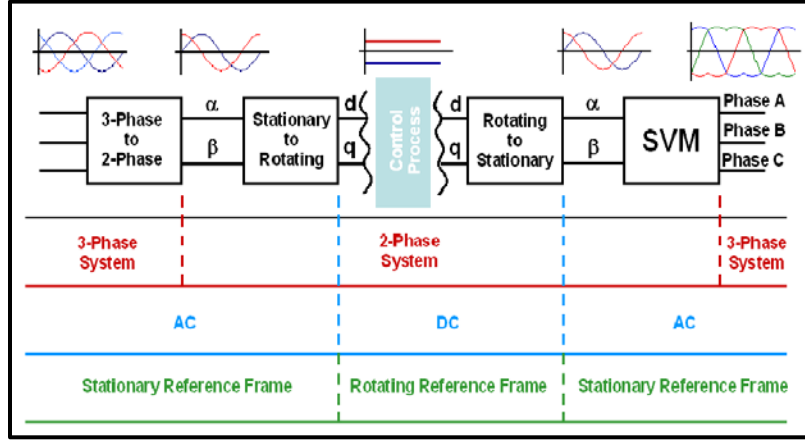


Figure 2-14: Vector control transformations [40]

There are three ways to achieve FOC; directly by using flux sensors mounted on the motor, or, indirectly by using parameters of the motor (e.g. supply current and frequency), and/or by means of rotational position measurement. Indirect FOC methods can be categorised into two groups [35]; closed-loop vector control which uses a pulse encoder to retrieve information on the rotor angle, and sensorless FOC which does not employ speed sensors.

The stator voltage expressed as:

$$V_{ds} = R_s i_{ds} - \omega_e L_s i_{qs} \quad (2.30)$$

$$V_{qs} = R_s i_{qs} + \omega_e (L_a + L_b) i_{ds} \quad (2.31)$$

Because the  $d$ -axis is aligned with rotor flux,  $\psi_{dr} = \psi_r$  and  $\psi_{qr} = 0$ ; “in squirrel-cage IMs,  $V_{dr}$  and  $V_{qr}$  are set to zero because the rotor cage bars are shorted [42]”.

The motor flux can be estimated using the equation below:

$$\psi_r = \frac{L_m}{1 + T_r S} (i_{ds}) \quad (2.32)$$

Furthermore, the motor torque can be described by the following relationship, which is useful in computing the current torque component  $i_{qs}$ :

$$T_{em} = \frac{3}{2} \frac{p}{2\omega_e} (\psi_{ds} i_{qs}) \quad (2.33)$$

The FOC scheme allows for a separate control of the torque, whilst maintaining a constant rotor flux amplitude ( $\psi_r$ ), leading to a linear function that can relate the electromagnetic torque  $T_{em}$  and the torque component  $i_{qs}$ . Therefore, by controlling  $i_{qs}$ , it is possible to control  $T_{em}$  indirectly [43, 44]. The following figure represents the FOC.

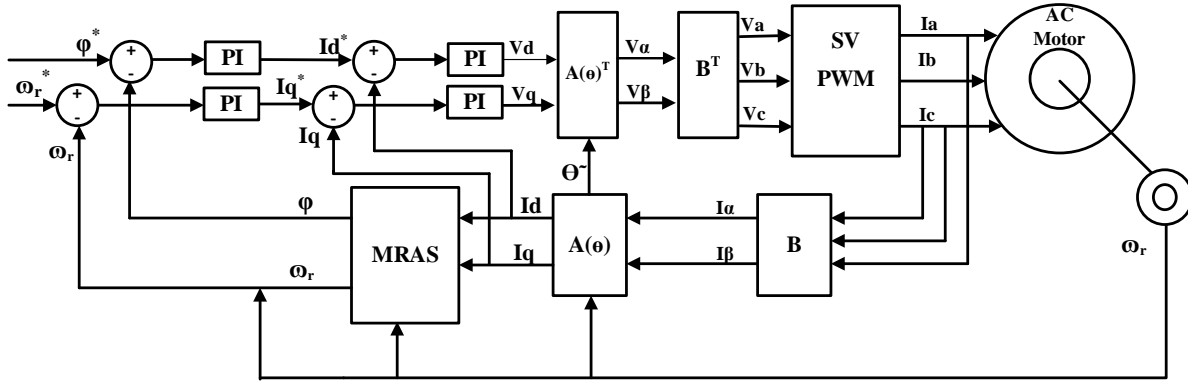


Figure 2-15: Sensorless FOC block diagram redrawn by the author [45]

As opposed to direct sensor-based techniques, MRAS estimators are often utilised in sensorless FOC drives in order to provide an estimate of the motor's speed and flux in real time [38]. Compared to other types of sensorless vector-controlled drive, the MRAS method benefits from simplicity in implementation given that the reference model is capable of representing the desired control metrics, the MRAS method can achieve a high performance, using two independent models, aiming at estimating the same state variables. The first model captures the stator voltage (i.e. the reference model) and the second uses the phase currents (i.e. the adaptive model), where both models operate within the stationary reference frame [40].

During on-line operations, the output of the reference model will be compared to the output of the adaptive model, followed by estimating the rotor speed based on the residual between these two variables. This residual (difference) term is then fed into a PI-type controller in order to be minimised and thus, tune the rotor speed ( $\omega_r$ ) with respect to the commanded value. The following figure illustrates a block diagram for the MRAS control technique.

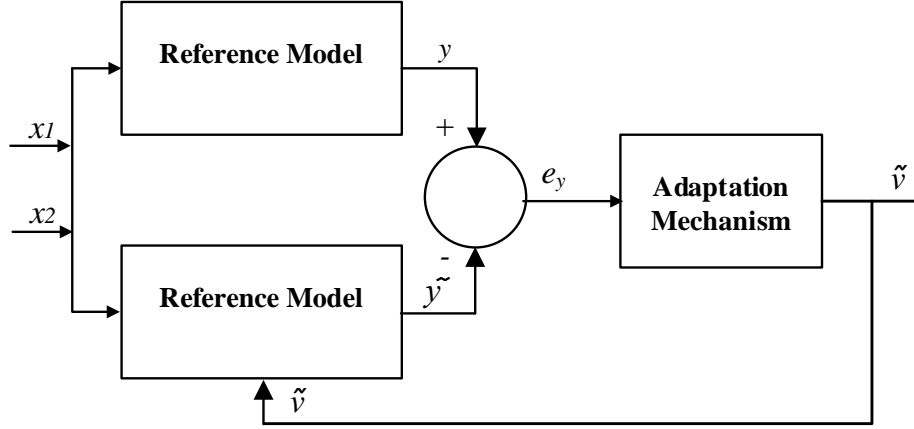


Figure 2-16: Block diagram for MRAS control redrawn from [46]

The equations of the reference model in the stationary frame, consisting of the stator voltage, can be given as [1, 2, 4, 9, 10, 16, 47-50]:

$$\frac{d\psi_{dr}}{dt} = \frac{L_r}{L_m} V_{ds} - \frac{L_r}{L_m} (R_s - \sigma L_s) i_{ds} \quad (2.34)$$

$$\frac{d\psi_{qr}}{dt} = \frac{L_r}{L_m} V_{qs} - \frac{L_r}{L_m} (R_s + \sigma L_s S) i_{qs} \quad (2.35)$$

$$\sigma = 1 - \frac{L_m^2}{L_r L_s} \quad (2.36)$$

Similarly, the adaptive model equations are obtained from the rotor circuit in the stationary frame and given as:

$$\frac{d\psi_{dr}}{dt} = \frac{L_m}{T_r} i_{ds} - \omega_r \psi_{qr} - \frac{1}{T_r} \psi_{dr} \quad (2.37)$$

$$\frac{d\psi_{qr}}{dt} = \frac{L_m}{T_r} i_{qs} + \omega_r \psi_{dr} - \frac{1}{T_r} \psi_{qr} \quad (2.38)$$

We have:

$$T_r = \frac{L_r}{R_r} \quad (2.39)$$

where  $T_r$  is the rotor circuit time constant, which can be expressed as:

$$T_r = \frac{1}{\text{Slip}} * \frac{i_q}{i_d} \quad (2.40)$$

The angle  $\theta_e$  of the rotor flux vector can be determined by:

$$\theta_e = \arctan\left(\frac{\psi_{qr}}{\psi_{dr}}\right) \omega_e = \frac{d\theta_e}{dt} = \frac{\psi_{dr}\psi'_{qr} - \psi_{qr}\psi'_{dr}}{\psi_{dr}^2 + \psi_{qr}^2} \quad (2.41)$$

The slip angular speed is given by:

$$\omega_s = \frac{L_m}{T_r} \left( \frac{\psi_{dr}i_{qs} - \psi_{qr}i_{ds}}{\psi_{dr}^2 + \psi_{qr}^2} \right) \quad (2.42)$$

The rotor speed can be calculated as:

$$\omega_r = \omega_e - \omega_s \Rightarrow \omega_r = \frac{1}{\psi_r^2} \left[ \psi_{dr} \frac{d\psi_{qr}}{dt} - \psi_{qr} \frac{d\psi_{dr}}{dt} - \frac{L_m}{T_r} (\psi_{dr}i_{qs} - \psi_{qr}i_{ds}) \right] \quad (2.43)$$

$$\psi_r^2 = \psi_{dr}^2 + \psi_{qr}^2$$

To calculate the electromagnetic torque, we have:

$$T_e = \frac{3pL_m}{4L_r} (\psi_{dr}i_{qs} - \psi_{qr}i_{ds}) \quad (2.44)$$

where:

$V_{ds}, V_{qs}$ : d–q axis stator voltages respectively,  $i_{ds}, i_{qs}$ : d–q axis stator currents,  $R_s$  is the stator resistance,  $L_m$  is the mutual inductance,  $L_s, L_r$  are stator, rotor leakage inductance, and  $\sigma$  is the motor leakage coefficient.

$$\psi' = \frac{d\psi}{dt},$$

where:  $T_r$  is the rotor time constant,  $\omega_s$  is the synchronous angular speed,  $\omega_r$  is the rotor angular speed,  $p$  is the numbers of poles; and  $\psi_{ds}, \psi_{qs}, \psi_{dr}, \psi_{qr}$ : d–q axis flux linkage of stator and rotor respectively [41].

## 2.12 Common Induction Motor's Faults

Despite the fact that induction motors are greatly effective and reliable, they are liable to many kinds of faults, which may cause catastrophic machine failure, causing components shutdowns, personal injuries and wasting raw material [51]. It is possible to detect the IMs faults in an early stages of development in order to avoid the system breakdown and related costs.

A fault can be defined as an unwanted abnormality in one or more characteristics of a variable compared to its normal behavior, which can initiate a system failure. It should be noted that a failure is a result of the fault occurrence, but a fault alone cannot cause a failure. In general, all failures can be considered faults but the opposite is not correct [52]. The induction motors have many benefits which among them low cost, high reliability, hardiness, simple construction and high reliability [53]. Although IMs are deemed reliable, but failure has the possibility to occur. As shown in Figure 2.17, faults of induction motors can be categorized into two categories of electrical and mechanical faults.

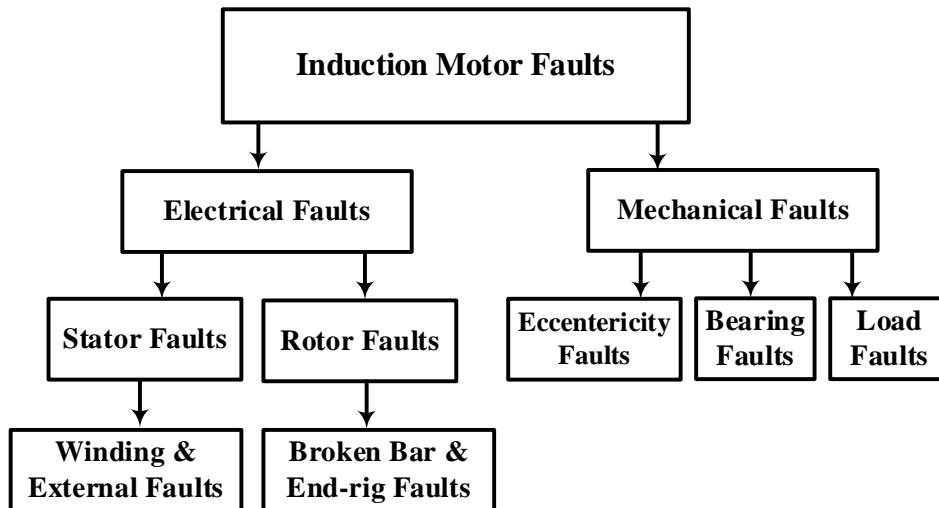


Figure 2-17: Classification of induction motor faults, redrawn from [54].

The ratio of different induction machine failures are shown in Figure 2.18, as mentioned in the Electric Power Research Institute (EPRI). It clear that bearing faults and stator-related faults are two of the main causes of IM failures. While around 10% of the machines failures are rotor related, the majority of the failures are associated with causes that are summarised in the following figure [52].

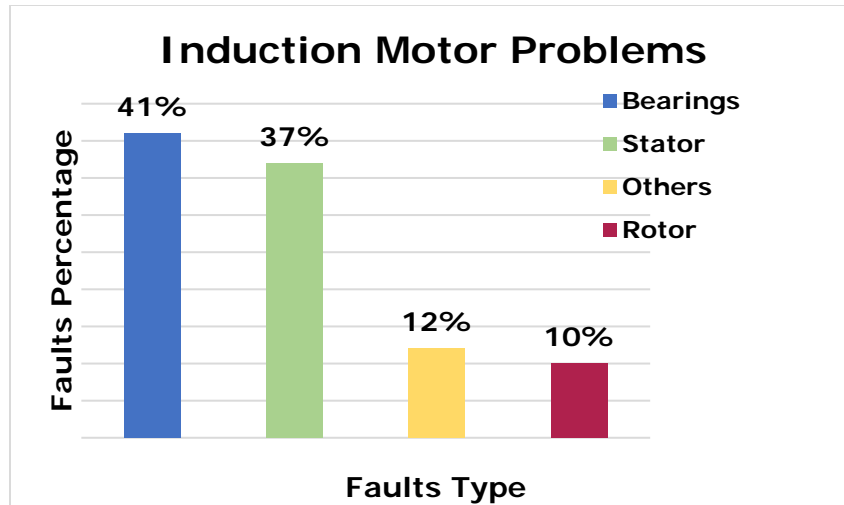


Figure 2-18: Problems in induction motor, redrawn from [53]

Some of the most common failures are listed below:

- Bearing fault related;
- Rotor broken bars and rings;
- Stator coils short-circuits; and
- Stator unbalance and eccentricities.

Consequently, these faults can lead to other faults in the motor, such as, imbalances in the stator voltage or current, torque oscillations, efficiency drops, overheating, increased vibration, and/or torque reduction in the motor [52].

### 2.12.1 Electrical Faults

The most known electrical faults in induction machines are associated with stator and/or rotor faults, which will be discussed next.

#### ❖ Stator Faults

Stator faults account for around 40% of all the reported induction machine failures. Thus, it is imperative to diagnose these faults in an early stage of development [21]. These faults can be placed into one of the five classes shown in Figure 2.19, which include [52]:

- 1- Phase to phase short circuit;
- 2- Phase to earth short circuit;
- 3- Short between coils of the same phase;
- 4- Open circuit in one phase (single phase); and

5- Turn to turn fault within a coil.

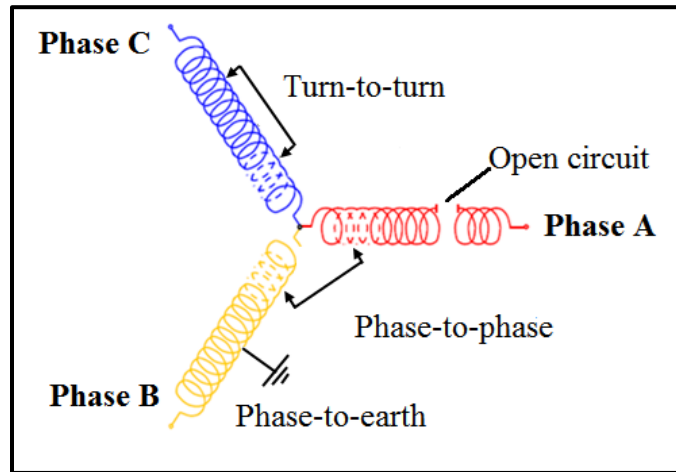


Figure 2-19: Graphical representation of stator faults amended from [55]

#### ❖ Rotor Faults

Mainly, rotor faults are caused by a breakage in the rotor bars caused by load variation. The main factors accounting for this breakage are thermal stresses, magnetic stresses, environmental stresses and mechanical stresses [56]. Broken rotor bars exhibit several indicators in induction motors, of which, one can mention the presence of additional sideband components in the power spectrum of the stator current. Whereas, the left sideband component is a result of electrical and magnetic asymmetries in the rotor cage, the right sideband component stems from the speed ripples caused by the pulsations in the motor torque [52]. Equation (2.45) defines the frequency of these sidebands [52].

$$f_b = (1 \pm 2S)f_s \quad (2.45)$$

#### 2.12.2 Mechanical Faults

Around 40-50% of IM faults are associated with mechanical defects and they can be classified into two categories which are eccentricity faults and bearing faults [54]

#### ❖ Eccentricity Faults

In electrical machines, eccentric rotor or eccentricity occurs as a result of a non-uniform air gap between the stator and rotor, where the rotor is no longer centred within the stator [52]. Air gap eccentricities are categorised as the static air gap eccentricity, the dynamic air gap eccentricity and mixed air gap eccentricity. The eccentricity of the air gap accounts for most of the known failures

in induction machines. In the static case, the rotational centre is offset from the main centre, while in the dynamic case, the rotational centre is at origin [53].

Eccentricity can also stem from intrinsic motor design and manufacturing imperfections, where, usually a tolerance of up to 10% eccentricity is allowed. However, for larger eccentricities, the resulting imbalances in radial forces can lead to a significant damage to the stator and/or the rotor. This detrimental phenomenon can also be caused by abnormal position of the bearing, wear in the bearings, bend in the shaft or motor operation under critical speeds, which can cause rotor whirl. The frequency components of the stator current caused by the air gap eccentricity are given by the following equation [52, 57]:

$$f_{slot+ecc} = f[(kR \pm n_d) \left[ \frac{1-S}{P} \right] \pm n_w] \quad (2.46)$$

where:  $f$  is the fundamental supply frequency,  $k = 1, 2, 3, \dots$ ,  $R$  is the number of slots,  $n_d = 1, 2, 3 \dots$  (Dynamic eccentricity),  $n_d = 0$  (Static eccentricity),  $S$  is the per-unit slip, and  $p$  is the number of pole pairs and  $n_w$  is the stator MMF harmonic order.

The air gap eccentricity in IMs produces unique spectral patterns, which can be seen in the current spectrum. According to the rotating wave approach, these patterns can be analysed, where the magnetic flux signals in the air gap are perceived as the product of permanence and MMF waves [58].

Consequently, variations in the eccentricity will manifest themselves as changes in the air gap flux that might have stator current components according to the following expression:

$$f_e = f_s \pm m f_r \quad (2.47)$$

where:  $f_e$  is the current components,  $f_s$  is the supply frequency,  $m$  is the harmonic number, and  $f_r$  is the rotational speed frequency of the rotor.

### ❖ Bearing Faults

In [52], it is mentioned that bearing faults account for ~41% of failures in electric motors in general, which is a fairly high percentage; thus, early detection of such faults is of a great interest to machines designers. Figure 2.20 depicts the structure of a typical bearing, consisting of two rings; the inner and the outer rings, in between which a set of rolling elements are put inside

raceways to allow for a smooth rotation. Now, depending on the location of the defect, bearing faults can be categorized as:

- Outer raceway faults;
- Inner raceway faults; and
- Ball faults.

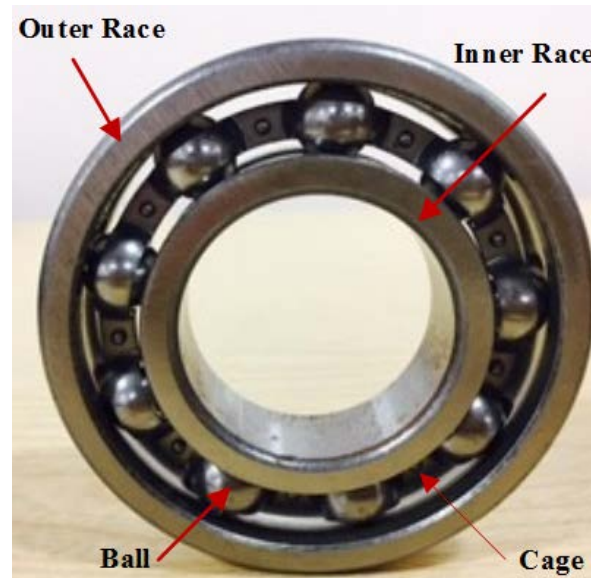


Figure 2-20: Bearing main components (Taken by the author)

Each type of bearing fault generates a distinctive fault frequency  $f_c$ , which is equal to the periodicity of the abnormality caused by the fault's presence [59]. These fault-dependent signatory frequencies are functions of the geometry of the bearing and the rotational frequency  $f_r$  of the motor's rotor. Since the rotor is supported by the bearings, any defects will result in a radial motion between the rotor and the stator, exhibiting frequencies that are closely linked to the dimensions of the bearing. Essentially, faulted elements in a bearing lead to vibrations at the motor's rotational speed. Given the dimensions of the bearing and the motor's rotational speed are known, the characteristics fault frequencies can be calculated. In practice, it is common to utilise mechanical vibration diagnosis methods to assess the condition of the bearing [59].

$$f_{bearing} = f + n_b f_{i,o} \quad (2.48)$$

where  $n_b$  is the number of balls,  $f_{i,o}$  is inner and outer race frequencies.

Also:

$$f_{i,o} = \frac{n_b}{2} f_r [1 \pm \frac{b_d}{d_p} \cos \beta] \quad (2.49)$$

$f_r$  is the rotational frequency,  $b_d$  is the ball diameter,  $d_p$  is the bearing pitch diameter, and  $\beta$  is the contact angle.

### Shaft Misalignment

Shaft misalignment in rotor-bearing structures is a common cause of vibration in rotating machinery, which can be either parallel or angular in nature [60]. According to [61], misalignment in a system occurs when the components of the system are not coaxial, thus, couplings are normally used to expand the misalignment between shafts by producing reaction forces in the coupling.

### 2.13 Key Findings

- VSDs have been increasingly spreading in many industrial applications to improve production efficiencies and provide a better performance in terms of cost, however, capturing the data is a hard task as the drive provides a background of noise which hides some frequency features.
- Mechanical defects give rise to additional oscillations in the speed and load, which can be obviously observed in the electrical signals. The drive will control the speed to maintain it close to the reference by changing the current, voltage and frequency, then compensate for any changes caused by the fault.
- Review the literature show that the ESA has gained extensive interest in the latest researches, however, the above review has shown that most studies were about open-loop or directly fed; mechanical systems driven by sensorless VSDs have received less attention in fault detection and diagnosis which a serious omission given the popularity and importance of sensorless VSDs in modern industry.

## **CHAPTER THREE: FAULT DIGNOSTIC BASED ON ELEECTRICAL SIGNATURE ANALYSIS**

---

*This chapter starts by reviewing the necessity of CM of induction motors. Next, it reviews the common techniques used for CM. It will then discuss and will provide a detailed explanation of the fundamentals of supply-based motor diagnosis methods with an in depth review of the analyses of the electrical signatures of induction motors; motor current, motor voltage, motor power, and motor power factor signature analysis.*

### **3.1 Introduction**

Condition monitoring is a necessity in the technology scope and industrial applications; it can be described as “the continuous evaluation of the health of plant and equipment throughout its serviceable life” by which a system’s symptoms are assessed [1]. CM and fault diagnosis have become increasingly important in the last decades for electrical machines applications and maintenance, with early fault detection vital in order to detect faults in time to carry out maintenance with minimum disruption to production. The key concept of CM is to use technology to evaluate the machine’s health and predict if and when a failure may happen. Ongoing CM enables operators to collect and store data for trend analysis. Another key is that the condition monitoring is its substantial task of identifying any changes in the system behavior. And by doing so, an advanced caution can be provided so a decision can be made to choose to maintain the machine or not which will be useful in terms of saving energy and money.

This technique has been used for many years where, typically the RMS vibration level was tracked and when it reached a prescribed level, the machine was deemed as requiring maintenance and, possibly, repair. Today, the sophistication of signal measurement and analysis is such that individual faults can be identified, which allows significant improvement in maintenance planning and scheduling with benefits such as reduction of the spare parts inventory. Such information also provides the opportunity for manufacturers to improve product quality and designers to improve machine reliability [1-3].

### **3.2 The Need for Condition Monitoring**

CM minimizes machine breakdowns by evaluating the machine condition, identifying machine component faults and predicting time to breakdown. CM has become very important in modern industrial because it has the potential to reduce operating costs by improving reliability of operation, and to improve service to customers by ensuring production better meets demand. One result has been increasing interest in CM methods for rotating machines [48]. The CM of an induction motor is an important technology for online diagnosis of primary faults. The extensive use of IMs in every area of industry and the costs incurred due to motor failure have meant the research into online diagnosis of primary faults of IMs is an important topic for enhancing the ability to detect defects in their early stages and avoid unexpected breakdowns. The required data

is obtained from monitoring specific parameters, e.g. vibration levels, temperatures, levels of radiated sound and other process parameters [62].

Effective CM will improve the reliability of the IM and maximize its performance and working life. However, good CM needs skilled personnel and strong management commitment [63].

### **3.3 Conventional Condition Monitoring Systems of Induction Motor Drives**

There are various monitoring techniques that can be used for the CM of IMs. For instance, Visual Inspection Monitoring, Vibration CM and diagnostics, Temperature Monitoring (Thermal Measurement), Oil analysis, MCSA, Acoustic Monitoring etc. All of them have their own drawbacks and benefits, some of them are all the more usually referred to, for example, vibration, while some of them have been developed more recently, e.g. ESA.

The selection of a suitable CM technique depends on the machine or components to be monitored, with cost of the CM system a significant factor. For instance, when a machine is near to failure, visual inspection can be sufficient to assess the machine situation. However, to detect faults at an early stage, or in the case of sophisticated and complex machines, advanced CM methodologies will be needed [64].

Generally, most of conventional CM consists of the following elements (see Figure 3.1) [1]:

(i) Sensors: used to measure the signal. Information about the machine's state (e.g. the vibration signal) will be transferred from the sensors to the CM system. These signals will usually be treated, making it suitable for the data acquisition system, (ii) The data acquisition system is used to acquire the signals from the sensor output, to amplify, and pre-process the signals to be analysed in preparation for fault diagnosis, and (iii) Signal processing for fault diagnosis, usually this mean detecting any difference between the signal from the fault-free machine and the signal as measured. This will include feature extraction from the signal [65, 66].

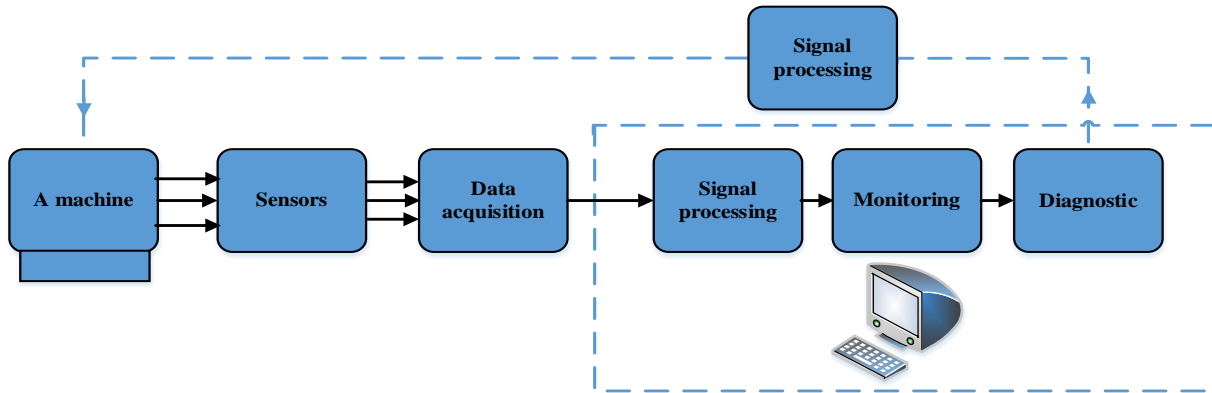


Figure 3-1: Block diagram of conventional CM, (image redrawn by the author)

The most common CM measurement and analysis techniques can be briefly summarised as follows:

### 3.3.1 Vibration Monitoring

One of the most powerful CM techniques is the vibration analysis. This can be explained by that all rotating machines generate vibration even when new or without fault [63]. The vibration signal is sensed then amplified and analyzed to reveal information on the state of the motor. The results are assessed for any necessary action. Vibration monitoring is not sufficient for every CM requirement; some types of fault may not significantly change vibration levels when compared to the healthy case [24].

Vibration CM is usually easy to implement [63], however, it can be expensive due to the sensors used, and difficult to implement as it requires direct access to the machine being monitored. Moreover, it is important that vibration sensors are correctly positioned and mounted on the motor, which needs specialist knowledge. Additionally, sensors are susceptible to failure [65]. Sometimes vibration signals can overlap with other sources of vibration such as nearby machines [50]. Another disadvantage for this method is that it is inappropriate for detecting faults at an early stage [66].

### 3.3.2 Acoustic Monitoring

For many years, acoustic methodology has been advancing. This approach uses the high frequency waveforms generated by machine processes. It often uses a piezo-electric microphone to detect the acoustic signals to compare them with vibration-monitored waveforms and extract features that contain information about the machine's condition. These microphones are sensitive, are easy to

mount and possess wide frequency ranges. Therefore, microphones are utilized in many applications including gearbox, bearing, tool and engine condition monitoring [50]. Acoustic approach can provide a high signal-to-noise in the industrial applications as compared with vibration technique because there is not much environmental noise at frequencies above 50 kHz. However, a CM system using acoustic can entail high system costs. Moreover, because acoustic signals are high frequency, they attenuate rapidly and it is usually necessary to place sensors nearby the source. In addition, it requires specialized expertise [25, 65].

### **3.3.3 Thermal Monitoring**

Use of temperature for CM is widespread as a general factor used to indicate a motor fault. [66, 67]. This method can give a good indication of any alterations that might happen in a machine. Further, if inexpensive thermocouples - which can be plugged into hand-held devices- can be used to monitor specific parts such as bearings, the windings of the drive and the core. Hand-held thermographs with real-time displays can be used to monitor the surface temperature and identify individual components, both external and internal. According to [29], thermal overloading leads to stator insulation breakdown which in turn will cause motor failure. A problem with using this technique is how to access the information concerning the rotor while the machine runs. Thermal monitoring requires the purchase and installation of additional sensors, and the user needs to be aware that reasons other than faults can give rise to temperature increase [65].

### **3.3.4 Electrical Signature Analysis (ESA)**

Even though the CM techniques mentioned previously are used widely in the monitoring scope, their expensive cost of installation and implementation made limits to use them, which has made the necessity to find alternative solutions aiming at saving time and money [68]. ESA is a promising method being developed to detect a wide range of IM faults and overcome problems related to conventional methods of CM. The great advantage of ESA, and the major reason for using it for fault detection and diagnosis, is the direct correlation between easily measured electrical signals and mechanical motor faults. ESA is a non-intensive method used to define the situation of the motor without interrupting the system's operation. The acquired signals are analysed to detect various faults. ESA has two additional advantages; the signals extracted from the control panel and can be analysis remotely, and there is no need for additional specialist

equipment or sensors. In addition, with ESA it is possible to detect defects in their early stages of development, avoiding unwanted breakdowns and consequently adding to production costs [69].

Recently, there have been numerous advances in CM based on ESA providing easier ways to detect and diagnose motor faults, confirming that analysis of electrical signals can capture the presence of both static and dynamic faults. E.g. it has been shown that it is possible to identify the impacts associated with the dynamic faults through analysed of the sideband components [4, 5].

It is possible to choose the current and/or voltage signals for motor diagnosis. The procedure of analyzing these signals is known as a signature analysis. In general, a non-defective motor generates a particular signatory signal. Once a fault occurs in the machine, this signature will change significantly. The new signature is compared with the healthy case and a developing defect, possibly in its early stages, may be detected. Depending on the degree of severity and nature of the detected fault, the operator can decide whether continue or stop the machine operating for maintenance purposes to avoid the fault becoming severe [11].

In terms of gearbox faults, mechanical oscillation within the gearbox produces eccentricity of the air gap in the IM which causes a change in the air-gap flux, which then produces variation of the stator current. This variation in the stator current will have harmonics of the oscillation frequencies and will generate sidebands around the fundamental frequency  $f_s$ . These sidebands contain sufficient information to be used for gear faults detection [4]. In other words, mechanical defects cause oscillations in speed and load, which can be clearly seen in the electrical signals. However, this approach has some limits; when the faults are small, the drive's noise and the control activities of the closed-loop can cover these features and make detection difficult [4, 70]. However, recent work has only just begun to investigate the possibility of ESA being able to detect and differentiate between two or more simultaneous faults [71].

The commonly used ESA features for fault detection and diagnosis are: motor current signature analysis (MCSA), motor voltage signature analysis (MVSA), motor power signature analysis (MPSA), and instantaneous power factor signature analysis (IPFSA).

#### **3.3.4.1 Motor Current Signature Analysis (MCSA)**

MCSA is regarded as an important technique for detection of IM and downstream equipment faults. MCSA has successfully diagnosed faults in large IMs and has become a standard of online motor diagnosis [47].

According to [55], MCSA refers to analysis of the stator current in the frequency-domain to detect faults such as air-gap eccentricity, broken bars, and bearing damage. Mehala reported that MCSA is based on the behaviour of sidebands in the spectrum of the current, each set of sidebands associated with a given fault. MCSA can provide a complete view of the IM's health but requires knowledge of machine construction.

In addition, MCSA has the ability to detect these problems at early stages and thus prevent motor complete failure to be occurred [47]. A complete view of the system's situation can be a result of using MCSA in motor diagnostics. With other CM detection systems, the severity of the fault has to be serious before it can be detected, which cannot happen with MCSA.

In terms of advantages, MCSA has:

- It is non-invasive,
- Maintenance time is reduced,
- Lower noise levels on the measured signal,
- Safety is improved due to no risk involved in data collection process,
- Improved ability to manage and plan the required maintenance,
- MCSA can be used anywhere there is a working electric motor,
- Simple in term of sensors and installation,
- Suitable for mechanical and electrical fault detection,
- Doesn't need to estimate the motor's parameters, and
- The possibility of online detection [72, 73].

Motor's fault diagnosis using the MCSA has been developed by some researchers using sophisticated signal-processing methods. The abnormal harmonic frequencies associated with certain faults don't depend on the types of drive-systems, making the MCSA a much more useful technique for fault detection than the others online diagnosis approaches (e.g. acoustic signal) [18].

Gearbox monitoring is important in industry because of its role in the power transmission. Any defect in the gears might cause a loss of performance and possible machine downtime. Additionally, it is possible to use the MCSA indirectly in gearbox monitoring, which means the gearbox can be monitored at a site some distance away from its actual location [74].

Jung et al., [75] provided an online IM diagnostic by using the MCSA associated with advanced signal-and-data-processing algorithms.

According to Barshikar et al., [4], a gear fault can create an abnormality in the torque which can be observed by the IM. The load will transmit this abnormality to the motor current and thus, it is possible to see unique frequency components in the current signals. The oscillations in the gearbox changes the eccentricity of the air-gap, causing changes in the flux waveform which in turn can induce stator current components. The oscillations in the load will increase additional components in the current spectrum. Another reason for increasing the current components is the gearbox itself. In particular, slowly rotating shafts will generate components around the supply frequency. Kar et al., [76] compared between the vibration signature and MCSA to diagnose gearbox defect using different signal processing methods “fast Fourier transform (FFT), Discrete Wavelet Transform (DWT), and Continuous Wavelet transform (CWT)”. The authors concluded that combining MCSA with the DWT can give a better performance than more conventional vibration methods.

In 1999, Benbouzid et al., used different advanced approaches such as high-resolution spectral analysis on motor current signals to diagnose several IMs faults such as a broken rotor bar, eccentricity, shaft speed oscillations, rotor asymmetry, and bearings failure. It was found that high-resolution spectral analysis of the stator current is very sensitive to fault’s existence in the IM, which noticeable modify the main spectral components [77].

It has been shown that MSB analysis can be usefully used with current signals to boost features components in order to detect stator faults using an open-loop control mode [78]. The application of MSB to the electrical current signals obtained with a VSD with open-loop control, for the monitoring of mechanical faults in a downstream gearbox was investigated in [79]. Results showed that the amplitude modulation (AM) bispectrum analysis improved performance due to its ability to reduce noise. It is possible to use both conventional spectrum and AM bispectrum for detecting tooth breakage and shaft misalignment. However, the AM bispectrum is more sensitive to small changes and consequently, it can provide a better performance in early stages of fault’s detection.

A study in [80] has investigated the use of MCSA in compressor fault detection. It was found that the current spectrum for a healthy compressor is dominated by the main supply frequency with a number of distinct sidebands, and that in case of a fault the amplitude of the existing sidebands increased, and new sidebands appear at higher harmonics of the crank shaft rotating frequency.

Previous work [71], has used current and voltage signals to diagnose stator faults open and closed-loop control, and shown that an accurate and reliable diagnosis can be provided by the sensorless strategy. MCSA has been also used to detect the loss of efficiency in IM controlled by sensorless VSDs [81]. In [82], the authors proposed a scheme for FOC with real-time on-line measurement for the resistance of the rotor and the speed of the motor. Both were estimated by neural network aiming at improving the performance of the IM.

A study in [83] used the instantaneous active and reactive current signatures in separating broken rotor bar faults from load fluctuations. It was found that the effect of load oscillations can be clearly marked in the spectrum of the instantaneous active current whereas the broken rotor bars demonstrated a smaller but still significant effect on the instantaneous active current which showed as sidebands components in the instantaneous reactive current.

In [81], the researchers presented MCSA methods used for detecting efficiency's reduction in early stages for a motor driven with a sensorless VSD.

In 2012, the MSB was used by Alwodai et al., to differentiate between different severities of stator fault. Their work showed that the MSB was capable of accurately estimating the degree of modulation and suppressing random and non-modulated components. It also has the ability to differentiate the amplitudes of the signals caused by stator defects [78].

#### **3.3.4.2 Motor Voltage Signature Analysis (MVSA)**

MVSA technique is much the same as the MCSA, except that it uses the motor supply voltage in the analysis. It is frequently used in generators analysis. Moreover, it can be used in motor's power faults, and stator imbalance simultaneously with the MCSA [84].

A previous work [85], investigated the production of different harmonics due to motor faults. This approach was based on imbalance impedance caused by applying a phase turn fault and considered only the fundamental component [85]. A comparative study was carried out to diagnose motor stator faults under open-loop and closed-loop control using MCSA and MVSA [71]. It was claimed that definitive characteristic features were obtained when MVSA was used. In addition, the voltage spectrum was shown to give a slightly better performance than the current spectrum. Further, it was also shown that a more reliable and accurate diagnosis was achieved using sensorless control. In [6], the voltage signature was used to diagnose a gear tooth breakage under sensorless VSD.

### 3.3.4.3 *Motor Power Signature Analysis (MPSA)*

The instantaneous power is a fault detection method based on the spectral analysis. It is similar to MCSA and MVSA except it considers the information present in voltage and current signals of a motor phase simultaneously [84].

A study [86] has stated that the instantaneous power can be used in place of the stator current as a medium for motor signature analysis to detect mechanical faults. It was found that the information provided by the power signals is higher than that carried by the current alone and thus, the diagnosis and detection reliability should be improved. Further components can be provided by the power spectrum at both modulated and fundamental frequencies and the two classical sideband components, which is an advantage since the fault harmonics are well bounded. However, the power spectrum as derived using the FFT is noisy and so further development is needed.

In [87], the diagnosis of a broken rotor bar within an IM with sensorless VSD was investigated. It was assumed that a fault in the motor caused sinusoidal modulation of the stator current amplitude, while the phase modulation of the current was negligible. The asymmetric nature of the fault meant that the MCSA, MVSA and MPSA all contained relevant information relating to the fault. However, experimental tests showed that the power spectrum was the most reliable and accurate source of components at twice the slip frequency and so was able to better separate different BRB faults, compared with either current or voltage signals.

A study in [88] developed a novel diagnosis approach for oil degradation based on the power supply measurement. Oil degradation leads to a change in the viscosity of the oil in a gearbox, variation, which will be seen by the IM as a change in the static and dynamic power requirements. Detecting the influence of water contamination on gearbox lubrication for a motor driven with a sensorless VSD has been discussed by [89]. The authors identified that the analysis of supply parameters obtained from both the VSD and external measurements were definitely affected by the level of oil contamination. More sensitivity has been shown by the voltage and power signals to the water contents than that of the current signals because the voltage signals control loop locates the inner loop in the VSD control system; thus, it has wider bandwidth than any other loop. Therefore, they correspond to mechanical faults more than the current signals. “The VSD thus, changes the terminal voltage more than the current due to its attempt to keep speed constantly and adapt any changes in the torque caused by a fault”.

One paper [90] investigated broken rotor bar faults based on the active & reactive power signals. In this study, the authors used the finite element technique for dynamic simulation, aiming at more reliable information.

#### **3.3.4.4 Instantaneous Power Factor Signature Analysis (IPFSA)**

The instantaneous Power factor can be defined as a unity of power consumed by an electrical load. Moreover, it is known as the ratio of the used power (real power- kW) to the distributed power (apparent power- kVA). The power factor value ranges from zero to one. In case of small power factor, the current becomes higher, which generates power fluctuations between the load and the source and affects the power supply [91]

Due to the electrical properties of the power factor metric, any electrical or mechanical frequency components generated either by a fault or as a result of background noise will inevitably be manifested in the form of harmonic components [58]. Moreover, the current zero-crossing points changed with load torque fluctuations. Thus, the instantaneous power factor will correspondingly fluctuate. If there is a fault, torque fluctuations will impose changes in the instantaneous power factor [92].

A study [93] used the power factor signature to diagnose broken rotor bars using the FFT. It has found that this kind of fault "broken rotor bar" can be detected in the sidebands and the power factor gave a good fault indicator. Using the power factor approach, Arabaci et al., investigated the detection and classification of broken rotor bars for steady state operation of an IM. The authors used one phase current and voltage of an IM to calculate the instantaneous power factor using the FFT. Then the Artificial Neural Network (ANN) was used to classify the IM fault [94]. The diagnosis of bearings faults in an IM by the exploitation of the instantaneous power factor was further discussed in [95]. This latter study compared the relative diagnostic performance of the instantaneous power factor spectrum with stator current and vibration measurements and confirmed that the power spectrum provided a "good performance" relative to the other two. However, the authors warned that advanced signal processing was necessary for reliable and accurate diagnosis. A series of papers and reports [96-98] have proposed various developments of the use of the power spectrum for fault detection and diagnosis. One [98] proposed a method of determining the IPF using the measured current. The others [96, 97] proposed using the power factor signature for the diagnosis and detection of static and dynamic eccentricities in IMs, and

further confirmed its effectiveness in IM fault detection. Lane, M. et al., researched the possibility of using the IPF signature for motor imbalance under both open-loop and sensorless VSD at different speeds and constant load [99]. Results showed that the power factor signals are improved using the sensorless VSD more than those of the open-loop system.

In [100], the instantaneous phase variation is used for detecting a broken rotor bar in an induction machine. Results showed that the instantaneous phase variation was capable of detecting the rotor bar fault particularly at full load condition.

For some thirty years the instantaneous power spectrum has been used to separate the frequencies present in the measured signal from, say, a gearbox to determine frequencies of interest, especially those linked directly to the presence of a fault making them more easily useable for CM and fault diagnosis [101].

However, these researches did not study the use of IPF signature for detection of faults in downstream mechanical equipment gearbox.

To calculate the instantaneous power factor, both current and voltage signals of only one of the stator phases were measured. Hilbert transform has been used to calculate the phase difference between voltage and current phase angles as represented in the block diagram Figure 3.2.

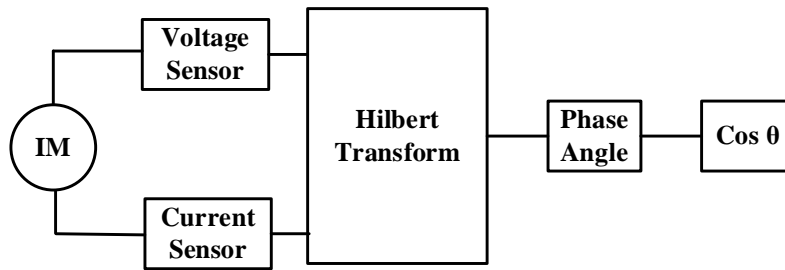


Figure 3-2: Instantaneous power factor's block diagram

Thereby, the power factor was determined by the meaning of the cosine of the calculated phase difference. The analytic expressions of instantaneous voltage and current can be obtained by applying the Hilbert transform to measured voltage and current signals respectively as represented in the following equations:

$$v = Ve^{j[2\pi f_s t + \theta_v(t)]} \quad (3.1)$$

$$i = Ie^{j[2\pi f_s t + \theta_i(t)]} \quad (3.2)$$

where  $V$  and  $I$  are the amplitudes of voltage and current signals respectively;  $f_s$  is the supply frequency;  $\theta_v(t)$  and  $\theta_i(t)$  are the instantaneous phase of voltage and current, denoted as IPV and IPI respectively. Thus, the complex power (units: VA) is:

$$\begin{aligned}
 S &= vi^* = Ve^{j(2\pi ft + \theta_v)} (Ie^{j(2\pi ft + \theta_i)})^* \\
 &= Ve^{j(2\pi ft + \theta_v)} Ie^{-j(2\pi ft + \theta_i)} \\
 &= VIe^{j(\theta_v - \theta_i)} \\
 &= VI \cos(\theta_v - \theta_i) + jVI \sin(\theta_v - \theta_i) \\
 &= P + jQ
 \end{aligned} \tag{3.3}$$

$$IPF = \frac{P}{|S|} = \cos[\theta_v(t) - \theta_i(t)] = \cos[\theta(t)] \tag{3.4}$$

Where  $S$  is the apparent power,  $P$  is the active power,  $i^*$  is the conjugate of the complex current  $I$  and  $Q$  is the reactive power.

The instantaneous power factor is the ratio between active and apparent power.

It means that the power factor can be calculated by finding the phase difference between the voltage and current measurements, whose key steps are presented earlier in Figure 3.2.

From Equation (3.4), it can be seen that the IPF combines the instantaneous phases from both voltage and current signals, which potentially improves the signal to noise ratio (SNR), aimed at more accurate and reliable diagnostic. However, because of the phase difference, some of instantaneous components of the same phases can be cancelled out, leading to a lower SNR, which can degrade the diagnostic performance. To avoid this it directly multiplies the analytic signals and obtains a phase summation quantities as [102]:

$$\begin{aligned}
 S &= vi = Ve^{j[2\pi f_s t + \theta_v(t)]} Ie^{j[2\pi f_s t + \theta_i(t)]} \\
 &= VIe^{j[4\pi f_s t + \theta_v(t) + \theta_i(t)]}
 \end{aligned} \tag{3.5}$$

For steady operation, the linear incremental trend due to “ $4\pi f_s t$ ” can be taken out easily, which gives the following relationship:

$$\theta_{vi}(t) = \theta_v(t) + \theta_i(t) \tag{3.6}$$

The phase summation presented in Equation (3.6) is the instantaneous phase of voltage-current (IPVC) and is different from IPF. “The “IPVC” is obtained from signal processing point of view and has no physical meaning. This “IPVC” can enhance the phase components that are of the same phases in both voltage and current signals, and also cancel out any random components to a great extent, producing more diagnostic information” [102].

Reviewing the literature show that the ESA has gained extensive attention in the latest researches, most of research work was focusing on using the open-loop or directly fed. However, less interest has been devoted to study faults detection of induction motors driven by sensorless VSDs. To fill this gap, this PhD study examines the use of electrical signatures for machines driven with sensorless VSD in fault detection and diagnosis using advanced signal processing methods to extract diagnostic features.

### **3.4 Key Findings**

- Condition monitoring is of key important to all industrial applications in order to detect faults at early stages which will help protecting the machine and reducing the system operation cost.
- Conventional condition monitoring methods have been presented in this chapter, including the vibration analysis, thermal analysis, acoustic analysis and electrical signatures analysis.
- The electrical signature analysis hasn't gained an extensive attention with mechanical systems driven by sensorless VSDs for machines fault detection and diagnosis.
- ESA is a good method to detect and diagnose the conditions of a machine used to define without interrupting the system's operation. The extracted signals from the control panel can be analysis remotely in their early stages of development to avoid unwanted breakdowns and their consequents costs.
- The literature showed that insufficient work have been done on IMs based on sensorless VSDs. In particular, very limited work has been carried out on detecting mechanical faults

in downstream equipment systems such as gearbox using all electrical signatures such as current, voltage, power, power factor and phase quantities.

- Especially, previous studies focused on the use of only the amplitude and frequency information offered by instantaneous ESA. The phase information from ESA has not fully explored for the purpose of machine diagnostics using ESA.

## CHAPTER FOUR: EXPERIMENTAL FACILITIES

---

*This chapter introduces the general specifications of the experimental facility which consists of the rig components, the specifications of the driving motor, the load generator, electrical drives, and the two-stage helical gearbox. Further, it also provides information about the data acquisition system, measurement system, thermocouples, accelerometers and speed measurements. It also provides a general overview of gears. Then, it explains the procedure for collecting the data and aspects of data analysis.*

## **4.1 Introduction**

In order to fulfil the planned aim and objectives, different experimental tests were carried out on a laboratory transmission test system developed at Huddersfield University. This system was designed to simulate a real industrial system and to achieve repeatable series of tests on a gearbox, healthy and with faults in order to obtain electrical signals measured under different operational conditions with different fault severities as would occur in real applications of mechanical systems.

## **4.2 Test Rig Description**

The test rig used in this work consists of two fundamental parts; the first one is the mechanical system and the second is the electrical control system. Further parts are the data acquisition system and the measuring devices.

### **4.2.1 Mechanical Systems**

It can be seen from Figures 4.1 and 4.2, the mechanical part of the system is composed of two helical gearboxes connected back to back via a flexible coupling, a three phase induction motor, DC generator; an encoder which is attached to the AC motor shaft; tachometer attached to the generator; and flexible spider rubber couplings connecting each element with the next. The induction motor (15 kW, 1460 rpm and four poles) is powered by 3-phase power supply. A two stage back to back helical gearbox is used in the test with a number of teeth for the first stage, 58/47, and 13/59 for the second stage. Both sets of teeth have the same mechanical specifications. The main gearbox which is connected to the induction motor via a flexible coupling plays a speed reducing role whereas the other gearbox acts to increase the speed. This can be explained by the fact that if we use one gearbox; for instance a speed reducer, the generator will not turn fast and consequently, cannot take enough load. Further, this is a back-to-back testing gearbox rig not a realistic engineering machine and it is conventional in CM. There is a need to fit at least one gearbox. However, the rated speed of the generator is the same as that of the AC motor speed. Hence, it needs to increase it again at the inverse rate it was decreased. This will have another benefit that is when we need to study a certain fault we have two identical boxes and it is possible to induce the fault into one gearbox and keep the other healthy. A comparison then is feasible as they are identical and running under the same load and speed as well as weather conditions. The rig is controlled using a programmable logic controller (PLC) which delivers the test profile to

both DC and AC variable speed drives. The operator enters the required test procedures via a touch screen on the main control panel. The photo below was taken in the lab before the experiments commenced.

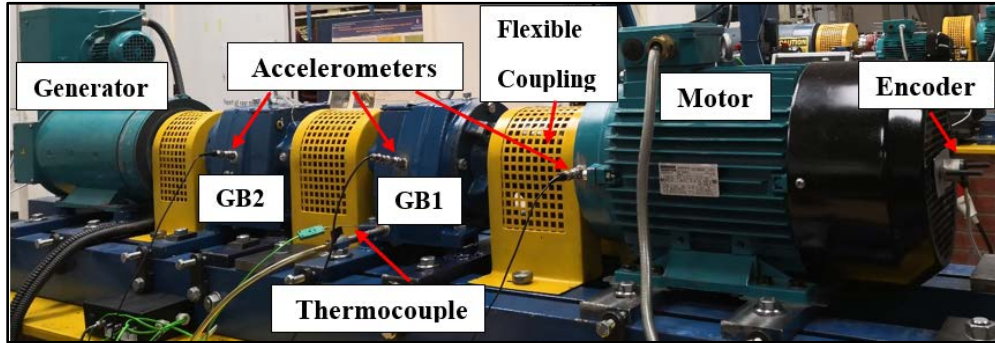


Figure 4-1: Photograph of the test rig

Figure (4.2) is a schematic diagram of the test rig used in the experimental work.

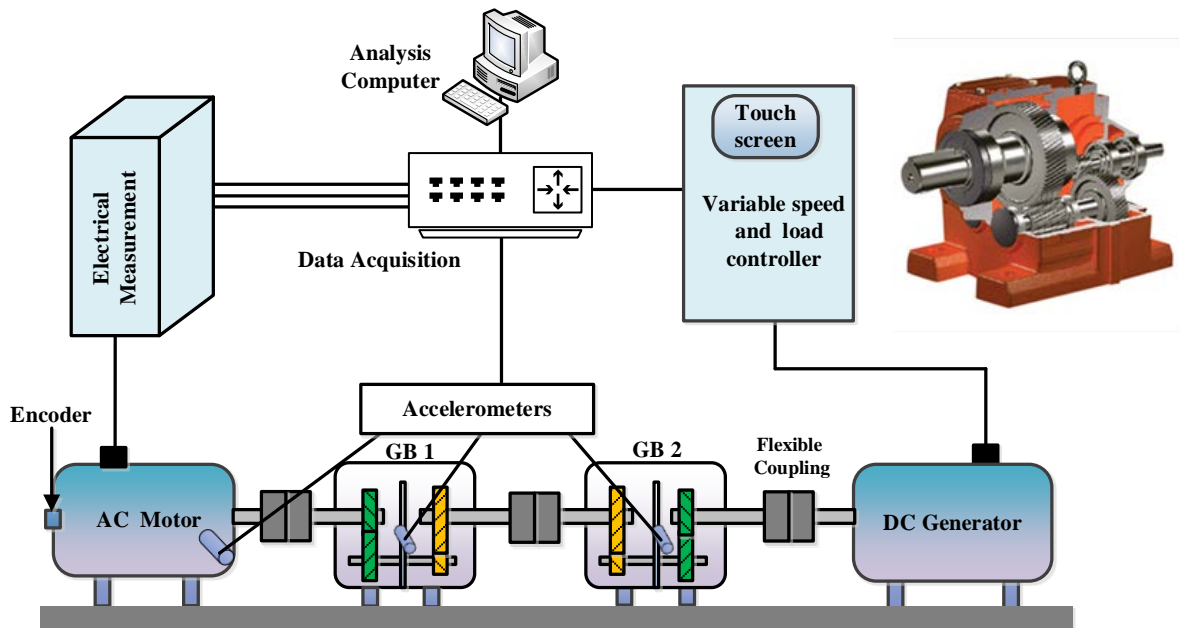


Figure 4-2: Schematic diagram of the test rig

Induction motor, DC generator, rubber couplings and helical gearboxes specifications (from manufacturer's data sheets) are given in Tables 4-1, 4-2, 4-3 and 4-4 respectively:

**Table 4-1: Induction motor specifications**

Description	
Manufacturer	Invensys, Brook Crompton

Motor model	T-DA160LA
Number of poles	4
Frequency	50 Hz
Power	15 kW
Voltage ( $f = 50$ Hz )	415 V
Rated current	27.13 A
Connection	Delta $\Delta$
Efficiency	89.1 %
Rated speed	1460 rpm
Full load torque	98.3 Nm
Power factor	0.87
Stator resistance	0.8607 ohm
Stator Leakage Inductance	0.01678 H
Rotor time constant	0.270 sec
Rotor resistance	0.5247 ohm
Rotor Leakage Inductance	0.08678 H
Mutual Inductance	0.1706 H
Inertia	0.09 kg.m <sup>2</sup>

**Table 4-2: Generator specifications**

<b>Description</b>	
<b>Manufacturer</b>	Invensys, Brook Crompton
Size	MD 132LC
No	B: 99021436
Ins Class	F
Power	15 kW
Armature voltage	380 V
Field current	2.37 A
Speed	2100 rpm
Duty type	S1
Wd	Shunt
Brg	N.D.E.6202Z
Enclosure	IP23
Mass	13.7 Kg

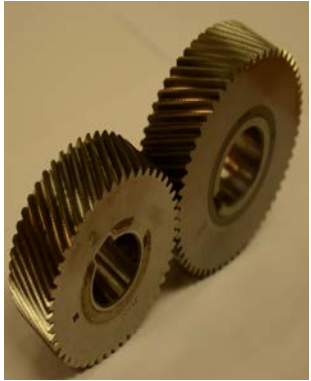
**Table 4-3: Rubber coupling specifications**

Description	
Manufacturer	Fenner
Type	HRC150H
Size	150 mm
Rated speed	1600 rpm
Nominal torque	600 N.m
Mass	7.11 kg
Inertia	0.01810 kg.m <sup>2</sup>
Dynamic stiffness	175 Nm/ <sup>o</sup>
Max parallel misalignment	0.4 mm
Max axial misalignment	+0.9 mm
Max angular misalignment	1°
Element type	Nitrile spider



**Table 4-4: Gearboxes specifications**

Description		
Manufacturer	Radicon	
Order No	1013102/ 2011	
Oil type	EP 320 (mineral oil)	
Oil volume	2.6 L	
Output torque	306 N.m @ 1450 rpm	
Overhung load	3.50 kN	
Reduction ratio	3.678*	
No of teeth	1 <sup>st</sup> stage 58/ 47	2 <sup>nd</sup> stage 13 / 59



\* Reduction ratio is calculated as: 
$$\frac{f_{r1}}{f_{r3}} = \left( \frac{z_2}{z_1} \right) \cdot \left( \frac{z_4}{z_3} \right) = 3.678$$

Figure 4.3 illustrates the schematic layout of the two-stage helical gearboxes:

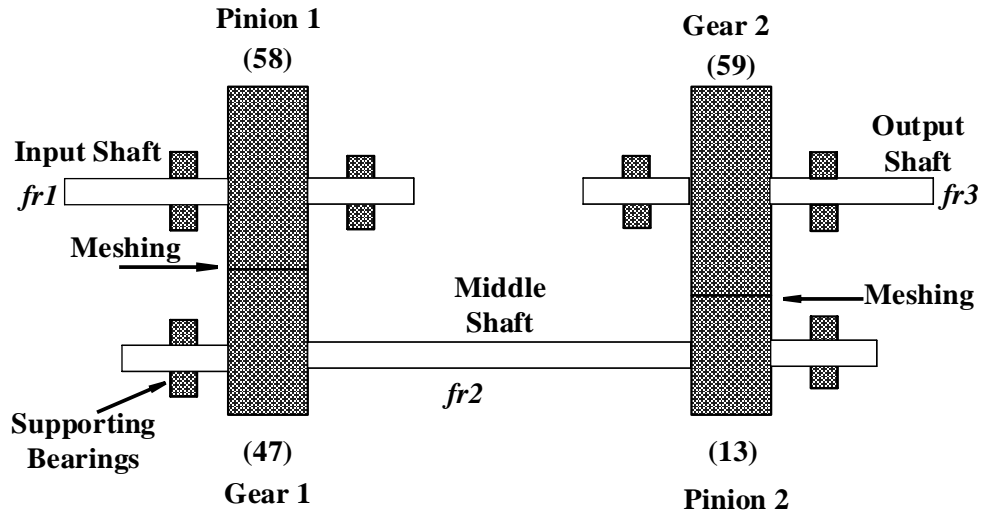


Figure 4-3: Two-stage helical gearbox schematic layout [author].

#### 4.2.2 Electrical System

The electrical system consisted of:

- A programmable logic controller (PLC),
- DC speed drive,
- AC speed drive,
- Circuit breakers for drivers to protect the AC induction motor, and the DC generator, and
- Power supplies

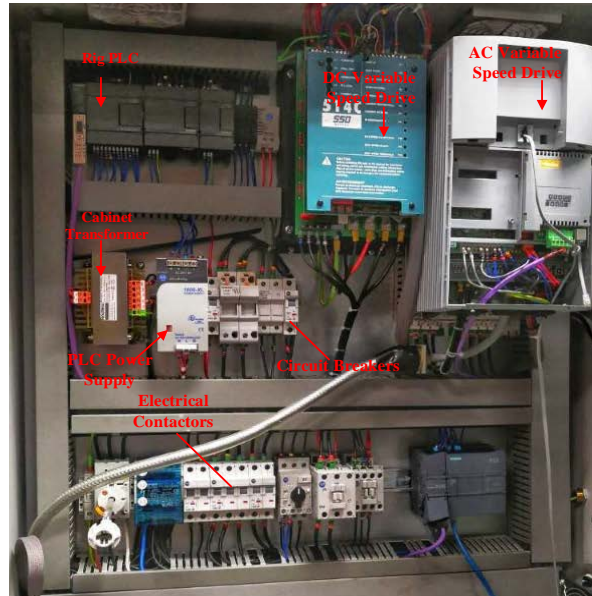


Figure 4-4: Control panel interior

- **The Programmable Logic Controller (PLC)**

Using a control panel, the test rig can be operated at different speeds and different loads in order to test its behavior under different working conditions and obtain accurate information. The program contains a setup panel screen, which includes time duration, number of steps, load set points and speed set points.

The PLC is a SIMATIC S67-200, manufactured by SEIMENS; with RAM and EEPROM slots.

Input Module, EM23 has four analogue inputs, output Module, EM232 transfers the out signals from the PLC to the external devices; as represented in the following tables.

**Table 4-5: EM231 input module technical specifications**

Description	
Model	EM231, 4 inputs × 12 bits
Power loss	2 W
Number of analogue inputs	4
Voltage input range: Bipolar	± 2.5 V, ± 5 V
Current input range	0~20 mA
Resolution	12 bits

Bipolar, full-scale range	32, 000 to +32, 000
Unipolar, full-scale range	0 to +32, 000
Input impedance	$\geq 10\text{M } \Omega$ Voltage Input, 250 $\Omega$ Current Input
Analogue to digital conversion time	< 250 $\mu\text{s}$
Maximum input voltage	30 V DC
Maximum input current	32 mA

**Table 4-6: EM232 output module technical specifications**

Description	
Model	EM232, 2 outputs $\times$ 12 bits
Power loss	2 W
Number of analogue outputs	2
Output voltage range	-10~+10 V
Output current range	0~20 mA
Resolution	12 bits
From L+ current consumption	70 mA
for voltage outputs	Min: 5 k $\Omega$
for current outputs	Max: 0.5 k $\Omega$
Basic error	$\pm 0.5\%$ of full range

▪ **AC Variable Speed Drive**

The Parker 650V AC variable speed drive consists of:

- Two analogue inputs,
- One analogue output,
- Six digital inputs,
- Two digital outputs,

- Two speed control modes,
- Volt/frequency control with linear or fan low profile, or
- Sensorless vector with automatic fluxing and slip compensation.

▪ **DC Variable Speed Drive**

The VSD provides a controlled variable load on the AC motor by regulating the test rig DC generator. The DC drive is the Parker 514C. The drive adjusts the speed of the DC shunt wound motor and controls the motor speed with a linear closed loop system and a feedback signal from the armature voltage.

The following tables show DC and AC variable speed drive specifications (from manufacturer’s data sheets):

**Table 4-7: AC variable speed drive specifications**

<b>Description</b>	
Product description	AC variable speed drive
Model	650 V
Output frequency	0-240 Hz
Switching frequency	3 kHz nominal
Voltage Boost	0-25%
Flux control	V/F control with linear or fan low profile  Sensorless vector with automatic flux control and slip compensation.
Pre-set speed	8 pre-sets
Stopping modes	Ramp, coast, DC junction and fast stop
S Ramp and Linear Ramp	Symmetric or asymmetric ramp up and down rates
Current Limit	Adjustable 110% or 150%  180% shock load limit -Inverse time
Voltage/Frequency Profile	Constant torque  Fan Law

Analogue Inputs	2 inputs – one is configurable; voltage or current
Analogue Outputs	1 configurable voltage output
Digital Inputs	6 configurable 24 V DC inputs (2 suitable for encoder)
Digital I/O	1 configurable 24 V DC open collector outputs/digital inputs
Basic error	± 0.5% of full range
Relay Outputs	1 configurable relay output

**Table 4-8: DC variable speed drive specifications**

Description	
Model	514C
Output frequency	0-240 Hz
Control Action	Closed Loop with Proportional Integral Control and Adjustable Stability
Speed Feedback	Armature Voltage or Tachogenerator
100% Load Regulation	Armature Voltage mode : 2% Tachogenerator mode : 0.1%
Maximum Torque/Speed Range	Armature Voltage mode : 20:1 Tachogenerator mode :100:1
Analogue inputs	7 non-configurable inputs
Analogue outputs	7 outputs: Set point Ramp, Total Set point, Speed, Current Demand, Current Meter (Bipolar or Modulus), +10V reference and -10Vreference.
Current Limit	Adjustable 110% or 150% 180% shock load limit Inverse Time
Voltage/Frequency Profile	Constant torque, Fan Low

Analogue Inputs	2 inputs – one is configurable; voltage or current
Analogue Outputs	1 configurable voltage output
S Ramp and Linear Ramp	Symmetric or asymmetric ramp up and down rates
Current Limit	Adjustable 110% or 150% 180% shock load limit Inverse Time
Supply Voltage	110 - 480 V AC $\pm$ 10%
Nominal Armature Voltage	90 V DC at 110/120 Vac 180 V DC at 220/240 Vac 320 V DC at 380/415 Vac
Overload	150% for 60 seconds
Field Current	3 A DC

### 4.2.3 Data Acquisition Systems (DAQS)

The data was collected via a DAQS software (GST YE6232B), the specifications of which are shown in Table 4-9.

**Table 4-9: YE6232B DAQS specifications**

Description	
<b>Manufacturer</b>	Global Sensor Technology YE6232B
Number of Channels	16
A/D Conversion resolution	24 bits
Sampling rate (Max)	96 kHz/channel
Input range	$\pm$ 10 V
Gain	$\times$ 1, $\times$ 10, $\times$ 100
Filter	Anti-aliasing
Interface	USB 2.0



The DAQS was connected to the test rig to collect the required information about the test. This system has 16 channels with a 24 bit analogue-digital converter for each channel at a 96 kHz of sampling frequency range of 96 kHz. Table 4.9 represents the specifications of the DAQS.

The data collected by the DAQS is then transferred to a PC for analysing. An encoder which is played the role of a speed indicator was linked to the DAQS. Then, all storage data was converted to a MATLAB format where it could be analysed using MATLAB code. The DAQS has the capability of analyzing in real time, both the time and frequency domains, and also performing statistical analysis of time and frequency domain signals.

#### **4.2.4 Measurements systems**

As the rig has been used before in different CM researches in the CEPE research group therefore a different number of transducers has been already installed such as current and voltage sensors, thermocouples, accelerometers and encoders.

The tools and measuring devices that were used in the tests are listed below:

- **Three-phase measurement unit:** A photographic of the three phase measuring device is shown in Figure 4.5.

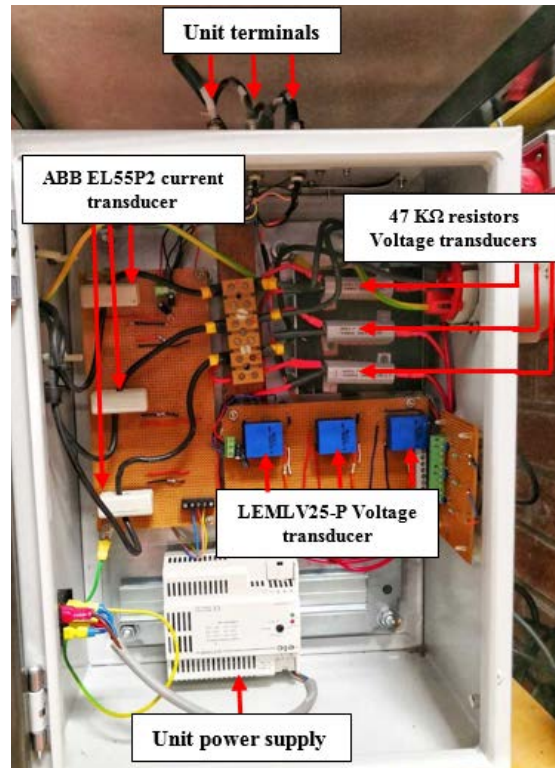


Figure 4-5: Three phase electrical signals measurement device

The unit measuring the instantaneous three phase currents and voltages using Hall Effect current and voltage transducers; the current transducer is the ABB EL55P2 while the voltage transducer is the LEM LV 25-P.

The following tables present the specifications of the current and voltage transducers respectively.

**Table 4-10: Current transducer specifications**

Description	
<b>Brand</b>	ABB
Type	Current Transducer EL55P2
Technology	Hall Effect
Primary Nominal Current ( $I_{pn}$ ) rms	50 A
Supply Voltage ( $V_a$ )	$\pm(11:15.7)V$
Measuring Range at $V_a$	0 : $\pm 80$ A
Secondary Nominal Current ( $I_{sn}$ ) rms	25 mA
Thermal Drift / $I_{sn}$	$2 \cdot 10^{-4} / ^\circ C$
Bandwidth (-1 dB)	0:200 kHz

Accuracy	$\pm 0.5\%$ @ ( $I_{pn}$ , 0:70 °C & $\pm 15V$ )
Linearity	Better than $10^{-3}$
Response Time	$< 0.1 \mu s$
No Load Current Consumption	16 (@ $\pm 15V$ $V_a$ ) mA

**Table 4-11: Voltage transducer specifications**

Description	
<b>Brand</b>	LEM
Type	Voltage Transducer LV 25-Pt
Primary Nominal Voltage ( $V_{pn}$ ) rms	10:500 V
Primary Nominal Current ( $I_{pn}$ ) rms	10 mA
Primary Current, measuring range	0: $\pm 14$ mA
Secondary Nominal Current ( $I_{sn}$ ) rms	25 mA
Supply Voltage ( $\pm 5\%$ )	$\pm (12:15)$ V
Current Consumption	10(@ $\pm 15V$ ) + $I_s$ mA
Overall Accuracy	$\pm 0.9\%$ @ ( $I_{pn}$ , 25°C & $\pm 15V$ )
Linearity error	$< 0.2\%$
Response Time to 90% of $I_{pn}$ step	40 $\mu s$

- **Thermocouples:** The gearbox oil temperature was measured using K-type thermocouples inside the gearbox. The measured signal from the thermocouple was transmitted to the temperature-processing unit to be filtered and magnified.
- **Speed encoder:** In order to measure the speed of the motor, an optical encoder (Manufactured by Hengstler; type RS32-O/100ER) was mounted on the non-driving end of the AC motor shaft and generated two outputs; one was 100 pulses per rotation and the other was one pulse per revolution. The encoder specifications are shown in the following table, and it was directly attached to the computer via the DAQS.

**Table 4-12: Encoder specifications**

Description	
<b>Manufacturer</b>	Hengstler

Type	RS 32	
Overall height	27 mm	
No of pulses	100 ppr	
Shaft diameter	6 mm	
Maximum speed	6000 rpm	
Operating temperature	-10 - 60°C	
Supply voltage	10- 30 V (DC)	

### 4.3 Gears - an Overview

Gears are widely used in the industry. Due to the importance of gears in power transmission, the condition monitoring of gearboxes is very important. Gearboxes consist of a number of gears mounted on rotational shafts supported by bearings.

Gearboxes are mechanical elements which are used for transmitting rotational motion directly between shafts; they are a critical component of all industrial applications and are invariably a component part of all commercial machines [103].

The monitoring of a gearbox's condition is an essential activity because of its importance in power transmission. Thus, there has been a constant improvement in monitoring techniques and analysis tools for detecting and diagnosing faults in gears, including shaft misalignments, using the current flowing through the motor driving the gearbox [4].

In gearboxes, load fluctuations and gear defects are two major sources of vibration and because defects in gears result in machine downtime, it is necessary to monitor the gearbox. Sometimes the measurement of vibration in real gearboxes is not easy because of the difficulty of mounting the vibration transducers [76] due, for example, to inaccessibility. The tested gearbox should be accessible for various transducers used with such monitoring techniques as vibration and acoustic emissions. It should also be possible to easily collect oil samples. But a machine in use in industry will experience a dusty environment, background noise, structural vibration etc., all of which may all obstruct the quality and efficiency of the technique. Hence, there is a need to monitor the gearbox using a signal that can be accessed away from its actual working location, this can be done using a non-intrusive technique; motor current signature analysis (MCSA). MCSA has already been successfully applied to condition monitoring of induction motor [4].

## 4.4 Types of Gears

The most common types being used in industry today are spur and helical gear.

- **Spur Gears**

Spur gears have a designed shape of straight cut teeth which connect parallel shafts and are used when both shafts rotate in the same plane. Due to the fact that they have a lower cost, these gears are widely used in most machine applications.

Figure 4.6 presents the spur gear.



Figure 4-6: Spur gear [104]

Spur gears have different features; [105] has listed the features of spur gears as: “ 1- The speed and change of the force depends on the gear ratio, the ratio of number of teeth. 2- A higher contact ratio that gives them the smoothness and quietness during operation. 3- No external thrust between gears. They give lower but satisfactory performance. 4- Corrosion resistant operation. And 5- Spur gears are easy to find, inexpensive, and efficient.”

Generally spur gears are used in simple machines like washing machines, clothes dryers or power winches, they are also used in construction equipment, machine tools, indexing equipment, multi spindle drives, roller feeds, and conveyors.

- **Helical Gears**

Helical gears are similar to the spur gear except that the teeth are at an angle to the shaft as illustrated in Figure 4.7. The helix angle creates an extended length of contact line. The resulting tooth length is longer than for the teeth on a spur gear of equivalent pitch diameter. Characteristics

of helical gears in [105] are listed as: “ 1- The basic illustrative geometry for a helical gear is the same as that of the spur gear, except that the helix angle must be added as a parameter. 2- Helical teeth result in a greater tooth width, which increases load and power transmissibility and results in a smoother engagement leading to less noise in operation than for straight spur gears. 3- Although helical gears are mainly used in parallel shaft applications, they may also be used to mesh two non-parallel shafts. 4- There is greater tooth strength due to the effective length of the teeth, which allows helical gears to carry more load than spur gears and to be used in power transmission. 5- It is possible to have a crossed gear mesh, in which the two shafts (drive and driven) are at right angles to each other.”



Figure 4-7: Helical gear

Helical gears have useful advantages:

- They can be used on non-parallel and perpendicular shafts as well.
- They are used in power transmission because they can carry higher loads.
- They are quiet even at high speed.

On the other hand, helical gearboxes have disadvantages:

- The resultant thrust along the axis of the gear needs to be accommodated by appropriate thrust bearings. To overcome this problem, double helical gears that have 'v' teeth shape can be used.
- They are relatively expensive [105].

## 4.5 Gear Teeth Failure Modes

Gear failure is associated with an increase in noise and vibration levels. The failure of gear tooth, generally, can be classified into two types:

**Distributed Faults:** With distributed faults, the time between fault initiation and the complete loss of serviceability is usually long, as the fault progresses slowly. The gear can still transmit power as the fault develops. These types of faults are usually uniformly distributed on the gear surface and typical examples of this would be wearing, pitting and scuffing.

**Local Faults:** The second types of failures are known as local faults and they are more insidious. This type of fault develops rapidly once it is initiated and most often, it significantly affects the transmission of power. It may have dramatic consequences if it is not detected early. Typical examples of this are tooth breakage, a cracked tooth and local wear involving one or more teeth [96, 106]. They are briefly summarized as:

**Tooth Breakage:** Mostly due to excessive load. Typically a broken tooth fault will begin with a small crack at the tooth root. The crack grows and will eventually cause tooth breakage. Sometimes teeth will suffer chipping at or near the working tip. This chipping can gradually extend until some portion of the tooth breaks away. When a gear operates under such conditions, a shock will be induced during gear mating which may cause the fault to extend to breakage in several adjacent teeth.

**Gear Crack:** Typically cracks first appear in the root fillet and gradually extend. The direction in which the crack will propagate cannot be predicted precisely but, typically, it propagates downwards the rim of the gear.

**Localised Tooth Wear:** Without adequate lubrication, the sliding motion of one tooth over another can remove metal from the tooth surface. As the depth of the layer of metal removed increases, it will start to have a deleterious effect on the capacity of the tooth to carry a load. Such wear typically takes place across the full face width. However, this wear is usually localised and will include only few teeth [96, 106].

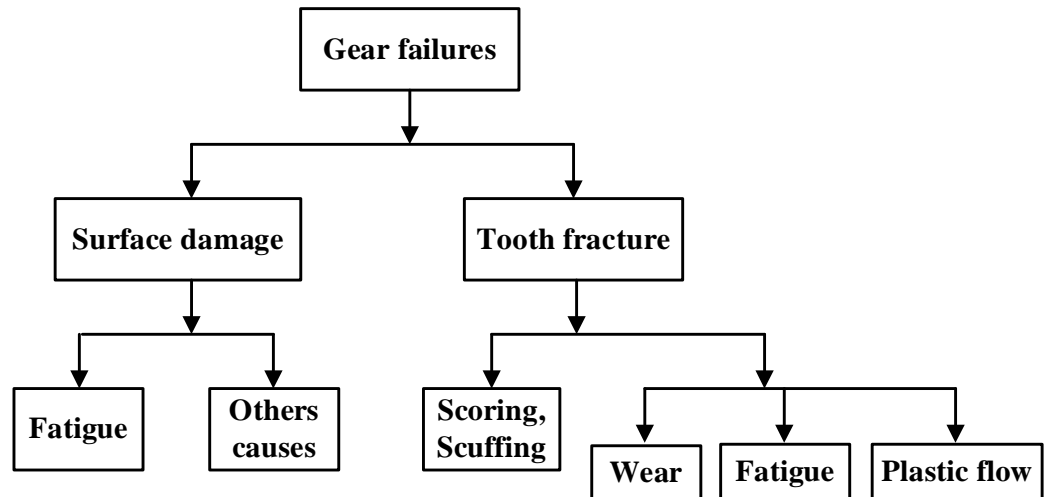


Figure 4-8: Classification of different gear failure modes

Gear failure may be due to erroneous application, poor design, or a manufacturing error, including such issues as improper gear geometry, or use of the wrong components. Application errors may be the result of problems in installation and mounting, inadequate cooling or lubrication, excessive vibration, or lack of proper maintenance.

Gear failure modes are characteristically due to:

- 1- Overload
- 2- Bending fatigue
- 3- Hertzian fatigue
- 4- Wear, scuffing and
- 5- Cracking

#### 4.6 Causes of Gear Failures

There are many causes for a gear to fail, but the most common fundamental causes include one or more of the following, which have been listed in [105] as : “ 1- High tooth loading for a long time. 2- The load is not distributed uniformly over the teeth. 3- Incorrect choice of gears. 4- Inherent material defect from manufacturing error. 5- Incorrect usage of gears. 6- Incorrect use of lubrication. 7- Faulty gearbox bearings. 8- Misalignment effects. 9- Extreme heat due high temperature operating conditions, and 10- Contamination in the lubricant by moisture and abrasive particles.”

## 4.7 Gearbox Characteristic Frequencies

The characteristic frequencies generated within a gearbox are the product of tooth meshing. Thus, each stage within the gearbox will generate its own frequencies depending on the speed of rotation of the respective shafts and the number of teeth on the gears. The rotation frequencies will have harmonics and sidebands [107]. A schematic of the two stage gearbox is shown in Figure 4.3.

The frequency components of the test rig are mainly derived from the gearbox and motor. These frequencies are generally modulated by the means supply frequency. A fault will cause a load and speed oscillations at fault frequency  $f_F$ , which is linked with both the fundamental frequency  $f_s$  and the rotational speed  $f_r$  in addition to extra sidebands for the basic frequencies involved. Therefore, investigating these components is advantageous for features extracting in fault detection.

The characteristic frequencies can be determined by Equations (4.1) to (4.3).

$$\text{Frequency of the first shaft: } f_{r1} = \frac{\omega_1}{60} \quad (4.1)$$

$$f_{r1} = \frac{1475}{60} \cong 24.58Hz$$

where:  $\omega_1$  represents the input shaft speed in rpm i.e. the speed of the AC motor; which is around 1475 rpm (full speed used in the test).

$$\text{Frequency of the middle shaft: } f_{r2} = \left( \frac{z_1}{z_2} \right) \cdot f_{r1} \quad (4.2)$$

$$f_{r2} = \left( \frac{58}{47} \right) \cdot 24.58 = 30.337Hz$$

$$\text{Frequency of the third shaft: } f_{r3} = \left( \frac{z_3}{z_4} \right) \cdot f_{r2} \quad (4.3)$$

$$f_{r3} = \left( \frac{13}{59} \right) \cdot 30.337 = 6.684Hz$$

“where:  $Z_1$  is the number of teeth on the pinion gear at the first stage,  $Z_2$  is the number of teeth on the driven gear at the first stage,  $Z_3$  is the number of teeth on the pinion gear at the second stage, and  $Z_4$  is the number of teeth on the driven gear at the second stage”.

## 4.8 Data Processing

### 4.8.1 Spectrum Analysis

The data obtained are converted to the frequency-domain using the FFT via MATLAB code. The FFT computations are based on the following equations:

$$x(t) = \int_{-\infty}^{\infty} F(f) e^{-2i\pi ft} \quad (4.4)$$

$$F(f) = \int_{-\infty}^{\infty} x(t) e^{2i\pi ft} \quad (4.5)$$

The FFT for digitally sampled time domain signals is obtained by the following formula:

$$F(f) = FFT[x(t)] = \sum_{-\infty}^{\infty} x(t) e^{-2i\pi ft} \quad (4.6)$$

where  $i = 0, 1, 2, \dots, n$ ,  $n$  is the number of samples.

To detect a fault, each signal is studied, extracting the amplitudes at the corresponding feature frequency components. Then, the different cases are compared to a baseline in order to assess performance and detect possible faults.

### 4.8.2 MSB Analysis

Higher order spectra (HOS) are used widely for noise reduction and nonlinear system identification [8]. Conventional bispectrum (CB) analysis is a common method used to take the third order measures of a signal.

The current sidebands can be detected by spectral analysis, but they are not good enough at clarifying the current signals through the characteristics of AM because it is not able to contain sideband pairs simultaneously and random changes in the sidebands' phases [108]. In addition, unwanted harmonics always exist when the motor is operated by a VSD; since it produces a random noise that overlaps with the spectral components to which faults are linked which complicate the detection process when the IM is connected to the power line [109].

If the amplitudes of the sideband components are small, they could be masked by the random noise, which reduces the SNR and consequently degrades the diagnostic performance [109, 110].

To calculate the second-order “power spectrum (PS)”, the following relationship should be used:

$$P(f) = E[X(f)X^*(f)] \quad (4.7)$$

where  $X(f)$  is the discrete Fourier transform (DFT),  $X^*(f)$  is the complex conjugate of  $X(f)$  and  $E[X(f)X^*(f)]$  is the statistical expectation.

The power spectrum is a linear transform and is a function of the frequency index  $f$ .

$$X(f) = \sum_{t=-\infty}^{\infty} x(t)e^{-2j\pi t f} \quad (4.8)$$

By increasing the spectrum order to three, this will rise the conventional bispectrum. For a modulation signal such as electrical current  $x(t)$  and its FFT transform of  $X(f)$ :

$$B(f_x, f_c) = E[X(f_c)X(f_x)X^*(f_c + f_x)] \quad (4.9)$$

where  $E[ ]$  is the statistical expectation; and for a modulation signal,  $f_x$  is the information signal frequency achieved by Fourier series integral;  $f_c$  is the carrier or supply frequency;  $f_c + f_x$  represents the higher sideband frequency; and  $X^*(f)$  is the complex conjugate of  $X(f)$ .

Comparing Equation (4.9) to Equation (4.7), it is clear that the bispectrum has a number of unique properties such as nonlinear components identification and phase information.

The bispectrum detects the interaction between two frequency components; which is known as quadratic phase coupling (QPC); which happens when two ripples interacting non-linearly and producing a third one with a frequency component amplitude and phase equal to summation or the difference of the first two ripples. The existence of sum and difference frequencies is necessary but not sufficient condition for QPC whereas by using the bispectrum the true phase coupling can be identified in the frequency domain, generally the bispectrum technique has the capability of detecting and characterizes the effects of nonlinear coupling in machinery [8].

From Equation (4.9). it can be seen that the conventional bispectrum detects the presence of QPC from a combination of related components of  $f_c$ ,  $f_x$  and the higher sideband component ( $f_c + f_x$ ). However,  $f_c - f_x$  component is neglected because of the non-linearity between  $f_c$  and  $f_x$ . Thus, the use of the conventional bispectrum is insufficient in describing both AM and FM signals [111].

To overcome problems related to the conventional bispectrum, the following formula of MSB, as represented in Equation (4.10), is used to enhance the traditional bispectrum performance in representing the electrical signals, reducing the level of the noise.

is presented as a new AM detector in order to improve the achievement of the traditional bispectrum in representing the electrical signals:

$$B_{MS}(f_x, f_c) = E[X(f_c + f_x)X(f_c - f_x)X^*(f_c)X^*(f_c)] \quad (4.10)$$

where  $B_{MS}$  is the modulation signal bispectrum of two frequency components and  $f_c + f_x$  and  $f_c - f_x$  are the higher and lower sideband frequency components. Both sideband components are considered simultaneously for possible QPC in AM signals. It illustrates that a bispectral peak will be clear at bifrequency  $B_{AM}(f_c, f_x)$ , if  $f_c + f_x$  and  $f_c - f_x$  are both due to QPC between  $f_c$  and  $f_x$  [111].

The total phase of the MS bispectrum can be determined by:

$$\varphi_{MS}(f_x, f_c) = \varphi(f_c + f_x) + \varphi(f_c - f_x) - \varphi(f_c) - \varphi(f_c) = \varphi(f_x) + \varphi(-f_x) \quad (4.11)$$

If  $f_c$  and  $f_x$  are in coupling, their phases are related by:

$$\begin{aligned} \phi(f_2 + f_1) &= \phi(f_2) + \phi(f_1) \\ \phi(f_2 - f_1) &= \phi(f_2) - \phi(f_1) \end{aligned} \quad (4.12)$$

If substitute Equation (4.12) into Equation (4.11), the MSB total phase will tend towards zero, however, the MSB amplitude will be a complex product of the four frequency components;  $f_c, f_x$  and  $(f_c \pm f_x)$ , consequently, a bispectral peak will appear at  $(f_c, f_x)$ . Thus,  $(f_c \pm f_x)$  components will be taken into account in Equation (4.10) to measure the nonlinearity of modulation signals.

If the frequencies at  $f_c$  and  $f_x$  are non-linearly coupled to each other, the total phase of these components will never be random even if the individual phases are random and a bispectral peak will appear at bifrequency of  $B_{MS}(f_c, f_x)$ , which is effective in representing sideband features of the modulated signals. If there is no coupling between these frequency components, however, no peaks will be seen and the bifrequency of  $B_{MS}(f_c, f_x)$  will lead to zero [111].

The phase of bispectrum responds only to the sideband components, operating parameters (except the fundamental component phase) and the design of the motor.

The amplitude of the supply frequency is set to be the dominant component in current and voltage signals and thus, it can be easily recognised. The current signals due to electrical and mechanical faults will include a series of sideband components around the fundamental frequency component;

therefore, a bispectrum part at the fundamental frequency is enough to describe sidebands features for machines fault diagnostic. The frequency component of  $f_c$  in Equation (4.10) will be set to a constant frequency value, say, the fundamental supply frequency “ $f_s = 50Hz$ ” [112, 113].

Likewise, the MSB will have its corresponding coherence function in order to confirm the influence of coupling between the sidebands and supply components and to examine the level of random noise and thus, the integrity of the MSB peaks are as indicated by the following relationship [8, 80]:

$$b^2_{MS}(f_x, f_c) = \frac{|B_{MS}(f_c, f_x)|^2}{E\langle |X(f_c)X(f_c)|^2 \rangle E\langle |X(f_c + f_x)|^2 \rangle} \quad (4.13)$$

The bicoherence doesn't rely on the amplitude of the three components with values between zero and one. If there is non-linear coupling, the bicoherence is near unity whereas in the case of non-coupling between components its value is close to zero, which can be used as an indicator to investigate the existence of coupling [114].

$$b^2_{MS}(f_x, f_c) = \frac{|B^n_{MS}(f_x, f_c)|^2}{E\langle |X(f_c)X(f_c)X^*(f_c)X^*(f_c)|^2 \rangle E\langle |X(f_c + f_x)X(f_c - f_x)|^2 \rangle} \quad (4.14)$$

## 4.9 Key Findings

In this chapter, details of the test rig components (including electrical and electromechanical parts) used in this work were provided to investigate the ability of using the ESA in diagnosing load fluctuations caused by mechanical faults. The specifications of the test facility including the structure of the test rig, the specifications of the motor, the generator, drives, and the two-stage helical gearbox were explained in details. This chapter also presents information about the data acquisition system and measurement system including the three phase measurement unit, the accelerometers, the thermocouples and speed encoder. It also reviews the gears and presents the procedure for collecting the data and aspects of data analysis.

## **CHAPTER FIVE: MODELLING AND SIMULATION FOR FIELD-ORIENTED INDUCTION MOTOR DRIVES FOR DIAGONSTIC**

---

*This Chapter introduces the mathematical modelling of a three-phase squirrel-cage IMs with field-oriented control technique. At first, a description of the induction motor model used in this work is presented. Then, the model structure of an open-loop control strategy and the FOC technique are discussed, followed by an in-depth understanding of the fault-detection techniques based on sensorless drives. In addition, this chapter will help the reader better understand the effect of a mechanical fault on electrical parameters of the motor drive. Finally, simulation results attained from the model will be experimentally verified for performance characteristics using a rig setup.*

## 5.1 Introduction

In induction motor CM, the implementation of a mathematical model will enable vital information to be extracted from the machine, creating a very effective way to not only strengthen the understanding of the behaviour of a sensorless VSD, but also to allow for a more accurate investigation of the system's response under different operational conditions. In this work, a ready-to-use software package, which is MATLAB/Simulink, has been used to analyse and simulate the dynamic response of an induction motor with the FOC drive. This ready-to-use software package has been used widely by researchers because of its simplicity, accuracy and appropriateness for different applications [97].

The built-in modules in MATLAB/ Simulink are suitable for simulation the dynamic behaviour in electrical systems such as power electronic converters and machines and in many cases can be amended to suit different applications [115, 116]. Herein, these modules are used, aiming to investigate the effects of load oscillations caused by mechanical faults on the response of the torque and electrical supply signals. The results obtained in this work will show that a distinctive behaviour in the machine's control system can be perceived in the presence of mechanical fault, which can be used in fault diagnosis and detection.

## 5.2 Induction Motor Model

The model of the induction motor is given in the form of space-vector voltage equations, which is symmetrical with a linear magnetic circuit. In order to gain a better understanding of the vector control operation, the underlying dynamic model of the induction motor must be known. This model can be obtained in space-vector or two-axis framework. Due to the fact that the system is considered to be under balanced conditions, the induction motor is conventionally modelled using the  $d$ - $q$  reference framework. This strategy can provide an elimination of the time-varying motor parameters and also yield an expression for the motor variables linked to a set of mutually decoupled orthogonal axes, namely  $d$  (direct) axis and  $q$  (quadrature) axis. It should be noted that the zero component is neglected and the subscript "s" indicates the variables and parameters are related to the stator, while the subscript "r" relates to the rotor variables and parameters [117].

The structure of the induction machine comprises of three identical windings equally spaced on the stator at  $120^\circ$  intervals and three identical phase windings set on the rotor with the same phase-shift configuration [118].

The stator current is mathematically decomposed into torque and flux components and both of these components can be separately controlled. This can be achieved by using a reference frame rotating at the same angular speed as that of the sinusoidal variables, therefore, reducing the speed difference between them to zero to produce the sinusoidal signal [92, 119]. The following figure represents the AC motor equivalent circuit in  $d$ - $q$  framework [42, 120]:

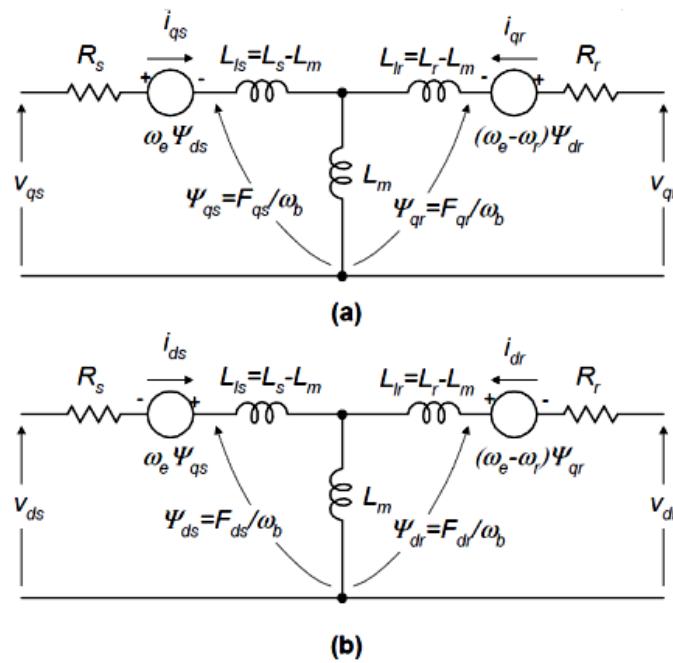


Figure 5-1: AC motor equivalent circuit in the  $d$ - $q$  framework

The relationship between the three phases (a-b-c) and the stationary  $d^s$  and  $q^s$  that are perpendicular to each other and the rotational  $d$ - $q$  axes, where 's' here refers to stationery frame; as illustrated in the next two figures [42, 117].

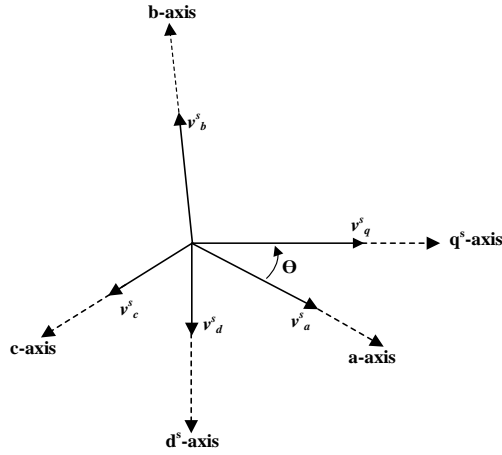


Figure 5-2: The transformation of the voltages from the (a-b-c) to the stationary  $d_s$ - $q_s$  axes (image redrawn by the author)

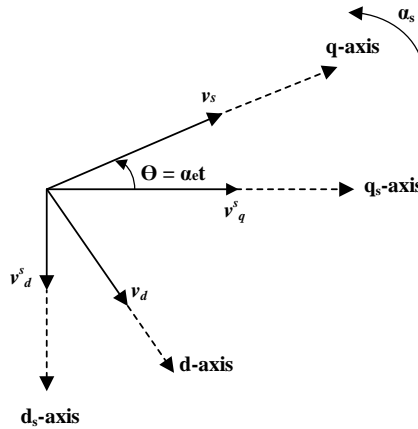


Figure 5-3: The transformation from the stationary  $d_s$ - $q_s$  axes to the rotating  $d$ - $q$  axes (Image redrawn by the author)

Solving the voltage, current and flux equations is a complex task as they have a time-varying nature. In order to reduce this complexity, variables must be changed to the  $d$ - $q$  reference frame, which allows to eliminate the time varying of motor parameters and variables [42, 92, 119].

The three-phase supply can be presented as:

$$\begin{aligned}
 v_a &= \sqrt{2}V_{rms} * \sin(\omega t); \\
 v_b &= \sqrt{2}V_{rms} * \sin(\omega t - \frac{2\pi}{3}) \\
 v_c &= \sqrt{2}V_{rms} * \sin(\omega t + \frac{2\pi}{3})
 \end{aligned}
 \tag{5.1}$$

The stator windings of a symmetrical three-phase induction motor are considered to be balanced, in a sinusoidal distribution at an angle of  $120^\circ$  with respect to each other, with  $N_s$  equivalent turns and a resistance of  $R_s$ . Likewise, the rotor windings are symmetrical and shifted by  $120^\circ$ , with  $N_r$  equivalent turns and a resistance of  $R_r$  as depicted in Figure 5.4. Here, the following assumptions hold true; the windings are symmetrical and sinusoidally distributed around the air gap, the air gap is uniform, and eddy currents, friction losses and saturation are all neglected [121].

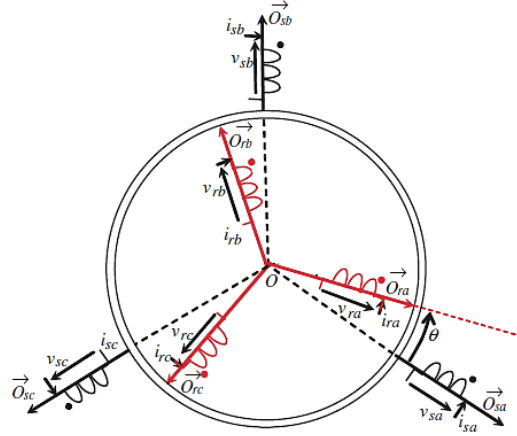


Figure 5-4: Three-phase representation of the rotor and stator windings [122]

The voltage equations can be obtained by applying Kirchhoff's voltage law for both stator and rotor as follows:

Stator voltage equations:

$$\begin{aligned}
 v_{sa} &= R_s i_{sa} + \frac{d\psi_{sa}}{dt} \\
 v_{sb} &= R_s i_{sb} + \frac{d\psi_{sb}}{dt} \\
 v_{sc} &= R_s i_{sc} + \frac{d\psi_{sc}}{dt}
 \end{aligned} \tag{5.2}$$

Similarly, for the rotor:

$$\begin{aligned}
 v_{ra} &= R_r i_{ra} + \frac{d\psi_{ra}}{dt} \\
 v_{rb} &= R_r i_{rb} + \frac{d\psi_{rb}}{dt}
 \end{aligned} \tag{5.3}$$

$$v_{rc} = R_r i_{rc} + \frac{d\psi_{rc}}{dt}$$

The aim is to transform the three-phase voltages in a stationary reference frame to only two phases  $d^s$ - $q^s$ .

$$\begin{bmatrix} v_d^s \\ v_q^s \end{bmatrix} = \frac{2}{3} \begin{bmatrix} 1 & \frac{1}{2} & -\frac{1}{2} \\ 0 & \frac{\sqrt{3}}{2} & -\frac{\sqrt{3}}{2} \end{bmatrix} \begin{bmatrix} v_a \\ v_b \\ v_c \end{bmatrix} \quad (5.4)$$

Then, convert these variables into direct and quadrature axes voltages as follows:

$$\begin{bmatrix} v_d \\ v_q \end{bmatrix} = \begin{bmatrix} \cos \theta & -\sin \theta \\ \sin \theta & \cos \theta \end{bmatrix} \begin{bmatrix} v_d^s \\ v_q^s \end{bmatrix} \quad (5.5)$$

Finally, the values of the stator and rotor currents in three-phase are calculated from the following transformation:

$$\begin{bmatrix} i_d^s \\ i_q^s \end{bmatrix} = \begin{bmatrix} \cos \theta & -\sin \theta \\ \sin \theta & \cos \theta \end{bmatrix} \begin{bmatrix} i_d \\ i_q \end{bmatrix} \quad (5.6)$$

$$\begin{bmatrix} i_a \\ i_b \\ i_c \end{bmatrix} = \frac{2}{3} \begin{bmatrix} 1 & 0 \\ -\frac{1}{2} & -\frac{\sqrt{3}}{2} \\ -\frac{1}{2} & \frac{\sqrt{3}}{2} \end{bmatrix} \begin{bmatrix} i_d^s \\ i_q^s \end{bmatrix} \quad (5.7)$$

The derivatives of the flux-linkage equations of both stator and rotor are expressed as [119]:

$$\frac{d\psi_{qs}}{dt} = \omega_b \left[ v_{qs} + \frac{R_s}{X_{ls}} (\psi_{qm} - \psi_{qs}) \right] \quad (5.8)$$

$$\frac{d\psi_{ds}}{dt} = \omega_b \left[ v_{ds} + \frac{R_s}{X_{ls}} (\psi_{dm} - \psi_{ds}) \right] \quad (5.9)$$

$$\frac{d\psi_{dr}}{dt} = \omega_b \left[ \frac{\omega_r}{\omega_b} \psi_{qr} + \frac{R_r}{X_{lr}} (\psi_{dm} - \psi_{dr}) \right] \quad (5.10)$$

$$\frac{d\psi_{qr}}{dt} = \omega_b \left[ \frac{\omega_r}{\omega_b} \psi_{dr} + \frac{R_r}{X_{lr}} (\psi_{qm} - \psi_{qr}) \right] \quad (5.11)$$

Subsequently, the model of the IM is provided from the  $d$ - $q$  motor equivalent circuit as presented in Figure 5.4, by writing the voltage equations for stator and rotor as follows:

$$v_{ds} = \frac{P}{\omega_b} \psi_{ds} + R_s i_{ds} \quad (5.12)$$

$$v_{qs} = \frac{P}{\omega_b} \psi_{qs} + R_s i_{qs} \quad (5.13)$$

$$0 = \frac{P}{\omega_b} \psi_{dr} - \frac{\omega_r}{\omega_b} \psi_{qr} + R_r i_{dr} \quad (5.14)$$

$$0 = \frac{P}{\omega_b} \psi_{qr} - \frac{\omega_r}{\omega_b} \psi_{dr} + R_r i_{qr} \quad (5.15)$$

In squirrel-cage induction motors,  $v_{dr}$  and  $v_{qr}$  are set to zero because the rotor cage bars are shorted [42].

Stator and rotor fluxes are denoted by [43]:

$$\psi_{ds} = L_{ls} i_{ds} + L_m i_{dr} \quad (5.16)$$

$$\psi_{qs} = L_{ls} i_{qs} + L_m i_{qr} \quad (5.17)$$

$$\psi_{dr} = L_{lr} i_{dr} + L_m i_{ds} \quad (5.18)$$

$$\psi_{qr} = L_{lr} i_{qr} + L_m i_{qs} \quad (5.19)$$

The stator and rotor currents can be given by:

$$i_{qs} = \frac{1}{x_{ls}} (\psi_{qs} - \psi_{qm}) \quad (5.20)$$

$$i_{ds} = \frac{1}{x_{ls}} (\psi_{ds} - \psi_{dm}) \quad (5.21)$$

$$i_{qr} = \frac{1}{x_{lr}} (\psi_{qr} - \psi_{qm}) \quad (5.22)$$

$$i_{dr} = \frac{1}{x_{lr}} (\psi_{dr} - \psi_{dm}) \quad (5.23)$$

where the mutual flux linkages are represented by the following equations [43, 119]:

$$\psi_{qm} = x_{lm} * \left[ \frac{\psi_{qs}}{x_{ls}} + \frac{\psi_{qr}}{x_{lr}} \right] \quad (5.24)$$

$$\psi_{dm} = x_{lm} * \left[ \frac{\psi_{ds}}{x_{ls}} + \frac{\psi_{dr}}{x_{lr}} \right] \quad (5.25)$$

where:

$$x_{lm} = 1 / \left[ \frac{1}{x_{ls}} + \frac{1}{x_{lr}} + \frac{1}{x_{lm}} \right];$$

$$x_{ls} = 2\pi * f * L_{ls};$$

$$x_{lr} = 2\pi * f * L_{lr}; \text{ and}$$

$$x_m = 2\pi * f * L_m$$

The electrical quantities are defined in the equations above; however, because induction machines are electromechanical devices, a relationship for the torque and speed is required. The following equations represent the electromagnetic torque and the rotational speed [43, 119]:

$$T_{em} = \frac{3}{2} \frac{P}{2\omega_b} [\psi_{ds} i_{qs} - \psi_{qs} i_{ds}] \quad (5.26)$$

$$\text{where: } \omega_b = 2\pi f;$$

The speed of the motor can be determined from the torque, load of torque, and moment of inertia (J) as follows:

$$\frac{d\omega_r}{dt} = \frac{1}{J} [T_{em} - T_{load}] \quad (5.27)$$

where:  $J$  is the moment of inertia;  $T_{em}$  is the electromagnetic torque;  $T_{load}$  is the load torque.

Considering that  $\omega_r/\omega_e$ ; represents the per-unit speed, the per-unit rotating speed can be expressed as [43]:

$$\frac{d(\omega_r / \omega_e)}{dt} = \frac{1}{2 * H} (T_{em} - T_{load}) \quad (5.28)$$

$$H = \frac{J * \omega_b * \omega_b}{2P * S_b} \quad (5.29)$$

The rotor and stator current in the three-phase framework are given as:

$$v_a = \sqrt{2} V_{rms} * \sin(\omega t) \quad (5.30)$$

$$v_b = \sqrt{2} V_{rms} * \sin(\omega t - \frac{2\pi}{3}) \quad (5.31)$$

$$v_c = \sqrt{2} V_{rms} * \sin(\omega t + \frac{2\pi}{3}) \quad (5.32)$$

Because the IMs inputs and outputs model are phase currents and voltages, it is necessary to convert them into the stationary frame then to  $d$ - $q$  stationary reference frame, respectively, by using the following relations:

$$v_{ds} = \frac{1}{\sqrt{3}} * (v_c - v_b) \quad (5.33)$$

$$v_{qs} = \frac{2}{3} * (v_a - \frac{1}{2}(v_b + v_c)) \quad (5.34)$$

$$i_{sa} = i_{qs} \quad (5.35)$$

$$i_{sb} = -\frac{1}{2} * (i_{qs} + \sqrt{3} * i_{ds}) \quad (5.36)$$

$$i_{sc} = -\frac{1}{2} * (i_{qs} - \sqrt{3} * i_{ds}) \quad (5.37)$$

where,  $V_{ds}$  and  $V_{qs}$  are  $d$  and  $q$  axes stator voltages respectively;  $V_{dr}$  and  $V_{qr}$  are  $d$ - and  $q$ -axis rotor voltages;  $i_{ds}$  and  $i_{qs}$  are  $d$  and  $q$  axes stator currents respectively;  $i_{dr}$  and  $i_{qr}$  are the  $d$ - and  $q$ -axis rotor currents;  $R_s$  is stator resistance;  $R_r$  is rotor resistance;  $L_m$  is mutual inductance;  $L_s$  and  $L_r$  are stator and rotor inductances;  $L_{ls}$ ,  $L_{lr}$  are the stator and rotor leakage inductances;  $x_{ls}$ ,  $x_{lr}$  are

the stator and rotor leakage reactance, respectively;  $x_m$  is the magnetization reactance;  $\omega_s$  is synchronous angular speed;  $V_a$ ,  $V_b$  and  $V_c$  are the phase voltages for the  $a$ ,  $b$ , and  $c$  phases;  $\omega_b$  is the base angular speed;  $\omega_r$  is the rotor angular speed;  $p$  is the number of poles;  $S_b$  is the rated power;  $H$  is the inertia constant;  $J$  is the moment of inertia;  $\Psi_{ds}$ ,  $\Psi_{qs}$ ,  $\Psi_{dr}$  and  $\Psi_{qr}$  are the d- and q-axis flux linkage of stator and rotor respectively; and  $\Psi_{dm}$  and  $\Psi_{qm}$  are the magnetizing flux linkage in  $d$  and  $q$  axis.

### 5.3 Open-Loop Control (V/Hz)

Open-loop control drives (V/Hz) is a type of steady-state controller where the air-gap flux is kept constant by adjusting the ratio of the voltage to frequency or V/Hz, in order to maintain the machine's torque over its entire operation range. In this case, only the magnitudes of the voltage and the supply frequency will be controlled and the speed can be adjusted by varying the supply frequency. However, this will lead to a change in the impedance, which results in the current, and consequently, the torque to change. In fact, if the voltage is increased beyond the ratings of the machine, the coils can be burned. Therefore, it is necessary to regulate both the voltage amplitude and the frequency of the drive system simultaneously. Pulse Width Modulation (PWM) is usually used by induction motor drives, aiming at varying the magnitude and frequency of the output voltage, where the drive continues feeding the motor with a constant V/Hz ratio using the inverter to keep the air-gap flux constant.

Even though the V/Hz control strategy is simplest and least expensive (because there is no feedback loop), it is not accurate and it cannot provide a torque for every load. Moreover, the switching caused by the inverter eventuates a slow transient response [123, 124].

The air-gap flux should be kept constant based on the following equation:

$$\psi_m = L_m |i_s + i_r| = \frac{v_s}{\omega_s} \quad (5.38)$$

$$T_{em} = \frac{3P}{2(\omega_s - \omega_r)} \left( \frac{v_s^2}{2 \left( \frac{\omega_b R_r}{\omega_s - \omega_r} \right)^2 - x_{lr}^2} \right) R_r \quad (5.39)$$

## 5.4 Modelling the Field-Oriented Control (FOC)

In an FOC scheme, a feedback loop is included aim at providing an accurate speed control and a better dynamic performance [43].

To implement the FOC scheme, the stator current component  $i_{ds}$  and the rotor field should be aligned, also the torque component  $i_{qs}$  and the stator current component  $i_{ds}$  would be orthogonal. To do so, the reference frame rotates with the rotor flux. This can be accomplished via choosing a value for  $\omega_e$  equal to the speed of the rotor flux, thus, information about the space-angle of the rotor flux space vector is needed [44]. Now, assuming the  $d$  axis is aligned with the rotor flux,  $\Psi_{dr} = \Psi_r$  and  $\Psi_{qr} = 0$ , the rotor flux can be approximated by:

$$\Psi_r = \frac{L_m}{1 + T_r S} (i_{ds}) \quad (5.40)$$

The torque also can be described by the following relationship, which is used to calculate the current torque component  $i_{qs}$ :

$$T_{em} = \frac{3}{2} \frac{p}{2\omega_e} (\Psi_{ds} i_{qs}) \quad (5.41)$$

The FOC scheme provides the ability to control the torque separately, while the amplitude of the rotor flux  $\Psi_r$  is maintained constant. This leads to a linear relationship between the electromagnetic torque  $T_{em}$  and the torque component  $i_{qs}$ . Thus, when the torque component of the stator current  $i_{qs}$  is controlled, the torque  $T_{em}$  can be regulated [43, 44]. In order to maintain the flux constant,  $v_{ds}$  must be close to the frequency of the supply, which will result in a speed above the rated value. When  $v_{ds}$  is maintained constant, the flux will decrease with the increase of the frequency, providing a flux-weakening phenomenon, ensuring the voltage limits of the motor are not exceeded [125].

## 5.5 Fault Effect on Electrical Parameters

“When a fault occurs, the angular speed will change, which will be detected by the speed estimator. Then, the speed regulator will transfer a speed error term to the control loop, promoting the torque control through the  $q$ -axis current component  $i_q$ . The output from the current controller sets the reference torque required so as to compensate for any changes. Consequently, the torque controller

will compare the new reference torque against the estimated torque, sending a proportional voltage demand  $V_q$  to the PWM controller and then to the motor. Furthermore, the field current component  $i_d$  sets the desired flux  $\Psi$ , which is kept constant at the rated speed when the measured speed is below the base motor speed.

However, in the case of small faults, the noise caused by the drive and the control actions of the closed-loop can mask the features in the current signal, making the detection of the current signal difficult” [6]. Therefore, signal processing methods have to be developed with high performance in noise suppression and weak signature highlights.

Abnormalities usually generate additional load alternations around the electrical torque, which are modulated at a frequency,  $f_F$ , that is related to the rotational frequency,  $f_r$ , and to the supply frequency  $f_s$  [8, 108].

A one phase motor current signal in a healthy case is presented as:

$$i_A = \sqrt{2}I \cos(2\pi f_s t - \alpha_I) \quad (5.42)$$

In a similar way, the flux of the stator is described as:

$$\psi_A = \sqrt{2}\Psi \cos(2\pi f_s t - \alpha_\Psi) \quad (5.43)$$

It is possible to get the electromechanical torque by the interaction of the rotor current with and air gap flux as follows:

$$T_{em} = 3P\Psi I \sin(\alpha_I - \alpha_\Psi) \quad (5.44)$$

where  $I$  and  $\Psi$  are the root-mean-square (RMS) values of the supply current and the air-gap flux,  $\alpha_I$  and  $\alpha_\Psi$  are the phases of the current and flux, respectively,  $f_s$  is the supply frequency and  $P$  is the number of pole pairs.

Consequently, the additional torque caused by the fault, supposing to be a sinusoidal wave with a current of  $I_F$ , a phase of  $\alpha_F$  and a frequency of  $f_F$  can be expressed as the following” [6]:

$$\Delta T_{em} = 3P\Psi I_F \sin(2\pi f_F t - (\alpha_I - \alpha_\Psi) - \alpha_F) \quad (5.45)$$

According to Equation (5.27), the IMs mechanical speed can be calculated as:

$$\frac{d\omega_r(t)}{dt} = \frac{1}{J} (T_{em}(t) - T_{load}(t)) \quad (5.46)$$

The motor's speed  $\omega_r$  will oscillate with the fault's presence by  $\Delta\omega_r$  as follows:

$$\Delta\omega_r = \frac{P}{J} \int \Delta T_{em} dt = -\frac{3P^2\psi I_F}{2\pi f_F J} \cos(2\pi f_F t - (\alpha_l - \alpha_\psi) - \alpha_F) \quad (5.47)$$

The angular variation in the rotor thus can be presented as:

$$\Delta\alpha_F = \Delta\theta = \frac{P}{J} \int \Delta\omega dt = \frac{3P^2\psi I_F}{4\pi^2 f_F^2 J} \sin(2\pi f_F t - (\alpha_l - \alpha_\psi) - \alpha_F) \quad (5.48)$$

“The oscillations in the load due to a mechanical fault will result in a torque component that modulates the motor speed and causes speed fluctuations, which in turn will change the rotor position. Therefore, these fluctuations in the rotor position will affect the slip frequency, and consequently, the torque current component will also be affected by the fault” [6].

The angular fluctuation will modulate the flux according to the following equation:

$$\psi_A^F = \sqrt{2} \psi \cos[2\pi f_s t - \alpha_\psi - \Delta\psi \sin(2\pi f_F t - (\alpha_l - \alpha_\psi) - \alpha_F)] \quad (5.49)$$

where, 
$$\Delta\psi = \frac{3P^2\psi I_F}{4\pi^2 f_F^2 J}$$

$$\psi_A^F = \sqrt{2}\psi \cos(2\pi f_s t - \alpha_\psi) + \sqrt{2}\psi \Delta\alpha_F \sin(2\pi f_F t - \alpha_\psi) \quad (5.50)$$

$$\begin{aligned} \psi_A^F = & \sqrt{2}\psi \cos(2\pi f_s t - \alpha_\psi) + \sqrt{2}\psi \Delta\psi \cos[2\pi(f_s - f_F)t - \alpha_l - \alpha_F] - \\ & \sqrt{2}\psi \Delta\psi \cos[2\pi(f_s + f_F)t - 2\alpha_\psi + \alpha_l - \alpha_F] \end{aligned} \quad (5.51)$$

From Equation (5.51), it is clear that the flux contains two components; the first is fundamental frequency component and the second one is the sidebands components [8].

Current and voltage sideband components around the fundamental frequency will be generated as a result to the compound influence of the stator flux and the impedance, as presented in Equation (5.52) [37, 113]:

$$\begin{aligned} i_A^F(t) = & \sqrt{2}I \cos(2\pi f_s t - \alpha_l) + \sqrt{2}I_l \cos[2\pi(f_s - f_F)t - \alpha_l - \alpha_F - \phi] \\ & + \sqrt{2}I_r \cos[2\pi(f_s + f_F)t - 2\alpha_\psi + \alpha_l - \alpha_F - \phi] \end{aligned} \quad (5.52)$$

$$\begin{aligned} u^F(t) = & \sqrt{2}U \cos(2\pi f_s t) + U_l \cos[2\pi(f_s - f_F)t - \alpha_F - \phi] \\ & + U_r \cos[2\pi(f_s + f_F)t - 2\alpha_\psi + \phi_F - \phi] \end{aligned} \quad (5.53)$$

Where  $\Psi$  is the angular displacement of the motor's equivalent circuit impedance at supply frequency,  $I_l$ ,  $I_r$ ,  $U_l$  and  $U_r$  are the RMS values of the lower and the upper sideband components of the current and voltage, respectively, at frequencies of  $f_s - f_F$  and  $f_s + f_F$ ,  $\alpha_l$  is the phase angle between voltage and current,  $\alpha_\Psi$  is the phase angle between the stator flux and voltage and  $f_F$  is the fault frequency.

When there is fault, the corresponding power will be:

$$\begin{aligned}
p^F(t) = & \frac{IU}{2}[1 + \cos(2\omega_s t)] + \frac{IU_l}{2}[\cos(\omega_f t) + \cos(2\omega_s t - \omega_f t)] \\
& + \frac{IU_r}{2}[\cos(-\omega_f t) + \cos(2\omega_s t + \omega_f t)] + \frac{I_r U}{2}[\cos(-\omega_f t) + \cos(2\omega_s t + \omega_f t)] \\
& + \frac{I_r U_r}{2}[1 + \cos(2\omega_s + 2\omega_f)t] + \frac{I_r U_l}{2}[\cos(2\omega_f)t + \cos(2\omega_s)t] \\
& + \frac{I_l U}{2}[\cos(-\omega_f)t + \cos(2\omega_s - \omega_f)t] + \frac{I_l U_r}{2}[\cos(2\omega_s)t + \cos(-2\omega_f)t] \\
& + \frac{I_l U_l}{2}[1 + \cos(2\omega_s - 2\omega_f)t]
\end{aligned} \tag{5.54}$$

where,  $\omega_s = 2\pi f_s$ ,  $\omega_s$  is the angular supply frequency and  $\omega_f = 2\pi f_F$ , is the angular fault frequency. "For simplicity, the phase angles are excluded from the trigonometric equations in which the presented features are close to a real power signal. As a result, an effective analysis can be applied such that" [6]:

$$\begin{aligned}
p^F = & \frac{IU + I_r U_l + I_l U_r}{2} \cos(2\omega_s t) + \frac{I U_l + I U_r + I_r U + I_l U}{2} \cos(\omega_f t) \\
& + \frac{I_r U_l + I_l U_r}{2} \cos(2\omega_f t) + \frac{I U_l + I_l U}{2} \cos(2\omega_s - \omega_f)t \\
& + \frac{I U_r + I_r U}{2} \cos(2\omega_s + \omega_f)t + \frac{I_r U_r}{2} \cos(2\omega_s + 2\omega_f)t + \frac{I_l U_l}{2} \cos(2\omega_s - 2\omega_f)t
\end{aligned} \tag{5.55}$$

In Equation (5.55), more frequency components have been shown by the power spectrum as compared to those of the current and voltage spectra. The first harmonic doesn't appear because of the modulation effect, alternately,  $2\omega_s$ , which represents the second harmonic.

Furthermore, two sideband components can be seen at  $2\omega_s \pm 2\omega_F$  in addition to another two sidebands at  $2\omega_s \pm \omega_F$ . "The amplitude of these two sidebands will change with the load fluctuations and hence, the sidebands will be different from that of healthy motor [8]. The sideband

components in each electrical parameter will stimulate the drive's regulators for the sake of maintaining the speed of the machine. However, such frequency components, and also the small changes due to incipient faults, may be obscured by the drive's noise and actions, making the detection difficult. Consequently, more advanced signal processing techniques need to be employed" [6].

When using a sensorless VSD, the fault will cause further oscillations in the load regulated at  $f_r$ , which is linked with both the fundamental frequency  $f_s$  and the rotational speed  $f_r$ . The speed control loop will feel these oscillations, given the oscillation frequencies are within the controller's bandwidth.

With PI controller, the components of  $i_{qs}^*$  and the  $i_{ds}^*$  can be determined as:

$$i_{qs}^* = (\omega_r^* - \omega_r + \Delta\omega_r)(K_p + \frac{K_i}{s}) \quad (5.56)$$

$$i_{ds}^* = (\psi_r^* - \psi_r + \Delta\psi_r)(K_p + \frac{K_i}{s}) \quad (5.57)$$

Where,  $K_p$  denotes the PI controller proportional gain,  $K_i$  is the PI controller integral gain and  $\psi_r$  is the rotor flux.

The loops of the field and the speed controllers are the outer ones while the torque, voltage, and current components represent the interior loops, which have wider range of bandwidth than that of the outer loops. Therefore, the current component loop will react faster than the speed loop and consequently detect faults at frequencies out of the bandwidth range of the outer loop "the speed". On the other hand, the voltage control loop which is the last loop has a wider bandwidth than that of the current loop, therefore, only limited amount of frequency levels will pass through the current regulators [37].

## 5.6 Fault Detection Based on Sensorless Drive

According to Rajendra *et al.*, (2013) [4], flaws to gear mechanisms, including malfunctioning teeth, lead to load torque differences (abnormality). In such cases, the spectrum of current frequency can be seen in an unusual bandwidth.

When the gear rotates, the number of teeth that are in contact changes and consequently the effective duration of the line of action will vary, which in turn will cause fluctuations in the mesh stiffness.

The mesh stiffness in helical gears are smaller than those in spur gears, which can be explained by the fact that the larger contact ratios cause relative changes in the length, leading to a smaller line of contact [126]. Mechanical oscillations within the gearbox lead to alteration of the air-gap eccentricity, which eventuates changes in the air-gap flux and may produce stator current components, as well as some mechanical oscillations that will produce extra current elements at rotating frequencies, in addition to extra sidebands for the basic frequencies involved.

$$f_x = f_1 \pm mf_r \quad (5.57)$$

where,  $f_1$  is the supply frequency,  $f_r$  is the rotational speed frequency of the rotor,  $m = 1, 2, 3, \dots$  represents the number of harmonic, and  $f_x$  is the current components due to air gap changes.

Internal flaws in the machine may be sensed as alterations in plant parameters. When a fault occurs, regulators make those controllable variable factors conform to reference values, causing a change in the output of the controller in line with the nature of the fault.

By analysing the signals from the motor current, it is possible to capture the effect of static and dynamic impacts on the motor's performance. In particular, those dynamic impacts can be identified through the analysis of the sideband elements [4, 5].

“When setting the VSD to a mode without sensor action, certain variables will be altered, including speed, terminal voltages and stator currents. The regulation mechanism for speed responds to this by compensating for changes based on altered loads or other factors” [6].

The drive tends to make more changes to the terminal voltage than to the current, in an attempt to keep the speed at a constant close to the reference level.

Thus, more information about the health of the motor can be obtained by means of analysis on the voltage signals. On the other hand, the noise from the drive and the controlling activities of the closed-loop control prevent the clarity of the captured data [6].

For high performance purposes, more than one control loop is employed. In case of motor drive control, the outermost loop is the speed PI controller, taking speed measurements and comparing

them against the reference value to produce an error term, which is used to make alterations to the output to match the commanded set-point. The variables of the process are handled by the outer control loop, note that; the speed control loop is with the process regulating loop, and the torque regulator loop represents the innermost loop.

The inner control loop comprises of two series-connected PI control loops with the following attributes:

- “ The current loop which compares between the estimated current and the reference to set the reference torque signal; and
- The torque control loop which regulates the required voltage component based on the output of the current loop.

Another loop is the voltage control loop, which outputs a reference voltage component to the PWM. Finally, the field control loop, which keeps the flux fixed at the rated speed in case the speed drops below the base motor speed. However, when the speed is at or higher than the rated speed, the flux will be lowered using the field weakening by  $(1/\omega_r)$  where  $\omega_r$  is the rotor angular frequency.

The innermost loop ‘torque loop’ has to be faster than the current loop which represents the outer loop by 3-10 times for constancy reason. The same should be for the current loop (inner) and the speed loop (outer) ” [6].

To control the electromagnetic torque, the  $i_{qs}$  must be changed as indicated in the following relationship:

$$i_{qs}^* = \frac{2}{3} \frac{1}{p} \frac{L_r}{L_m} \frac{T_e^*}{\psi_r} \quad (5.57)$$

Whereas the motor flux can be governed by the stator current component  $i_{ds}$  as represented in the following equation:

$$i_{ds}^* = \frac{\psi_r^*}{L_m} \quad (5.58)$$

Using the slip frequency, it is possible to determine the torque current reference as follow [127, 128]:

$$\omega_{sl} = \frac{L_m}{T_r \psi_r} i_{qs}^* \quad (5.59)$$

The angle of the electrical flux can be determined as follows:

$$\theta = \int (\omega_{sl} + \omega_m) dt \quad (5.60)$$

where  $\omega_{sl}$  is the slip angular frequency,  $\omega_m$  is the rotor angular mechanical frequency.

According to Equation (5.60), the alterations in the position of the rotor will influence the slip frequency, which will influence torque current component, see Equation (5.59). This can cause important oscillations to the rotor flux; this can be explained by that the rotor flux depends on the slip frequency and the torque signal as presented earlier in Equation (5.40). As a result, modulations occur in speed, rotor position and rotor flux signals, which manifest themselves as load oscillations in both torque and field current components.

As represented earlier in Figure 2.15, when a fault occurs, a change in the speed also takes place, which is detected and acted upon by the drive system, by transferring a speed error term to the speed control loop, promoting the torque control component  $i_q$ . The output from the current loop will adjust the reference torque desired in attempt to compensate for the changes caused in the motor's behaviour. The torque controller will compare the desired torque with the estimated torque, producing the reference torque voltage  $V_q$  which will be the input of the pulse width modulator and then to the motor. Further, the field current component  $i_d$  will set the required flux  $\Psi$ , which remains stable at the rated speed when the speed is lower than the motor rated speed. Though, for small faults, the background noise from the control activities hide some characteristics in the current and voltage signals, making the detection of the signals difficult [59, 89, 129].

## 5.7 Simulation Results and Validation

### 5.7.1 Healthy Case

Both the IM, together with an FOC scheme modelled using ready-to-use tools provided by MATLAB/Simulink. Some parameters were provided from the nameplate of the motor whereas others have been estimated by the VSD. The specifications of the motor are illustrated in table 4-1.

Figure 5.5 represents the three line currents under 0% load, 100% load at full speed condition.

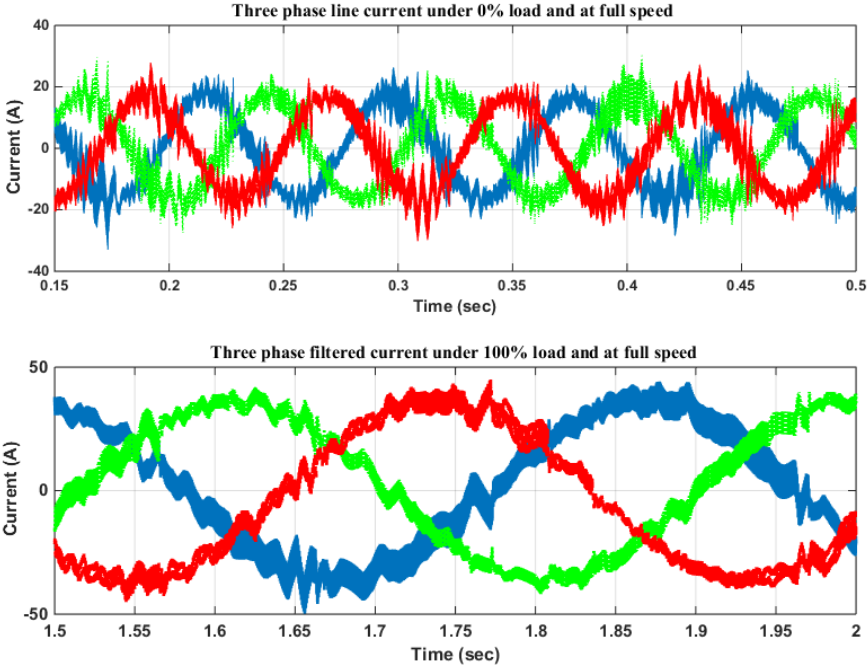


Figure 5-5: Three phase currents from the model

Similarly, the voltage signals under two different loads 0% and 100% at full speed are presented in Figure 5.6.

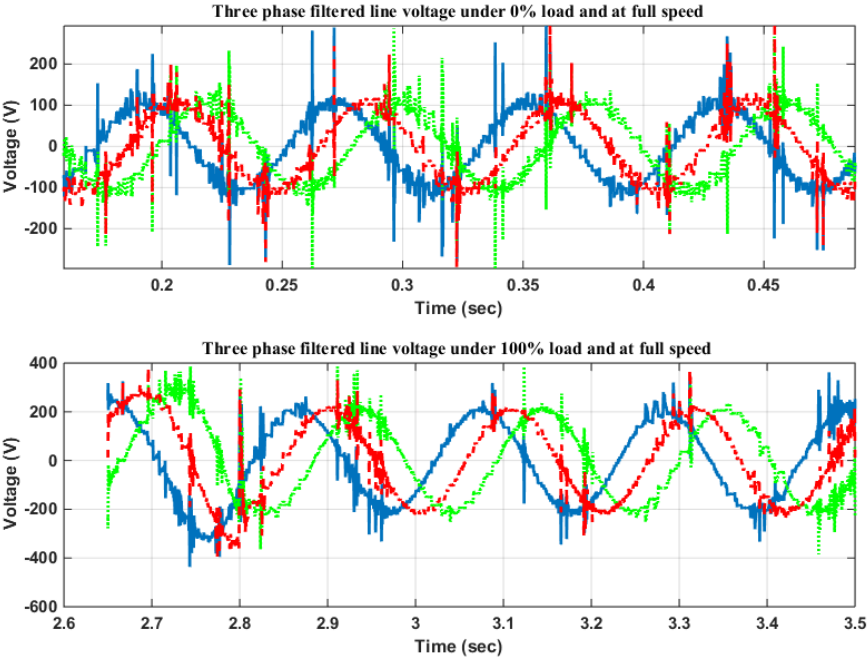


Figure 5-6: Three phase voltages from the model

The power signals (electrical and mechanical) under different load settings (0% and 100%) are presented in Figures 5.7 and 5.8.

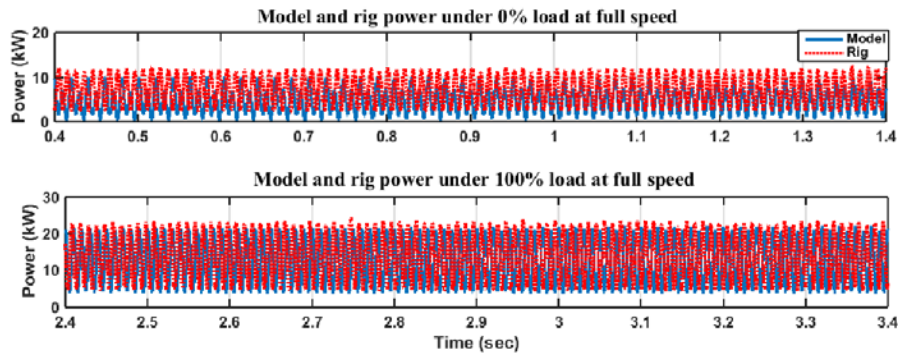


Figure 5-7: Power signals under different conditions

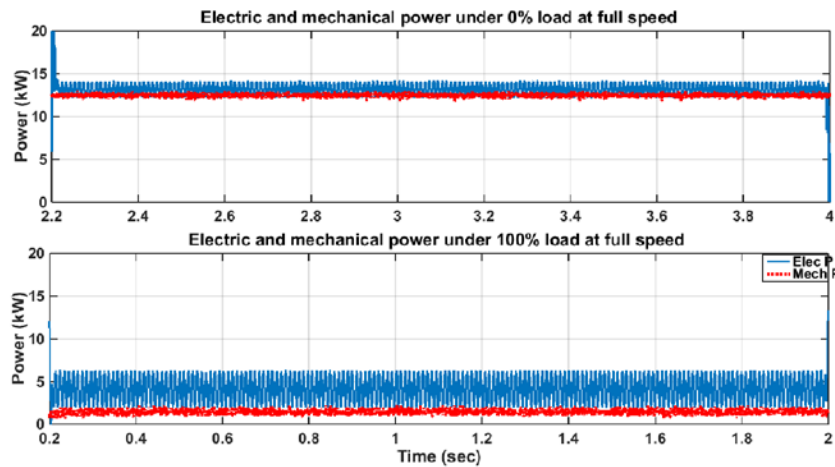


Figure 5-8: Power signals comparison

The speed reference was set to 25, 50, 75 and 100% of the full speed and under 0% and 100% load condition, in order to examine the system's response to the change in the speed reference as represented in Figure 5.9. It is worth mentioning that the drive kept the speed of the motor close to the reference speed, demonstrating excellent performance. Furthermore, it can be seen that the speed response of the drive improves as the speed of the motor increases.

The speed percentage error is shown in Figure 5.9 (b) with a minimal percentage error for no more than 0.3% of the full speed, which is acceptable.

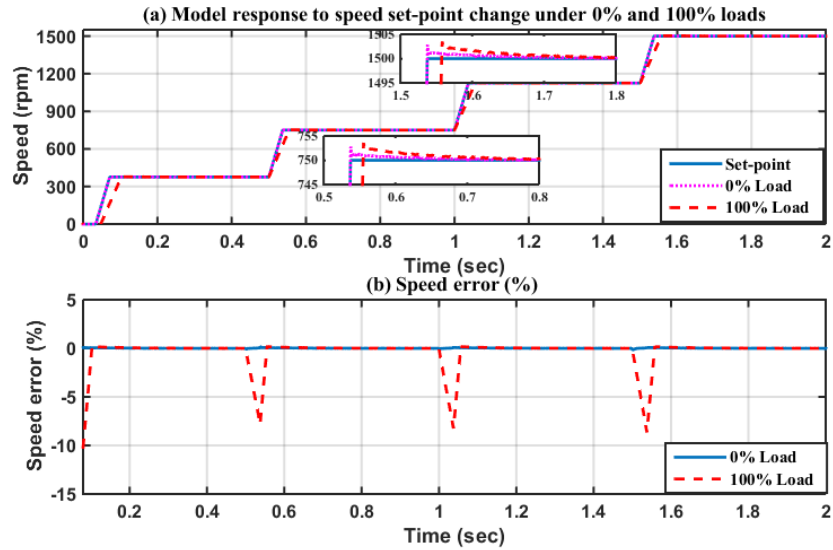


Figure 5-9: Model response and speed errors under 0% and 100% load

The model was run at full speed and under four incremental loads of, 0%, 30%, 70% and 100%. A good response to the speed reference is shown in Figure 5.9 (a), posing a very small error. The drive provides a satisfactory behaviour in monitoring the speed of the motor and maintaining at the reference speed with a reasonable error.

In Figure 5.9 (b), which represents the speed error for both loads at 0% and 100%, it can be seen that the error is small, implying that a satisfactory model response of the model has been achieved.

Furthermore, to compare the performance of the experimental rig with that of the model, the controller's speed response with respect to the reference set-points was studied. A good response of the model to variable loads is illustrated in Figure 5.10 (a). It is shown that even though different loads were applied, the drive can track the reference speed very well. In addition, in Figure 5.10, the controller's torque response is shown to have a good tracking capability with respect to the reference torque.

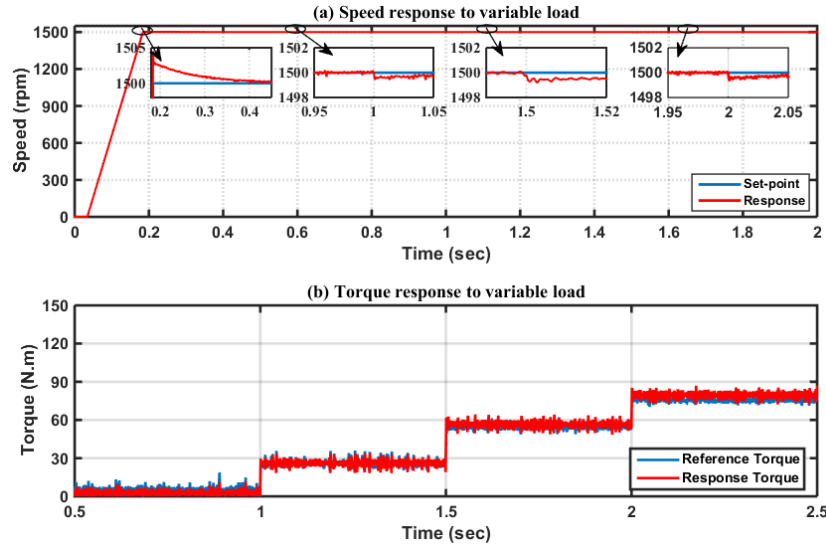


Figure 5-10: Speed and torque response to variable loads

A comparison of the current and voltage signals in the time-domain, for both the rig and the model, has been carried out, as demonstrated in Figure 5.11 and Figure 5.12, at 100% of the full speed and under two different operating loads of 0% and 100%. Figure 5.11 represents the current signals, while Figure 5.12 illustrates the voltage signals. In a similar way, current and voltage graphs show same alterations regarding the model and the rig. This similarity indicates the possibility of using the model to validate the effect of the fault on the behaviour of the speed and torque.

$$\text{Overshoot} = \frac{(1505 - 1500)}{1500} \times 100 = 0.3333$$

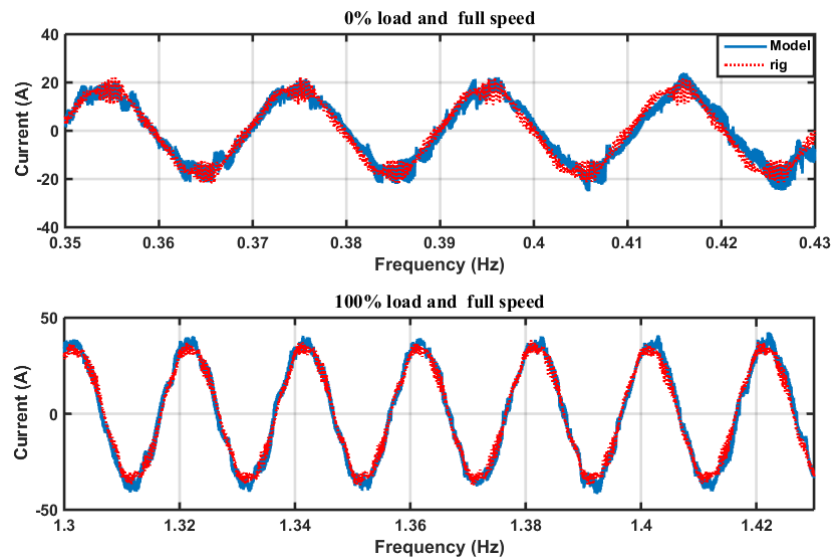


Figure 5-11: Current signals comparison under different loads

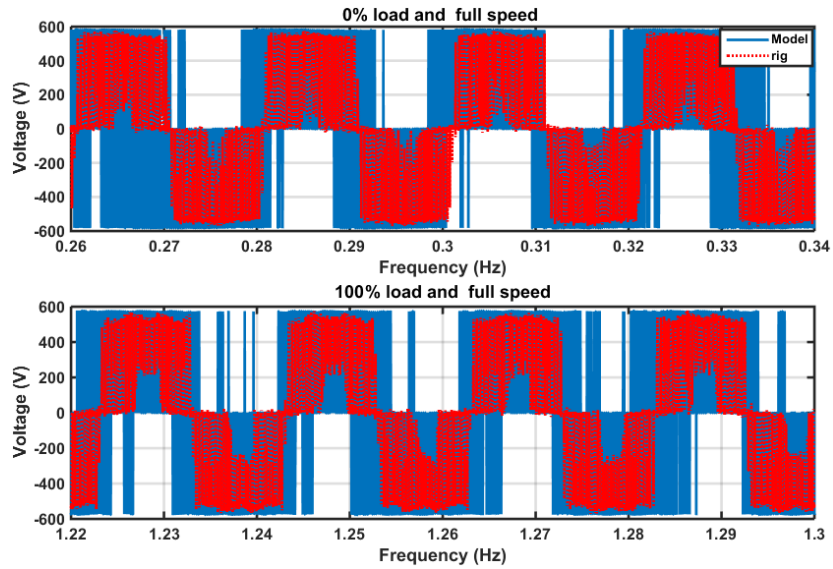


Figure 5-12: Voltage signals comparison under different loads

The two next figures present the current and voltage responses in the frequency domain. Figure 5.13 illustrates the spectra of the current at full speed and under two different loads (0% and 100%) representing similar variations in both the model and the rig especially at 100% load.

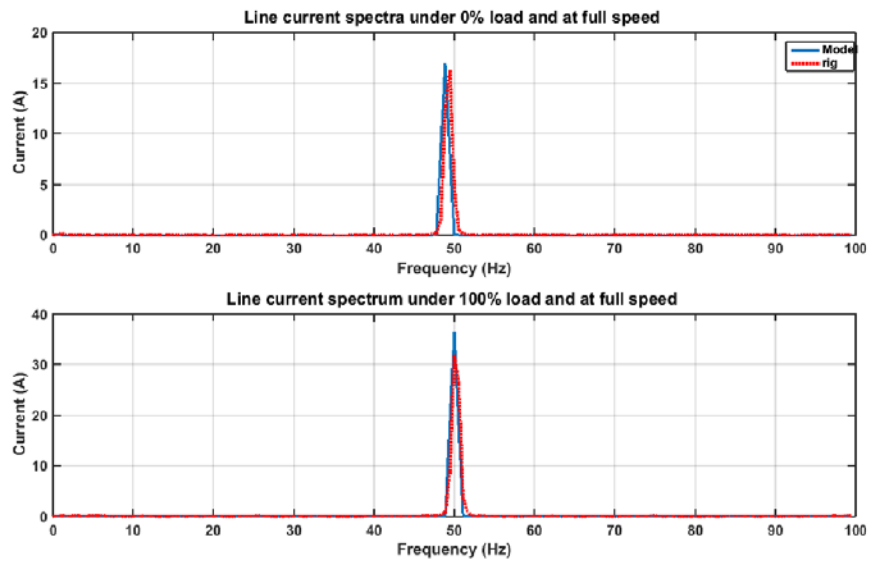


Figure 5-13: Current spectra comparison under different loads

The voltage spectra, which are represented in Figure 5.14, show a similar trend to those of the current spectra with a noticeable increase with the increments in the load from 0% to 100%.

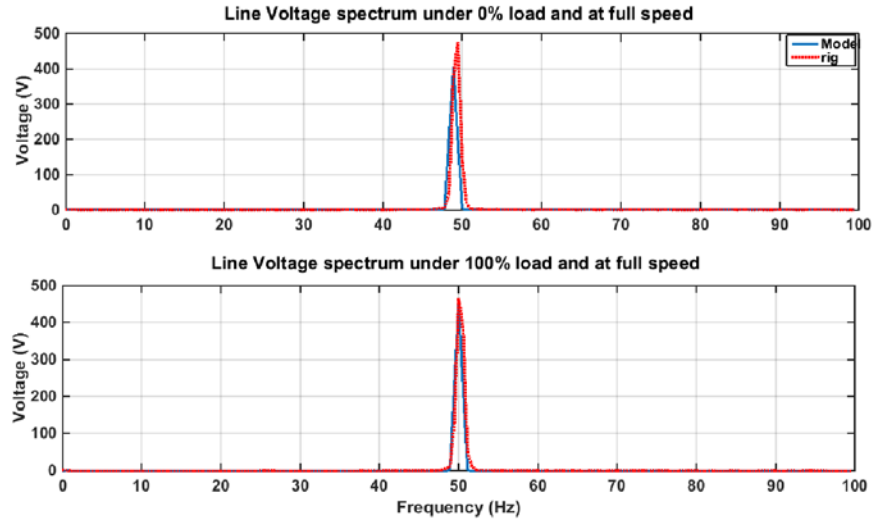


Figure 5-14: Voltage spectra comparison under different loads

The power signals have been shown in Figure 5.15 at full speed and under two different load conditions (0% and 100%).

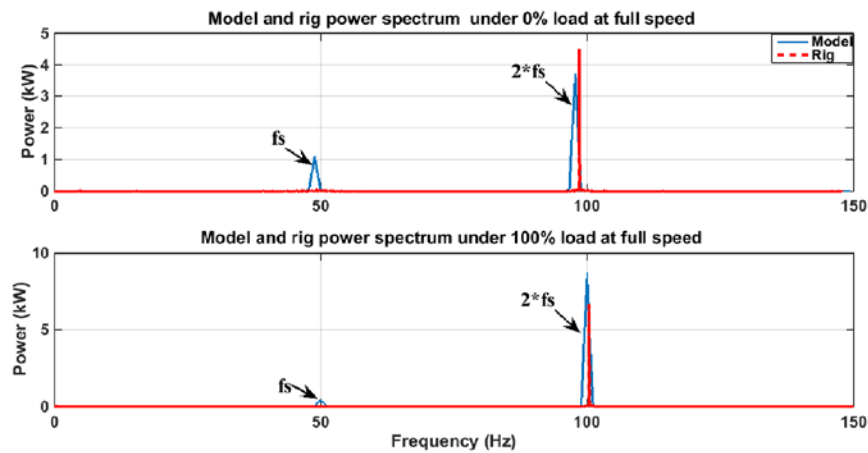


Figure 5-15: Power spectra comparison under different loads

### 5.7.2 Faulty Case

The system's response in case of oscillations conditions was studied by firstly adding an oscillatory signal to the angular speed of the load reference. Then, this angular speed was integrated and passed throughout a cosine function and finally it is multiplied by a gain and added to the load reference. The speed will modulate the oscillations with  $\Delta T$  which will set the oscillations size to represent the degree of the fault, which is an amount to describe what a fault may cause [125].

The added oscillation to the load torque reference can be described by the following equation:

$$T_{osc} = \Delta T \cos(\theta) \quad (5.61)$$

$$\theta = \int \omega, dt \quad (5.62)$$

To represent different fault severities degrees, four different values of  $\Delta T$  were used, denoting the baseline (BL), 10% fault, 20% fault and 40% fault.

In mechanical fault's case, the load alternations will modulate the supply parameters; consequently, then, the drive will responds to these alternations, aiming at keeping a smooth speed response. Thus, analysing the electrical signals can provide an image about the machine situation.

In case of a mechanical fault such as a tooth breakage, excessive bearings clearance values or gear lubricant, it is possible to detect the fluctuations caused by the mechanical faults when the motor is driven with a VSD. The oscillations modulate the electrical supply parameters "current, voltage and power" at a frequency component related to the oscillation frequency. The drive control system acts against the oscillations preventing them from affecting the speed of the system. Hence the speed demand and electromagnetic torque reference will be set by the drive, compensating for any load changes and maintaining the motor speed stable at the desired value. These mechanical faults will give rise to additional fluctuations which are modulated at fault frequency, thus, they can be seen in the voltage and current signals and detected. However, it might not be easy to detect small as the drive cause a level of noise that might mask some features [125].

The frequency components of the rig are mainly derived from the gearbox and motor. These frequencies are generally modulated by the supply frequency. When a fault occurs, it will cause a load and speed oscillations at fault frequency  $f_F$ , which is linked with both the fundamental frequency 50Hz and the rotational speed  $f_r$  ( $f_{r1}$ ,  $f_{r2}$ , and  $f_{r3}$  components which represent the input, middle and output shaft rotational frequencies respectively) in addition to extra significant sidebands which are correlated with the dynamics of the gearbox i.e. the speed oscillations at  $f_s \pm f_{r1}$  and  $f_s \pm f_{r2}$ . Therefore, investigating these components is advantageous for features extracting in fault detection. However, the amplitudes at  $f_{r3}$  component are not presented because they are very small and mainly masked by the background of random noise and hard to be extracted.

Figure 5.16 represents the current spectra under 0% and 100% of the full load and at full speed. Frequency components and sidebands around the supply frequency can be clearly noticed, which are a result of the load oscillations. These components increase in amplitudes as the load fluctuations level increase.

It is clear that the supply frequency increased with the increase in the load in attempt to compensate for any change by maintaining the speed close to the “reference speed”.

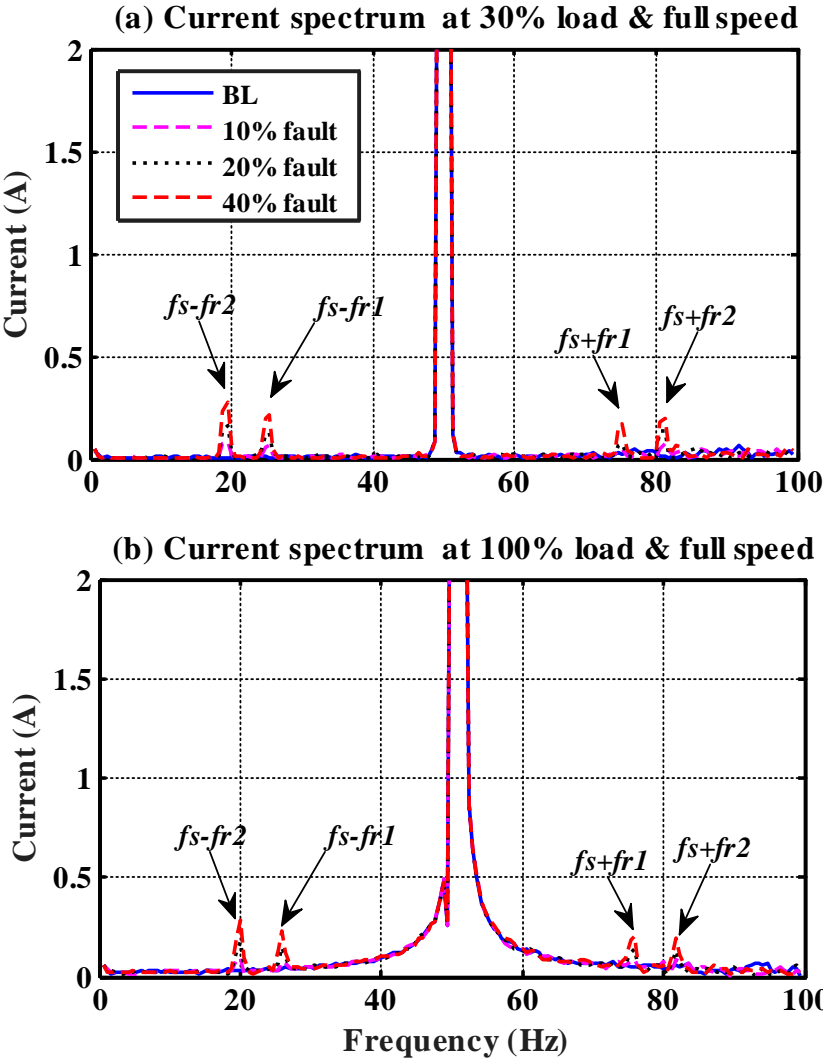


Figure 5-16: Current spectra comparison under different loads

Similarly, in the voltage spectra, Figure 5.17, an increase in the sideband amplitudes can be seen, which is due to the increase in the load oscillations level.

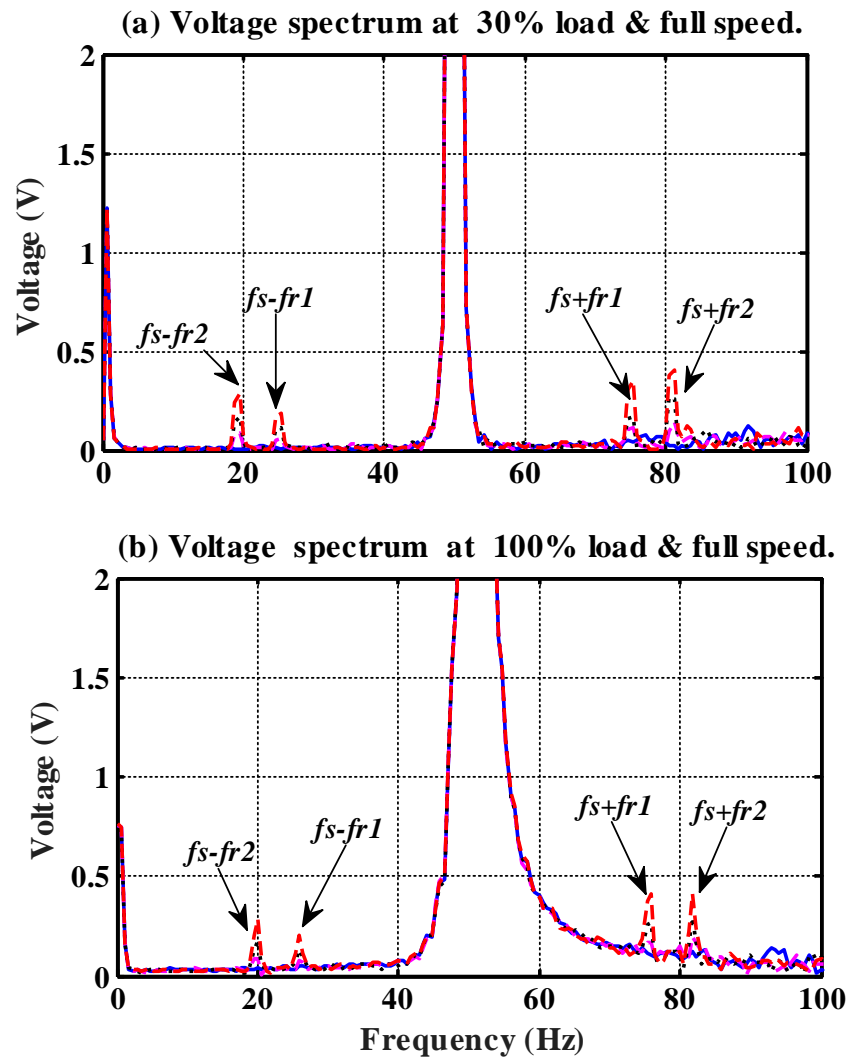


Figure 5-17: Voltage spectra comparison under different loads

In addition, the power spectra show a similar observation to those of current and voltage spectra, showing the supply frequency  $f_s$  and its multiplication  $2f_s$  as presented in Figure 5.18.

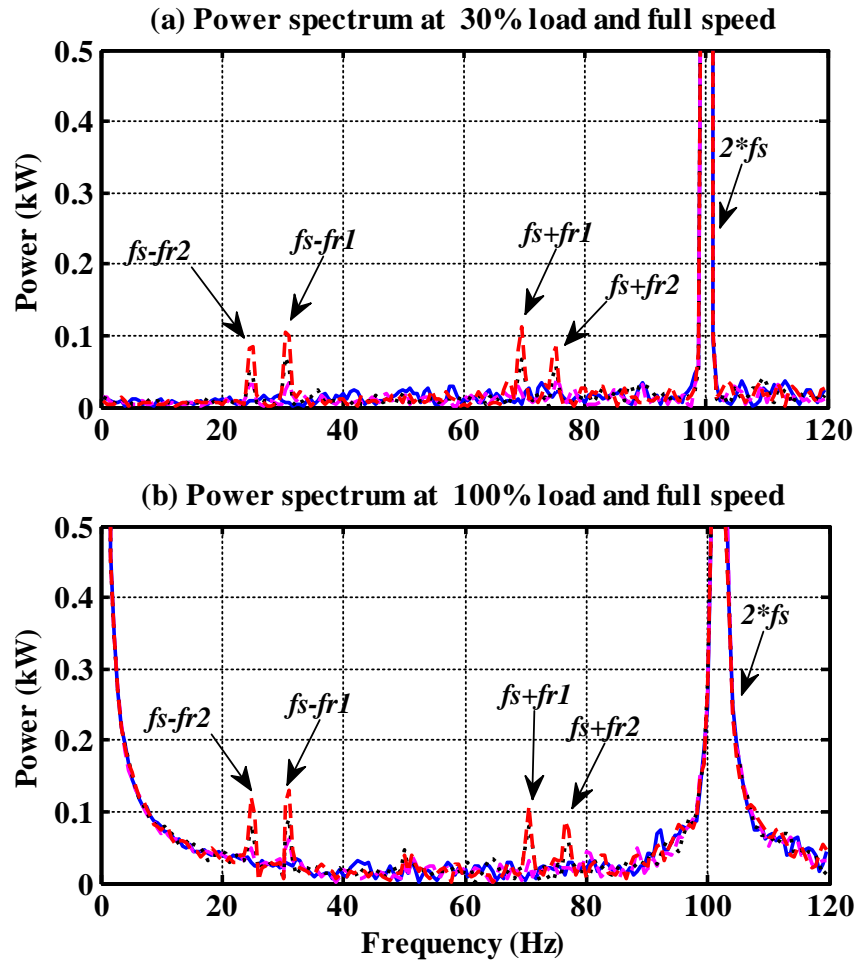


Figure 5-18: Power spectra comparison under different loads

This trend can approve that when a mechanical fault occurs, such a breakage in a gear tooth or oil shortage, oscillations in the load will increase. These oscillations will modulate the electrical supply parameters and in that case the drive will act for such fluctuations to retain the speed of the system. By analysing the supply parameters, faults in downstream systems can be detected.

Figure 5.19 represents the average peaks features extracted at the middle rotational frequency  $fr_2$  for the current, voltage, and power signals. It can be seen that the trend for all cases can be good differentiated, with the high fault severity being the highest one and the others are followed that in a descending order (from high to low severity). These peaks increase also in amplitudes with the load increment, which also could be good indicator for detecting and diagnosing mechanical faults.

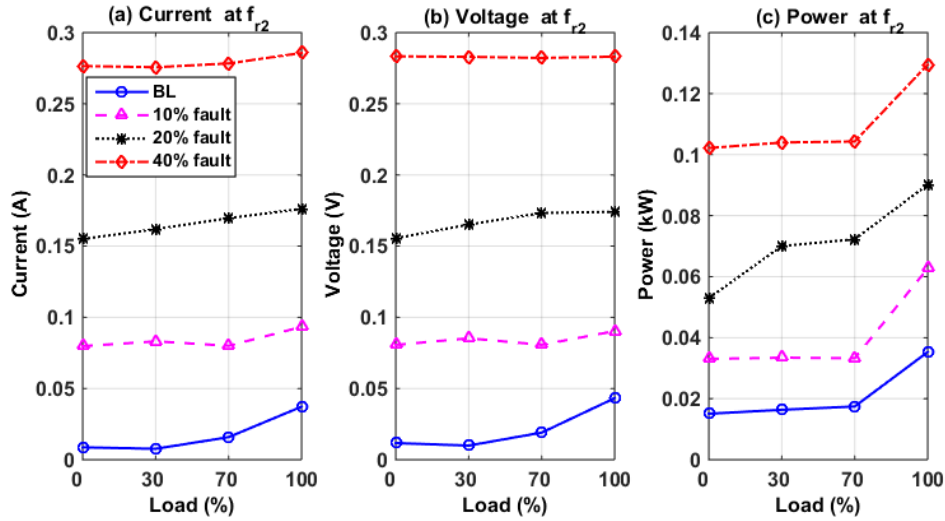


Figure 5-19: Features at  $f_{r2}$  and full speed

Figure 5.20 shows the sideband components at  $f_{r2}$  of the current, voltage and power signals for all load values (0%, 30%, 70% and 100% of the full load) at full speed. It is noticeable that the signals amplitudes increase with the load and fault degrees increase. The three faults representations can be differentiated from the baseline case.

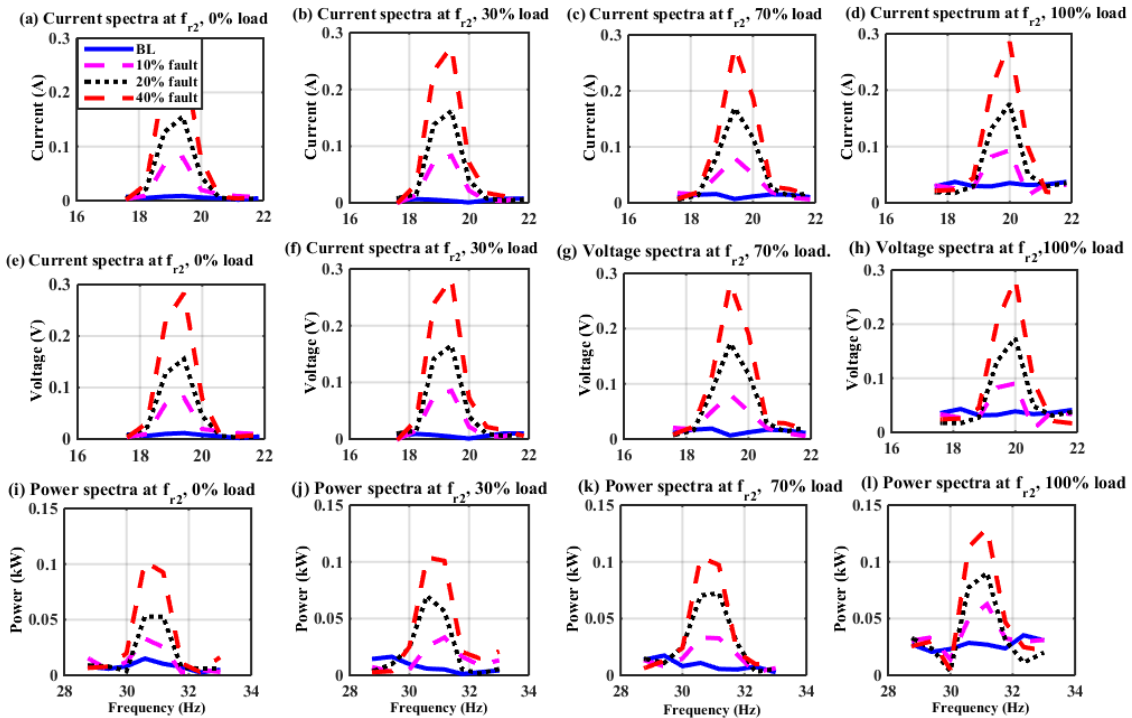


Figure 5-20: Fault case comparison

## 5.8 Key Findings

A ready to use models using Simulink/MATLAB environment were used to mimic the IM driven with sensorless VSD. These modules were used to simulate the load oscillations cussed by the fault. After loading the rig and drive data, the results from the model and the rig were then compared to each other to see if the motor succeed representing the motor operation.

- The voltage signals respond to mechanical oscillations more than the current signals this can be explained by the location of the voltage control loop which is the innermost one thus, it contains wider bandwidth than any other loops. The drive automatically adjusts the motor speed by changing the power supply parameters and compensating for any oscillations caused by the fault in order to avoid them from affecting the speed.
- Results show that the model behaves in a way similar to that of the rig and its response is somehow good and satisfactory.

## **CHAPTER SIX: DETECTION AND DIAGNOSIS OF GEAR TOOTH BREAKAGE**

---

*This chapter studies fault detection using motor electrical signatures (current, voltage, and power). It begins by describing the procedure of the test, then it details the faults that were introduced. Next, the chapter describes and discusses data collection and analysis for healthy and faulty conditions. It reports the experimental results obtained using the spectra of the FFT and the MSB for the motor current, voltage, power signals and the instantaneous power factor with and without any seeded faults, under different operating conditions in order to study the effectiveness of using these signatures for fault detection.*

## 6.1 Introduction

Tooth breakage is one of the common dangerous gear faults due to the serious damage that can be caused by the broken pieces to other gearbox components. Consequently, such a fault could cause a failure in the power transmission system [130]. This kind of fault is generally caused by extreme loads. It often begins with a little crack in the root of the tooth, which extends and leads to a breakage in the tooth. If a defective gear remains operating under this condition, it may lead to the breakage of several consecutive teeth. Generally, tooth breakage can be seeded by a partial/complete removal of a tooth face along its length. This may lead to a decrease in the contact zone between teeth and that will cause an increase in tooth deflection. If there is no tooth breakage, the teeth fully mesh, “in a line along the length of the tooth”, whereas in the case of tooth damage, the amount of contact will decrease due to the defect and removal of material [106].

## 6.2 Effect of Gear Tooth Breakage

Mechanical faults in both internal motor rotors and external downstream machines such as a gearbox will lead to alteration of the air-gap eccentricity and oscillations, which result in changes in the air-gap flux and may produce additional components in electrical signals, which exhibit modulation phenomena between the supply component and the fault components in the following form:

$$f_x = f_s \pm m f_r \quad (6.1)$$

Consequently, the sideband frequencies can be calculated from the following relationships:

$$f_{r1sb} = f_s \pm m f_{r1} \quad (6.2)$$

$$f_{r2sb} = f_s \pm m f_{r2} \quad (6.3)$$

$$f_{r3sb} = f_s \pm m f_{r3} \quad (6.4)$$

where,  $f_s$  is the supply frequency,  $f_r$  is the rotational speed of the rotor,  $m = 1, 2, 3, \dots$  and represents the number of harmonics, and  $f_x$  is the frequency of the current components due to, for example, air gap changes,  $f_{r1}$ ,  $f_{r2}$ , and  $f_{r3}$ , represent the input, middle and output rotational frequencies.

These fault induced changes can be detected and acted upon by the VSD system by transferring a speed error to the speed control loop, the torque component  $I_q$  then will be promoted as shown in

Figure 2.19 in a previous chapter. The reference torque required will be set by the output from the current controller to compensate for the changes caused in the motor's behaviour. Therefore, the torque controller will compare this reference torque with the estimated torque and outputs the desired torque voltage  $V_q$  to the PWM and then to the motor. Furthermore, the component of the field current  $I_d$  adjusts the required flux  $\Psi$ , which is maintained constant at the rated speed when the speed is less than the desired or referenced motor speed [59, 89, 129].

Flaws in gear mechanisms, including malfunctioning teeth, lead to load torque differences or "abnormalities". These abnormalities are transferred from the load to the motor current. In some cases, the spectrum of the current frequency can be seen to include unusual frequencies. When the gear rotates, the number of teeth that are in contact changes and consequently the effective duration of the line of action will change due to the presence of a broken tooth, which causes a periodic variation in the mesh stiffness. With helical gears, the mesh stiffness will be less than in spur gears. This is explained by the larger contact ratio causing a difference in relative length, which leads to a smaller line of contact [4, 126].

### **6.3 Fault Simulated and Test Procedure**

The rig used in this work allows many kinds of faults such as tooth breakage; to simulate it and then monitor its effects as shown earlier in Figure 4.1.

The test commenced with warming up the rig by running it for 30-40 minutes until the thermocouple reading reached between 41-42 ° C; which is found suitable after repeating the test many times because after this temperature the change in temperature is little which avoids the effect of temperature on the test. Next, the motor was run for 3 minutes at zero load after which each test was 2 minutes duration with load setting of 30%, 70% and 100% of the full load (15 kW) and the speed was set at one of three values 50%, 75% and 100% of the full speed, which is 1460 rpm, as represented in Figure 6.1. The speed was changed in descending order (100%, then 75% and then 50% of the full speed) because the temperature of the oil inside the gearbox was a maximum at 100% of the full speed, and cooled down as the speed decreased. The oil heated up much more quickly than it cooled down, therefore, arrangement gives more chance of running the tests at nearly the same conditions.

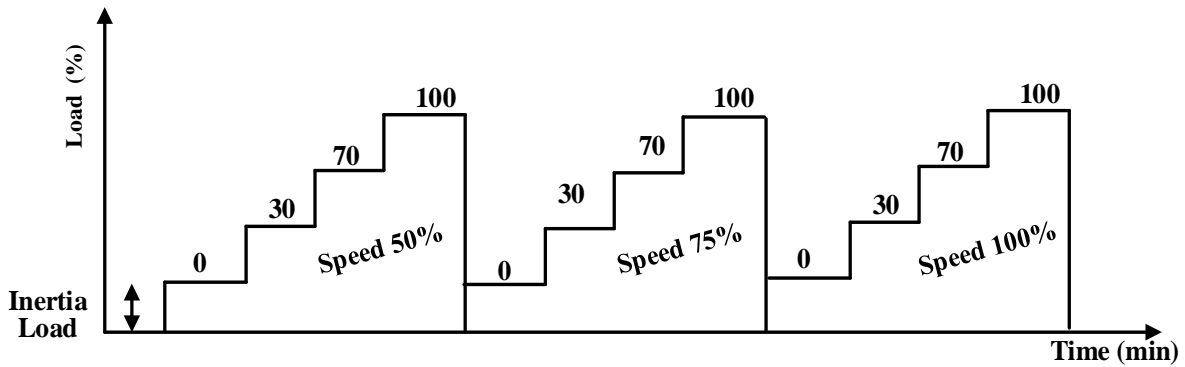


Figure 6-1: Typical test cycle

In this research work, two incremental severities of gear tooth breakage were introduced (20% and 40% of the tooth width) as shown in Figure 6.2. The tests were carried out on the gear for GB1 aiming at examining the capability of using ESA for diagnosing small mechanical faults.

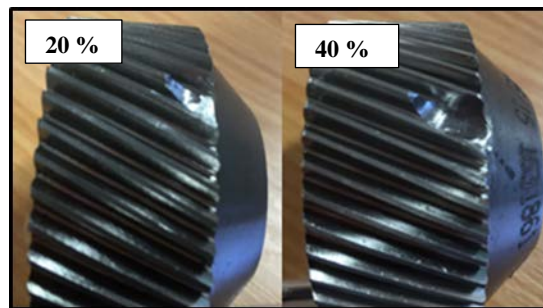


Figure 6-2: A photograph of the broken gears (20% - 40%)

This rig was controlled by a programmable logic controller (PLC) which allowed the rig to operate at different specific speed-load conditions. An AC VSD (Parker 650V) was used to regulate the speed, and could be adjusted either to a V/Hz mode, or a sensorless FOC type with a DC VSD (Parker 550c) controlling the torque of the load. In this experimental work, the VSD was set to the sensorless mode, and the drive estimated the speed based on the Model Reference Adaptive System (MRAS).

To record the electrical measurements, six sensors were used for three-phase currents and voltages. In order to record the data from the different sensors, a high-speed data acquisition system (YE6232B) with 16 channels was used, with a “sampling frequency” of 96 kHz. Then, the data collected through the acquisition system was transferred to a PC to be processed and analysed. A shaft encoder was connected directly to the data acquisition system to measure the motor angular speed.

In general, each set of gears creates its own vibration patterns in addition to which there will be the effects of manufacturing errors which can be specific to each gear set. In order to minimize such differences, the faults were introduced in the same gear set. The number of channels in the DAQS is 16, but channels nos 6, 7, 8 and 10 were not used.

After that, the electrical signals for the healthy and faulty gear were analysed in the frequency domain using the spectrum analysis and the MSB analysis. These were studied for any differences between healthy and faulty cases.

Depending on the current spectrum, we can obtain the sidebands at the shaft rotational frequencies  $f_{r1}$ ,  $f_{r2}$  and  $f_{r3}$ .

To compare the detection performance between the two schemes, i.e. MSB and FFT, the electrical signals, i.e. current, voltage, power signals, and power factor were treated using the two schemes and the results obtained were studied and analyzed. In the following section a discussion of some results is provided.

## **6.4 Results and Findings**

### **6.4.1 Spectrum Analysis**

As there are limits for thesis words number, only results at high speed were shown.

Figure 6.3 represents the change in temperature of the oil in the GB1 under different loads and at 1475 rpm, which is the full speed, for the baseline condition of the gears (BL), with the first fault ,20% tooth breakage, (TB20) added and then with the second fault ,40%, (TB40). It is noticeable that there are differences between the three cases, which means that the presence of the faults has an effect on the oil temperature. The difference between the two faulty cases and from the baseline is clear and could be used as a fault indicator.

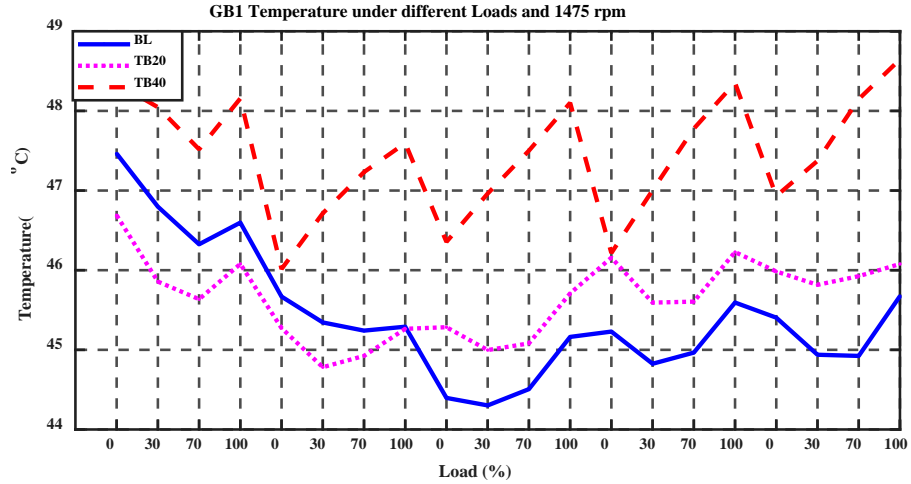


Figure 6-3: Oil temperature under different loads and full speed

To identify and track individual frequency components, spectra of various electrical signals are used as they are particularly effective to enhance the periodic oscillations in these signals. Of particular interest is the significant sidebands around 50Hz as they are correlated with the dynamics of the gearbox i.e. the speed oscillations at  $f_s \pm f_{r1}$  and  $f_s \pm f_{r2}$ . The amplitudes at  $f_{r3}$  is not presented because they are very small, being less than one third of the other two. Therefore, its amplitude is mainly masked by random noise and hard to be extracted. Figures 6.4, 6.5 and 6.6 represent the current, voltage and power spectra, respectively, of the baseline and the faulty cases at full speed under two different loads, 30% and 100% of full load. From spectrum of the current; Figure 6.4, it is clear that the sidebands amplitudes considerably increase with the increase of load and fault severity [6].

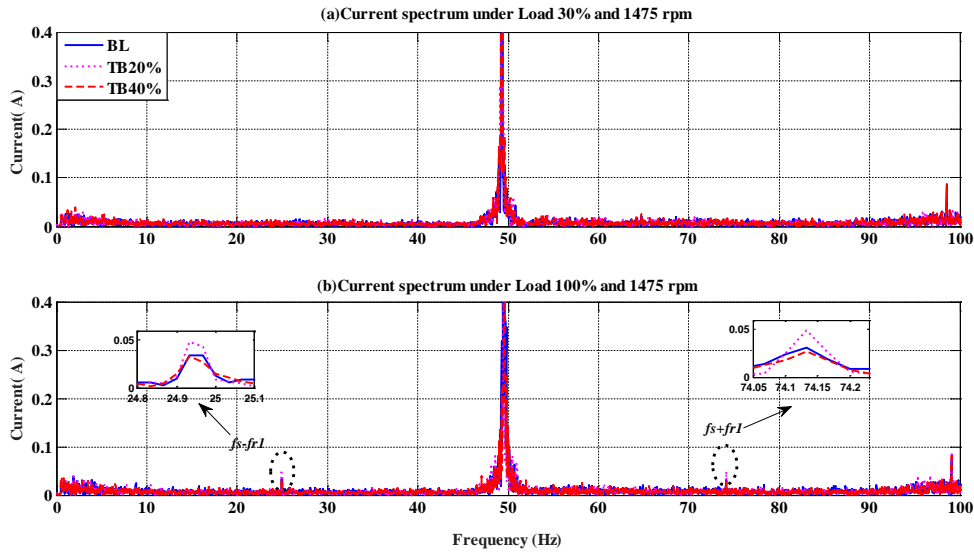


Figure 6-4: Current spectrum under 30% and 100% full load at full speed

As these components are linked to the motor shaft frequency, the appearance of them in spectrum is a result of the tooth defect. A broken tooth in a gear causes notable changes in the dynamics at shaft frequency of  $f_{r2}$  and  $f_{r1}$ .

Figure 6.5 shows voltage spectrum comparison. The amplitude of the upper and lower sidebands at  $(f_s + f_{r1})$  and  $(f_s - f_{r1})$  also increase with load change and fault severity.

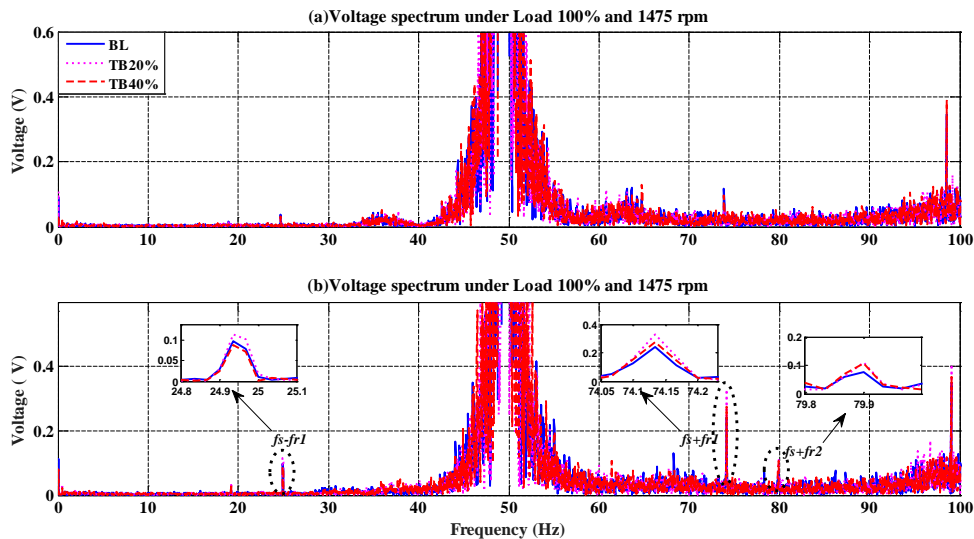


Figure 6-5: Voltage spectrum under 30% and 100% full load and full speed

The power signal spectra of Figure 6.6 also exhibit changes in a similar way to the current and voltage spectra. The amplitudes of the upper and the lower sidebands can be clearly seen and show an increase in amplitude with increase with fault severity and the applied load. However, the

power spectrum has a peak at  $2f_s$  (100 Hz) as explained in Equation (5.55). It is clear that the power spectrum has more frequency components than those for current and voltage induced by the multiplication of two signals [6] i.e. the power spectrum contains also the shaft rotational frequency components  $f_{r1}$  and  $f_{r2}$  in addition to the sideband components according to Equations (5.52-5.54).

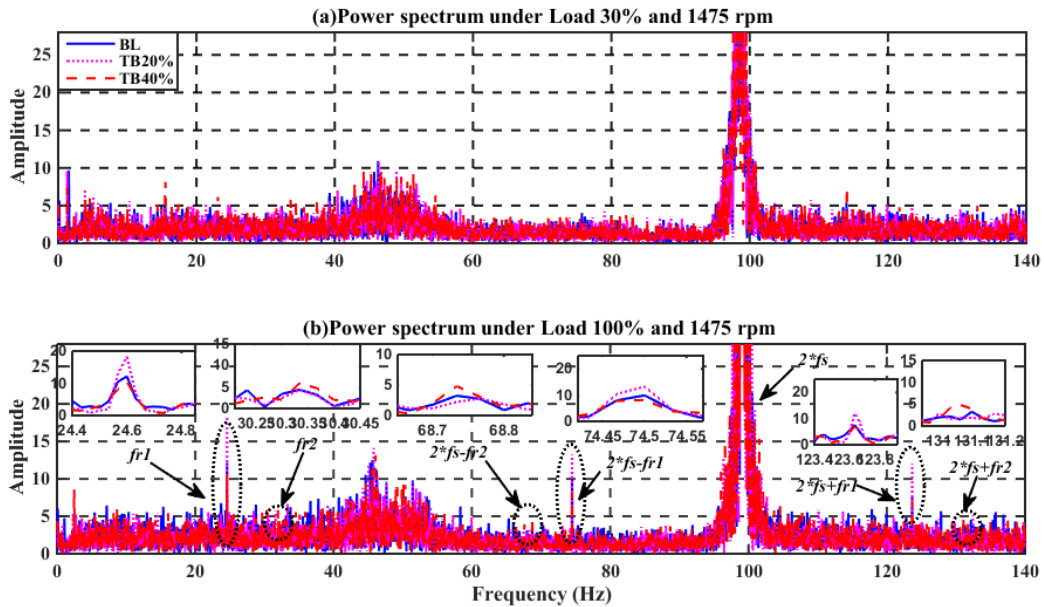


Figure 6-6: Power spectrum under 30% and 100% full load and full speed

The sideband frequency components are related to the shaft frequencies, and it is believed that the amplitude of peaks related to the 20% tooth breakage at  $f_{r2}$  are, at some points, greater than those for 40% (or overlapped). “This is can be attributed by the interaction between tooth fault, misalignment, gear errors (from manufacturing and installation) and load variations”. For more reliable information, the experiment was repeated five times. Figure 6.7 shows the amplitudes of the current at upper and lower sideband frequency. Noticeable difference can be seen between the three cases.

However, when the fault severity increase, the noise level will increase, which consequently causes overlapping in the attained signals, affecting the fault detection. Moreover, the figure shows an inconsistent trend in the upper and lower sidebands amplitudes with the load and fault severity increase.

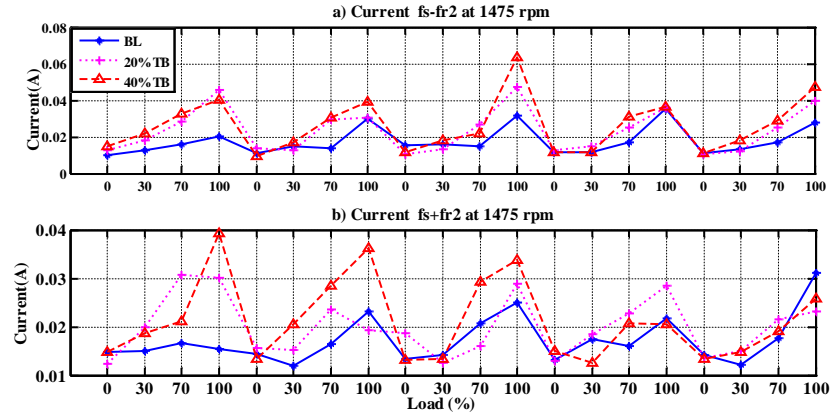


Figure 6-7: The current amplitudes at upper and lower sidebands frequency

The upper and lower sidebands frequency amplitudes in the voltage signal are shown in Figure 6.8. Because some features are affected by the noise caused by the drive, the main focus will be on the features that give most consistent results. The fault was simulated in the gear of the first stage of GB1; thus, the second shaft frequency component  $f_{r2}$  is expected to be influenced by the fault more than the first and third shaft frequency components  $f_{r1}$  and  $f_{r3}$ . Note that the voltage spectrum provides a more consistent change compared to the current spectrum.

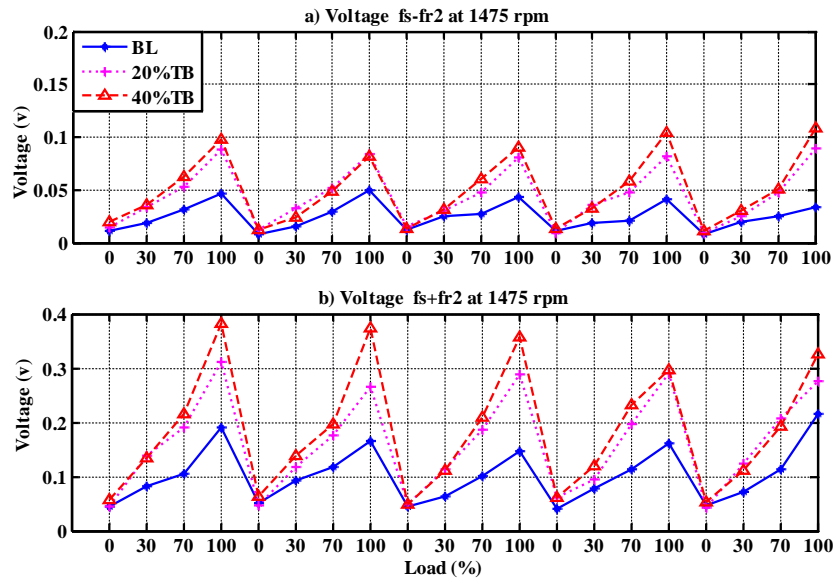


Figure 6-8: Amplitudes of the upper and lower sidebands in voltage signal

A considerable difference between the above cases is shown by the power spectrum as presented in Figure 6.9. The power spectrum shows more consistent change with the fault degrees.

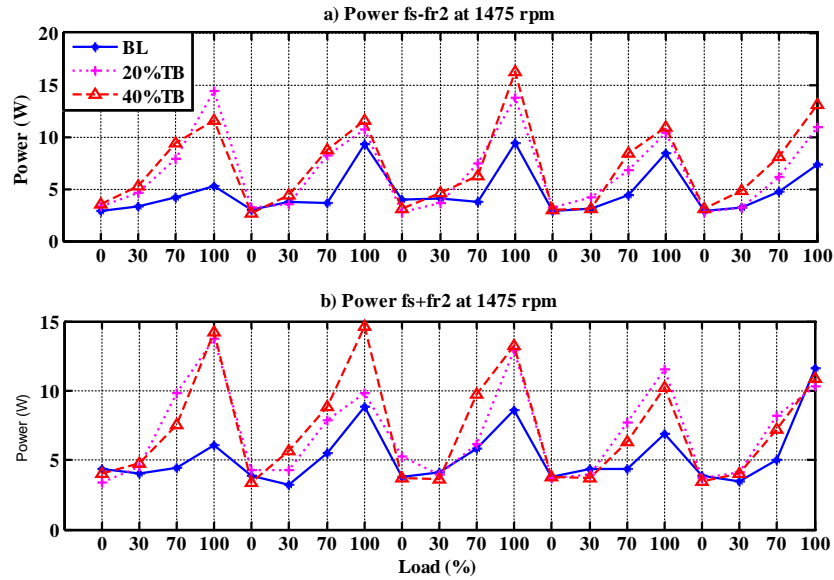


Figure 6-9: The power amplitudes at upper and lower sidebands frequencies. Additionally, the performance of the IPF in detection and diagnosis of a tooth breakage in gears was investigated. The equations used to obtain the IPF are shown in Chapter 3; Equations (3.3-3.6). Moreover, the instantaneous power factor signature was investigated. Figure 6.10 shows the IPF signals for the healthy and the two faulty cases represented with time.

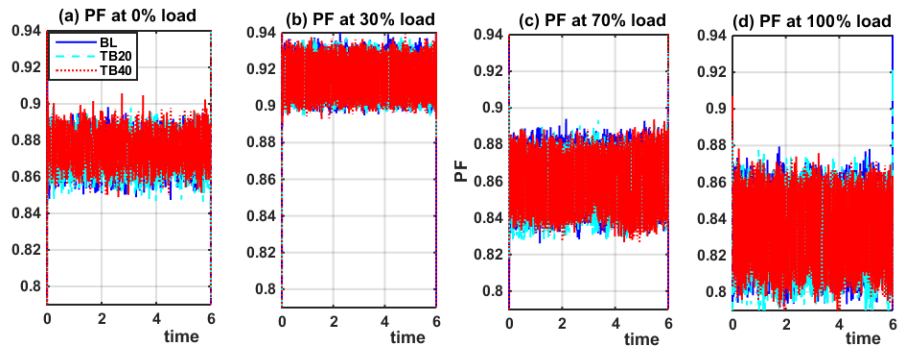


Figure 6-10: Instantaneous power factor variations with faults severity at full speed (5th-run) in the time-domain.

As it can be seen that, no much details and information can be extracted. Therefore, the average of each signal at every particular load is taken for comparison as depicted in Figure 6.11.

The IPF change with load variations was calculated from phase quantities and repeated five times in order to obtain reliable and accurate information as shown in the following figure which exhibits the mean value of the entire.

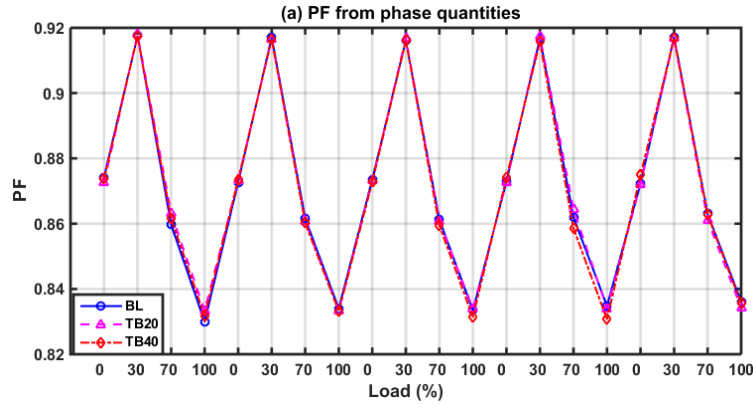


Figure 6-11: Features averaged from instantaneous power factor

For more information and better diagnostic performance, IPF spectra are calculated using the FFT. In the IPF spectrum, which is represented at full motor speed Figure 6.12, it can be seen that the two components according to the rotor shaft speeds appear at 24.57 Hz and 30.3 Hz, which are explained by that the fault causes torque oscillations which in turn will induce speed fluctuations. These components are advantageous for features extracting in gear tooth breakage detection.

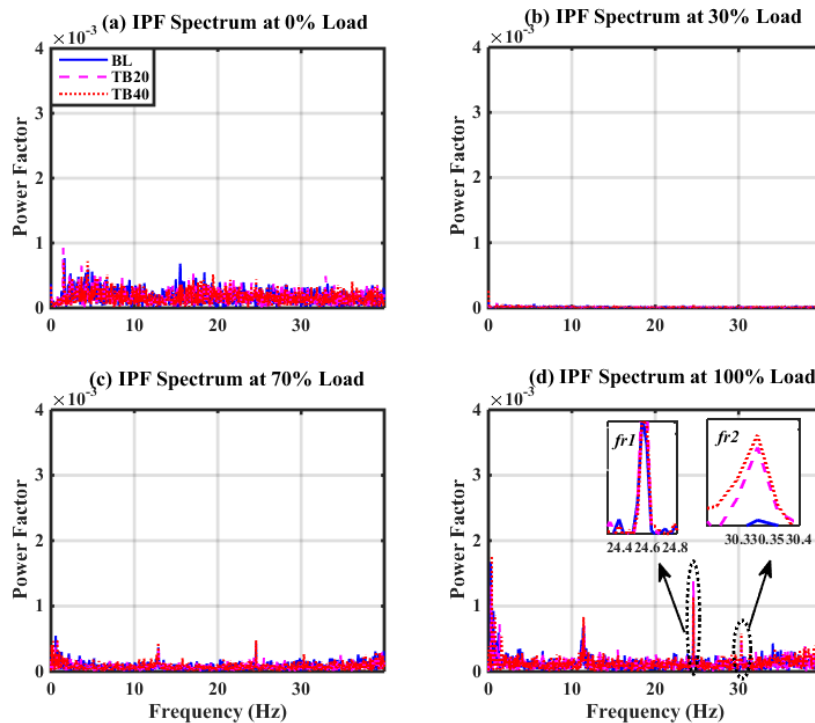


Figure 6-12: The instantaneous power factor spectra

The average peaks of the instantaneous power factor at the characteristic components of  $f_{r1}$ ,  $f_{r2}$ , and  $f_{r3}$  are illustrated in the figure below. As it can be observed on this figure these features are

increased linearly with the load and fault severity making it a good indicator of the machine condition. However,  $f_{r2}$  displayed a clear difference between the three cases (baseline, 20% of tooth breakage, and 40% of tooth breakage).

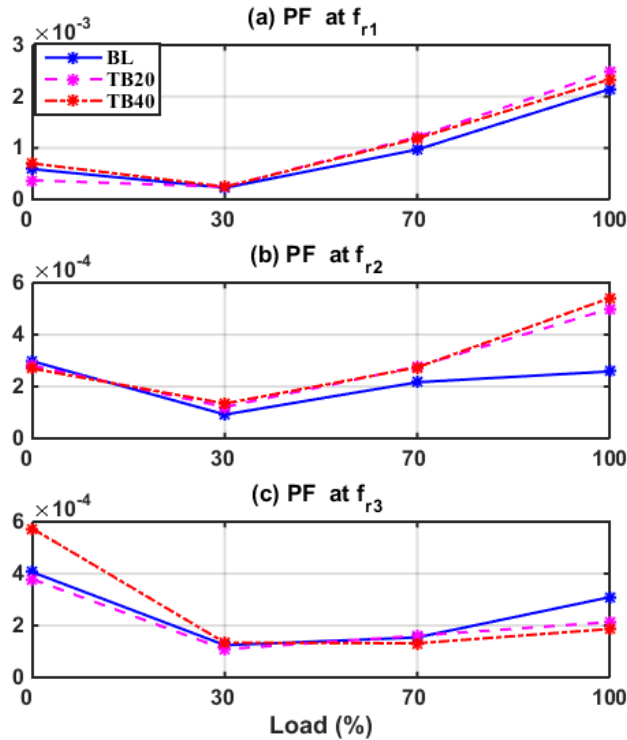


Figure 6-13: Features averaged from power factor spectrum from the 5th test run

To make it more effective, a comparison between the performances of the current, voltage and the power factor has been done as illustrated in the Figure 6.14. The IPF is based on demodulation of the phase modulation effect and it produces a slight better diagnosis as the phase obtained by voltage and current signals jointly, and consequently, can have better signal to noise ratio.

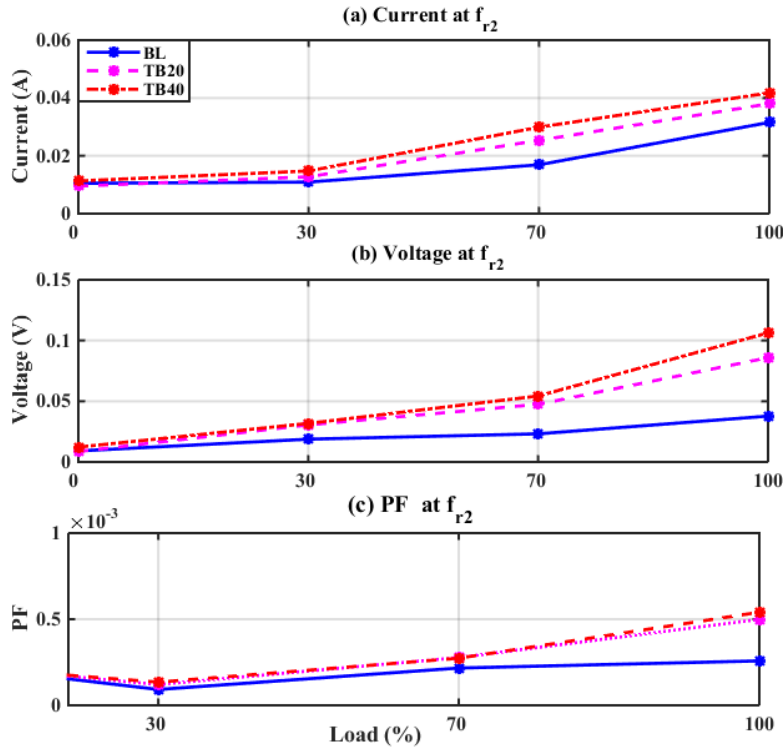


Figure 6-14: Performance comparison between current, voltage, and power factor from the 5th test run

#### 6.4.2 MSB Analysis

For more reliable and clearer features, the MSB analysis was implemented. The next figures represents the current, voltage and power at full speed and full load. Figure 6.15 represents the current MSB magnitude and its corresponding bicoherence for the baseline case. It is clear that only a single component can be seen clearly at the bifrequency of (24.5, 50) which is related to the dynamic oscillations of input shaft. Moreover, another significant peak appeared at about 50 Hz, which is the second harmonic of the input shaft rotational frequency  $f_{r1}$ .

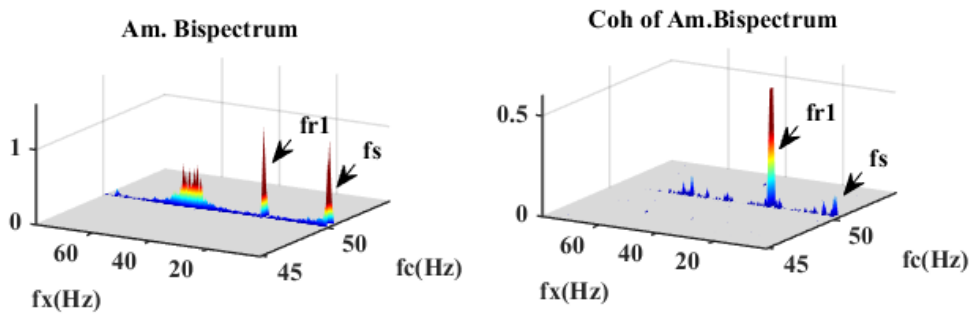


Figure 6-15: Current MSB at 100% load for the healthy case.

Figure 6.16 and 6.17 represent the current MSB and its corresponding bicoherence at 20% tooth breakage and 40% tooth breakage, respectively. Again, in both cases, it is clear that a component can be seen clearly at the bifrequency (24.5, 50) Hz, which represents the dynamic oscillations due to the modulating effect between the input shaft  $f_{r1}$  and the supply frequency. Further, the rotational frequency component  $f_{r1}$  is distinctive, which is due to the occurrence of the fault. The middle shaft component  $f_{r2}$  start appearing in the current MSB magnitude in Figure 6.17 with a small peak. The fault was introduced in  $Z_2$  and therefore,  $f_{r2}$  should be expected to be the strongly affected by the fault. However,  $f_{r1}$  appears in the MSB and the coherence as the dominant peak because it is directly connected to the motor.

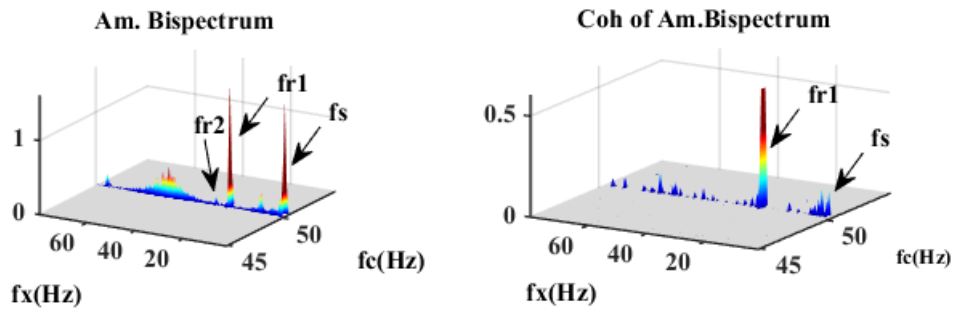


Figure 6-16: Current MSB for 20% tooth breakage

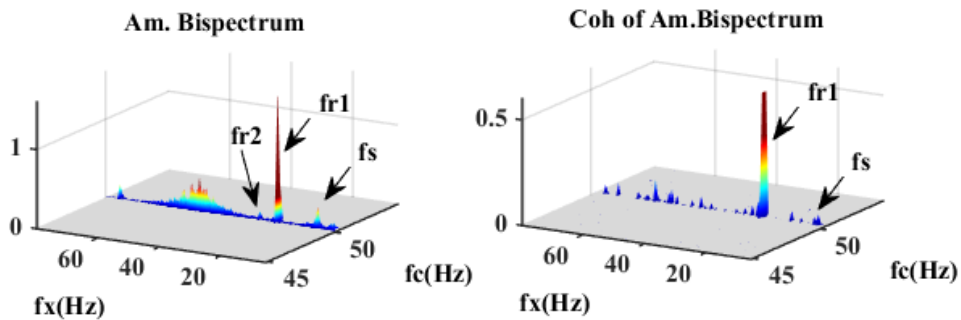


Figure 6-17. Current MSB for 40% tooth breakage

The graph shown in Figure 6.18 represents the voltage MSB and its corresponding bicoherences for the baseline case. It is obvious that two components can be seen clearly at bifrequencies (24.5, 50) and (30.33, 50), which are related to the two shaft frequencies; the middle shaft and the output shaft. The major peak is at about (24.5, 50) representing the input rotational frequency ( $f_{r1}$ ), which can be explained by the fact that  $f_{r1}$  is directly connected to the motor, and a secondary peak at (30.33, 50).

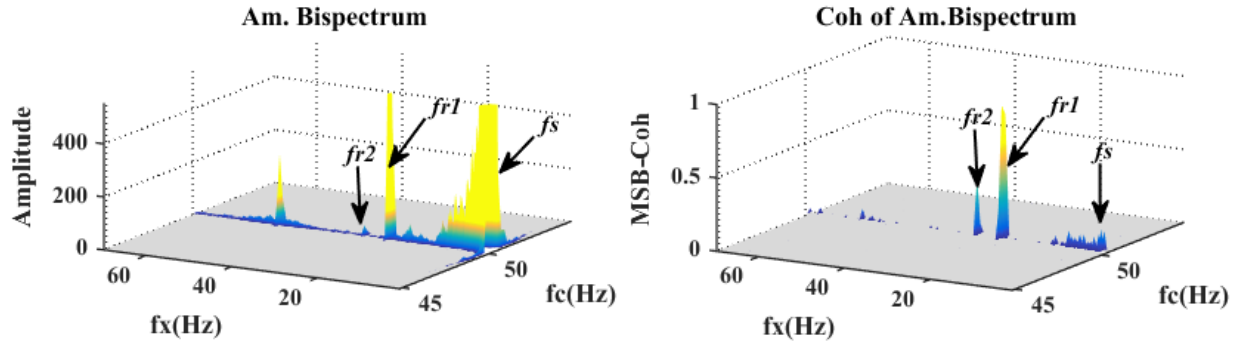


Figure 6-18: Voltage MSB at 100% load for baseline case

The voltage signals shown in Figure 6.19 represents the MSB and its corresponding bicoherence for 20% tooth breakage. A clear difference can be seen when comparing the voltage for 20% tooth breakage with the corresponding current MSB; no much difference can be seen;  $f_{r1}$  and  $f_{r2}$  become more distinct;  $f_{r1}$  appeared in the MSB as the major peak.

In the coherence, a peak appears at  $f_{r2}$  and peak at  $f_{r1}$  increases substantially in amplitude.

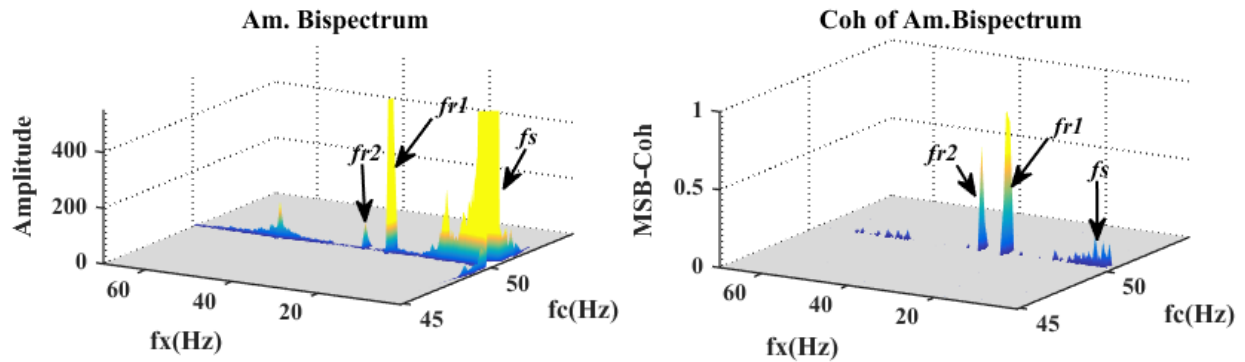


Figure 6-19: Voltage MSB at 20% tooth breakage

The 40% fault case shows a progression of fault signal compared to the 20% tooth breakage, which is a good indicator for existence of a fault, as is clear in Figure 6.20. In the coherence a peak appears at  $f_{r2}$  and peak at  $f_{r1}$  increases substantially in amplitude.

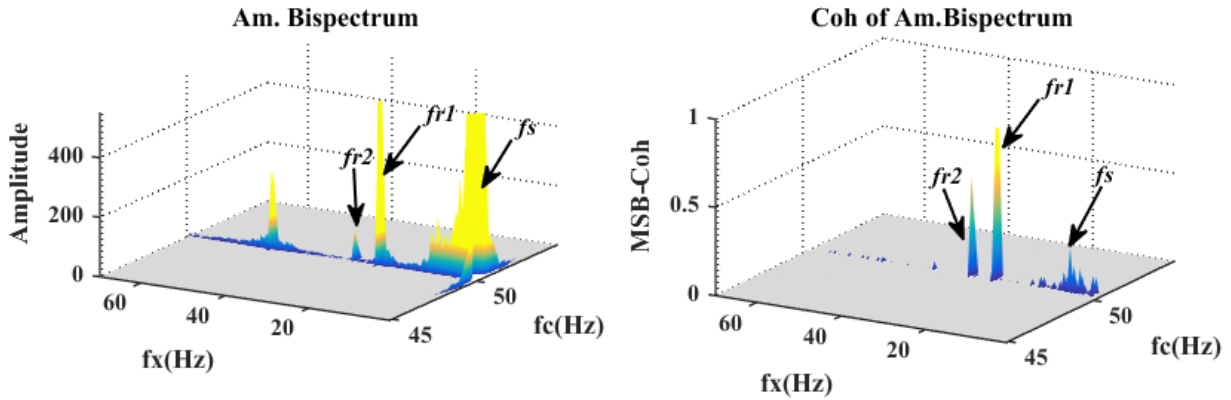


Figure 6-20. Voltage MSB at 40% tooth breakage

More distinctive features are shown by Figure 6.21, which presents the power MSB for the healthy case.

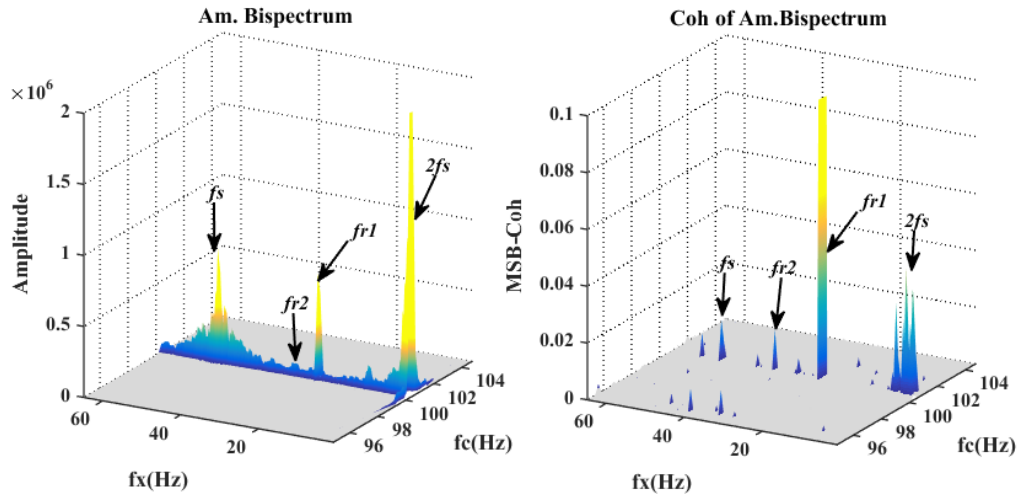


Figure 6-21. Power bispectrum for the healthy case

Figures 6.22 and 6.23 represent the power signal MSB and its corresponding bicoherence for 20% tooth breakage and 40% tooth breakage, respectively.

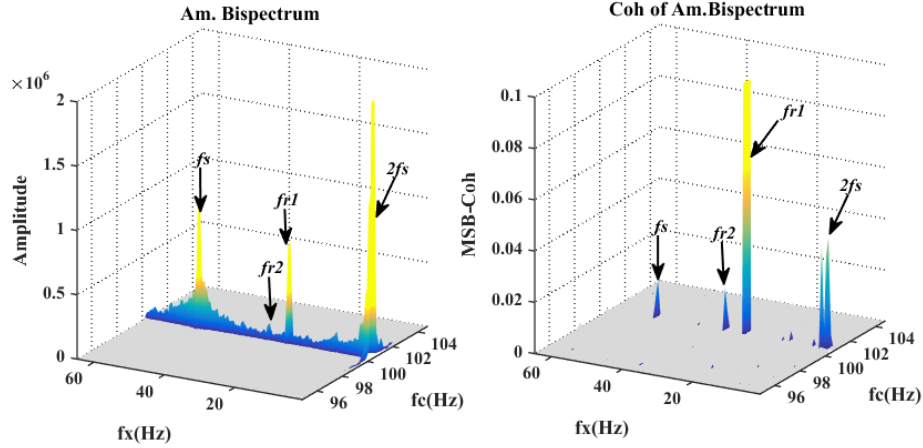


Figure 6-22: Power bispectrum at 20% tooth breakage

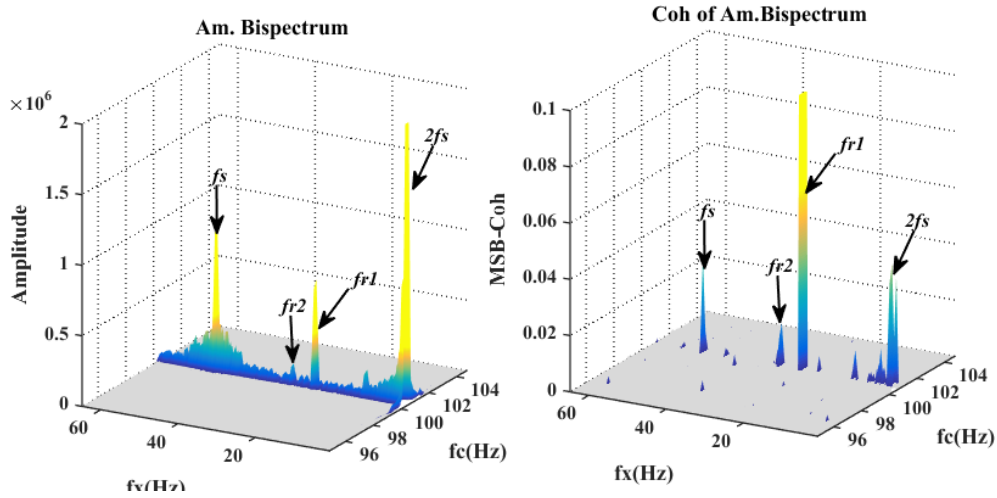


Figure 6-23: Power spectrum at 40% tooth breakage

It can be seen that the peaks of the bifrequency components for the rational frequencies, supply frequency and twice the supply frequency are more distinct in both 20% and 40% tooth breakage, confirming that the MSB based on power signals is more sensitive to the faults more than that of current or voltage.

### 6.4.3 Comparison between FFT and MSB

A comparative study between the spectrum (FFT) and the MSB has been carried out to examine the diagnostic performance of electrical signals for healthy and simulated cases under sensorless control mode.

The following figures depict the average  $f_{r2}$  peaks for the current, voltage and power by the FFT analysis; Figure 6.24, Figure 6.25 and Figure 6.26 respectively; and the MSB; Figure 6.27, Figure 6.28 and Figure 6.29 respectively, represent magnitudes extracted at  $f_{r2}$ .

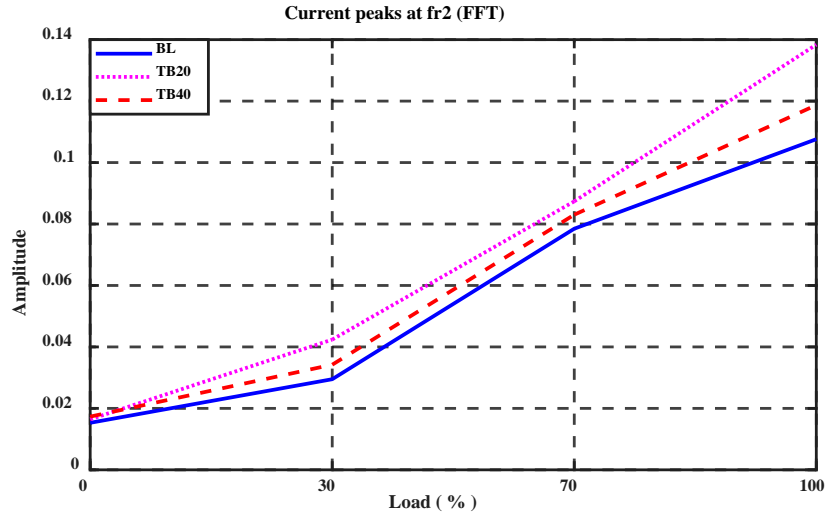


Figure 6-24: Amplitude of current peaks for sidebands  $f_{r2}$  for FFT

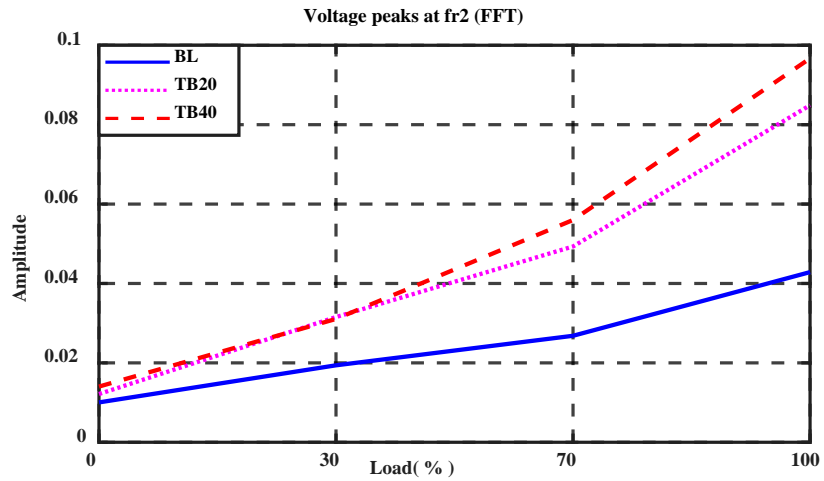


Figure 6-25: Amplitude of voltage peaks for sidebands  $f_{r2}$  for FFT

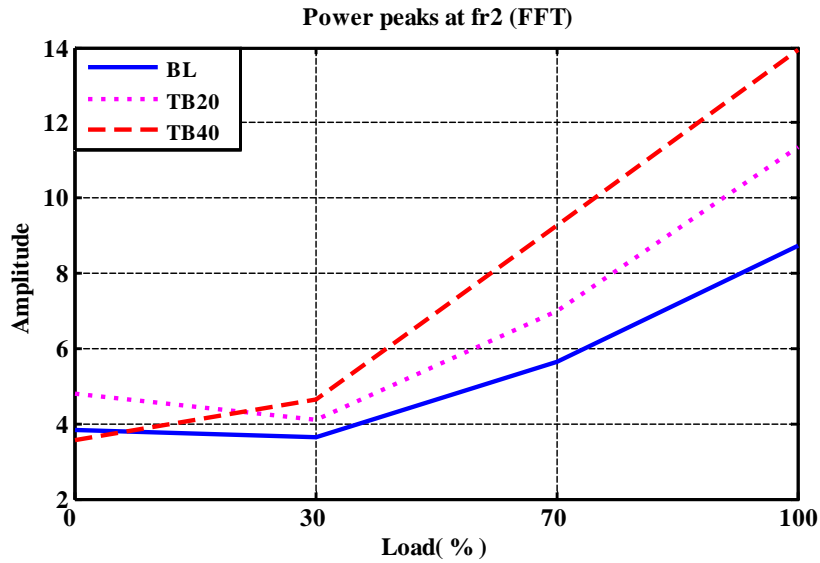


Figure 6-26. Amplitude of power peaks for sidebands  $f_{r2}$  for FFT

An increase in the features magnitudes with the change in the load and fault severity can be clearly seen in both techniques the FFT. A better performance has been shown by the voltage signals as compared to the current signals, which is attributed to the impact of the VSD on the voltage signals more than on the current one. The VSD attempts to retain the speed constant and compensate for any torque's change which might be caused by the fault.

On the other hand, the different fault cases were better separated in the power spectrum, which is the multiplication of the current and voltage signals.

The shortcomings in figures provided by the FFT method is the overlapping between the baseline and the faulty cases at low speed which might affect the diagnosis [131].

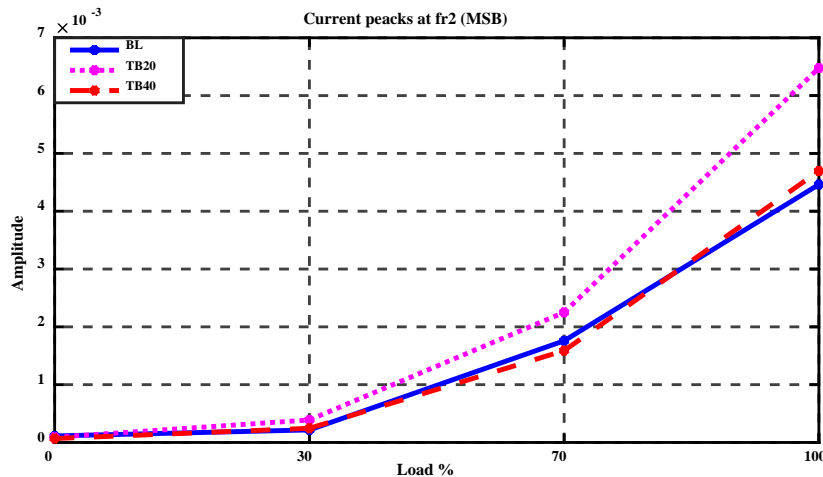


Figure 6-27. Amplitude of current peaks for sidebands  $fr_2$  for MSB

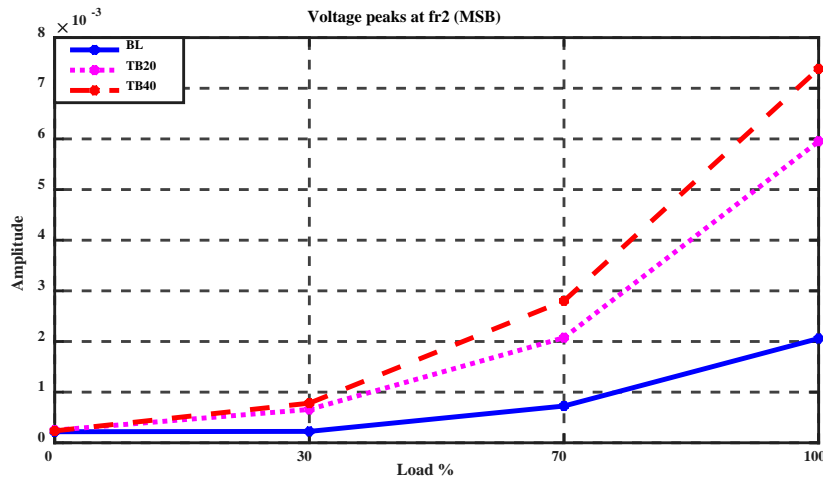


Figure 6-28. Amplitude of voltage peaks for sidebands  $fr_2$  for MSB

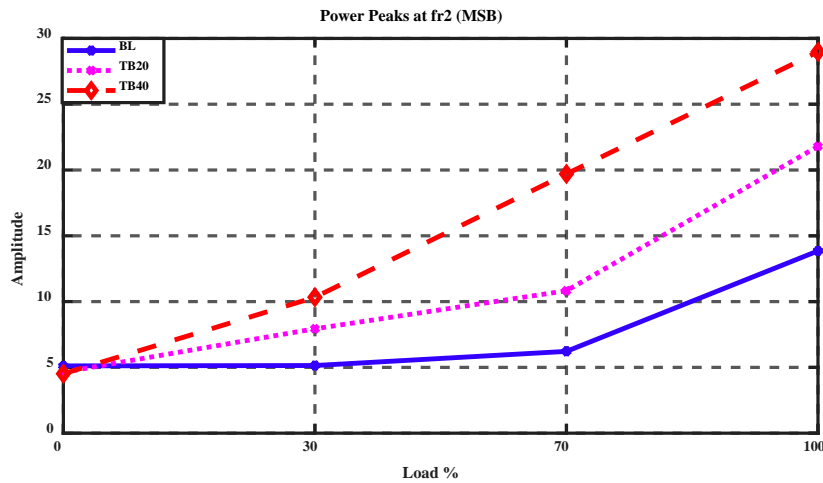


Figure 6-29. Amplitude of power peaks for sidebands  $fr_2$  for MSB

However, it is seen that the MSB has the better performance in characterizing the sidebands, and greater consistency when using power signals as compared to current and voltage as shown in Figures (6.27-6.29). The MSB also shows greater clarity at the medium rotational frequency  $f_{r2}$  compared to the FFT, which shows less capability for fault separation. This can be explained due to the superior noise suppression and nonlinearity characterization that the MSB possesses and the phase inclusion, which the MSB provides. In addition, MSB has showed better capability to differentiate between different faults and provides more reliable and accurate diagnosis. In particular, the power signal provides a consistent change with fault severity and good separation between fault cases. This is because MSB has unique properties of modulation enhancement and noise reduction.

As the results provided by the MSB analysis are clear enough and the faulty cases are well separated from the healthy case, thus, the author believed that no further investigation using another signature is needed.

## 6.5 Key Findings

These tests have provided the following key findings for monitoring, detecting and diagnosing tooth faults in a two stage helical gearbox:

- Fault features increased with load and fault severity for both FFT and MSB.
- The power spectrum gives a slightly better differentiation between fault cases as power signals result from the multiplication of the current and voltage.
- The IPF is based on demodulation of the phase modulation effect and produces a slight better diagnosis as the phase obtained by voltage and current signals jointly.
- The MSB has the ability to provide a better performance in characterizing the sidebands and greater consistency when using power signals as compared to current and voltage.
- The MSB also showed greater clarity at the intermediate rotational frequency  $f_{r2}$  compared to that from the FFT, which is due to the superior noise suppression and nonlinearity characterization of the MSB due to the phase inclusion. In other words,  $f_{r2}$  could be appropriate to detect and diagnose this kind of faults.
- The MSB has showed better capability to differentiate between different fault cases and provides more reliable and accurate diagnostic information. In particular, a consistent change with fault severity and good separation between fault cases have been provided by the power signals.

## CHAPTER SEVEN: DIAGNOSIS OF DIFFERENT OIL LEVELS TEST

---

*Three different oil levels of lubricant were used to test the capability of electrical signature analysis for detecting and diagnose lubrication degradation and the presence of too much or too little oil in the gearbox. This chapter starts with an introduction to the important role of lubrication in industrial applications, then explains the test facilities and procedure. After that it discusses the results obtained using the FFT and MSB combined with generalised instantaneous phase quantities: IPF and IPVC, then it compares the results obtained by the two techniques. Finally, the key findings are summarised.*

## 7.1 Introduction

Oil is essential for the lubrication of gears in order to avoid gearbox failures. The lubricant must cover the surfaces of the gear teeth in the all-important contact zone, separating the gear teeth by a thin film of oil. Lubricant is also used to flush away abrasive particles resulting from wear of the gear teeth, dirt or other contaminant that would wear the tooth surfaces where they come into contact [132]. However, in practical industrial applications, inadequate lubrication (e.g. using lubricant of the wrong grade, or too low an oil level (insufficient lubricant)) is a frequent occurrence and will produce additional wear of gears which can cause tooth breakage with the debris causing severe damage to downstream components. Too low an oil level will mean gear teeth will be in contact, with no layer of lubricant to separate them, increasing surface shear stresses. The resulting friction will generate heat and raise the temperature of the oil itself, which can contribute to deterioration in lubricant quality and leaks in seals and gaskets. It is also recognised that too much oil in a gearbox will bring its own problems, in particular excessive power loss caused by unnecessary churning of the extra lubricant.

Höhn et al., consider that the failures of the majority of gearboxes can be ascribed to inadequate or improper lubrication [133]. Today it is generally accepted that monitoring of the oil quality and level is essential for the effective CM of any lubricated system [134].

Thus optimum gear performance and maximum operational life requires the proper oil level [135]. The active monitoring of the oil level in gearboxes is now well established in industry and is used for early stage identification of possible failures in order to avoid expensive repairs, and plan for downtimes that will minimise the interruption of production [103, 104, 136].

The gearbox in industrial processes will often be driven by an electrical motor, and gearbox lubrication will be a significant factor in electrical power requirements. For example, as mentioned above, too much oil and a significant amount of additional power will be dissipated as viscous losses and heat energy, and it has been shown [136] that this can be detected by measurement of the average motor supply voltage and current. Thus, there is the possibility that electrical power measurements can be used to detect lubricant degradation and the presence of too much or too little oil.

Brethee, et al., studied the effects of inadequate oil level on the gearbox vibration signal [137]. These authors noted that the amplitude of the signal grew as the oil level fell, and explained this

as being due to the lubrication on the sliding surfaces as the teeth meshed being inadequate and friction increasing. Unfortunately, vibration measurement is relatively expensive and are often problematic to apply, since it is necessary to have sufficient access to attach the sensors (accelerometers) on the machine's surface. Accordingly, a number of researchers have used ESA for remote monitoring of the health of a gearbox in terms of such factors as broken teeth, and also in terms of monitoring the health and quantity of the lubricant [137].

Previous research has investigated problems associated by gear lubricant using voltage and/or current signatures and conventional signal processing. For example, Abusaad et al., [37], developed observers for speed, flux and torque to examine their residuals under two different faults: tooth breakage and shortage of lubricant at different levels. The author used voltage signature analysis (VSA) combined with the MSB technique. However, the author didn't investigate any other signals (except the voltage signals) to evaluate the performance of different signature in fault diagnosis. There has been relatively little work with motors employing sensorless VSDs seeking to obtain maximum information from both current and voltage signals by using their product - electrical power. This has motivated this author to develop his method by applying MSB to power measurements.

A study [138] has reported the use of radial vibrations of paired steel "rotating roller - fixed segment" in detecting lubrication condition: e.g. starved or ample supply. Experimental results showed that inappropriate levels of lubrication could be detected as an increase in the amplitude of the vibration signals. The detection of inappropriate levels of lubrication bearings using vibration signal was examined in [139]. The author stated that the influence of an improper level of lubrication could be seen as an increase in the amplitude of the frequency components in the vibration signals.

It should be noted that sections of this chapter have been published in a paper of which this author was the lead author and which, where relevant, will be quoted here. "When setting the VSD to a sensorless action mode, certain variables will be altered, including speed, terminal voltages and stator currents. The regulation mechanism for speed responds to this by compensating for changes due to altered loads or other factors. The drive tends to make more changes to the terminal voltage than to the current, in an attempt to keep the speed at a constant close to the desired level. Thus, more information about the health of the motor can be obtained by means of analysis on the voltage

signals” [6]. However, it has been a matter of concern that noise from the drive and control actions of the closed-loop could reduce the precision of the acquired data.

A general energy balance equation is required relating electrical power and torque. Electrical power because we are interested in measuring voltage and current and combining these to maximum effect for fault detection, and torque because it is a measure of the power delivered and directly affected by the level of lubricant, its viscosity and speed of rotation [133, 140].

Following Hamad et al., [6], Seetharaman, et al., [11] and Saad [141], the following equation can be obtained.

$$J \frac{d\omega}{dt} + D\omega = \frac{3}{2} \frac{P}{2\omega} [\psi_{ds} i_{qs} - \psi_{qs} i_{ds}] - T_L - T_{ch} \quad (7.1)$$

where:  $J$  is the moment of inertia;  $D$  is the viscous friction coefficient;  $\psi_{ds}$  and  $\psi_{qs}$  are the  $d$  and  $q$ -axis flux linkage of the stator respectively;  $P$  is the number of poles;  $i_{ds}$  and  $i_{qs}$  are the  $d$ - and  $q$ -axis stator currents;  $T_L$  is the gear load torque, and  $T_{ch}$  is the gear churning torque which can be found from Equation (7.2).

$$T_{ch} = \frac{\rho}{2} \omega^2 S_m R_p^3 C_m \quad (7.2)$$

where:  $\rho$  is the density of the lubricating oil;  $\omega$  is the rotational speed of the gear,  $R_p$  is the gear pitch radius,  $S_m$  is the submerged surface area of the gear, and  $C_m$  is a non-dimensional torque parameter which depends on the flow regime around the gear [140, 142-144].

In deriving Equation (7.2), it was assumed that the churning losses were directly proportional to the wetted surface area of the gear; assuming all other parameters remain constant. It follows that a change of lubricant will have an effect on the dynamic behaviour of the system and each and all of the components driven by the shaft [141].

Moreover, the damping effect can be reduced by the churning effect whereas the moment of the inertia of the rotational system would be increased [141].

At the fundamental frequency, the magnitude of current spectrum will often be substantially greater than the magnitudes of its surrounding sidebands. There will also be harmonics of the fundamental with their own sidebands. The magnitudes of the fundamental, harmonics and

sidebands will be closely linked to the operation of the machine or engine, its rotational speed, load, out-of-balance forces, and so on.

There will often be considerable overlap in the harmonics of the fundamental frequency (of the current) and the sets of sidebands [131]. This makes identification of the fundamental's sidebands non-trivial as one set of sidebands could mask another and make fault identification more difficult. There could also be more than one contributor to the presence of sidebands; these would include shaft misalignment, and errors in the manufacture of the gears. All these different factors call for expertise in signal analysis to ensure accurate fault identification and separation [38, 93, 94].

There are additional problems, the signal produced by faults in their early stages are likely to be much smaller than the general background mechanical noise, which makes detecting them a challenge. This problem has attracted the interest of both industry and academia; to find either alternate parameters that can be an indicator for the fault existence, or methods of extracting low level repetitive signals from a noisy background [101].

The instantaneous phase angle is an electrical quantity, which is used in the description of power systems. This quantity should be also affected when there is a fault.

The instantaneous power factor spectrum and the instantaneous phase include relative frequencies directly linked to the fault, which are as clear as that of the fundamental frequency component and related harmonics, therefore monitoring of these components makes condition monitoring and diagnosis easier [102].

This chapter will seek to establish the effectiveness of the instantaneous power factor and the instantaneous phase of voltage-current for detection and diagnosis of faults in gears, including the level of lubricant. The equations used to calculate the instantaneous power factor are presented earlier in Chapter 3.

## **7.2 Faults Simulated and Test Procedure**

The experimental setup shown in Figure 4.2 (described in Chapter 4), has been devised to investigate the power factor quality estimated using the oil-level detection for the first gearbox (GB1). In this setup, GB1 is a helical gear comprising three stages: input, middle and output, with signature frequencies denoted by  $f_{r1}$ ,  $f_{r2}$  and  $f_{r3}$ , respectively, see Equations (4.1)-(4.3). These equations show that the three frequencies will be modulated as and when the fundamental supply

frequency is modulated, but also that any independent modulation of any one of the gears will affect the others.  $f_{r1}$  is the frequency component of the input shaft, which is coupled to the induction motor via flexible coupling;  $f_{r2}$  is the frequency component of the middle shaft; and  $f_{r3}$  is the frequency component of the output shaft.

The study was carried out on a gearbox system driven by a 10 kW AC motor controlled by a sensorless drive, to drive the system at different speeds and loads, see Figure 7.1. Two back-to-back gearboxes: GB1 and GB2 were installed in which GB1 is the test subject. A DC generator was the load applied to the gearboxes. The test gearbox is an off-shelf product and commonly used in many industries. Its technical specifications are presented in Table 7-1.

Prior to any test runs, the gearbox was drained and then flushed with lubricating oil. After which the gearbox was filled with the prescribed amount of oil, 2.6 liters of grade EP320, as recommended by the manufacturer. Covering the gearbox with a top gave greater structural integrity which improved shaft alignment consistency.

Two other oil levels were also tested to mimic faulty operation; these are denoted as “LV600” and “LV1100”, representing a reduction of 600 ml (2.0 liters of oil, 77% of the recommended oil level) and a further reduction of 500 ml (1.5 liters of oil, 57.7% of the recommended oil level), respectively.

Different levels of lubricant will result in different churning losses, with different fluctuations of the shaft speeds. The control system will seek to maintain a steady speed by adjusting the current and voltage to balance the changes to the mechanical forces at work in GB1. Thus, if the changes are due to the change in level of the lubricant then the measured changes should be a measure of the change in oil level. Unfortunately, the trial runs showed the changes to be very small. The gearbox was then tested at full speed (1475 rpm), since it was expected that the viscous forces would be greatest at maximum speed. The loads for the tests were 0%, 30%, 70% and 100% of the rated full load (10 kW). To ensure signal reliability, every load condition was tested five times, each taking 8 minutes to complete. The VSD was utilised in its sensorless mode, in order to assess the performance of fault detection using this particular control technique. Throughout the test, the oil temperature was monitored, see below. The data was acquired for steady-state conditions. The data collected was then analysed using first the FFT signal processing and then the MSB with instantaneous power factor (IPF).

Details about the measurements systems are previously provided in Chp4.

Table 7-1: Specifications of test gearbox, GB1

Parameters	value
Type of tested gear	Helical
Manufacturer	Radicon
Oil type	EP 320
Oil volume	2.6 L
Gear ratio	3.678
Tooth number	$Z1/Z2=58/47- Z3/Z4 = 13/59$
$fr_1$	24.58 Hz
$fr_2$	30.337 Hz
$fr_3$	6.684 Hz

Figure 7.1 illustrates the gears construction and simulated oil levels.

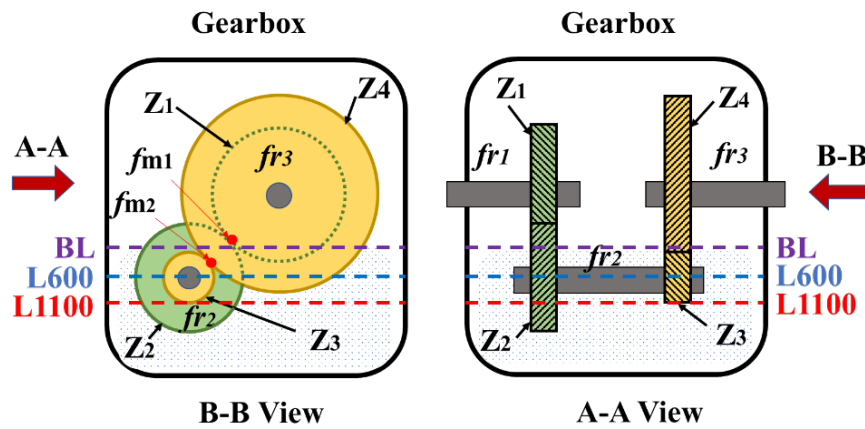


Figure 7-1: Schematic illustration of the test gearbox and oil levels

## 7.3 Results and Discussion

### 7.3.1 Spectrum Analysis

The purpose of the tests is to determine whether there is sufficient oil in the gearbox to maintain smooth operation and maximise the gears' life.

The essence of this investigation was to determine the capability of IPF for detection and diagnosing of inadequate oil levels in GB1. The first step was to monitor the lubricant temperature during the tests. This provided information on the effect of oil level on the operating temperature of GB1 when analyzing the measured signals.

Figure 7.2 (a) presents the average temperature for each test run at drive speed 1475 rpm at four different loads and three lubrication levels.

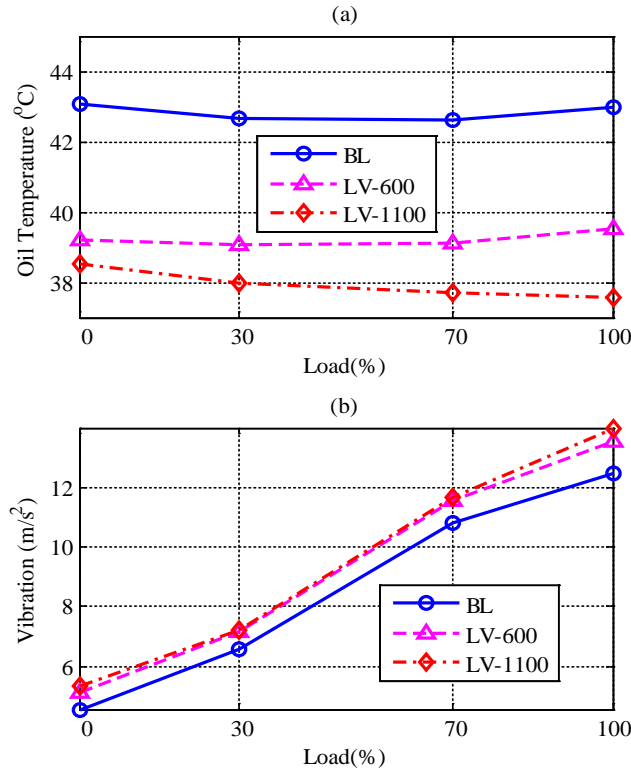


Figure 7-2: Gearbox oil temperature and surface vibration under different operations

It can be seen that the average temperature falls with falling oil level. This consistent temperature decrease can be a good indicator for oil shortage. However, such a decrease will be influenced by other factors such as environmental temperature, oil quality changes, etc., thus temperature change may be not very reliable for indicating oil shortages. Nevertheless, the changes in temperature and vibration did show that these oil reductions can cause both static and dynamic changes to the gearbox, which allows for a comprehensive evaluation of the electrical supply signature based diagnosis.

A certain minimum quantity of oil is required before the level reaches the lowest gear, Z<sub>2</sub>. Once above this level, the oil is churned, so once this level is reached adding more oil means

proportionately more oil is being churned, which means a relative increase in temperature. It is noted that at all three lubricant levels the oil temperature is within specified limits (that is the limits specified by the oil supplier.).

The vibration increased with reduced oil level, as shown in Figure 7.2 (b). This can be the combined effects of less dampening of the rotational dynamics and increased friction of gear teeth. This increase in the vibration is certainly a good indicator of the oil shortage. However, more detailed analysis is needed to diagnose the cause of such increases.

Generally, the increase in vibration is due to the poor lubrication when the oil level was reduced. However, the heat is mainly generated between the mating surfaces, when oil level decreases, the mesh position will be beyond the oil level, which means less heat has transmitted into the oil. That's why the temperature decreases with reducing the oil level.

Change in temperature and/or vibration demonstrate that the oil reduction will generate both static and dynamic changes to gear behaviour, which should allow an evaluation of electrical supply signature based diagnosis.

The shaft speeds were also monitored to determine what effect the reduced oil levels had. Figure 7.3 shows the averaged speeds for the different lubrication levels under four incremental loads.

The figure shows that it would be very difficult indeed to differentiate low lubricant levels at low loads from the speed alone. At higher loads, 70% and above, it might be possible to differentiate oil levels using the measured shaft speeds.

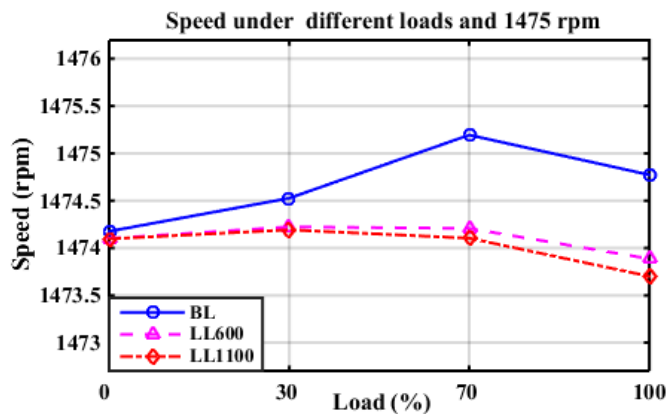


Figure 7-3: Shaft speed under different lubricant levels

The spectra for typical voltage and current signals can be seen in Figure 7.4, this shows a significant number of higher order harmonics of the 50 Hz supply ( $= f_s$ ), against a high level of

background noise. There are sidebands either side of  $f_s$  at  $f_s \pm f_{r1}$ ,  $f_s \pm f_{r2}$  and  $f_s \pm f_{r3}$ . The first two readily seen, but the high level of background noise especially the frequency modulation “FM” effect of “PWM” hides the small peaks at  $f_s \pm f_{r3}$ . These sidebands provide information on the dynamic behaviour of the gearbox since they are generated by the signature frequencies of the three stages in the gearbox. Unfortunately, these sidebands have not been observed to relate to depleted oil levels.

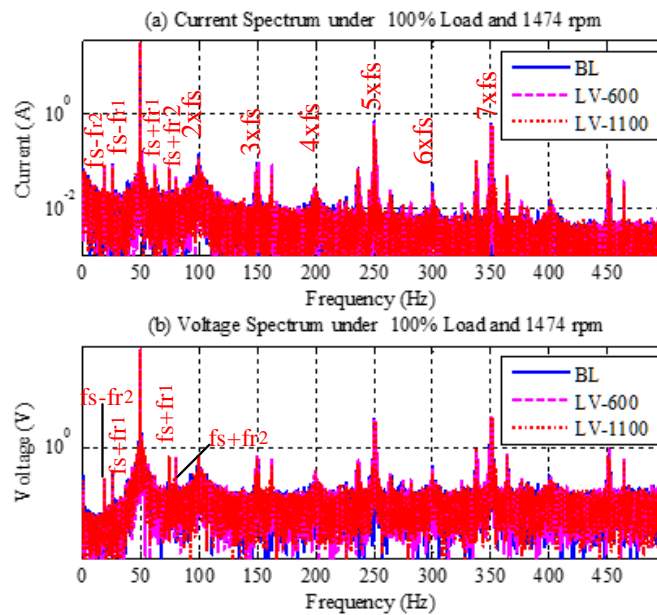


Figure 7-4: The spectra for a typical set of current and voltage signals

The instantaneous power factor can be obtained from the current and voltage signals via the Hilbert transform, see Equations. (7.1) and (7.2). Figure 7.5 shows three IPF signals, each one for a different oil level in the gearbox; BL- base level (2.6 litres), LV-600 (2 litres) and LV-1100 (1.5 litres) of oil, also shown are the corresponding spectra. The IPF signals have been normalised to unity as this makes comparison more convenient and more suitable for diagnosis. The IPF signals are considered to contain useful information on gearbox operation. Inspecting Figure 7.5 (b) we see peaks in the spectrum at  $f_{r1}$ , and note that the amplitude of this peaks increases as the oil level decreases; this indicates greater friction effects at the first stage as the oil level falls.

For the peak at  $f_{r,2}$ , we note that the shaft corresponding to  $f_{r,2}$  is submerged in oil for both levels BL and LV-600, and suggest that it is the churning motion that generates the vibration signal, which decreases as the oil level falls.

These results suggest that the IPF analysis can provides adequate information for oil level diagnosis.

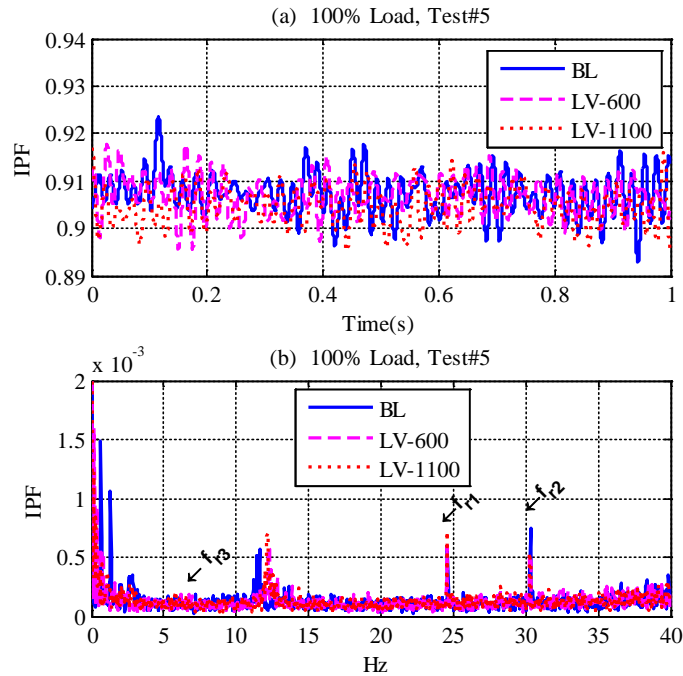


Figure 7-5: Upper panel IPF signal, lower panel IPF spectrum, for three oil levels

Figure 7.6 shows the IPF normalised with respect to its value measured at a drive speed of 1475 rpm. The measurements were made for three oil levels, BL, LV-600, LV-1100 and four applied loads; zero load, and 30%, 70% and 100% of full load. The mean of the IPF was found for each test, no significant differences with oil level could be discerned between corresponding tests.

In Figure 7.6 (b), the average IPF shows differences, exhibiting higher efficiency and advantages of using VSDs as the motor is supplied from a PWM source which will adjusted accordingly with the load and speed's change and then vary the voltage terminals fed the motor to retain a normal operating conditions. In a sensorless control based VSD system, the power supplied to the motor is from a PWM source. Corresponding to changes in the load and speed, the width of applied pulses is adjusted and thereby varying the average DC voltage applied to the motor terminals to

maintain nominal operating conditions maintaining a stable speed and this will enhance the machine performance.

The consistent drop in IPF level observed at all loads with decrease in oil level, seen in Figure. 7.6 (b) may be due to larger system oscillations resulting from less damping provided by lower oil levels.

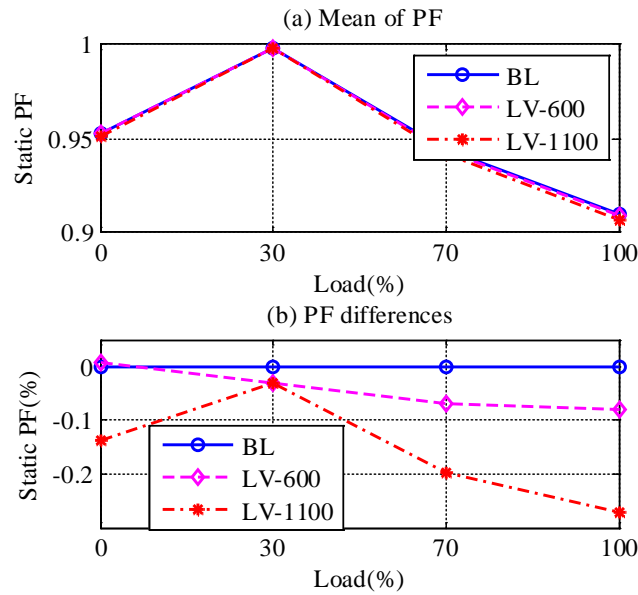


Figure 7-7: Mean levels of normalized static PF for three oil levels and four applied loads  
Note that static PF is expressed as a percentage, this is because it is normalised:

$$\omega = 2\pi f_r \quad (7.3)$$

And,

$$\omega(t) = \frac{d\theta(t)}{dt} = 2\pi f_r \Xi(f_r) \quad (7.4)$$

(Equation, (7.3) is contained within Equation. (7.4);  $\omega = 2\pi f_r$  is the same as  $\omega(t) = 2\pi f_r$ )

Where  $\Xi(f_r)$  is the frequency peak at  $f_r$ . Thus shifts in the peak value of the IPF will reflect gear speed fluctuations caused by faulty gears.

Figure 7.7 presents the percentage amplitude deviations in percentages in IPF at  $f_{r1}$  and  $f_{r2}$  with load and oil level.

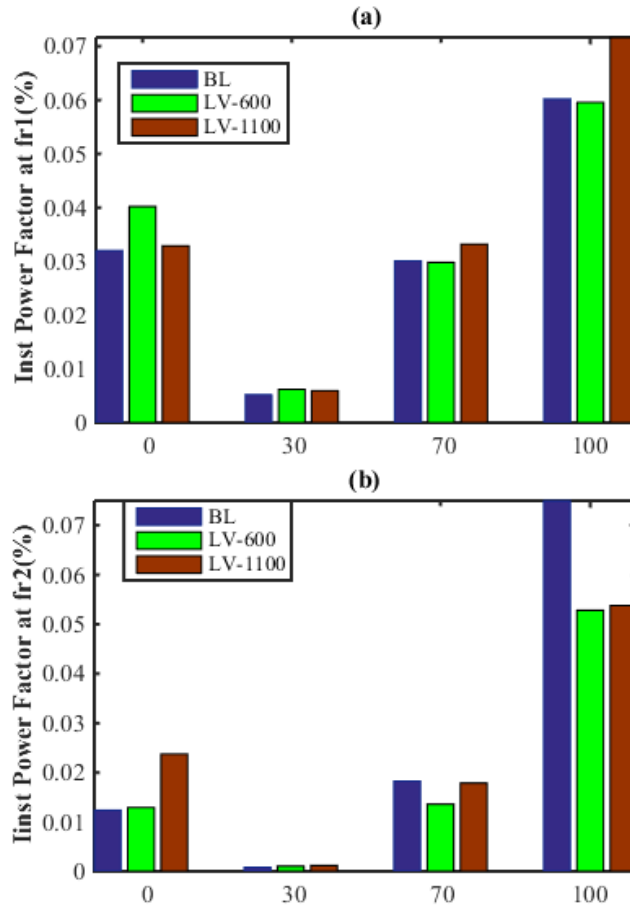


Figure 7-6: IPF at characteristic frequencies

For  $f_{r1}$  and  $f_{r2}$ , the figure shows no clear or consistent trend between IPF at frequency  $f_{r2}$  with change in load. At full load, it is possible to separate the relative amplitudes for  $f_{r2}$  and it is suggested that the decrease in amplitude with less oil present at full load is due to reducing churning.

To better discern these small changes: IPVC obtained by a summation of current and voltages phases rather than the difference in conventional IPF, is used. Figure 7.8 presents the magnitudes of the IPVC at the characteristic frequencies for different load conditions and different cases. Clearly, the overall amplitudes are much higher than those of Figure 7.7. This measure allows greater discrimination between loads for all three oil levels, but there is no greater discernment between oil levels at any load. Certainly, the difference in frequency peak levels can differentiate between low and high loads for  $f_{r1}$  where there is a more consistent increase in levels with decrease of quantity of oil. Figure 7.8 (b) exhibits less improvement as shown by the amplitudes at  $f_{r2}$ .

It is clear that the amplitudes components at the input shaft frequency  $f_{r1}$  displays a generally increasing trend as oil quantity decreases, indicating the effects of the higher friction and lower damping, as well due to the reduction oil quantities. Figure 7.8 (b) on the other hand, exhibits a decrease in the amplitudes at  $f_{r2}$  with the oil reduction, most markedly at the highest load. This decrease indicates that the effect of reduced churning and the submerged areas of the gear set “2” becomes less, as illustrated previously in Figure 7.1. Even though a joint difference of the amplitudes at both rotational frequencies  $f_{r1}$  and  $f_{r2}$  allows separation of the full load cases, it is not easy to separate the other lower load cases in terms of amplitudes differences. This can be attributed by the effect of phase cancellation. Thus, the phase summation quantity IPVC is investigated as a diagnostic of small changes in oil level.

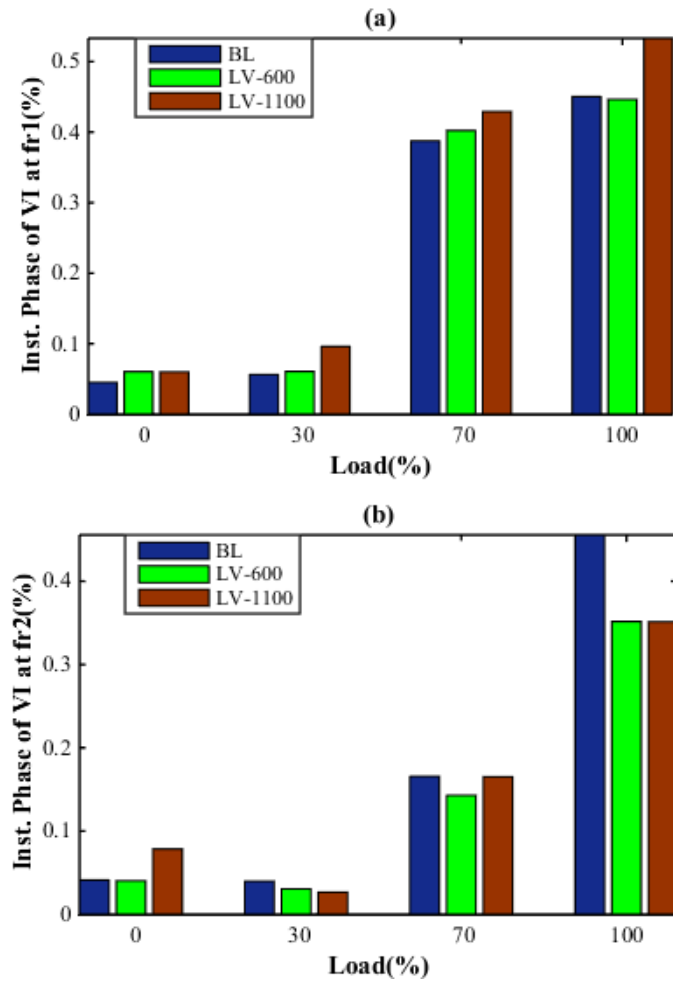
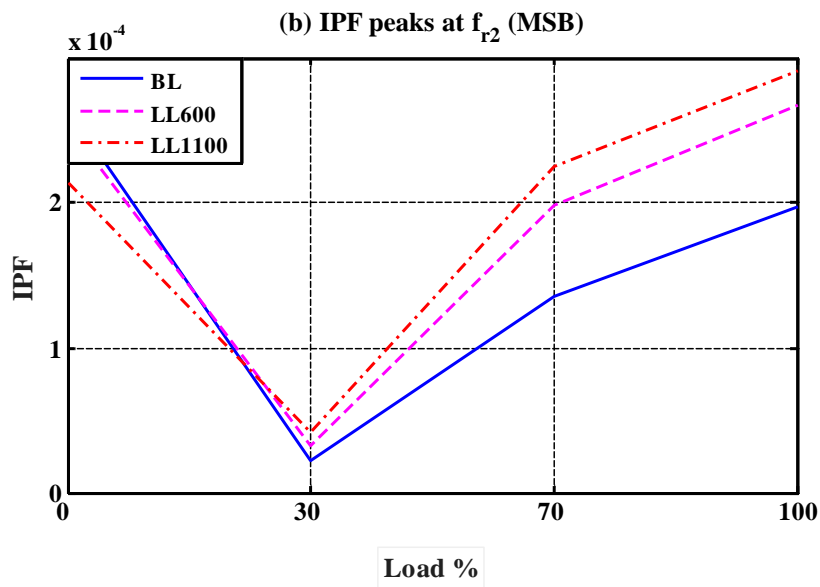
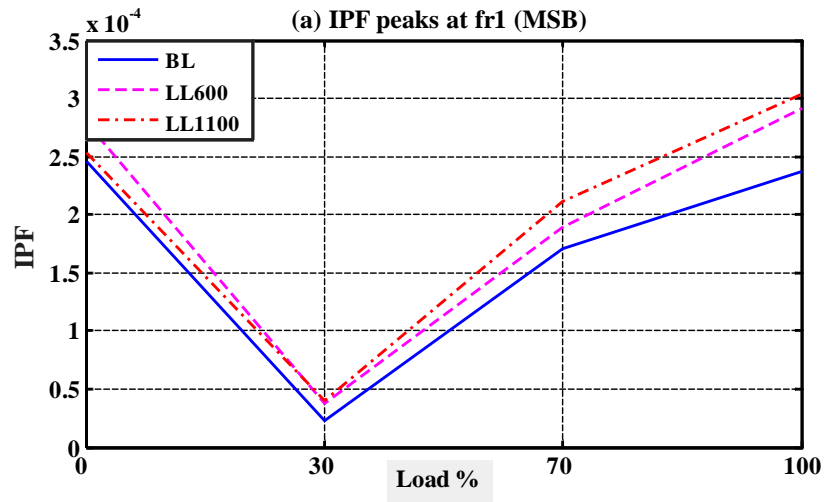


Figure 7-7: IPVC at characteristic frequencies

### 7.3.2 MSB Analysis

To investigate whether the IPF could be of further use in oil level detection, the signal was interrogated using the MSB which acts to suppress random noise in the signals and so help detect small changes in the feature frequency components. The derived MSBs were used to investigate the major gearbox frequencies, ( $f_{r1}$ ,  $f_{r2}$ , and  $f_{r3}$ ), see Figure 7.9.



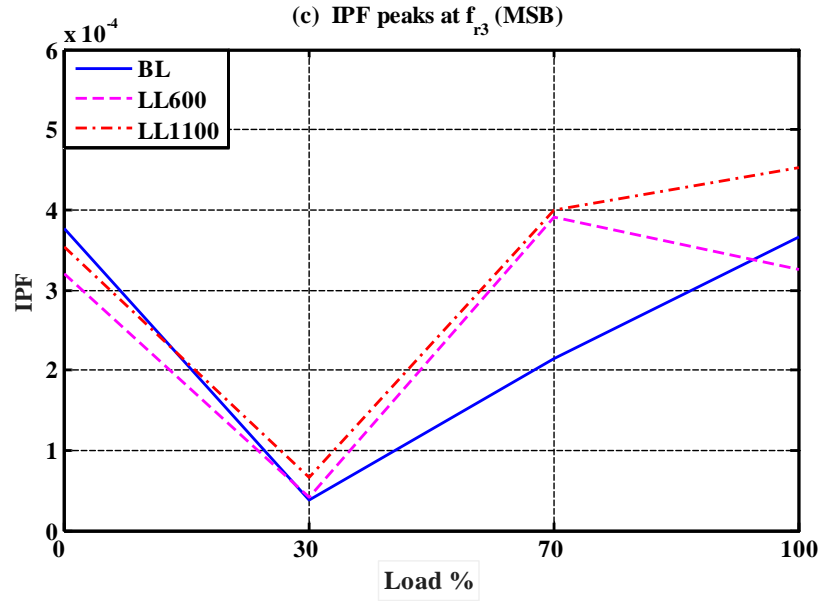


Figure 7-8: IPF MSB magnitudes at feature frequencies, ( $f_{r1}$ ,  $f_{r2}$  and  $f_{r3}$ ), for four loads and three lubrication levels

MSB amplitudes were determined at each of the three major gearbox frequencies, ( $f_{r1}$ ,  $f_{r2}$ , and  $f_{r3}$ ), for the three lubricant levels and the four loads. Figure 7.9 (a) shows the MSB amplitudes for  $f_{r1}$ . Differentiation of oil levels is good at higher loads but not at low loads. Because  $f_{r1}$  is coupled to the induction motor driving the systems, the changes in  $f_{r1}$  will be also due to any changes in motor speed in addition to the influence of the lubricant level in the gearbox. This effect appears to outweigh the effect of change in oil level, so  $f_{r1}$  is not expected to be suitable for detecting and diagnosing oil level problems.

However,  $f_{r2}$  is the rotational speed of the shaft connecting  $Z_2$  to  $Z_3$ , and for the three levels of oil used should be entirely immersed in the oil and located inside the gearbox. Figure 7.9 (b) shows that at loads of 70% and above, the amplitude of the MSB correlates well with lubricant level. There are clear differences in the amplitudes with different levels of lubricant. However, for loads of 30% or less, the differences in levels are not significant. When the system is unloaded, the churning forces would be expected to be dominant under steady state conditions. The greater the quantity of oil the greater the mass of oil that is churned and the higher the forces opposing motion - the frictional force. This can be seen at zero load in Figure 7.9 (b), highest amplitude for  $f_{r2}$  occurs when the system contains maximum oil (2.6 litres) and minimum when the oil level is a minimum (1.5 litres).

For 30% load and above the amplitude of the MSB signal increases with load, and the amplitude decreases with increase in lubricant level. At these higher oil levels it would be expected that as the load increases so the frictional forces within the system also increase. Additionally, the frictional force would be expected to increase as oil level fell. The differences in the magnitudes of the MSB amplitudes can be correlated to the lubricant level inside the gearbox. It appears that  $f_{r2}$  could be an indicator of the need to top up the lubricant level in the gearbox.

The plot of the MSB amplitude for the output shaft frequency,  $f_{r3}$ , Figure 7.9 (c), shows the least consistent detection performance. This is because the output shaft connects the load to the gearbox outlet via a flexible coupling and is subject to relatively complex interactions between load and coupling as well as the dynamic behaviour of the gears. It appears that this frequency component is unlikely to be useful for diagnosing and detecting oil degradation faults.

### **7.3.3 Comparison between FFT and MSB**

It can be seen from Figure 7.9 that the application of the MSB technique gave much better differentiation of the signals than the FFT alone. It is believed that this is due to the much better noise suppression and the nonlinearity characterization that is obtained with the MSB. The MSB method had the advantage of enhancing the SNR by including signal phase interactions for more reliable and efficient diagnostic results. Moreover, it had the ability of constructing and preserving the signal magnitude as well as the phase information.

## **7.4 Key Findings**

- The average power factors for specific frequencies gave a good detection of oil shortage for the gearbox operating at higher loads.
- The spectral peaks at characteristic frequencies of gear rotational motion generate less diagnostic information as compared with that of IPVC.
- The IPVC yields better diagnostics in separating the oil shortages in wider operating conditions. This mainly because that IPVC is a summation of the two-phase quantities which enhances the signal to noise ratio and consequently the diagnostic performance.
- The use of MSB greatly improved the lubricant level detection capability based on IPF signal and made it possible to detect small changes in amplitudes corresponding to changes in oil level.

- The rotational frequency of the internal shaft,  $f_{r2}$ , obtained from MSB analysis of the IPF showed the best performance regarding determining lubrication levels in the gearbox because the gear at  $f_{r2}$  is at a higher speeds which are more sensitive to damping effects of lubricating oil changes.
- The rotational frequencies of the input and output shafts  $f_{r1}$  and  $f_{r3}$  respectively, were not found suitable for detecting or diagnosing lubricant levels.
- The utilization of the MSB improved the detection capability of the signal and made it possible to detect such small changes.

## **CHAPTER EIGHT: ELECTRICAL SIGNATURE BASED DIAGNOSIS OF INCREASED BEARING CLEARANCE**

---

*This chapter examines the detection of increased bearing clearance based on the MSB analysis of the electrical signals (motor current, voltage and power). It starts with an introduction to the increase in bearing clearances, then presents the fault simulations and test procedures for studying the influences of excessive bearing clearance. After that, it discusses the results obtained and analysed using FFT and MSB spectra, allowing for testing the capability of ESA in the detection of excessive bearing clearance. After that, both results obtained by the two methods are compared. Finally, the key findings are summarised.*

## 8.1 Introduction

Bearings are essential to rotating machinery by supporting rotating elements, including gear shafts. In addition to manufacturing errors and errors in assembly (e.g. excessive radial clearance), gradual wear will take place during the operation of the machine. This is the result of material loss due to metal fatigue and the removal of surface material due to the lubricant becoming contaminated with the material lost. Consequently, the dynamic behaviour of gears and bearings will vary during their lifetimes. Long-term operation of gears and bearings means the clearance will gradually increase, which means greater impacts when gear surfaces mesh, and this means strongly nonlinear effects appear in signals monitoring the system's behaviour [139]. However, such deterioration will affect not just one item, but several. Such behaviour is now considered a major challenge to fault detection using condition monitoring [145].

Thus, this chapter evaluates the capability of detecting the increase in bearing clearance, using ESA with signal processing tools of both FFT and MSB.

## 8.2 Effect of Bearing Clearance

Ball bearings are an essential component in rotating machines. They support rotating parts such as gear shafts which are invariably operated in extreme environmental conditions, and that makes them vulnerable of failure. According to a study [146], a change in bearing clearance can significantly affects the vibration signals, thermal, noise and load distribution in a bearing which affects bearing life. Thus, monitoring bearings is an important task.

An important factor that affects bearing performance is clearance, but this will systematically and inevitably increase with use, and will affect both the gear's dynamic behavior and system stability.

Normally, bearings are installed with some error in either, or both, the outer or inner races and this results an error in the clearance see Figure 8.2 [139, 147].

For defects in the outer race of a bearing, Bai et al., [5] have shown that the greater the clearance, the greater the resulting impact forces and the resulting wear, and the larger the amplitudes of the diagnostic features produced [147, 148]. Note that such increased clearances can induce torsional and transverse vibrations that could result in gear tooth separation that could lead to deterioration in durability and reliability of the gears. It was also shown, however, that for defects on the inner

race, the larger the clearance the less the amplitudes of the diagnostic feature produced. The level of vibration has a consequential effect on the electrical signals.

Imperfectly positioned bearings will cause an eccentricity resulting in an imbalance in radial forces, leading to a significant change in the stator and/or the rotor. However, even a bearing-shaft assembly supported by perfect ball bearings will still generate vibrational forces because of the variation in mechanical compliance as the bearing rotates. i.e. the ball bearing races will flex to a certain degree.

This eccentricity will feed back to the motor as a change in load, and produces unique spectral patterns that manifest themselves in the air gap flux that might contain stator current components according to the following expression [58]:

$$f_e = f_s \pm m f_r \quad (8.1)$$

where:  $f_e$  is the current components,  $f_s$  is the supply frequency,  $m$  is the harmonic number, and  $f_r$  is the rotational speed (frequency) of the rotor.

The rotational frequency components of the shaft in the two gearboxes can be calculated from the following equations (calculated at 70% of the full motor speed, which is around 1060 rpm):

$$f_{r1} = \frac{\text{Motor speed}}{60} = \frac{1060}{60} \cong 17.67 \text{ Hz}$$

$$f_{r2} = \left( \frac{z_1}{z_2} \right) * f_{r1} = \left( \frac{49}{55} \right) * 17.67 = 15.12 \text{ Hz}$$

$$f_{r3} = \left( \frac{z3}{z4} \right) * f_{r2} = \left( \frac{13}{59} \right) * 15.12 = 3.33 \text{ Hz} \quad (8.2)$$

$$f_{r4} = \left( \frac{Z_{i1}}{Z_{i2}} \right) * f_{r3} = \left( \frac{59}{13} \right) * 3.33 = 15.11 \text{ Hz}$$

$$f_{r5} = \left( \frac{Z_{i3}}{Z_{i4}} \right) * f_{r4} = \left( \frac{47}{58} \right) * 15.11 = 12.24 \text{ Hz}$$

As the fault was introduced on the first stage of GB2 (pinion gear), the frequencies of interest will be  $f_{r3}$  and  $f_{r4}$  as they are connected to the faulty bearing, which will be investigated.

### 8.3 Fault Simulation and Test Procedure

To assess the effect of the change in bearing clearance values, an experiment was performed using ESA (motor current, voltage and power), see Figure 8.1 for the test rig used. The rig consisted of a 15 kW Brook Crompton three-phase AC induction motor (type T-DA160LA) at 1460 rpm connected via two Radicon transmission two-stage helical gearboxes arranged back-to-back, and flexibly coupled by Fenner type HRC150H couplings to a Brook Hansen DC generator. Both motor and generator were controlled by a PLC (closed-loop control system) to operate automatically at set speeds and specified loads. Tests were performed for three different values (C2, C3, and C5) of clearance under the same conditions in the input shaft of the first stage of GB2. The aim was to examine the possibility of ESA diagnosing changes in the characteristics of the electrical signal as clearance increased.

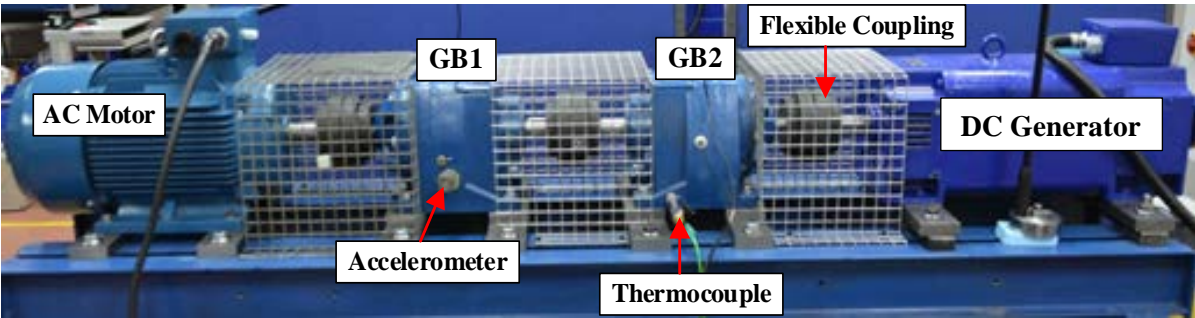


Figure 8-1: Mechanical elements of the test rig

The ball bearing used to support the drive gear ( $Z= 59$ ) of the first stage of GB2 was an SKF type 6207. The bearing was changed with different clearance values as described in the Table 8-1.

Table 8-1: Bearing clearance values

Condition	Deep Groove ball bearing 6207	Clearance value
Too small	C2	0.006 mm
Recommended/Baseline	C3*	0.028 mm
Too large	C5	0.051 mm

\* C3 is recommended value by the gearbox manufacture, which is considered as the baseline case. The specification of the bearing is shown in Table 8-2

Table 8-2: Bearing specifications

Principal dimensions	Value	
Inside Diameter, (d)	35.0 mm	
Outside Diameter, (D)	72.0 mm	
Race Width, (B)	17.0 mm	
OD Inner Ring ( $d_1$ )	46.9 mm	
ID outer ring ( $D_2$ )	62.7 mm	
Chamfer ( $r_{1,2}$ )	1.1 mm	

Figure 8.2 represents the clearance between the inner race, the ball, and the outer race of the ball bearing.

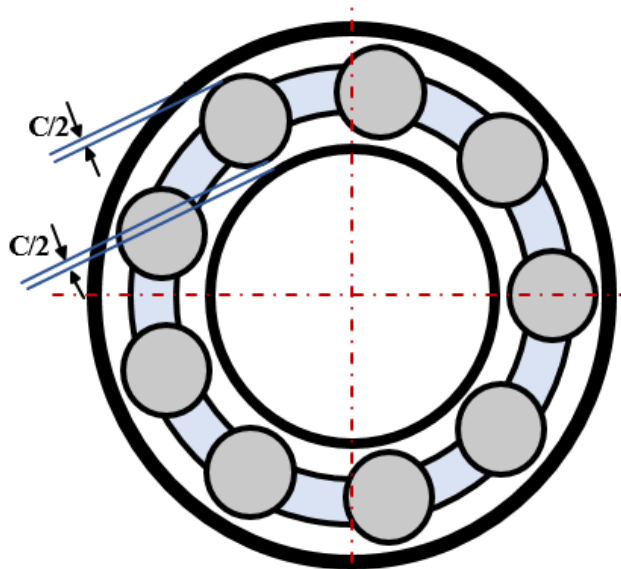


Figure 8-2: Schematic diagram of deep groove ball bearing

Induction motor, DC generator specifications (from the data sheet) are given in Chapter 4. Tables 4-1, 4-2. Specification of the gears are presented in Table 8-3.

**Table 8-3: First gearbox specifications**

Description	GB1 input shaft 1	GB1 output shaft 3
Number of teeth	$Z_1/ Z_2 = 49/55$	$Z_3/ Z_4 = 13/59$
Reduction ratio	1.224	4.5385
Centre Distance	74.0 mm	74.0 mm
Shaft diameter	24.0 mm	39.5 mm
Normal pitch	1.25mm	2.00 mm
Helix angle	$\beta_1=13$	$B_2=27$
Pressure angle	$\alpha =20^\circ$	$\alpha =20^\circ$
Module	$M_1=2.0$ mm	$M_2=1.25$ mm
Working face width	$b_1=25.0$ mm	$b_2=26.0$ mm
Contact ratio	$\epsilon_{a1}=1.521$	$\epsilon_{a2}=1.669$
Overlap ratio	$\epsilon_{b1}=1.289$	$\epsilon_{b2}=2.89$

**Table 8-4: Second gearbox specifications**

Description	GB2 input shaft 3	GB2 output shaft 5
Number of teeth	$Z_1/ Z_2 = 59/13$	$Z_3/ Z_4 = 47/58$
Increase ratio	4.5385	0.8103
Centre distance	74.0 mm	74.0 mm
Shaft diameter	39.5 mm	24.0 mm
Normal pitch	2.0 mm	1.25 mm
Helix angle	$\beta_1=27^\circ$	$B_2=13^\circ$
Pressure angle	$\alpha =20^\circ$	$\alpha =20^\circ$
Module	$M_1=2.0$ mm	$M_2=1.25$ mm

Working face width	b1=36.0 mm	b2=25.0 mm
Contact ratio	$\epsilon_{a1}=1.469$	$\epsilon_{a2}=1.45$
Overlap ratio	$\epsilon_{b1}=1.289$	$\epsilon_{b1}=2.89$

The gear schematic diagram is presented in Figure 8.3. The bearing on Pinion 3 was replaced with the three tested bearings of Table 8-1 one-by-one when fully opening the gearbox.

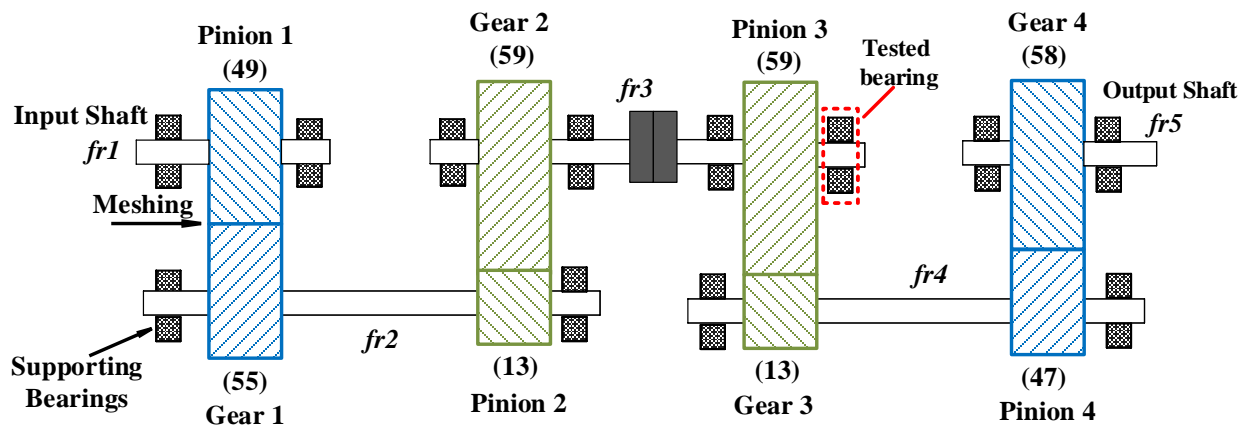


Figure 8-3: Schematic diagram of gear arrangement used in the test

The test rig was implemented under two different speeds; 50% and 70% of the rated speed under the load set to 0%, 25%, 50%, 75% and 100% of the full load as represented in Figure 8.4.

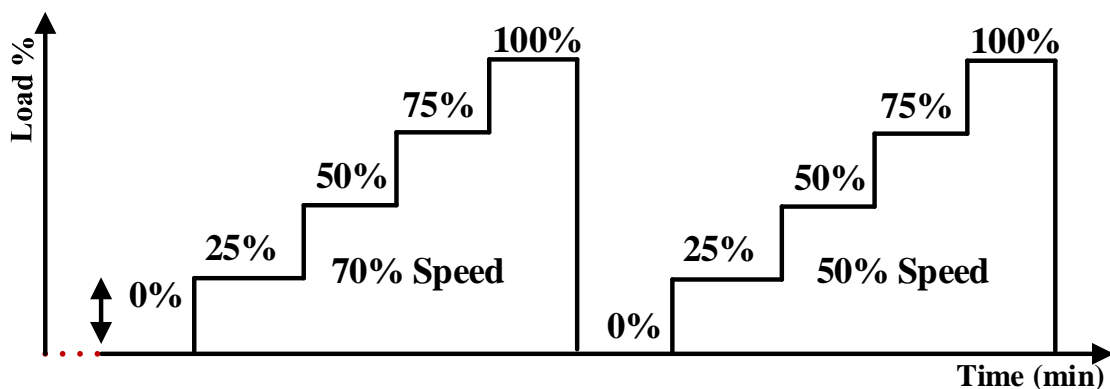


Figure 8-4: Schematic diagram of operating condition profiles

Each load set to run for two minutes then automatically changes to the step after using a PLC controller.

Six sensors were used for three-phase currents and voltages to record the electrical measurements. The data was recorded using a high speed GST YE6232B DAQS which collects signals from sensors with maximum sampling frequency rate of 96 kHz. (Test rig schematic diagram, specifications and more details about the test procedure were previously provided in Section 4.2 and Section 6.3).

The data collected through the acquisition system was transferred to a PC to be processed and analysed in time- and frequency-domains using a MATLAB program. A shaft encoder was connected directly to the data acquisition system to measure the motor angular speed.

## 8.4 Results and Discussion

### 8.4.1 Spectrum Analysis

In order to detect and diagnose change in bearing clearances, the signals were measured from three phase measurement unit to measure the three phase electrical signals using Hall Effect current and voltage transducers. Attained signals were recorded then sent to a PC to be analysed in either time or frequency domain. Recorded data was first analysed using the FFT to extract features information of the gear rational frequency components. Sideband extraction equations is as presented in the following equations:

$$f_{r1sb} = f_s \pm m f_{r1} \quad (8.3)$$

$$f_{r2sb} = f_s \pm m f_{r2} \quad (8.4)$$

$$f_{r3sb} = f_s \pm m f_{r3} \quad (8.5)$$

$$f_{r4sb} = f_s \pm m f_{r4} \quad (8.6)$$

$$f_{r5sb} = f_s \pm m f_{r5} \quad (8.7)$$

where,  $f_s$  is the supply frequency,  $f_r$  is the rotational speed of the rotor,  $m = 1, 2, 3, \dots$  and represents the number of harmonics,  $f_{r1}, f_{r2}, f_{r3}, f_{r4}$  and  $f_{r5}$  represent the shaft rotational frequencies.

However, the fault was introduced on pinion 3 (GB2); which is directly connected to  $f_{r3}$ , and also linked with  $f_{r4}$ . Thus, investigating these frequency components with their associated frequency sidebands will give an indication to the fault existence. Therefore, the presented work in this chapter will focus only on  $f_{r3}$  and  $f_{r4}$  components.

Current, voltage and power spectra are shown in Figures 8.5, 8.6, and 8.7, respectively for different bearing clearances under different load conditions and at 70% of the full speed, a considerable increase in the amplitude of the sidebands with increase of load and fault severity.

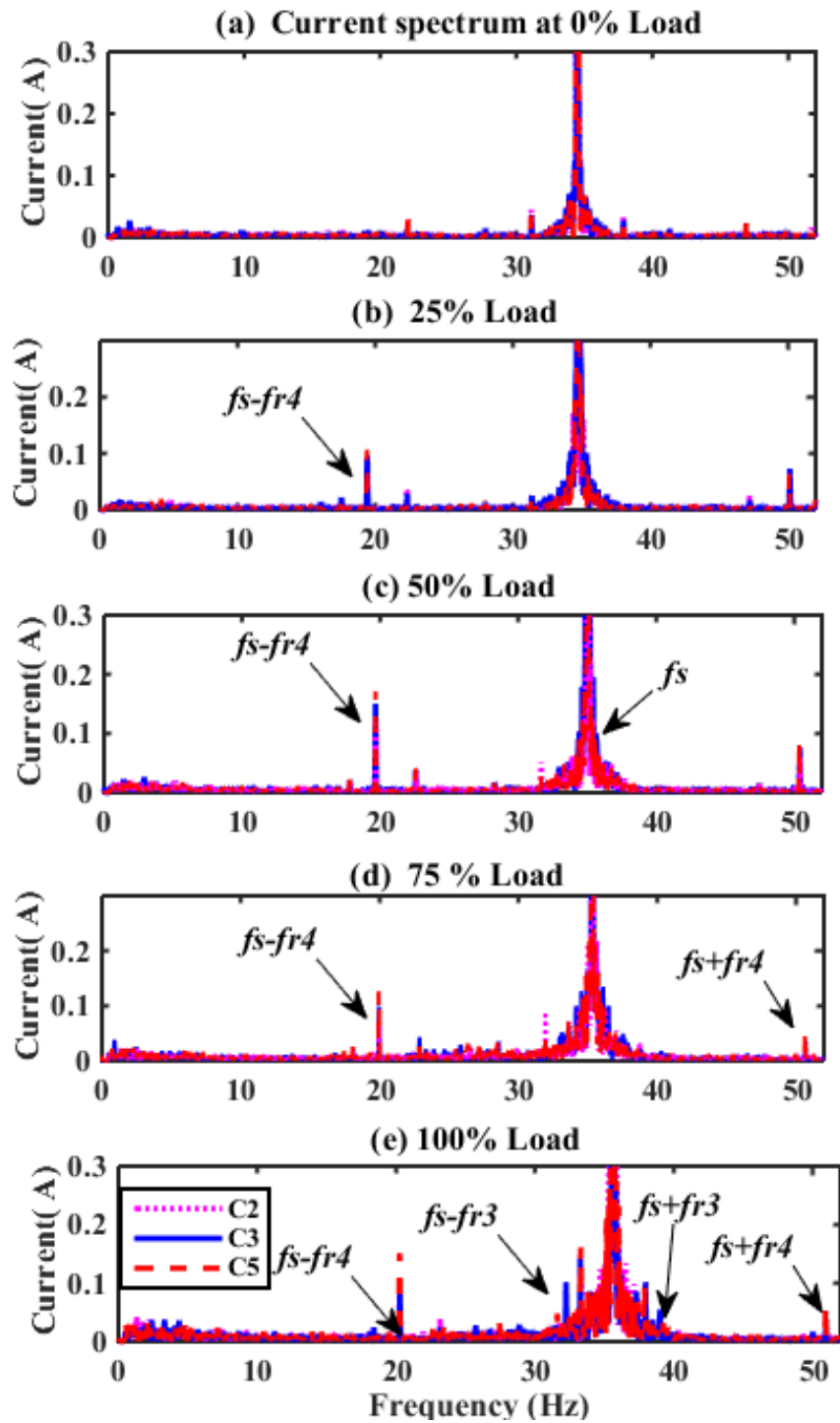


Figure 8-5: Current signal spectra at different loads and 70% of full speed for three bearings

These sidebands confirm the modulation of the current signal by the load fluctuations generated by the clearance fault. Moreover, more characteristics features are exhibited by the power spectrum as the power is the multiplication of the current and voltage signals.

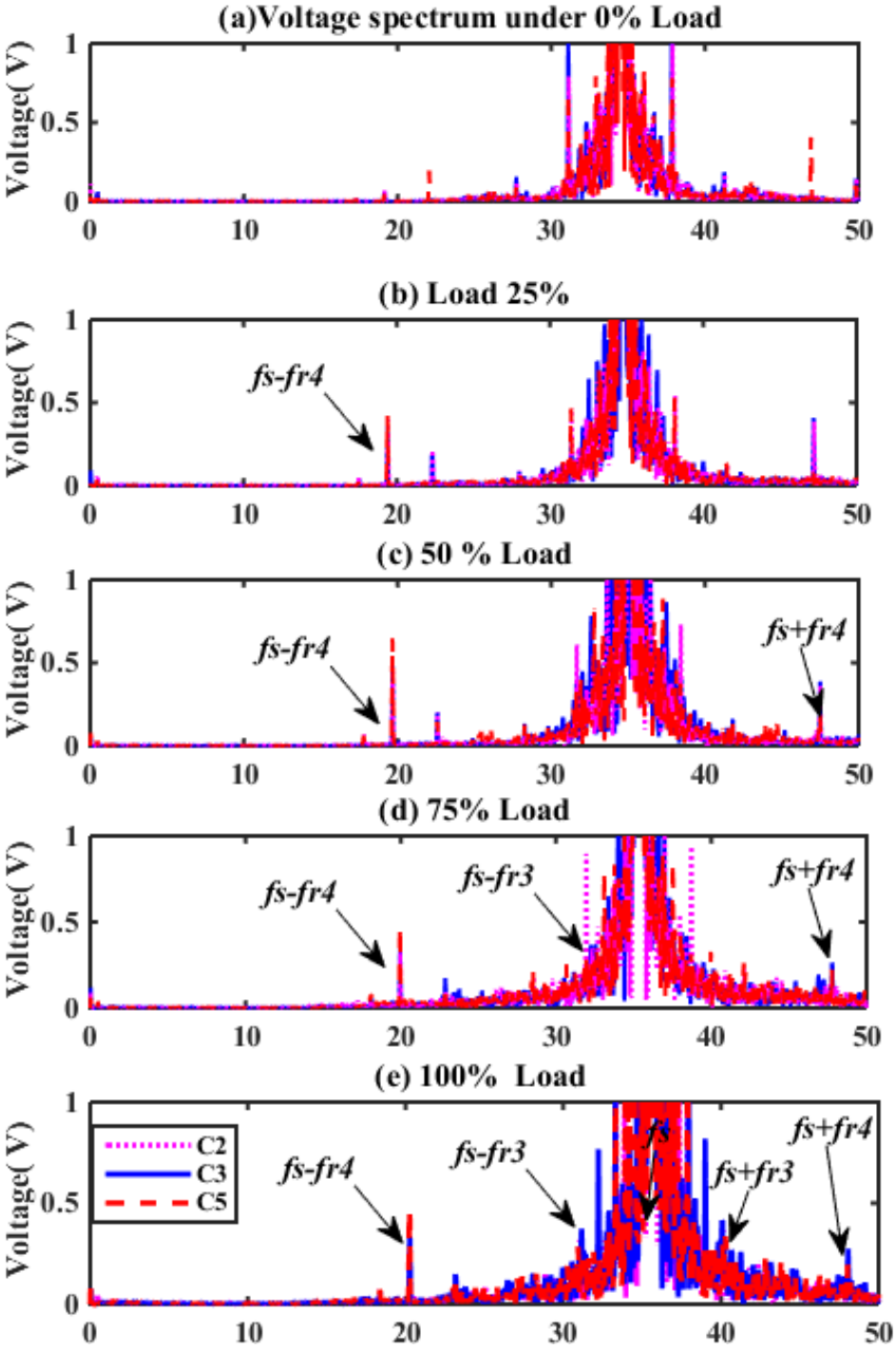


Figure 8-6: Voltage signal spectra at different loads and 70% of full speed for three bearings

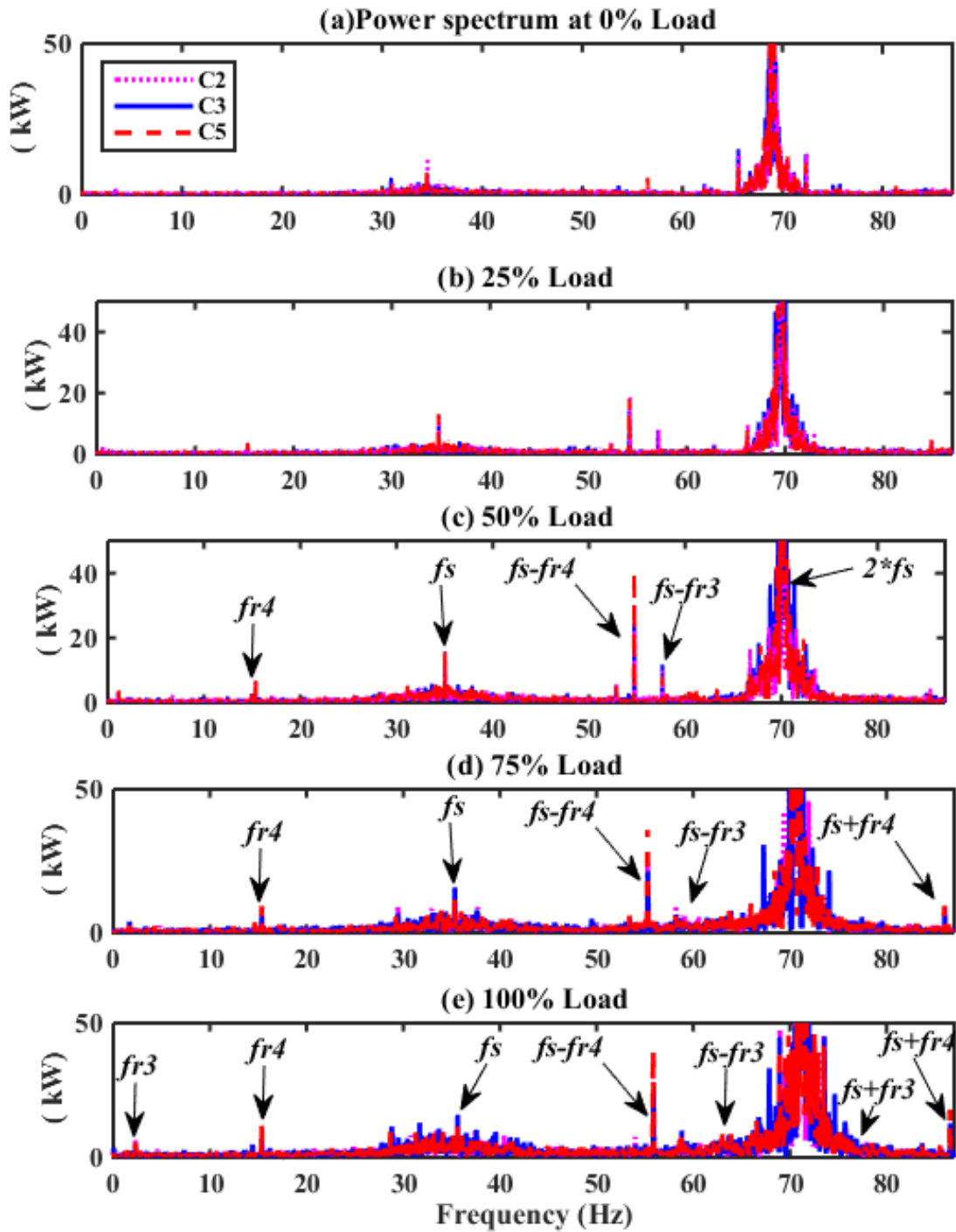


Figure 8-7: Power signal spectra at different loads and 70% of full speed for three bearings

Considering Figures 8.5, 8.6 and 8.7 we see more characteristic features exhibited by the power spectrum (including  $fr_3$ ,  $fr_4$ ) than for current and voltage, as the power is the product of current and voltage.

As the bearing fault was introduced into the first stage of GB2, only the peaks at  $fr_3$  and  $fr_4$  will be investigated as they are directly related to the faulty bearing. The current peak magnitudes for  $fr_3$  and  $fr_4$  are presented in Figures 8.8, 8.9, respectively. It can be seen that the frequency peak components  $fr_4$  exhibit a clearer and more distinct features trend, in which the bearing clearance of C5 was the dominant peak.

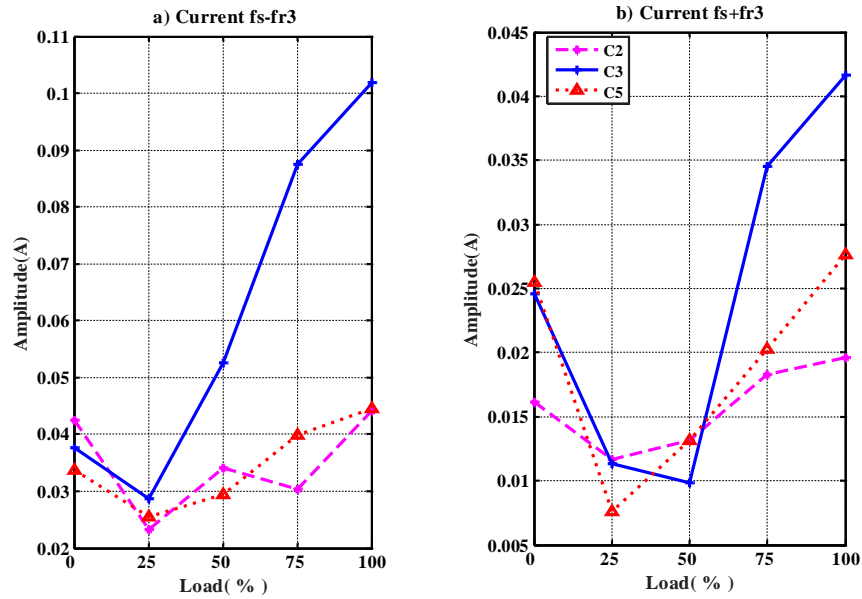


Figure 8-8: Amplitude of current peaks of sidebands at  $fs \pm fr_3$  obtained using FFT

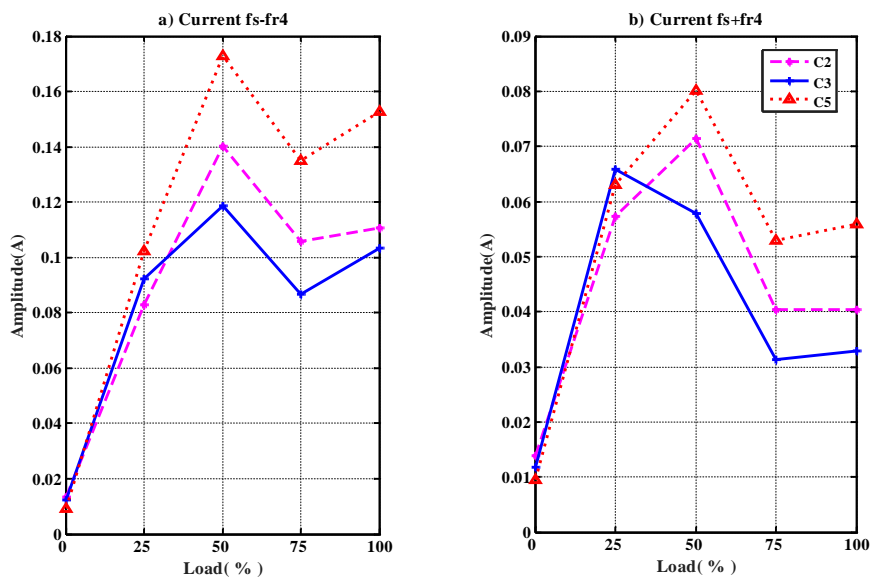


Figure 8-9: Amplitude of current peaks of sidebands at  $fs \pm fr_4$  obtained using FFT

Similarly, the amplitudes of the sidebands around  $f_s$  ( $f_s \pm fr_3$  and  $f_s \pm fr_4$ ) in the voltage spectrum obtained using FFT, shown in Figures 8.10 and 8.11, present a good fault identification at  $fr_4$  but an inconsistent trend for  $fr_3$ .

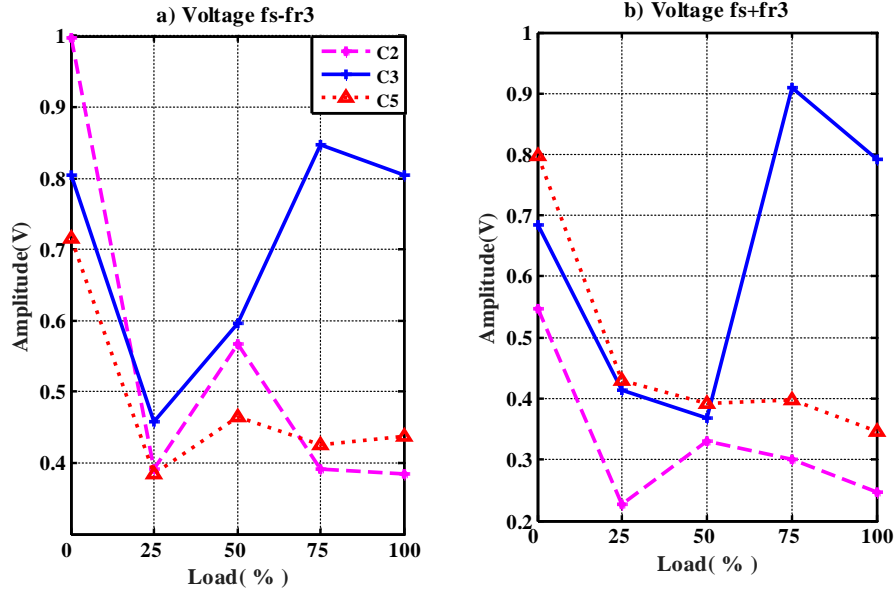


Figure 8-10: Amplitude of voltage peaks of sidebands at  $f_s \pm fr_3$  obtained using FFT

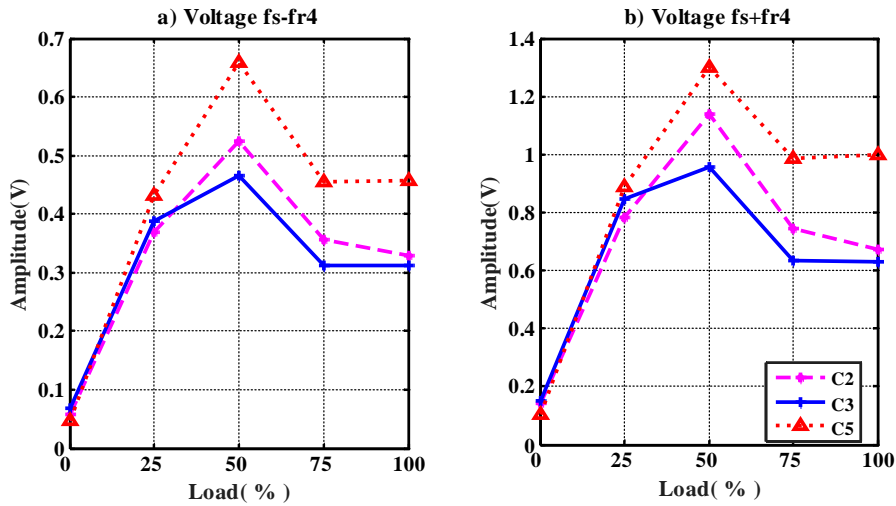


Figure 8-11: Amplitude of voltage peaks for sidebands  $f_s \pm fr_4$  obtained using FFT

The power spectral amplitudes for  $2f_s \pm fr_3$  and  $2f_s \pm fr_4$  (as the power is twice the supply frequency) are presented in Figures 8.12 and 8.13. It can be seen that the averaged peaks at  $fr_4$  show an enhanced trend as the power signals are the result of multiplying the current and voltage.

As would be expected, it should be noted that in all six figures the signatures present a lower response at low loads.

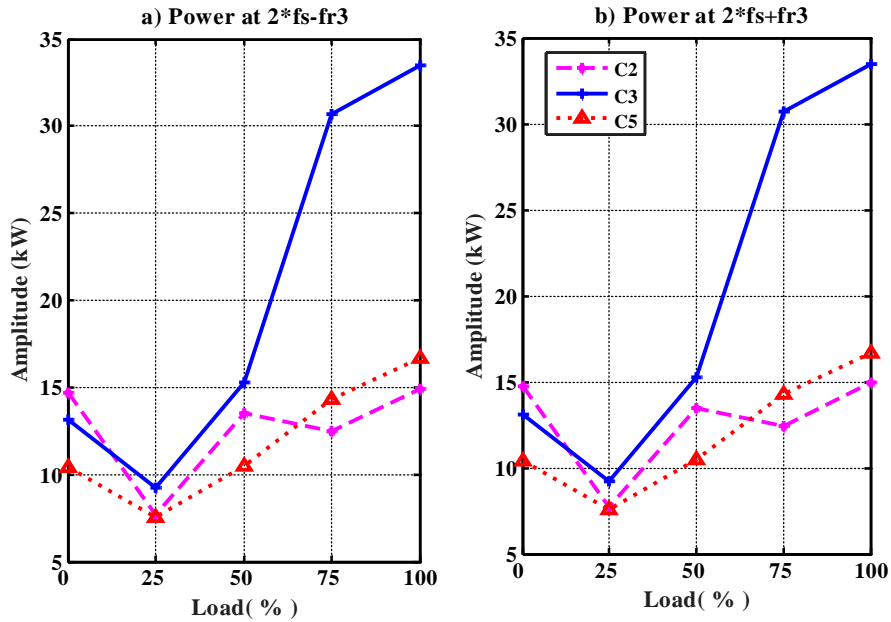


Figure 8-12: Amplitude of power peaks of sidebands at  $2f_s \pm fr_3$  obtained using FFT

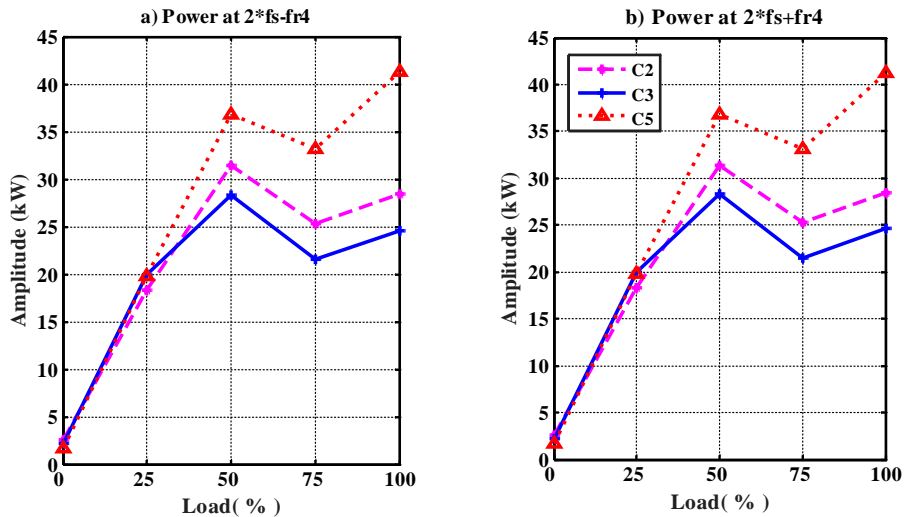


Figure 8-13: Amplitude of power peaks for sidebands  $2f_s \pm fr_4$  obtained using FFT

However, it should be mentioned that features provided by the FFT analysis are overlapping which might be caused by the installation errors and the noise caused by the drive. As the fault severity increases, the noise will accordingly increase.

### 8.4.2 MSB Analysis

For further assessing the complex effects of the change in clearance on the electrical spectrums, the modulated signals were subjected to Higher Order Spectral analysis. To accurately characterise the signals, the MSB signal processing was used as it has the advantage of suppressing the background (Gaussian) noise so that the extracted features are more clearly seen.

The features shown in this section were extracted at 70% of the full speed. Thus, the supply frequency “ $f_c$ ” is about 35 Hz; which is different from the frequency values used in the previous chapters.

Figure 8.14 presents the current MSB magnitude with its bicoherence for the baseline condition (C3) at 70% of full speed and under full load. Distinctive peaks can be seen at the bifrequencies of (3.35 Hz, 35.3 Hz), (17.67 Hz, 35.3 Hz), with the highest peak at (15.37 Hz, 35.3 Hz). These are all related to shaft oscillations caused by the presence of the fault and these peaks can undoubtedly be used in detecting excessive bearing clearance.

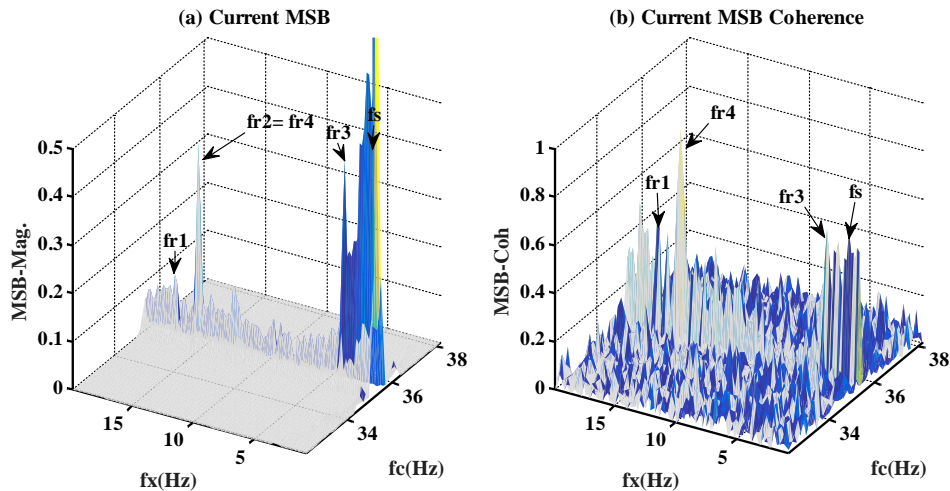


Figure 8-14: Current MSB at 70% full speed and full load for the baseline condition of C3 bearing.

The current MSB with its corresponding bicoherence for the faulty case of C5 bearing at 70% of full speed and under full load is shown in Figure 8.15. Similar to the previous figure, distinctive peaks can be seen at the bifrequencies (3.53 Hz, 35.3 Hz), (17.12 Hz, 35.3 Hz), with the highest peak at (15.53 Hz, 35.3 Hz). It is clear that the peaks for C5 bearing are higher than those for the baseline case (C3), confirming the effect of the increase in bearing clearance on the current signal.

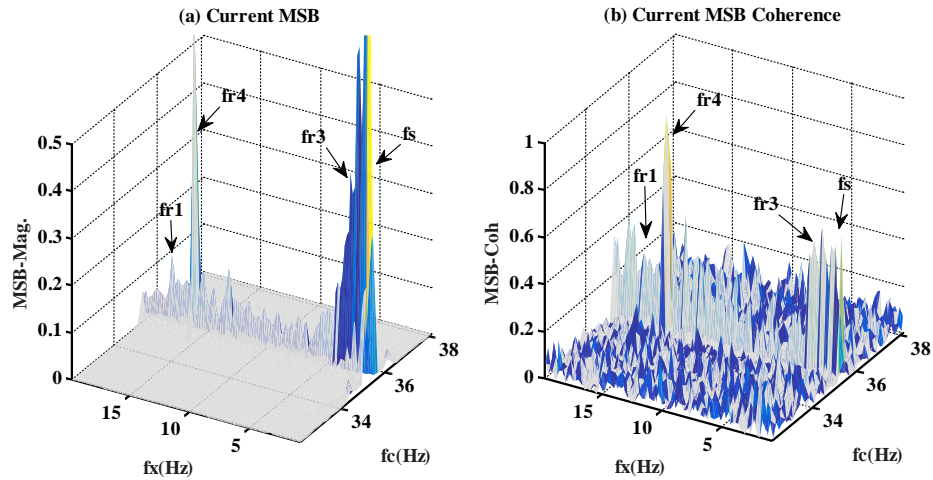


Figure 8-15: MSB at 70% speed and full load with C5 bearing

Figure 8.16 represents the MSB results for both voltage MSB and its coherence for the baseline case. The same distinctive peaks appear clearly at the same bifrequencies as for the MSB for current, and can be used in fault diagnosis.

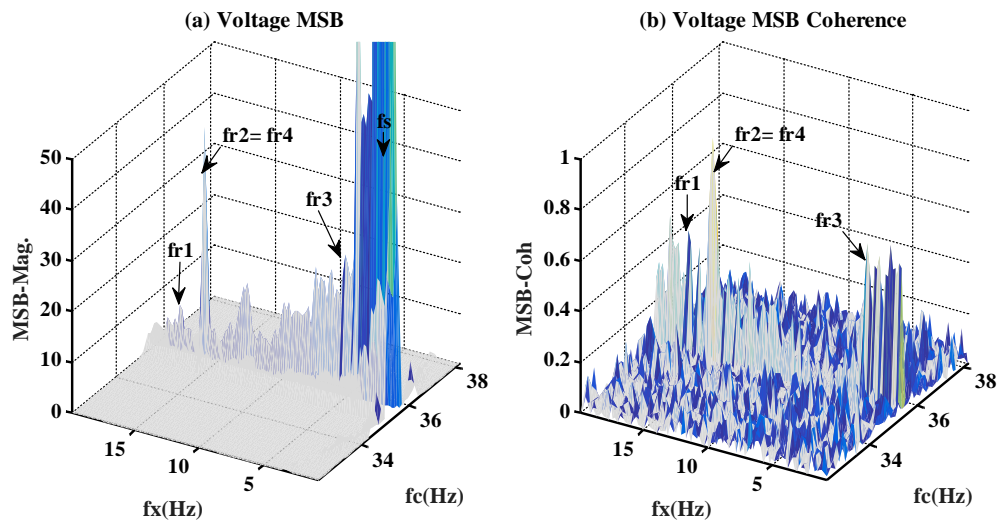


Figure 8-16: Voltage MSB at 70% full speed and full load for C3 bearing.

The voltage spectra for the faulty case with fault C5 are shown in Figure 8.17 under the same operating conditions and we observe the same distinctive peaks. This graph also clearly shows that the MSB based voltage signal is generally higher than those of the current, which means that the MSB for the voltage signals is more sensitive to the presence of a fault because the VSD tends to regulate the terminal voltage to compensate for any differences that might be caused by the presence of a fault, as mentioned above in Section 5-6.

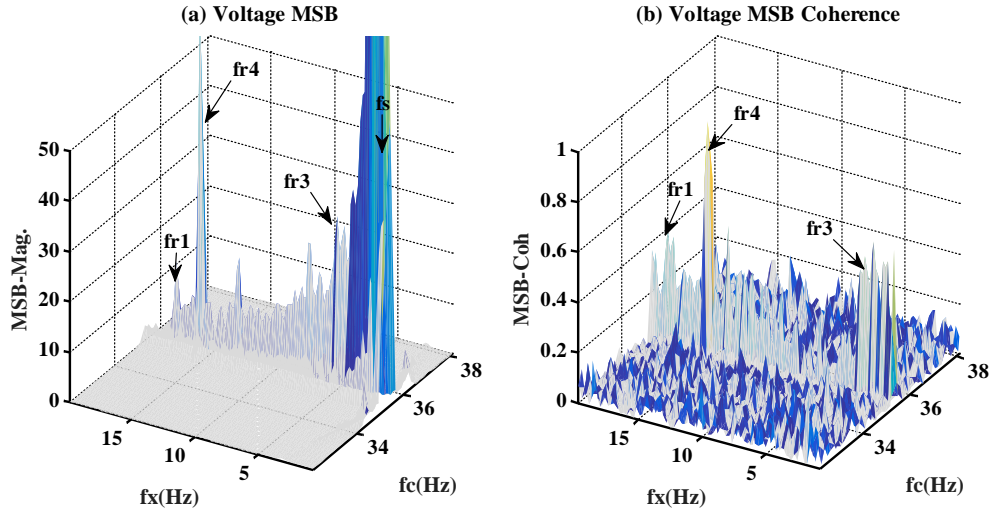


Figure 8-17: Voltage MSB at 70% speed under full load with C5 bearing

The MSB analysis of the power signal shows the same rising trend of MSB peaks with the fault severity as those of the current and voltage signals, which is illustrated in Figure 8.18. For the healthy case, a major peak can be found at about (15.55 Hz, 70.5 Hz) and a second peak at (3.60 Hz, 70.5 Hz), in addition to the supply frequency component at  $2 \times f_s$ . The peaks are significantly increased in the coherence in term of amplitudes.

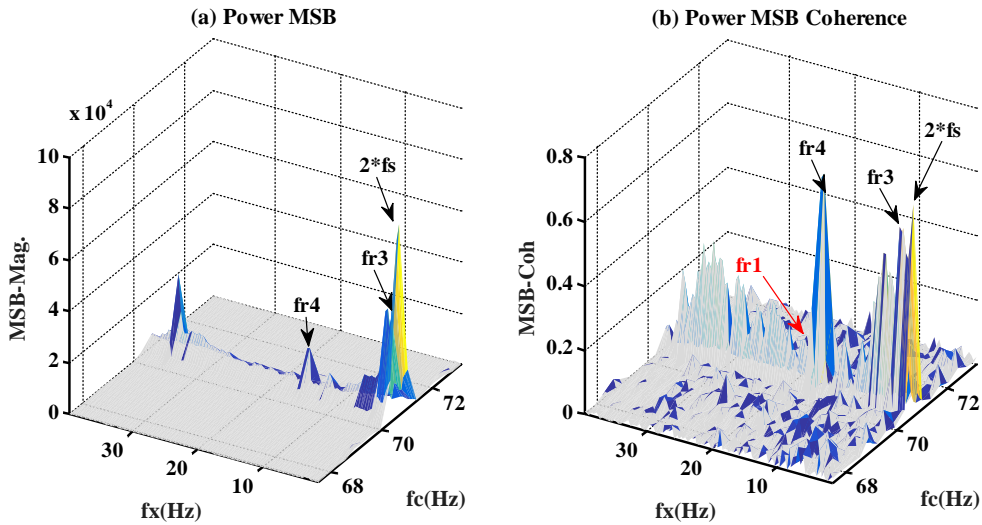


Figure 8-18: Power signal MSB at 70% of full speed under full load for C3 bearing.

Figure 8.19 is the corresponding MSB power spectral analysis of bearing with clearance condition C5. It can be seen that in this figure the peak characteristics are more clearly discernible, which confirms that the MSB based power signature is the most sensitive of the three electrical signatures to the fault, with a considerable increase in the peak values in the power MSB and coherence.

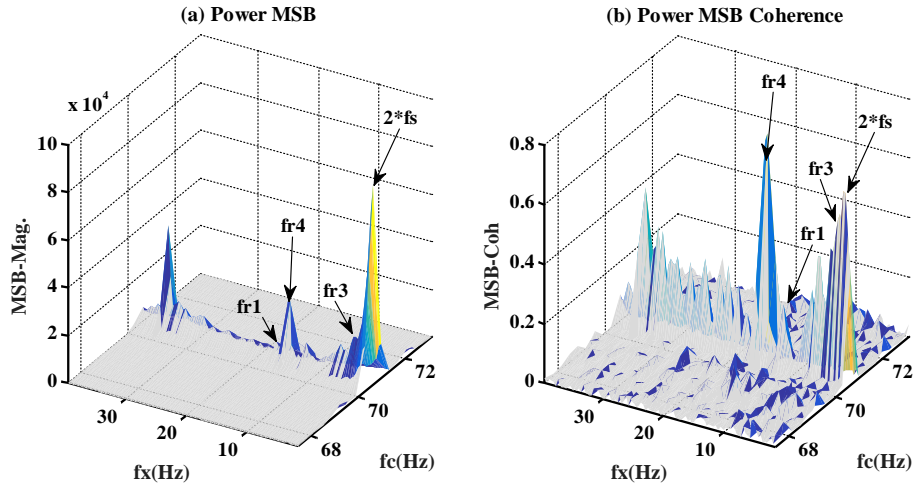


Figure 8-19: Power signal MSB magnitudes at 70% of full speed under full load for C5 bearing. As the faults were introduced on the bearing that supports the pinion gear of the first stage in GB2 (see Figure 8.3), the main focus here will be on frequencies  $f_{r3}$  and  $f_{r4}$  as they are directly related to the faulty bearing.

Figures 8.20, 8.21 and 8.22 respectively represent the average of the peaks extracted from the current, voltage and power signals, at  $f_{r3}$  and  $f_{r4}$  for the MSB analysis.

Even though the current and voltage signatures show a good separation between the different fault cases especially at  $f_{r4}$ , the trend tends to be inconsistent and overlapping. However, the power signals exhibit a consistent change with the load increment, confirming that the power signature is better in fault detection and diagnosis than either the current or voltage.

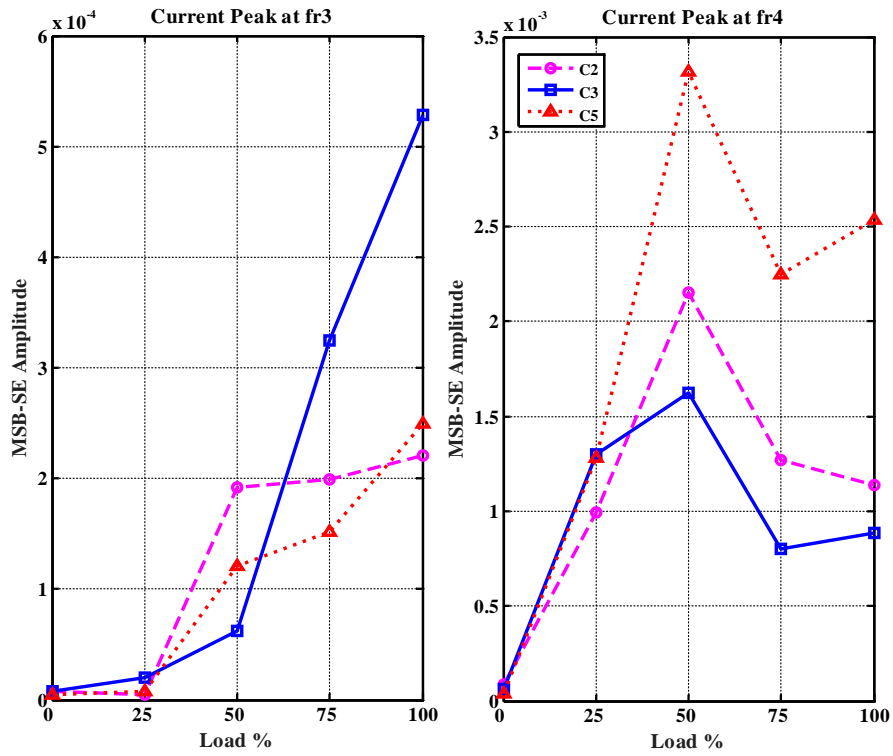


Figure 8-20: Current signal at fr3 and fr4

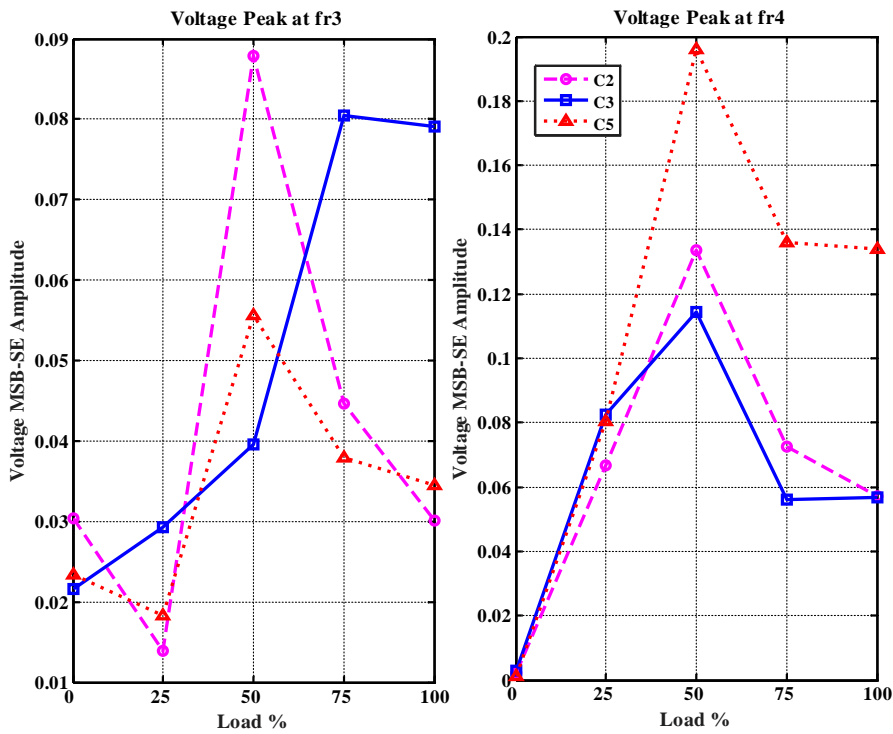


Figure 8-21: Voltage MSB peaks at fr3 and fr4

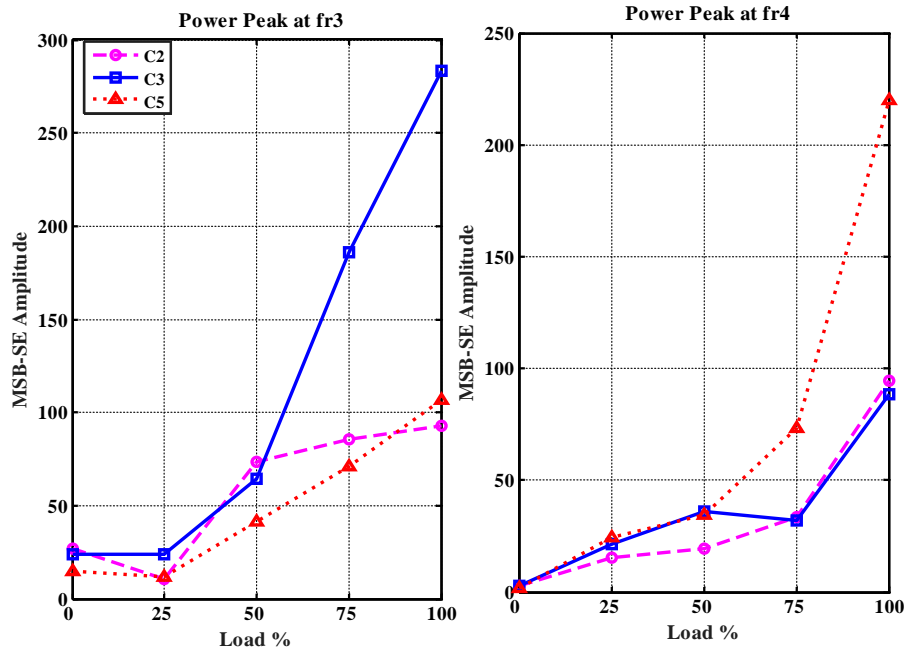


Figure 8-22: Power signal MSB peaks at fr3 and fr4

### 8.4.3 Comparison between Spectrum and MSB

The performance of the FFT and MSB techniques based on the three different signatures; current, voltage and power was compared for the baseline and the two faulty cases.

The peaks indicative of the presence of a fault increased in magnitude with fault severity for both of FFT and MSB analyses. As was demonstrated, the voltage peaks in Figures 8.10, 8.11, 8.16, 8.17 and 8.21 exhibited greater magnitudes compared to the corresponding peaks in the current signals in Figures 8.8, 8.9, 8.14, 8.15 and 8.20. This is explained by the fact that the VSD acts more on the voltage than the current; in attempt to maintain a constant system speed, the VSD compensates for any differences in the torque component as a result of the presence of a fault.

However, the FFT did not completely differentiate between the three fault cases. As there was an overlapping between the cases. However, a better and more consistent differentiation is obtained between the faults using the power signature and MSB analysis. This is because of the MSB's ability to reduce background noise, enhance modulation and provide a more consistent trend with increase in fault level.

## 8.5 Key Findings

This chapter has investigated the effectiveness of using electrical signatures in detecting and diagnosing increased bearing clearance values; first using the FFT and then the MSB to suppress the background noise for a more reliable diagnosis. An abnormal bearing clearance can cause an eccentricity and increased central distance between the gear pair, which eventually leads to poor mesh quality and more oscillatory motion and load to the motor. As such it will generate a corresponding modulation in the current and voltage signals in the VSD system.

- FFT analysis is able to detect the excessive bearing clearance; however, features extracted were overlapping and noisy.
- MSB analysis proves to produce stable results in detecting the excessive clearance because of its property of suppressing random noise. Moreover it can present the complicated modulated signals clearly and reliably.
- Spectral peaks at rotational frequency components can provide the diagnostic information to identify which bearing may have problems.
- The power signature provides slightly more consistent results than those of the current and the voltage alone.

## **CHAPTER NINE: CONCLUSIONS AND FUTURE WORK**

---

*The achievements and conclusions drawn from this research project are summarized. In this chapter, the contributions to knowledge are presented. Finally, recommendations for further researches in the CM of gear transmission systems are suggested.*

## 9.1 Objectives and Achievements

The aim of this study is to develop a new and efficient method for fault detection and diagnosis of machine faults using electrical signatures in a sensorless VSD system. Specifically it has rigorously evaluated the state of art MSB analysis and the generalised instantaneous information based on a series incipient faults of downstream gearboxes driven by the AC motor controlled with a sensorless VSD, which has filled the gaps of using ESA to a great degree. A summary of the objectives and the key achievements of this research work is as follows:

**Objective 1:** Provide an overview of the principles of the induction motors and sensorless VSDs.

**Achievement 1:** An overview of the principles of induction motors has been provided, also the theory of AC drives has been presented in depth. Different conventional methods used to control torque and speed were reviewed. Detection based on sensorless VSDs was discussed.

**Objective 2:** Implement an experimental programme for the practical investigation of different faults; gear tooth breakage, different lubricant levels, and excessive bearing clearance, for different degrees of fault severity under different operating conditions.

**Achievement 2:** The experimental facilities; rig components, data collection procedure and data analysis were explained. An industrial two-stage helical gearbox transmission system driven by a sensorless VSD was used as the test rig. Further, fault simulation was discussed. Three different experimental procedures for testing system response to seeded faults under different operating loads and speeds were implemented. The seeded faults were gear tooth breakage, insufficient lubricant and a slack bearing.

**Objective 3:** Apply a new signal processing technique, MSB, to analysis the data obtained from the test rig in order to examine its capability for fault detection.

**Achievement 3:** The collected data for electrical signatures was first analysed using FFT and then MSB. A comparative investigation including MCSA, MVSA, MPSA, IPF and IVPF signatures was carried out.

**Objective 4:** Investigate and compare different CM signatures; current, voltage and power obtained under sensorless control for the detection of different mechanical faults under different loading conditions, with particular attention paid to the capability of the system to detect small degrees of mechanical faults.

**Achievement 4:** A comparison between the electrical signatures was completed to evaluate the detection performance and make the research work more effective.

**Objective 5:** To study the mathematical model for three-phase induction motor with the field oriented control (FOC) drive with different mechanicals faults under different operating conditions, by using a ready-to-use software package “MATLAB/Simulink”. To examine the response of the model to the different faults under different loads and speed conditions.

**Achievement 5:**

The theoretical model of an AC IM driven by a sensorless VSD was presented in Chapter 5. The IM model was introduced first, followed by the model for open-loop control and lastly the model for FOC. The effect of mechanical load oscillations on electrical parameters and the detection of the fault based on sensorless VSDs were discussed in depth. Finally, results from the model were compared to those from the test rig, and the verification process showed that predicted and experimental results exhibited reasonably similar behaviour.

**Objective 6:** Apply different signal processing methods to extract faults features for use in detection.

**Achievement 6:** Conventional power spectrum signal processing was used first, and then the MSB which provided a more accurate and reliable diagnosis.

**Objective 7:** Detect and diagnose different mechanical faults (including tooth breakage, low lubricant levels, and excessive bearing clearance) in a two-stage helical gearbox using both FFT spectrum analysis and MSB bispectrum analysis.

**Achievement 7:** Chapters 6, 7, and 8 present the signal features due to mechanical faults that were extracted. Sideband characteristics were found to be particularly useful when investigating the effect of load oscillations due to faults on the electrical signals of a motor.

## 9.2 Conclusions

This study has investigated the detection and diagnosis of three different mechanical faults by analysing the electrical signals from a sensorless VSD system using the FFT and an advanced signal processing method, MSB. The work can be summarized in the following conclusions:

- Unlike traditional drives, sensorless VSDs respond to changes in rotor system dynamics by changing the IM current and/or voltage to adjust the motor speed to maintain performance. Thus information concerning the IM can be obtained by analyzing the current

and voltage signals. However, at its simplest there will be a high level of background of noise so extraction of useful data is not simple.

- The literature review revealed that ESA is gaining considerable interest, but that most studies have been concerned with open-loop or direct control; fault detection and diagnosis of electro-mechanical systems controlled by sensorless VSDs have been given substantially less attention which is a major oversight given the wide use of sensorless VSDs in industry.
- It has been shown that voltage signals correspond more closely than current signals to changes (faults) in the mechanical system. This characteristic is credited to voltage control being the final loop in the control system and hence will encompass a wider bandwidth than any other loop.
- Mechanical system defects (faults) generate oscillations in load which have an impact on the speed of the IM. These oscillations can be seen clearly in the spectrums of the electrical signals. The drive attempts to keep the speed of the IM close to the specified reference and so will change motor current and terminal voltage (and frequency, depending on the control system used) to counteract the change caused by the defect.
- Three faults were seeded into an IM driven system; the first was a broken tooth on a gear, the second was excessive bearing clearance, and the third was a deficiency in lubricant.
- In all tests, the stator current, voltage and power spectra showed an increase in sideband amplitudes with load and fault severity increase under sensorless operation.
- The tooth breakage could be detected using FFT analysis. Changes in the power spectrum were able to consistently separate the different levels of fault severity. Compared to the FFT, the MSB made the spectral differences even more clear, and the diagnosis more reliable and accurate. The voltage MSB provided greater definition than the current.
- Regarding lubricant shortage, the spectra for typical voltage and current signals can be seen in reveal a significant number of higher order harmonics of the 50 Hz supply against a high level of background noise. In addition, the spectral peaks associated with the IPF at the characteristic gear rotation frequencies provided less diagnostic information than IPVC which was able to separate the severities of the two reduced lubricant levels. This is ascribed to the IPVC being the sum of the individual current and voltage phases (see Equation 3.6) which improves diagnostic ability by enhancing the SNR. However, it was

a spectral peak at  $fr_2$  (the rotational frequency of the internal shaft) in the IPF spectrum as obtained using MSB analysis, that showed the best performance in determining lubrication levels. The frequencies  $fr_1$  and  $fr_3$  corresponding to the rotation of the input and output shafts respectively, were not useful for detecting or diagnosing inadequate lubrication. Using MSB was a great improvement in the ability to detect lubricant level, and using the IPF signal relatively small changes in oil level could be detected.

- Features given by the rotational frequency components can provide a good indication for the excessive bearing clearances. Moreover, peak characteristics are more clearly discernible, which confirms that the MSB based power signature is the most sensitive of the three electrical signatures to the fault, with a considerable increase in the peak values in the power MSB and coherence.

### 9.3 Research Contributions to Knowledge

**Contribution 1:** A sensorless VSD based mechanical system can exhibit observable AM and FM effects in both current and voltage signals. These effects are caused by a combined interaction of speed and load oscillations due to a variety of common faults such as gear tooth defects, oil shortages and excessive bearing clearances.

**Contribution 2:** The motor IPF calculated from current and voltage signals in a sensorless VSD has been shown to be more suitable for detecting and diagnosing tooth breakages and oil shortages in a downstream gearbox. In particular, the IPF has been shown to provide good, and consistent, separation between the faults of different severities under high loads, compared to that of using signal amplitudes extracted from amplitude spectrum.

**Contribution 3:** Additional knowledge on the use MSB analysis based on electrical signals, demonstrating its ability to improve the use of spectral sidebands in fault characterisation. Moreover, the MSB has been shown to possess a greater capability to reliably detect and differentiate the degrees of mechanical faults used.

**Contribution 4:** This study has made an innovative use to the instantaneous phase of voltage-current: IPVC, which is the summation of instantaneous phase, rather than the difference of IPF, to detect gear lubricant shortfall and gives better diagnostics in separating the oil shortages in wider operating conditions, compared to IPF.

## 9.4 Suggestions for Further Work

- For additional and accurate information regarding the use of electrical signals in CM, future investigations should focus on using advanced signal processing methods to extract periodic signals from noise especially noise caused by the drive that affects feature extraction.
- Since the majority of work reported in the literature concerns open-loop control, future experimental research should be conducted based on sensorless VSD. The additional work could include: gear wear, bearing faults, compound faults and should use different fault severities and a range of operating conditions.
- Additional experimental work could use IPF to detect mechanical faults such as misalignment.
- The IPF could be developed to detect and diagnose compound faults.
- Develop more effective signal processing approaches for detection and location of multiple simultaneous faults.

## REFERENCES

---

- [1] Tavner, P., *Review of condition monitoring of rotating electrical machines*. Electric Power Applications, IET, 2008. **2**(4): p. 215-247.
- [2] Bravo-Imaz, I., et al., *Mechanical fault detection in gearboxes through the analysis of the motor feeding current signature*. 2014.
- [3] Tsypkin, M. *Induction motor condition monitoring: Vibration analysis technique-A practical implementation*. in *Electric Machines & Drives Conference (IEMDC), 2011 IEEE International*. 2011. IEEE.
- [4] Rajendra, B.R. and S.V. Bhaskar, *Condition Monitoring of Gear Box by Using Motor Current Signature Analysis*. International Journal of Scientific and Research Publications: p. 563.
- [5] Tian, X., et al., *The investigation of motor current signals from a centrifugal pump for fault diagnosis*. 2014.
- [6] Hamad, N., et al. *An investigation of electrical motor parameters in a sensorless variable speed drive for machine fault diagnosis*. in *Automation and Computing (ICAC), 2016 22nd International Conference on*. 2016. IEEE.
- [7] Patton, R.J. and J. Chen, *Observer-based fault detection and isolation: Robustness and applications*. Control Engineering Practice, 1997. **5**(5): p. 671-682.
- [8] Gu, F., et al., *Electrical motor current signal analysis using a modified bispectrum for fault diagnosis of downstream mechanical equipment*. Mechanical Systems and Signal Processing, 2011. **25**(1): p. 360-372.
- [9] Akin, B. and M. Bhardwaj, *Sensored Field Oriented Control of 3-Phase Induction Motors*. Texas Instruments Incorporated, 2013.
- [10] De Almeida, A., et al., *VSDs for electric motor systems*. Final Report, SAVE Programme, European Commission, Brussels, 2001.
- [11] Shehata, S.A., et al. *Detection of induction motors rotor/stator faults using electrical signatures analysis*. in *International Conference on Renewable Energies and Power Quality (ICREPQ'13) Bilbao (Spain)*. 2013.
- [12] Krause, P.C., *Analysis of electric* 1986: p. 564.
- [13] Parekh, R., *AC Induction Motor Fundamentals*. Microchip Technology Inc, 2003.
- [14] Okamoto, K., et al., *Three-phase induction motor*. 1989, Google Patents.
- [15] Zorbas, D., *Electric Machines: Principles, Applications, and Control Schematics*. 2014: Nelson Education.
- [16] Rgeai, M.N., *Helical gearbox fault detection using motor current signature analysis*. 2007, University of Manchester.
- [17] Automation, R., *Application basics of operation of three-phase induction motors*. Sprecher+ Schuh AG Rockwell Automation, Aarau, 1996.
- [18] Abdelhamid, F., *Detection and Diagnosis of Electrical Faults in Induction Motors Using Instantaneous Phase Variation*. 2005, The University of Manchester.
- [19] Lapa, R., *Remote machine condition monitoring based on power supply measurements*. 2013, University of Huddersfield.
- [20] Da Silva, A.M., *Induction motor fault diagnostic and monitoring methods*. 2006, Faculty Of the Graduate School, Marquette University.
- [21] Chalmers, B.J. and A.C. Williamson, *AC machines: electromagnetics and design*. Vol. 4. 1991: John Wiley & Sons.

- [22] Daware, K. *Working principle and types of an Induction Motor*
- [23] Turkel, S.S. and S. Solomon, *Understanding Variable Speed Drives*. Engineering, Construction and Maintenance, 1997.
- [24] Polka, D., *Motors and drives: a practical technology guide*. 2003: Isa.
- [25] Bose, B.K. and B.K. Bose, *Power electronics and variable frequency drives: technology and applications*. Vol. 996. 1997: IEEE press New York.
- [26] O'Brien, J., *Frequency-domain Control Design for High-performance Systems*. Vol. 78. 2012: IET.
- [27] Radcliffe, S., *Teaching machines and programed instruction. An annotated bibliography*. NSPI Journal, 1963. **2**(7): p. 9-12.
- [28] U.A.Bakshi, S.C.G., *Control Systems Engineering*. 2007, India: Technical Publications Pune. 952.
- [29] Warne, D.F., *Newnes electrical power engineer's handbook*. 2005: Elsevier.
- [30] Vancil, R.F., J. Bracken, and C.J. Christenson, *Leasing of industrial equipment*. 1963: McGraw-Hill Book Company.
- [31] Buja, G.S. and M.P. Kazmierkowski, *Direct torque control of PWM inverter-fed AC motors-a survey*. Industrial Electronics, IEEE Transactions on, 2004. **51**(4): p. 744-757.
- [32] Santisteban, J.A. and R.M. Stephan, *Vector control methods for induction machines: an overview*. IEEE Transactions on education, 2001. **44**(2): p. 170-175.
- [33] Wu, B., *High-power converters and AC drives*. 2006: John Wiley & Sons.
- [34] Lane, M., *Using the AC Drive Motor as a Transducer for Detecting Electrical and Electromechanical Faults*. 2011, University of Huddersfield.
- [35] Crowder, R., *Electric Drives and Electromechanical Systems: Applications and Control*. 2006: Newnes.
- [36] Carino-Corrales, J.A., et al. *Novel methodology for improving performance of sensorless speed observers in induction motors at variable load conditions*. in *IECON 2012-38th Annual Conference on IEEE Industrial Electronics Society*. 2012. IEEE.
- [37] Abusaad, S., F. Gu, and A. Ball, *Observer-based Fault Detection and Diagnosis for Mechanical Transmission Systems with Sensorless Variable Speed Drives*. 2015.
- [38] Vas, P., *Artificial-intelligence-based electrical machines and drives: application of fuzzy, neural, fuzzy-neural, and genetic-algorithm-based techniques*. Vol. 45. 1999: Oxford University Press.
- [39] Holtz, J., *Sensorless control of induction motor drives*. Proceedings of the IEEE, 2002. **90**(8): p. 1359-1394.
- [40] Abu-Rub, H., A. Iqbal, and J. Guzinski, *High performance control of AC drives with Matlab/Simulink models*. 2012: John Wiley & Sons.
- [41] Paladugu, A. and B.H. Chowdhury, *Sensorless control of inverter-fed induction motor drives*. Electric Power Systems Research, 2007. **77**(5): p. 619-629.
- [42] Aktaibi, A. and M. Rahman, *Dynamic Simulation of a Three-Phase Induction Motor Using Matlab Simulink*. currents, 2011. **8**: p. 9.
- [43] Ong, C.-M., *Dynamic simulation of electric machinery: using MATLAB/SIMULINK*. Vol. 5. 1998: Prentice Hall PTR Upper Saddle River, NJ.
- [44] Khan, H., *Field Oriented Control*. 2008, Renesas.
- [45] Concari, C., G. Franceschini, and C. Tassoni. *Rotor fault detection in closed loop induction motors drives by electric signal analysis*. in *Electrical Machines, 2008. ICEM 2008. 18th International Conference on*. 2008. IEEE.

- [46] Sasi, A.B., et al., *THE EXPLOITATION OF INSTANTANEOUS ANGULAR SPEED FOR CONDITION MONITORING OF ELECTRIC MOTORS*. Condition Monitoring and Diagnostic Engineering Management, 2001: p. 311.
- [47] Vas, P., *Parameter estimation, condition monitoring, and diagnosis of electrical machines*. 1993: Oxford University Press, USA.
- [48] Han, Y. and Y. Song, *Condition monitoring techniques for electrical equipment—a literature survey*. Power Delivery, IEEE Transactions on, 2003. **18**(1): p. 4-13.
- [49] Zhou, W., T.G. Habetler, and R.G. Harley. *Bearing condition monitoring methods for electric machines: A general review*. in *Diagnostics for Electric Machines, Power Electronics and Drives. SDEMPED. IEEE International Symposium on*. 2007. IEEE.
- [50] Sasi, A.Y.B. and A. Ball, *Exploitation of Instantaneous Angular Speed for Machinery Condition Monitoring*. 2005: University of Manchester.
- [51] Malhotra, S. and M. Soni, *Fault diagnosis of induction motor*. European Scientific Journal, 2013.
- [52] Bin Hasan, M., *Current based condition monitoring of electromechanical systems. Model-free drive system current monitoring: faults detection and diagnosis through statistical features extraction and support vector machines classification*. 2013, University of Bradford.
- [53] Sabaghi, M. and H.F. Farahani, *Monitoring of induction motor temperature under unbalanced supplying by stator resistance estimation*. Indian Journal of Science and Technology, 2012. **5**(3): p. 2354-2359.
- [54] Pandey, K., P. Zope, and S. Suralkar. *Review on fault diagnosis in three-phase induction motor*. in *IJCA Proceedings on National Conference*. 2012. Foundation of Computer Science (FCS).
- [55] Mehala, N., *Condition monitoring and fault diagnosis of induction motor using motor current signature analysis*. 2010, NATIONAL INSTITUTE OF TECHNOLOGY KURUKSHETRA, INDIA.
- [56] Huang, X., *Diagnostics OF Air Gap Eccentricity IN Closed-Loop Drive-Connected Induction Motors*. 2005, Citeseer.
- [57] Siddiqui, K.M., K. Sahay, and V. Giri, *Health monitoring and fault diagnosis in induction motor—a review*. International Journal of Advanced Research in Electrical, Electronics and Instrumentation Engineering, 2014. **3**(1): p. 6549-6565.
- [58] Mehala, N. and R. Dahiya, *Motor current signature analysis and its applications in induction motor fault diagnosis*. International journal of systems applications, engineering & development, 2007. **2**(1): p. 29-35.
- [59] Schoen, R.R., et al., *Motor bearing damage detection using stator current monitoring*. Industry Applications, IEEE Transactions on, 1995. **31**(6): p. 1274-1279.
- [60] Verma, A.K., S. Sarangi, and M. Kolekar, *Experimental investigation of misalignment effects on rotor shaft vibration and on stator current signature*. Journal of Failure Analysis and Prevention, 2014. **14**(2): p. 125.
- [61] Mehala, N. and R. Dahiya, *Rotor faults detection in induction motor by wavelet analysis*. International journal of engineering science and technology, 2009. **1**(3): p. 90-99.
- [62] ; Available from: <https://www.joliettech.com/products/variable-frequency-drive-systems-and-controls/what-is-a-variable-frequency-drive-part-1/>.
- [63] Singh, G., *Induction machine drive condition monitoring and diagnostic research—a survey*. Electric Power Systems Research, 2003. **64**(2): p. 145-158.

- [64] Bonaldi, E.L., et al., *Predictive maintenance by electrical signature analysis to induction motors*, in *Induction Motors-Modelling and Control*. 2012, InTech.
- [65] Zerdali, E. and M. Barut. *MRAS based real-time speed-sensorless control of induction motor with optimized fuzzy-PI controller*. in *Sensorless Control for Electrical Drives and Predictive Control of Electrical Drives and Power Electronics (SLED/PRECEDE), 2013 IEEE International Symposium on*. 2013. IEEE.
- [66] Tavner, P., *Review of condition monitoring of rotating electrical machines*. IET Electric Power Applications, 2008. **2**(4): p. 215-247.
- [67] Payne, B.S., *Condition monitoring of electric motors for improved asset management*. 2003: University of Manchester.
- [68] El Hachemi Benbouzid, M., *A review of induction motors signature analysis as a medium for faults detection*. Industrial Electronics, IEEE Transactions on, 2000. **47**(5): p. 984-993.
- [69] Drif, M.h. and A.M. Cardoso. *Rotor cage fault diagnostics in three-phase induction motors, by the instantaneous non-active power signature analysis*. in *Industrial Electronics, 2007. ISIE 2007. IEEE International Symposium on*. 2007. IEEE.
- [70] Pires, V.F., et al., *Motor square current signature analysis for induction motor rotor diagnosis*. Measurement, 2013. **46**(2): p. 942-948.
- [71] Shaeboub, A., et al. *Detection and diagnosis of motor stator faults using electric signals from variable speed drives*. in *Automation and Computing (ICAC), 2015 21st International Conference on*. 2015. IEEE.
- [72] Nandi, S., H.A. Toliyat, and X. Li, *Condition monitoring and fault diagnosis of electrical motors-a review*. Energy Conversion, IEEE Transactions on, 2005. **20**(4): p. 719-729.
- [73] Ye, Z., B. Wu, and A. Sadeghian, *Current signature analysis of induction motor mechanical faults by wavelet packet decomposition*. Industrial Electronics, IEEE Transactions on, 2003. **50**(6): p. 1217-1228.
- [74] Thomson, W.T. and R.J. Gilmore. *Motor current signature analysis to detect faults in induction motor drives-fundamentals, Data interpretation, and industrial case histories*. in *Proceedings of 32nd Turbo machinery Symposium, A&M University, Texas, USA*. 2003.
- [75] Jung, J.-H., J.-J. Lee, and B.-H. Kwon, *Online diagnosis of induction motors using MCSA*. Industrial Electronics, IEEE Transactions on, 2006. **53**(6): p. 1842-1852.
- [76] Kar, C. and A. Mohanty, *Monitoring gear vibrations through motor current signature analysis and wavelet transform*. Mechanical systems and signal processing, 2006. **20**(1): p. 158-187.
- [77] Benbouzid, M.E.H., M. Vieira, and C. Theys, *Induction motors' faults detection and localization using stator current advanced signal processing techniques*. Power Electronics, IEEE Transactions on, 1999. **14**(1): p. 14-22.
- [78] Alwodai, A., et al. *Modulation signal bispectrum analysis of motor current signals for stator fault diagnosis*. in *Automation and Computing (ICAC), 2012 18th International Conference on*. 2012. IEEE.
- [79] Haram, M., et al. *An Investigation of the electrical response of a variable speed motor drive for mechanical fault diagnosis*. 2011. COMADEM.
- [80] Naid, A., et al. *Bispectrum Analysis of Motor Current Signals for Fault Diagnosis of Reciprocating Compressors*. in *Key Engineering Materials*. 2009. Trans Tech Publ.
- [81] Lane, M., et al., *Investigation of Motor Current Signature Analysis in Detecting Unbalanced Motor Windings of an Induction Motor with Sensorless Vector Control Drive*, in *Vibration Engineering and Technology of Machinery*. 2015, Springer. p. 801-810.

- [82] Gutierrez-Villalobos, J.M., et al., *Sensorless FOC Performance Improved with On-Line Speed and Rotor Resistance Estimator Based on an Artificial Neural Network for an Induction Motor Drive*. *Sensors*, 2015. **15**(7): p. 15311-15325.
- [83] Mabrouk, A., et al., *On-line fault diagnostics in operating three-phase induction motors by the active and reactive currents*. *International Journal of System Assurance Engineering and Management*, 2017. **8**(1): p. 160-168.
- [84] Bonaldi, E.L., et al., *Predictive maintenance by electrical signature analysis to induction motors*. 2012: INTECH Open Access Publisher.
- [85] Kumar, K.V., *A Review of Voltage and Current Signature Diagnosis in Industrial Drives*. *International Journal of Power Electronics and Drive Systems*, 2011. **1**(1): p. 75.
- [86] Legowski, S.F., A. Ula, and A.M. Trzynadlowski, *Instantaneous power as a medium for the signature analysis of induction motors*. *Industry Applications, IEEE Transactions on*, 1996. **32**(4): p. 904-909.
- [87] Ashari, D., et al., *Detection and Diagnosis of Broken Rotor Bar Based on the Analysis of Signals from a Variable Speed Drive*. 2014.
- [88] Abusaad, S., et al. *The detection of lubricating oil viscosity changes in gearbox transmission systems driven by sensorless variable speed drives using electrical supply parameters*. in *Journal of Physics: Conference Series*. 2015. IOP Publishing.
- [89] Abusaad, S., et al., *Investigating the Effect of Water Contamination on Gearbox Lubrication based upon Motor Control Data from a Sensorless Drive*. 2014.
- [90] Mabrouk, A., et al. *Discriminating time-varying loads and rotor cage fault in induction motors*. in *Diagnostics for Electric Machines, Power Electronics and Drives (SDEMPED), 2013 9th IEEE International Symposium on*. 2013. IEEE.
- [91] Khodapanah, M., A.F. Zobaa, and M. Abbod. *Monitoring of power factor for induction machines using estimation techniques*. in *Power Engineering Conference (UPEC), 2015 50th International Universities*. 2015. IEEE.
- [92] Ratnani, M.P.L., *Mathematical Modelling of an 3 Phase Induction Motor Using Matlab/Simulink*. 2014. **4**: p. 62-67.
- [93] Drif, M. and A.M. Cardoso. *The instantaneous power factor approach for rotor cage faults diagnosis in three-phase induction motors*. in *Power Electronics, Electrical Drives, Automation and Motion, 2008. SPEEDAM 2008. International Symposium on*. 2008. IEEE.
- [94] Arabacı, H., O. Bilgin, and A. Ürkmez, *Rotor bar fault diagnosis by using power factor*. *Power*, 2011. **500**: p. 1.
- [95] Ibrahim, A., et al., *A new bearing fault detection method in induction machines based on instantaneous power factor*. *IEEE Transactions on Industrial Electronics*, 2008. **55**(12): p. 4252-4259.
- [96] Merritt, H.E., *Gear engineering*. 1971: John Wiley & Sons.
- [97] Stefani, A., *Induction Motor Diagnosis in Variable Speed Drives*. PhD in Electrical Engineering Final Dissertation, University of Bologna, 2010.
- [98] Shnibha, R. and A. Albarabar. *Smart Technique for Induction Motors Diagnosis by Monitoring the Power Factor Using Only the Measured Current*. in *Journal of Physics: Conference Series*. 2012. IOP Publishing.
- [99] Lane, M., et al., *Investigation of reductions in motor efficiency and power factor caused by stator faults when operated from an inverter drive under open loop and sensorless vector modes*. *Systems Science & Control Engineering*, 2017. **5**(1): p. 361-379.

- [100] Alshandoli, A.F., A. Ball, and F. Gu. *Instantaneous phase variation (IPV) for rotor bar fault detection and diagnosis*. in *Electrical Engineering, 2008. ICEE 2008. Second International Conference on*. 2008. IEEE.
- [101] Ratnani, M.P.L. and A. Thosar, *Mathematical Modelling of an 3 Phase Induction Motor Using MATLAB/Simulink*. International Journal Of Modern Engineering Research (IJMER), 2014. **4**(6): p. 62-67.
- [102] Naima.Hamad, X.S., Ruiliang Zhang, Samieh Abusaad, Fengshou Gu and Andrew D. Ball, *The Diagnostics of Lubricant Shortages in a Two Stage Gearbox Using the Instantaneous Phases of the AC Motor with Sensorless Drives*, in *Automation and Computing (ICAC), 2018 24th International Conference on*. 2018, IEEE.
- [103] de Almeida, A.R. and G. ENERGIA. *Lubricant condition monitoring*. in *Gears and transmission workshop, Faculdade de Engenharia da Universidade do Porto, Portugal, 5th June*. 2003.
- [104] Otto, H.-P., *Flank load carrying capacity and power loss reduction by minimised lubrication*. 2009, Technische Universität München.
- [105] A. Bhatia, B.E. *Basic Fundamentals of Gear Drives*. 2012.
- [106] Radzevich, S.P. and D.W. Dudley, *Handbook of practical gear design*. 1994: CRC press.
- [107] Mehta, N.S., N.J. Parekh, and R.K. Dayatar, *Improve the thermal efficiency of gearbox using different type of gear oils*. International Journal of Engineering and Advanced Technology (IJEAT), ISSN, 2013: p. 2249-8958.
- [108] Gu, F., et al. *Motor current signal analysis using a modified bispectrum for machine fault diagnosis*. in *ICCAS-SICE, 2009*. IEEE.
- [109] Romero-Troncoso, R., et al. *Broken rotor bar detection in VSD-fed induction motors at startup by high-resolution spectral analysis*. in *Electrical Machines (ICEM), 2014 International Conference on*. 2014. IEEE.
- [110] Zhang, R., et al., *Gear wear monitoring by modulation signal bispectrum based on motor current signal analysis*. 2017. **94**: p. 202-213.
- [111] Haram, M., et al. *Electrical Motor Current Signal Analysis using a Modulation Signal Bispectrum for the Fault Diagnosis of a Gearbox Downstream*. in *Journal of Physics: Conference Series*. 2012. IOP Publishing.
- [112] Gu, F., et al., *A Novel Method for the Fault Diagnosis of a Planetary Gearbox based on Residual Sidebands from Modulation Signal Bispectrum Analysis*. 2014.
- [113] Gu, F., et al., *A new method of accurate broken rotor bar diagnosis based on modulation signal bispectrum analysis of motor current signals*. Mechanical Systems and Signal Processing, 2015. **50**: p. 400-413.
- [114] Jang, B., et al. *Machine fault detection using bicoherence spectra*. in *Instrumentation and Measurement Technology Conference, 2004. IMTC 04. Proceedings of the 21st IEEE*. 2004. IEEE.
- [115] Ong, C.-M.-M.O., *Dynamic simulation of electric machinery using Matlab/Simulink*. 1998: Prentice-Hall PTR.
- [116] Group, M.R.W., *Report of large motor reliability survey of industrial and commercial installations, Part I*. IEEE Trans. Ind. Appl, 1985. **21**(4): p. 853-864.
- [117] Richard, C., *Electric Drives and Electromechanical Systems: Applications and Control*. 2006.
- [118] Eutrotherm, *"The Theory of Vector Control"*, *Eutrotherm Drives Training*, issue K, 2011.

- [119] Salahat, M., et al., *Modular Approach for Investigation of the Dynamic Behavior of Three-Phase Induction Machine at Load Variation*. Engineering, 2011. **3**(05): p. 525.
- [120] De Doncker, R., D.W. Pulle, and A. Veltman, *Advanced electrical drives: analysis, modeling, control*. 2010: Springer Science & Business Media.
- [121] Adisa A. Jimoh, P.-J.V.a.E.K.A., *Modelling and Analysis of Squirrel Cage Induction Motor with Leading Reactive Power Injection*. 2012.
- [122] Robyns, B., *Vector Control of Induction Machines: Desensitisation and Optimisation Through Fuzzy Logic (Power Systems)*. 2012: Springer Verlag London Limited.
- [123] Bose, B., *Modern Power Electronics and AC Drives*” by Prentice-Hall. Inc, Publication, 2002: p. 70-74.
- [124] Behera, P.K., M.K. Behera, and A.K. Sahoo, *Comparative Analysis of scalar & vector control of Induction motor through Modeling & Simulation*. international journal of innovative research in electrical, electronics, instrumentation and control engineering, 2014. **2**(4): p. 1340-1344.
- [125] Abusaad, S., *The Utilization of Information Available in the Sensorless Control System of an AC Induction Motor for Condition Monitoring in Computing and Engineering School*. 2016, Huddersfield University.
- [126] THEODOSSIADES, S. and S. NATSIAVAS, *Non-linear dynamics of gear-pair systems with periodic stiffness and backlash*. Journal of Sound and vibration, 2000. **229**(2): p. 287-310.
- [127] Krause, P., et al., *Analysis of electric machinery and drive systems*. Vol. 75. 2013: John Wiley & Sons.
- [128] Le-Huy, H. *Comparison of field-oriented control and direct torque control for induction motor drives*. in *Industry Applications Conference, 1999. Thirty-Fourth IAS Annual Meeting. Conference Record of the 1999 IEEE*.
- [129] ABB, *Technical Guide No. 100, High Performance Drive-speed and torque regulation, in High Performance Drives-speed and torque regulation*. ABB Industrial Systems, Editor 1996, ABB Industrial Systems, Inc, 1996.
- [130] Dudley, D.W., *Gear handbook*. 1962: New york, McGraw-hill.
- [131] Naima Hamad, S.a.S., Fengshou Gu and Andrew Ball, *Electrical Signature Analysis using Modulation Signal Bispectrum for Faults Diagnosis of Induction Motor Systems with Sensorless Variable Speed Drives*, in *Libyan International Conference on Electrical Engineering and Technologies*. 2018: Tripoly/ Libya. p. 312-318.
- [132] Salgueiro, J., et al., *On-line oil monitoring and diagnosis*. Strojniški vestnik-Journal of Mechanical Engineering, 2013. **59**(10): p. 604-612.
- [133] Höhn, B., K. Michaelis, and H. Otto, *Flank load carrying capacity and power loss reduction by minimized lubrication*. Gear Technology, 2011: p. 53-62.
- [134] Banks, J.C., K.M. Reichard, and M.S. Brought. *Lubrication level diagnostics using vibration analysis*. in *Aerospace Conference, 2004. Proceedings. 2004 IEEE*. 2004. IEEE.
- [135] Rajora, R. and H.K. Dixit, *Effect of Lube Oil Temperature on Turbine Shaft Vibration*. Journal of Mechanical Engineering and Robotics Research, 2013. **2**(2): p. 330-333.
- [136] Gorla, C., et al., *CFD simulations of splash losses of a gearbox*. Advances in Tribology, 2012.
- [137] Brethee, K.F., et al., *Influence of Lubricant Starvation on Gearbox Vibration Signatures for Condition Monitoring*. 2016.

- [138] Mokšin, V., A. Kilikevičius, and I. Tetsman, *7. Investigation of vibrational behavior of friction pair under starved lubrication conditions*. 2013.
- [139] Bai, Z.F., H. Zhang, and Y. Sun, *Wear prediction for dry revolute joint with clearance in multibody system by integrating dynamics model and wear model*. Latin American Journal of Solids and Structures, 2014. **11**(14): p. 2624-2647.
- [140] Seetharaman, S., et al., *Oil churning power losses of a gear pair: experiments and model validation*. Journal of Tribology, 2009. **131**(2): p. 022202.
- [141] SAAD, S.A.A., *THE UTILISATION OF INFORMATION AVAILABLE IN THE SENSORLESS CONTROL SYSTEM OF AN AC INDUCTION MOTOR FOR CONDITION MONITORING*, in *Computing and Engineering School*. 2015, Huddersfield.
- [142] Changenet, C. and P. Velex, *A model for the prediction of churning losses in geared transmissions—preliminary results*. Journal of Mechanical Design, 2007. **129**(1): p. 128-133.
- [143] Diab, Y., F. Ville, and P. Velex, *Investigations on power losses in high-speed gears*. Proceedings of the Institution of Mechanical Engineers, Part J: Journal of Engineering Tribology, 2006. **220**(3): p. 191-198.
- [144] Brethee, K., F. Gu, and A. Ball, *Condition Monitoring of Lubricant Starvation Based on Gearbox Vibration Signatures*. International Journal of COMADEM, 2017. **20**(3).
- [145] Luo, C., et al., *Research on the sparse representation for gearbox compound fault features using wavelet bases*. Shock and Vibration, 2015.
- [146] Oswald, F.B., E.V. Zaretsky, and J.V. Poplawski, *Effect of internal clearance on load distribution and life of radially loaded ball and roller bearings*. Tribology Transactions, 2012. **55**(2): p. 245-265.
- [147] Rehab, I.A., *The Optimization of Vibration Data Analysis for the Detection and Diagnosis of Incipient Faults in Roller Bearings*. 2016, University of Huddersfield.
- [148] Sheng, D.-p., et al., *Bifurcation and chaos study on transverse-torsional coupled 2K-H planetary gear train with multiple clearances*. Journal of Central South University, 2016. **23**(1): p. 86-101.